DIFFUSION OF METEORIC PLASMA

A thesis

presented for the degree

of

Doctor of Philosophy in Physics

in the

University of Canterbury

by

T.H. Webb

University of Canterbury

1980

CONTENTS

LIST OF FIGURES

LIST OF TABLES

ABSTRACT

A summary of the present understanding of the behaviour of meteoric ionization is given and cooling times for meteoric particles are calculated. While the cooling time for neutral atoms and positive ions is short compared to echo life-times, that for electrons is not and thermalization effects may be observed above 100 km.

The effect of winds and sky noise on diffusion coefficient measurements has been investigated and it appears that the scatter in measurements predicted accounts for that observed in practice.

A magnetic effect on meteor train diffusion has been observed in underdense meteors by using a backscatter radar, with a 40 kW pulsed transmitter operating at 26.36 MHz. Echo heights were measured with a spaced interferometer. The observed magnetic effect is consistent with that expected from the formation of electron and ion ellipses of ionization. Other results recorded when anisotropic, ambipolar diffusion is more likely do not show this effect. Previous observations, limited to overdense meteors, are shown to be consistent with theoretical predictions and the expected magnetic effects on diffusion for general train orientations are discussed.

Phase variations caused by Fresnel diffraction as meteor trains are formed have been studied and shown to be a cause of systematic decreases in echo heights (during the

lifetime of an echo) measured with spaced antennas. An experiment to verify this is suggested.

A chemical model developed to take into account ionization loss may account for anomalously high D values below 90 km observed in previous data. High D values measured in this work cannot be explained by this simple model.

CHAPTER 1

INTRODUCTION

A meteoroid entering the earth's atmosphere is usually completely ablated, leaving a cylindrical column of neutral meteoric atoms, positive ions and electrons, referred to as a meteor train. These trains are produced predominantly in the 80 to 110 km height range known as the meteor region. The train ionization can be studied by radar because electrons in the column will reflect incident radio waves if the operating wavelength is not too small in comparison with the train radius.

The reflecting properties depend on the electron density within the train. When the density is sufficiently high the train reflects as if it were a metal cylinder - in this case electron line densities, q, greater than 2×10^{14} m^{-1} are necessary: such trains are referred to as overdense. In less dense trains ($q << 2 \times 10^{14}$ m^{-1}) the radio wave penetrates the column and the electrons backscatter independently. These trains, referred to as underdense, are the type of interest in this present work. When an underdense train expands under the action of diffusion, phase interference attenuates the reflected radio wave. Thus, the rate of decrease of a radar echo can be used to infer the effective diffusion coefficient of the train by using the well known classical relation (McKinley, 1961)

$$\tau = \frac{\lambda^2}{16\ \pi^2 D}$$

where τ is the time taken for the echo to decrease in amplitude by the factor exp(1), λ is the radar wavelength and D is the diffusion coefficient.

Observationally this ideal picture is distorted for a sample of radio-meteors in several ways: the trend with height of measured D values does not agree with laboratory measurements and there is a large scatter in the D values measured at a particular height as well. Furthermore it is predicted that the diffusion of meteor trains above 95 km will be affected by the earth's magnetic field. The geomagnetic field reduces the transverse diffusion coefficient of electrons to below that for ions above this height and thus inhibits train diffusion in certain directions for particular train orientations. Some of these magnetic effects have been observed in overdense meteor trains, but not in underdense ones: geomagnetic effects on underdense meteor trains are the prime subject of this present work.

In Chapter 2 the evolution of the ionized train immediately after its formation is discussed. The expected ion diffusion coefficient is calculated for meteor heights; the cooling times of hot meteoric particles are computed and other aspects of train behaviour are summarised.

The factors affecting measurements of meteor diffusion such as the shape of train cross-sections, atmospheric winds

and sky noise are discussed in Chapter 3. Also mentioned are the effect of Fresnel phase variations and of atmospheric refraction on measurements of train heights.

Chapter 4 summarises the first two chapters and then previous work on both magnetic effects and the variation of diffusion coefficients with height is discussed. The experiment performed in this work is then described.

Chapter 5 presents the geometrical aspects relevant to the study of the magnetic effects both by a backscatter radar and with use of forward-scatter with a remote transmitter so that meteor train orientations can be measured.

Chapter 6 contains the description of the system used in the experiment. A 40 kW pulsed transmitter with an operating frequency of 26.36 MHz was used for the backscatter results while a similar 10 kW transmitter, located 150 km to the west, was used for forward-scatter. Echo heights were located by measurements of the phase differences between signals received by three spaced antennas. These data, as well as echo range, received amplitude and doppler information, were stored on paper tape before further processing.

The method of data analysis and the results are presented in Chapter 7. First, general characteristics of the results are examined. Secondly, the observed magnetic effect is discussed and shown to be consistent with theoretical predictions, but other effects that could be expected on theoretical grounds are not observed. Finally the observed variation of measured diffusion coefficient with height is discussed in terms of the effect of the earth's magnetic field and of chemical reactions.

In Chapter 8 this work is summarised and some suggestions are made for future research. The appendices contain listings of computer programs used in the data analysis.

[NOTE: Throughout this thesis $\log_{10}$ is written as log and $\log_e$ is written as ln.]

CHAPTER 2

PROCESSES IN THE IONIZED COLUMN

2.1 INTRODUCTION

When a meteoroid enters the earth's atmosphere atoms are ablated from it by collisions with air molecules. Further collisions with the atmospheric species ionize some of the ablated atoms so that a column of neutral atoms, positive ions and electrons is formed. In this chapter the subsequent behaviour of this column of ionization is examined. The discussion is limited to faint meteors, that is meteors leaving trains whose line density of electrons, q, is less than 2×10^{14} m^{-1}. As these meteors are studied primarily by radar, the discussion is orientated to those effects that are observed by radar techniques.

First, the formation of a train with a certain initial radius is discussed. Further expansion of the column is then controlled by ambipolar diffusion. The relevant diffusion coefficients, as measured in the laboratory, are presented. However, the rate of ambipolar diffusion depends on the temperature of each species in the train. Initially the meteoric atoms, ions and electrons will not be in thermal equilibrium with the ambient atmosphere. The time for neutral particles and positive ions to thermalize is discussed and the thermalization time for the electrons is found.

Ambipolar diffusion may be further affected by the earth's magnetic field. These effects are discussed and the expected distribution of the meteor ionization with respect to the geomagnetic field direction is described.

The ions and electrons formed in the train take part in chemical reactions, some of which reduce the electron density. The effective loss of ionization is presented for different heights in the meteor region.

Finally, the distribution of the ionization density along the train is discussed. When considered in relation to atmospheric motions, the irregular nature of this distribution is expected to introduce a large scatter in the measured diffusion coefficients. These effects are considered in the next chapter.

2.2 INITIAL RADIUS

The initial radius is usually defined as the radius of the meteor train when species present have reached thermal velocities. The train radius is defined as the radius at which the axial number density of electrons has decreased by the factor exp(1). The radial density distribution is assumed to be a Gaussian. Atoms ablated from the meteor on impact with air molecules initially travel with nearly the original meteor velocity. Positive ions are formed during subsequently collisions with atmospheric molecules. The collisions with air molecules rapidly slow the atoms and positive ions to thermal velocities. Lebedinets and Portnyagin (1966) suggest that

the initial radius depends mainly on the mean free path lengths between the first few collisions as the effective collision cross-section increases rapidly when the particle velocity decreases. For a given species, there is little difference between the effective diffusion cross-section of the atoms and ions at meteor velocities (Portnyagin, 1966). Thus the initial radius for ions and neutral atoms of a particular element is the same. Electrons will be confined to the train by the strong electrostatic forces.

The reflection coefficient of the train depends on the column dimensions. The reflected wave is attenuated by interference effects when the initial radius is of the order of the radar wavelength. This may cause selection effects in the radar measurements so that it is important to know how the initial radius varies with height for underdense meteors.

In a theoretical study, Manning (1958) predicts that the initial radius, r_o, varies as

$$r_o \approx 2.8\ell$$

for a meteor velocity of 40 km/s, where ℓ is the mean free path of the ions at thermal energies. There is a small dependence of r_o on meteor velocity. Here no account is taken of the variation in effective diffusion cross-section, Q_d, with ion velocity. It is assumed that each ion undergoes many collisions before reaching thermal velocities.

Kashcheyev and Lebedinets (1963) found that

$$r_o \approx 7.8\ell$$

for a meteor velocity of 40 km/s. They found a much stronger dependence on meteor velocity as the change in Q_d with ion velocity is considered. Again it is assumed that the ions undergo many collisions before becoming thermalized. This assumption is not made by Lebedinets and Portnyagin (1966) who place limits on r_o of

$$0.93\ \ell_o < r_o < 1.5\ \ell_o\ .$$

Here ℓ_o is the ion (or atom) mean free path before the first collision. This value also has a strong velocity dependence.

In all of the studies mentioned r_o is predicted to increase exponentially with height, since

$$\ell \propto \rho^{-1}$$

where ρ is the atmospheric density. The experimental results of Greenhow and Hall (1960) show a weaker dependence of r_o on height. For

$$r_o \propto \rho^{-a}$$

they find a = 0.35. These results have been criticised for being measurements of transition-type decays instead of truly underdense ones, although Greenhow and Hall state that mainly underdense decays were used. The results of Baggaley (1970) give $a = 0.45 \pm 0.03$. In this experiment only underdense

decays were used. Both of these experiments have estimated the meteor height from echo decay rate. This is not an accurate method as a large scatter is observed in values of diffusion coefficient for a given height. This scatter will be introduced into the r_o-height measurements, but should not change the height dependence of r_o.

An explanation for the difference between the theoretical and experimental results is offered by Hawkes and Jones (1978). They use a meteor ablation model in which grains of material are held together by a "glue" that has a lower melting point than the grains. In the ablation process the glue melts, releasing the grains, which in turn ablate when their radiation losses are exceeded by their incident energy flux. If the meteor was originally rotating, the grains may disperse radially before ablating, increasing the predicted initial radius. High in the meteor region the grains have had insufficient time to disperse far, so that the effect of rotation is to lessen the ρ dependence of initial radius in one particular train. Collisions of meteoroids in interplanetary space are shown to give sufficient rotational speeds to explain the observed differences in r_o at heights less than 100 km. Unfortunately the dependence of initial radius on height for a population of meteors is not easy to predict from this theory.

The results of Baggaley (1970), shown in Table 2.1 are used in this thesis.

Table 2.1: Values of initial radius.

Height(km)	80	85	90	95	100	105	110	115
Initial Radius(m)	0.20	0.35	0.48	0.72	1.06	1.54	2.14	2.90

2.3 AMBIPOLAR DIFFUSION

After the rapid radial expansion of the ionized meteor train to the initial radius, further expansion is controlled by ambipolar diffusion. The diffusion equations for a cylindrical column of ionization can be solved to find the volume density of ionization, N. (See Kaiser, 1953 and McKinley, 1961 for a more detailed treatment.)

$$N = \frac{q}{\pi(4Dt + r_o^2)} \exp\left[-\frac{r^2}{(4Dt + r_o^2)}\right] \qquad 2.1$$

The radial ionization distribution is thus a Gaussian. Here q is the electron line density of the train, t is the elapsed time from the initial radius formation, r is the radius and D is the ambipolar diffusion coefficient. It has been assumed that there is no magnetic field and that the number densities of positive ions and electrons (N_+ and N_-) and their derivatives are approximately equal. Thus

$$N_+ \approx N_- = N. \qquad 2.2$$

This is a valid assumption because of the strong electrostatic forces. The effect of the geomagnetic field is considered in section 2.6. It has also been assumed that there is no loss

of ionization by chemical processes. This is not true for lower heights and is considered in section 2.7.

It can be shown from kinetic theory (see for example Kaiser (1953) that the ambipolar diffusion coefficient is

$$D_a \approx D_+(1 + \frac{T_e}{T_i}) \qquad 2.3$$

where D_+ is the ion diffusion coefficient, T_i is the positive ion temperature and T_e is the electron temperature. After the initial radius formation the positive ions have thermalized so that T_i is equal to the ambient temperature. Thermalization is considered further in section 2.5.

The positive ion diffusion coefficient can be derived from the work of Dalgarno (1961) to be

$$D_+ = 3.35 \times 10^3 \frac{T}{\sum_s N_s(\alpha_s\mu_s)^{\frac{1}{2}}} \text{ m}^2/\text{s} \qquad 2.4$$

T is the ambient (and ion) temperature, N_s are the number densities of the atmospheric species (m^{-3}), α_s are the polarizabilities of these species (m^3) and μ_s are the reduced masses (u) where

$$\mu_s = \frac{m_+ \cdot m_s}{m_+ + m_s} .$$

Here m_+ is the positive ion mass (u) and m_s are the masses of the atmospheric species (u). The dominant species are molecular nitrogen and oxygen and atomic oxygen. Values used for N_s and T are those of Blank (1974). Diurnal and seasonal variations in these values are discussed in section 2.4.

Equation 2.4 gives the diffusion coefficient for one species of ion, mass m_i, in a neutral gas. A meteor train is a mixture of many ions, so that equation 2.2 is not strictly applicable. Portnyagin (1971) has presented a full analysis of this problem and finds up to 35% scatter in the measured value of D.

However, values of initial radius used were those of Lebedinets and Portnyagin (1966). These values do not agree with the experimental measurements for heights above 100 km. Secondly, a dependence of

$$D \propto \frac{1}{\mu}$$

is stated as being used whereas

$$D \propto \frac{1}{\sqrt{\mu}}$$

agrees with equation 2.2. Thirdly, it is assumed that all atomic species have an equal probability of becoming ions. This does not agree with the results of Sida (1969). Fourthly, the scatter of 35% for D is found by comparing meteors of different composition. As over 90% of meteorites are classed as chondrites which have a consistent composition (Brown, 1973) it is reasonable to assume that the same is true for meteors. This means that the 35% variation should be regarded as an unusual event and not a characteristic variation.

Each of the first three points mentioned will reduce the scatter in D. By using an average mass for the ions in the train, D may be found more easily. Any scatter in D due to the different ion species would normally be less than $\pm$ 5%.

To find the relevant values for the polarizability and positive ion mass in order to calculate D_+, the composition of the train ionization must be found. Sida (1969) gives the ionization probability for the most abundant atoms found in the meteor wake over the range of meteor velocities. The relative abundance for a typical chondrite meteorite is also given so that the abundance of positive ions in the train can be calculated for each meteor velocity. The relative abundance for a typical meteoroid could differ from a chondrite as the more fragile meteoroids will fragment and be completely ablated. The presence of metallic ions and oxygen ions has been deduced from meteor spectra (Baggaley, 1979a) which is consistent with a chondrite composition.

For meteor velocities greater than 30 km/s, O^+ is the dominant ion formed. It is shown in section 2.7 that this ion reacts rapidly with O_2 and N_2 to form O_2^+ and NO^+ ions. If this reaction proceeds much more rapidly than the time in which D is measured, the average ion mass is increased. The time in which D is measured is approximately the echo decay time, τ.

$$\tau = \frac{\lambda^2}{16\pi^2 D}$$

Table 2.2 shows values of decay time (for λ = 11.38m) with the combined time constant for the reaction of O^+ with O_2 and N_2 for some heights in the meteor region. The values of D were taken from Kaiser et al (1969) who derived them from rocket measurements of electron diffusion coefficient.

Table 2.2: Decay and reaction times

Height(km)	90	95	100	105	110
Decay time(ms)	370	164	68	29	13
Reaction time(ms)	2	6	17	50	135

From these results O_2^+ is used for heights of less than 105 km in the calculation of average ion mass and polarizability. For heights greater than or equal to 105 km O^+ is treated as dominant.

Table 2.3 shows the average ion mass for the range of meteor velocities.

Table 2.3: Average ion mass

Meteor velocity(km/s)	20	30	40	50	60	70
Average ion mass(u) H < 105 km	38.2	35.0	33.6	33.2	33.1	33.0
Average ion mass (u) H $\geqslant$ 105 km	35.1	26.0	21.4	19.9	19.4	19.3

The polarizabilities used for calculating D_+ are given in Table 2.4.

These values are only valid for the diffusion of ions in an unlike gas. Since both O_2^+ and O^+ are dominant at different times in meteor trains, their diffusion in molecular and atomic

Table 2.4: Polarizability of atmospheric species.

Species	Polarizability (m^3)	Source
N_2	1.76×10^{-30}	Hirschfelder et al. (1964)
O_2	1.60×10^{-30}	Hirschfelder et al. (1964)
O	7.7×10^{-31}	Alpher and White (1959)

oxygen should be considered. Banks (1966b) finds that the contribution to the collision cross-section of O_2 undergoes a transition from polarizability to charge exchange at 800 K. The transition temperature for atomic oxygen is at 240K. Temperatures above 240 K do occur high in the meteor region so that the use of polarizability alone as the contribution to the collision cross-section for atomic oxygen will introduce errors of 10-20% to its polarizability. This will give an error in D_+ of 1-2%.

Dalgarno et al (1958) mention that quantum symmetry effects will also change the value of the polarizability for ions in a parent gas, but values are tentative. Banks (1966b) does not consider these effects and they have not been included in the calculations presented here.

Table 2.5 shows values of D_+ for heights in the meteor region for a meteor velocity of 40 km/s. The percentage departure from these values for velocities of 20 km/s and 70 km/s is also shown.

Meteor velocity will not introduce much scatter in D_+ as low velocity meteors tend to ionize at lower heights than

Table 2.5: Ion diffusion coefficients

Height (km)	D_+ (m^2/s)	Departure for V = 20 km/s (%)	Departure for V = 70 km/s (%)
75	0.154		
80	0.322		
85	0.697	-3	+0.4
90	1.69		
95	4.41		
100	11.8		
105	34.9		
110	88.5	-15	+3
115	194		

high velocity meteors (McKinley, 1961). These results show good agreement with those of Kaiser et al. (1969).

2.4 DIURNAL AND ANNUAL VARIATIONS OF ATMOSPHERIC TEMPERATURE AND DENSITY.

Variations of atmospheric temperature and density will directly affect the ion diffusion coefficient. Thus a knowledge of these variations is needed to see if measured values of diffusion coefficient may be averaged over diurnal or annual periods to yield meaningful results.

Most temperature measurements in the 80 km to 100 km region are made by rocketsonde. In a comparison of four different rocketsonde experiments Finger and Gelman (1975) find

a departure of 20 K at 65 km between U.S.S.R. and U.S. results and suggest that corrections need to be used. In this type of experiment diurnal corrections are probably needed too, the size of the correction increasing with height. Butko et al. (1975), using the U.S.S.R. rocketsonde, find a 7% departure from the mean temperature over 24 hour periods at 80 km, increasing to 40% at 110 km. Butko et al. (1976) find that the departure is 5% at 80 km, increasing to 15% at 110 km. Using an incoherent scatter radar, Salah and Evans (1973) find temperature departures of about 20% at 110 km. Murgatroyd (1970) finds small time-scale temperature departures of 10% from mean values in 20% of measurements at 80 km.

Theoretical models of the atmospheric temperature take account of heat sources in the atmosphere. Volland and Mayr (1970) find a 5% variation in temperature at 100 km in this way. In another model Mayr (1977) assumes a temperature variation of 15% at 130 km to fit observations. Considering the experimental and theoretical results, diurnal temperature variations of about 5% at 80 km and up to 20% at 110 km appear likely. The results of Murgatroyd (1970) and Volland and Mayr (1970) indicate that percentage variations in density are about twice as large as those in temperature.

Annual variations in temperature of 8% from mean values in the 90-100 km region are reported by Murgatroyd (1970) and U.S. Standard Atmosphere Supplement (1966). The variation at 110 km is less than that for lower heights. They also observe annual density variations of 3% at 90 km, and variations of about 20% in the 100-110 km region.

The signs of the temperature and density variations are important because of the dependence of D on these quantities (equation 2.4). If heating occurred only above a certain height then the pressure at this height would remain constant as it is dependent only on the number of molecules in a column above. In this case

$$N \alpha T^{-1}$$

so that

$$D \alpha T^{2}.$$

In other words, the two variations combine to give a larger variation in D. In practice, the heating increases with height so that this relation will tend to be true in the meteor region - the heating below a given height being small in comparison to the heating at that height. The real dependence is probably not quite as strong as a square law, but stronger than in direct proportion to temperature.

To summarise, diurnal variations in meteor ion diffusion coefficient of up to 5% can be expected at 80 km due to density and temperature variations. At 90 km up to 15% variability could occur increasing to 40% and greater above 100 km. Annual variations will be similar, but will not be as large above 100 km, remaining at about 40% above 110 km.

2.5 THERMALIZATION

(1) Introduction

Ambipolar diffusion coefficient, D_a, is affected by the temperatures of the electrons and ions in the meteor train. D_a is also dependent on the ion diffusion coefficient, D_+, which in turn is temperature dependent. A knowledge of the electron, positive ion and neutral particle temperatures is thus necessary in a study of ambipolar diffusion.

Within this section the electron, ion and neutral particle temperatures in underdense meteor trains are investigated. In each case an estimate is obtained of the time for each species to reach near-thermal temperatures. For ions and neutral particles the maximum time is estimated while for electrons a more accurate thermalization time is calculated.

(2) Neutral Particle Temperature

The temperature increase of neutral meteor atoms and atmospheric particles immediately after the formation of the initial radius can be estimated by the expression

$$\delta T = \frac{mV^2 q}{3\pi\beta r_0^2 N_a k} \qquad 2.4$$

given by Kaiser (1953). V is the meteor velocity, N_a is the atmospheric number density in the train region and k the Boltzmann constant. This assumes that all of the meteor's original kinetic energy is transformed into heat. It will be shown in sub-section (3) that the formation of the initial radius is a rapid process which ends when both neutral

atoms and ions are slowed to thermal velocities. At this stage there is a localised temperature equilibrium over lengths that are small compared to the train radius. The subsequent behaviour of these hot neutral particles is now considered.

An estimate of the pressure in the train may be obtained by assuming an ideal gas so that

$$P = N_a kT$$

where P is the pressure and T the temperature at some point in the train. Here N_a is an approximation for the total number density, N, where

$$N = N_a + N_m \quad .$$

N_m is the number density of neutral meteor atoms, which is at least three orders of magnitude smaller than N_a over the meteor region for underdense meteors. As the train is formed it will expand to equalise the pressure; the effect of this process can be estimated by assuming that it is adiabatic. The temperature after this expansion, T_2, can then be found by assuming some uniform initial temperature T_1 in the train. Then

$$T_2 = T_1 \left(\frac{T_a}{T_1} \right)^{\frac{\gamma-1}{\gamma}}$$

where T_a is the ambient temperature and γ is the ratio of

the heat capacities of the gases. As diatomic species are predominant $\gamma = 1.4$ and

$$T_2 = T_1 \left(\frac{T_a}{T_1}\right)^{0.29} \qquad 2.5$$

This adiabatic expansion will reduce the initial temperature by less than 10% in underdense meteors. If the expansion is not adiabatic the reduction will be less so that in either case the process is not important.

Further cooling of the neutral particles will be by eddy diffusion, bulk particle motion, radiation and thermal conduction. Eddy diffusion will only be important if the scale size of the eddy is of the order of the meteor train diameter. Observations by Greenhow and Neufeld (1959) indicate that the scale of the smallest eddies is tens of metres. Therefore they will not be important in underdense meteors, but will contribute to the dispersal of energy and ionization in large overdense meteors. Cooling by radiation is expected to be small compared with that by thermal conduction and is not considered further.

The effect that bulk motions of particles, such as convection currents, will have on the neutral cooling is difficult to determine. An estimate of the cooling time due to convection alone is the time for a small volume of the hot gas to traverse the train. The acceleration on the small volume of gas, a, at temperature T_2, due to the buoyancy force is

$$a = \left[\left(\frac{T_2}{T_a}\right)^{0.7} - 1\right]g$$

where g is the acceleration due to gravity at that height. The time to traverse one initial radius is then

$$t = \left(\frac{2r_o}{\left[\left(\frac{T_2}{T_a} \right)^{0.7} - 1 \right] g} \right)^{\frac{1}{2}} . \qquad 2.6$$

This time is a lower limit as the effect of viscosity has been neglected. For a meteor with $q = 2 \times 10^{13}$ m^{-1} at 95 km

$$t > 1 \text{ s} .$$

Thermal conductivity is shown to cool underdense trains more rapidly than this.

The cooling of neutral particles by thermal conduction is described by

$$\frac{\partial T}{\partial t} = \frac{2}{3kN_a} \nabla \cdot (K \nabla T)$$

where K is the thermal conductivity of the neutral particles. From the kinetic theory for an ideal gas

$$K = \frac{3}{2} N_a \, k \, D_n$$

where D_n is the diffusion coefficient for the neutral particles. Then

$$\frac{\partial T}{\partial t} = \nabla \cdot (D_n \nabla T) \quad . \qquad 2.7$$

An elastic sphere model of diffusion is appropriate for neutral

particles over a temperature range of a few hundred degrees Kelvin. For this model

$$D_n \propto \sqrt{T} \quad .$$

Equation 2.7 is now solved assuming that D_n is independent of temperature and the effect of this is considered later.

A Gaussian distribution best describes the distribution of ions and neutral meteor atoms. A Gaussian temperature distribution should thus give a good description of the initial temperature in the train and is used here. A solution to equation 2.7 in cylindrical coordinates is then

$$T(r,t) = T_a + \frac{T_2 - T_a}{\frac{4D_n}{r_o^2} t + 1} \exp\left[-\frac{r^2}{4D_n t + r_o^2}\right] \qquad 2.8$$

where r is the radial distance from the train axis and all temperatures are absolute. Now, combining 2.8 with equation 2.5 gives

$$t = \frac{10 r_o^2}{4D_n}\left[\left(1 + \frac{\delta T}{T_a}\right)^{0.71} - 1.1\right] \qquad 2.9$$

where δT can be found from equation 2.4. The time t is the time for the neutrals to cool to within 10% of the ambient temperature. Times less than zero show that the initial temperature was less than 10% above the ambient value.

Equation 2.9 is largely independent of height because both the initial temperature and cooling rate increase with height. Table 2.6 shows the dependence of cooling time on

meteor velocity at a height of 95 km for $q = 10^{13}$ m^{-1} and $q = 10^{14}$ m^{-1}. Values of β are from Sida (1969) and times less than zero are shown as zero.

Table 2.6: Neutral cooling times

Meteor velocity (km/s)	20	30	40	50	60	70
Cooling time (ms) $q=10^{13}$ m^{-1}	101	6.5	0	0	0	0
Cooling time (ms) $q=10^{14}$ m^{-1}	770	160	45	17	7.3	2.5

The diffusion coefficient used here was for an ambient temperature and would increase by 6% for the initial neutral temperature produced in a meteor train with $q=2x10^{13}m^{-1}$ at 95 km and V = 40 km/s. This would reduce the cooling time by 6%. A more rigorous solution of equation 2.7 could be expected to give a result between these two.

The results in Table 2.6 are an upper limit for the cooling time as some cooling processes already mentioned have not been included. However, the results show that neutral particles will cool in times much shorter than the lifetime of an underdense meteor echo for all but low velocity meteors. A study of overdense meteors would need to consider neutral temperatures higher than the ambient temperature.

(3) Positive Ion Temperature

The positive ions will possess up to several hundred eV of translational energy when they are formed. These ions will

undergo many more collisions with neutral particles than with other ions as they cool. Thus the concept of ion temperature is not applicable here because a Maxwellian velocity distribution will not have time to become established while the ions are hot. Here an effective ion temperature, T_i, is used. A useful estimate of the ion thermalization time will then be obtained.

The main ion cooling processes are collisions with neutral particles and thermal conductivity. In addition, there is a heat input from collisions with hot electrons. The thermal equation is then

$$\frac{dT_i}{dt} = -\frac{2}{3k}\sum_j C_j(T_i,T_N)N_j + \frac{2}{3k}C_e(T_i,T_e)N_- + \frac{2}{3kN_+}\nabla\cdot(K\nabla T_i) \qquad 2.10$$

where C_j is a collision term for ion collisions with the jth atmospheric species and C_e is the term for ion collisions with electrons. N_j and N_- are the atmospheric and electron number densities respectively.

The contribution to the ion cooling due to thermal conduction is much smaller than that due to collisions. Solving equation 2.10 with $C_j = C_e = 0$ for a Gaussian temperature profile gives equation 2.8, where D_n is replaced by the ion diffusion coefficient, D_+. As D_+ has been assumed independent of temperature this is not a precise solution, but can be used to find the approximate time for ions to cool to $\frac{1}{e}$ of their initial temperature. Then

$$t = \frac{r_o^2}{4D_+} [\exp(1) - 1]$$

for the train axis. The result for cooling due to thermal conduction is of the order of tens of milliseconds over meteor heights whereas collisional cooling will be shown to take less than one millisecond. It is therefore appropriate to neglect thermal conduction in solving equation 2.10.

The collisions considered are for O^+ ions with N_2, O_2 and O. The collisions with N_2 and O_2 are elastic and that for O is mainly a charge exchange process for temperatures above 500 K. Using expressions by Banks (1966b) the coefficients in equation 2.10 become

$$C_{N_2} = 1.1 \times 10^{-38}(T_i - T_n) \ Jm^3/s$$

$$C_{O_2} = 9.3 \times 10^{-39} \ (T_i - T_n) \ Jm^3/s$$

$$C_O = 3.4 \times 10^{-40} \ (T_i + T_n)^{\frac{1}{2}}(T_i - T_n) Jm^3/s.$$

Initially these coefficients will not be valid because of the high ion temperature. The energy lost per collision by the ions is high so that the ions will soon reach a temperature where these coefficients are valid. It must be remembered, however, that a Maxwellian distribution of velocities will not necessarily be reached so that only an estimate of the cooling time will be obtained. The time for the first few ion-neutral collisions to occur for a particle with meteor velocities is much less than one millisecond. From Banks (1966a) the contribution to ion heating from hot electrons is

$$C_e = 8.0 \times 10^{-32} T_e^{-\frac{3}{2}} (T_e - T_i) \text{ Jm}^3/\text{s} \quad .$$

Equation 2.10 was solved numerically. As the electron temperature was involved the solutions for ions and electrons were found simultaneously. The electron cooling is described in the next sub-section. Table 2.7 shows the time for the positive ions to cool to within 10% of the ambient temperature.

Table 2.7: Ion cooling times

Height (km)	80	90	100	110
Cooling time (ms)	0.02	0.1	0.5	1.4

These results show that ion cooling will occur very early in a meteor echo lifetime. The initial ion temperature does not affect the cooling time because of the strong temperature dependence of the coefficient C_j. The heat input from the hot electrons was negligible compared to that lost in the cooling processes for underdense meteors. Overdense meteors could not be considered in this analysis as an ambient temperature was assumed for the atmospheric atoms.

(4) Electron Temperature

As for the ions an effective electron temperature is used in this analysis. A Maxwellian velocity distribution may not have time to become established so that the cooling time is an estimate. The electrons are produced by impact

ionization and may be expected to possess a few eV of translational energy. In this energy range the main collisional cooling processes are the vibrational and rotational excitation of the ground electronic states of N_2 and O_2 and the transitions between the fine structure levels in the ground states of atomic oxygen. Elastic collisions with atmospheric neutrals are less important, but elastic scattering with meteor ions is important in a dense meteor plasma. Because of this simultaneous solutions were found for the electron and ion cooling. The thermal conductivity of the electrons should be considered in addition to the collision processes. The thermal equation is then

$$\frac{dT_e}{dt} = -\frac{2}{3k}\sum_j C_j(T_e,T_g)n_j + \frac{2}{3kN_-}(\nabla\cdot K\nabla T_e) \qquad 2.11$$

where K is the electron thermal conductivity. Terms on the right hand side are considered separately.

(a) Thermal Conduction Because of the collisional ionization process it is likely that the effective electron temperature at the centre of the meteor train is higher than that near the edges so that thermal conduction may contribute to the electron cooling. Ions with initial energies of ~ 100 eV cool to energies of a few eV in ~ 0.1 ms at 95 km whereas electrons at this height will be shown to take about one hundred times longer. Comparing the respective diffusion coefficients (D_+ and D_-) at this energy shows that

$$D_- \approx 10^3 \times D_+$$

(Dalgarno, 1961). Thus the ions may be regarded as fixed in the plasma column. Since charge neutrality must hold, the radial electron distribution will be the same as that for the ions - a Gaussian given by

$$N_-(r) = \frac{q}{\pi r_o^2} \exp[-\frac{r^2}{r_o^2}] \quad .$$

The time for the electron temperature distribution to reach equilibrium may be illustrated by considering hot (') and cold (") populations of electrons. Then

$$N_-'(r) + N_-''(r) = N_-(r) \qquad 2.12$$

where N_-' is more concentrated near the axis than the Gaussian and N_-'' is more spread out. Assuming no chemical loss, one continuity equation is

$$\frac{\partial N_-'}{\partial t} = D_-' \nabla^2 N_-' \qquad 2.13$$

and likewise for N_-''. The electron diffusion coefficient is

$$D_- = \frac{kT_e}{m_- \nu_{-n}}$$

where m_- is the electron mass and ν_{-n} is the electron-neutral collision frequency. ν_{-n} is used as it will dominate the electron - ion and electron - electron collision frequencies

in meteor trains. As ν_{-n} is nearly proportional to T_e at high temperatures (Dalgarno, 1967) then

$$D_-' \approx D_-'' = D_- \quad .$$

To find the exact behaviour of the overall electron population equation, 2.12 would need to be solved simultaneously with equations 2.13. The solutions would depend on the choice of initial distributions N_-' and N_-''. However, it is clear that these distributions will tend to similarity in a time, τ, given by

$$\tau = \frac{r_o^2}{4D_-} \quad .$$

This is, then, a measure of the time for the electrons to establish an isotropic distribution inside the ionized column. τ is largest at low meteor heights and values for 80 km are shown in Table 2.8. Atmospheric parameters are taken from the CIRA (1972) model atmosphere and r_o = 0.2 m.

Table 2.8: Electron redistribution time

Electron temperature (K)	1000	5000	10000
Time (s)	4.1×10^{-6}	3.8×10^{-6}	3.7×10^{-6}

Values of r_o for large overdense meteors may be about 1m (Greenhow and Watkins, 1964) and the corresponding values of τ would be increased by a factor of 25. Even time

intervals of 0.1 ms are small compared with the electron thermalization time so that during the thermalization process

$$\nabla T_e = \nabla^2 T_e = 0 \quad .$$

This means that thermal conduction will not contribute to the electron cooling process.

(b) Cooling By Collisions Energy transfer rates for electron-ion and electron-neutral collisions are derived from collision cross-sections and are available from both experimental and theoretical work. The theoretical treatments give the time rate of energy exchange for a binary gas mixture in which each component gas has a Maxwellian velocity distribution - each distribution being characterised by a different kinetic temperature. Here electron energies from thermal to about 2eV ($\approx 2 \times 10^4$K) are considered. The values of the coefficients C_j given below are in units Jm^3/s.

Elastic collisions between electrons and neutral particles contribute very little to the electron energy loss as the electron mass is much less than that of the neutrals. From Banks (1966a) the coefficients in equation 2.11 for these collisions with N_2 and O_2 are

$$_{elas}C_{N_2} = 2.9 \times 10^{-44} T_e (T_e - T_a)(1 - 1.2 \times 10^{-4} T_e)$$

$$_{elas}C_{O_2} = 1.9 \times 10^{-43} T_e^{\frac{1}{2}} (T_e - T_a)(1 + 3.6 \times 10^{-2} T_e^{\frac{1}{2}}) \quad .$$

For elastic encounters with atomic oxygen the energy transfer

rate from Henry and McElroy (1968) is used to give

$$_{elas}C_O = 8.5 \times 10^{-44} T_e^{\frac{1}{2}} (T_e - T_a)(1 + 5.7 \times 10^{-4} T_e).$$

Elastic collisions with positive ions are an important energy exchange process in bright meteors. The main meteoric ions (M^+) are O^+, Fe^+, Mg^+ and Si^+ and have a larger effective collision cross-section for elastic encounters than the neutral particles present. Assuming singly charged ions and the ion composition given by Sida (1969) for a meteor velocity of 40 km/s, the cooling coefficient becomes (Banks, 1966a)

$$_{elas}C_{M^+} = 8.0 \times 10^{-32} T_e^{-\frac{3}{2}} (T_e - T_i).$$

Energy transfer through inelastic collisions is important at some electron energies. Vibrational levels of the ground electronic state of N_2 can be excited efficiently by electrons with energies of 1 or 2eV. Values of $_{vib}C_{N_2}$ were calculated using the curves of Dalgarno et al. (1968) together with the analytical energy transfer rates given by Stubbe and Varnum (1972) at higher temperatures. Similarly, $_{vib}C_{O_2}$ values were evaluated from Lane and Dalgarno (1969) and Stubbe and Varnum (1972).

It is expected that rotational excitation of both N_2 and O_2 will play an important role in electron cooling for energies < 0.1 eV. The energy transfer rates are taken from Dalgarno (1969).

$$_{rot}C_{N_2} = 4.6 \times 10^{-39} T_e^{-\frac{1}{2}} (T_e - T_a)$$

$$_{rot}C_{O_2} = 1.1 \times 10^{-38} T_e^{-\frac{1}{2}} (T_e - T_a) \quad .$$

The oxygen atom has a triplet ground state (^3P) with J = 2, 1, 0 - the $^3P_1$ and $^3P_0$ levels being 0.0196 and 0.0281 eV above the lowest $^3P_2$ level. Transitions between these levels contribute to electron collisional cooling particularly at low energies. Using the expressions of Dalgarno (1969) for the fine structure excitation assuming an excitation temperature equal to the ambient neutral temperature gives

$$_{J}C_{O} = 5.4 \times 10^{-37} T_a^{-1} (1 - 7 \times 10^{-5} T_e)(T_e - T_a) \quad .$$

Excitation of the low-lying electronic states of O_2, the $O_2(a^1\Delta_g)$ and $O_2(b^1\sum_g^+)$ states (0.98 and 1.63 eV above ground), will not contribute significantly to electron cooling. The excitation of the metastable $O(^1D_2)$ state, having excitation energy 1.97 eV, will not contribute significantly either.

The only energy transfer rate mentioned that has a spatial dependence is that due to elastic scattering from meteoric ions. For simplicity the number density of ions used was that on the train axis,

$$N_{M^+} = N_- = \frac{q}{\pi (r_o^2 + 4D_a t)}$$

where D_a is the ambipolar diffusion coefficient already mentioned.

(c) Results Solutions to equations 2.10 and 2.11 were found simultaneously for heights between 80 and 110 km by numerical integration. Values of N_{N_2}, N_{O_2} and T_a were from CIRA (1972) and N_O were from Henderson (1974). For each height, solutions were computed for the electron line densities $q = 2.5 \times 10^{14}$, 2.5×10^{15} and 2.5×10^{16} m^{-1}. Line densities below 2.5×10^{14} showed no change from that density as the electron - positive ion collision term had become negligible. An example of the results is shown in Fig. 2.1 for a height of 96 km. Because of the large contribution made to the energy transfer cross-section for energies between 1 and 3eV by vibrational excitation of N_2, the initial cooling rate is very rapid at high temperatures. Thus computations showed that cooling from 2×10^4K to 1.2×10^4K is achieved in 1×10^{-5}s and from 1.2×10^4K to 6×10^3K in 2×10^{-6}s. These times are small compared to the overall cooling time of several milliseconds so that the initial temperature does not affect the result if it is sufficiently high. $T_e(0)$ = 6000 K is used here.

The numerical results enabled the contributions from the various processes to be compared. Fig. 2.1 shows the importance of meteoric ions for bright meteors and it is clear that ions play a dominant role for meteors with $q > 2.5 \times 10^{16}$ m^{-1}. For meteors with $q \leqslant 2.5 \times 10^{14}$ m^{-1} at 80 km vibrational excitation of N_2 is dominant for $T_e > 1500$K with rotational excitation of N_2 and O_2 being the major process for $T_e < 1500$ K. For these meteors at 110 km: N_2 excitation is dominant for $T_e > 1500$ K with fine structure excitation important for $1500 > T_e > 350$ K and N_2 and O_2

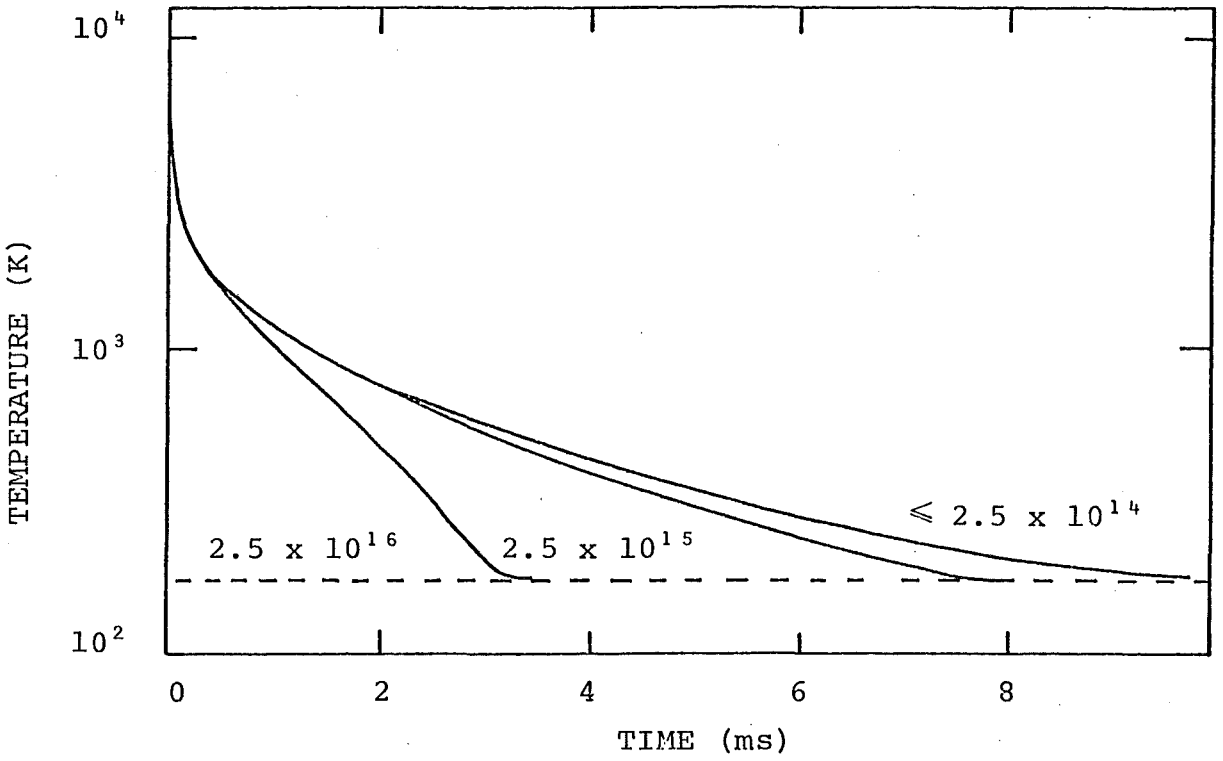

Figure 2.1: Electron temperature, T_e, as a function of time for a height of 95 km and different line densities (m^{-1}). The dashed line indicates the ambient temperature at 95 km.

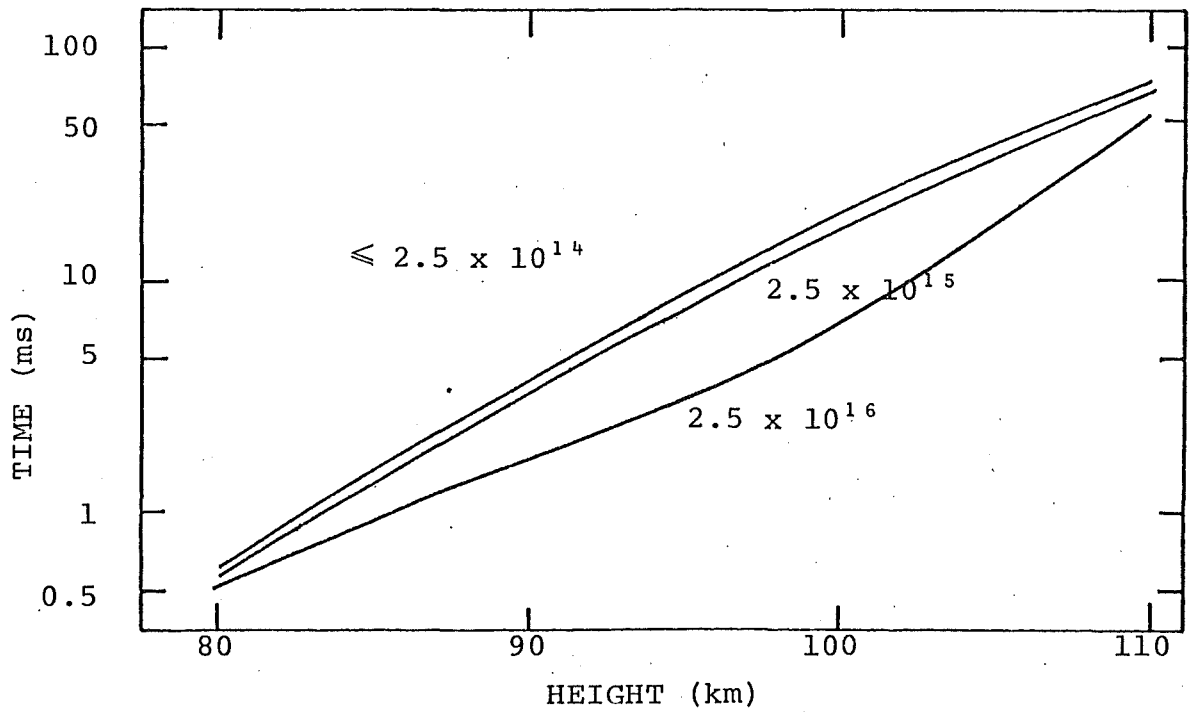

Figure 2.2: The electron thermalization time as a function of height for different electron line densities (m^{-1}).

rotational excitation being the primary loss process for $T_e < 350$ K. Neutral particle elastic scattering plays only a minor role throughout the cooling range.

Fig. 2.2 shows the thermalization time, defined as the time interval for which the electron kinetic temperature exceeds that of the neutral atmosphere by more than 10%. The thermalization time is 0.1s at 110 km whereas at 80 km it is less than 10^{-3} s as a result of the higher atmospheric density. Note that this analysis has assumed a neutral particle temperature equal to that of the ambient atmosphere. This may not be true for the brighter meteors considered, but the results may still be used to see how quickly the electron temperature reaches the neutral temperature.

(5) Discussion

This analysis has shown that in underdense meteors both ions and neutral particles thermalize in less than 10^{-3} s. An exception to this may be meteors with velocities less than 30 km/s. The neutral particles in brighter meteors will take longer to cool because of the high initial energy input. This should be considered when studying diffusion in enduring radio meteor echoes. However, the longer echo duration of these meteors reduces the importance of this effect.

The effects of electron thermalization time may be noticeable in echoes above 100 km. Firstly, reflection heights inferred from echo decays could be systematically overestimated. Secondly, a change in the value of diffusion coefficient during an echo could be observed. The results of experiments

measuring changes in diffusion coefficient with time need to be interpreted carefully. Poulter (1978) has shown that the inferred diffusion coefficient may vary with time due to plasma resonance effects which are discussed in the next chapter. These effects are quite consistent with the results of Delov (1975), who interpreted them as being due to electron thermalization.

In a further paper Delov (1976) interpretes the results of two experiments as showing electron thermalization during the echo lifetime. In the first experiment he looked at changes in the Doppler frequency of the received echo. From the predominance of increasing Doppler frequency with time, it was concluded that a moving sphere effect was operating. This effect is said to be consistent with diffusion of unthermalized electrons. However, Poulter (1978) has found that reflection processes early in the echo lifetime give rise to phase changes. Such phase changes may account for Delov's observations. No consideration was given to these effects. It would seem wise to do so before looking to electron thermalization as a cause of phase changes. Furthermore, a moving sphere effect is observed for a train near the finite velocity ceiling (see Chapter 3).

The second experiment of Delov investigates the wavelength dependence of diffusion coefficient measurements. If the time for an echo to decay by a factor e is τ, then with

$$\frac{\tau_{\lambda_1}}{\tau_{\lambda_2}} = \left(\frac{\lambda_1}{\lambda_2}\right)^n \qquad 2.13$$

it would be expected that $n = 2$ if the echo decay was due to diffusion alone. Delov points out that the main cause of echo decay for a non-thermalized train is due to the movement of the meteor and the destruction of the train behind it - the moving sphere effect. For this situation the measured value of D is smaller on the shorter wavelength so that $n < 2$.

Numerical integration over the length of the train was performed to check this interpretation. The mathematical details are given in section 3.5. An exponential decay was used as a model for the electron temperature starting with $T_e = 1000$ K (the expected electron temperature after the formation of the initial radius). The rate of thermalization could be varied and two values were used - that corresponding to the predictions of Portnyagin (1972) and that already presented here.

It was found that for the radar wavelengths used by Delov (8.13 m and 5.2 m) n was less than 2. However, for wavelengths of 10.53 m and 30 m (used by Baggaley, 1979c) values $n > 2$ were found. This is probably because at longer wavelengths the moving sphere effect, arising from the finite meteor velocity, is no longer important. In that case you would expect the measured D to be larger on the shorter wavelength because the decay time is shorter. This means that the average value of D will be greater over the time of measurement. However, for higher values of D this will be reversed, as it was for $\lambda = 5.2$ m. Thus scatter will be introduced into an experiment comparing decay times on different frequencies. The variation of thermalization time with height will complicate this further.

There are two sets of experimental data with sufficient echoes on two frequencies to look at the wavelength dependence - those of Delov (1976) and Baggaley (1979c). However, Delov describes the average values from which n can be derived as arithmetic mean values. This would seem to indicate that arithmetic means of D values were used. If true this could account for his results, giving n ~ 1.3. The frequency distribution of diffusion coefficients is skew because that of log D is a Gaussian. It would seem safer to average the log D value as this avoids the spread of values influencing the result. The spread could be expected to be larger on the longer wavelength because the effect of an irregular ionization profile will be more pronounced. An even better analysis would be to find the ratio of decay times for individual trains before finding a mean value, as Baggaley has done.

Baggaley's results are presented in Table 2.9. Also shown are computed values of n for the two thermalization rates mentioned. The decay times used to find the theoretical

Table 2.9: Theoretical and experimental wavelength dependence of diffusion coefficient measurements.

Height (km)	n: Baggaley (1979c)	n:Portnyagin (1972)	n: This work
92	2.07 $\pm$ 0.07	-	-
97	2.37 $\pm$ 0.04	2.19	2.10
102	2.43 $\pm$ 0.04	2.73	2.17

n values were the times for each echo to decay to 1/e of its peak amplitude which is consistent with the procedure of Baggaley. This is different to finding the slope of a logarithmic plot, as D varies with time. The uncertainties shown for the experimental data are one standard error. Meteor velocities used were those appropriate to each height (McKinley, 1961). Values were not calculated for 92 km because of the large amount of computing time needed for long decays and the fact that thermalization would not change n significantly from 2.

The results in Table 2.9 indicate that thermalization cannot explain the observed n values. Other factors must be operating such as plasma resonance or wind effects.

Poulter (1978) suggests a two wavelength experiment to find the wavelength dependence of the rate of change in diffusion coefficient. This could determine whether thermalization or plasma resonance was important. The results of such an experiment would be difficult to interpret due to the wavelength dependence of D itself and the variability that is observed in this wavelength dependence.

Portnyagin (1972) has made a theoretical study of electron thermalization that has already been mentioned. The thermalization times found are about five times longer than those presented in Fig. 2.2. There are several reasons for this difference. His study does not consider the excitation of fine structure levels in atomic oxygen which are important higher in the meteor region because [O] becomes significant. The effect of elastic collisions with

positive meteoric ions has not been considered, but has been shown here to be important in bright meteors. Furthermore, some collision cross-sections used by Portnyagin had been underestimated by earlier workers (Dalgarno, 1969) so that thermalization times were overestimated.

To summarise, electron thermalization may affect meteor echo characteristics for meteors above 100 km. Observed changes in measured diffusion coefficient with time can be caused by plasma resonance effects as well as thermalization. The results of dual frequency experiments do not seem to be explained by thermalization effects alone.

2.6 INFLUENCE OF THE EARTH'S MAGNETIC FIELD

(1) Introduction

The effect of the earth's magnetic field on the diffusion of meteor trains is now considered. Previous discussion of ambipolar diffusion did not consider this. Magnetic fields affect the diffusion of ions and electrons when their gyrofrequencies become greater than their collision frequencies with neutrals. This occurs for electrons at meteor heights, but not for ions. The change in electron diffusion coefficient affects the overall behaviour of the meteoric ionization.

The basic equations governing this diffusion process are now described. This analysis is mainly that used by Kaiser et al. (1969). The methods used by various workers in solving these equations are then briefly outlined. Results obtained are discussed and the resulting ionization distribution is described.

(2) Basic Equations

There are two basic conditions governing the diffusion of the meteor train ionization. The first condition is represented by the continuity equations for electrons (-) and ions (+)

$$\frac{\partial N_{\pm}}{\partial t} + \nabla \cdot (N_{\pm} \underline{V}_{\pm}) = 0 \qquad 2.14$$

where $\underline{V}_{\pm}$ are the flow velocities of the ions and electrons. This assumes no loss of ionization through chemical processes (discussed in section 2.7) and is shown not to be important over the heights where magnetic effects are prominent.

The second condition is that of quasi-neutrality, mentioned in section 2.3, and is represented by

$$N_{+} \approx N_{-} = N \quad . \qquad 2.2$$

This is valid if the dimensions being considered are large in comparison with the Debye shielding length. This length is about 1 cm for the smallest meteors considered here and is therefore much smaller than the shortest dimensions considered (about 1m).

The velocities of flow may be found from the equations of motion

$$m_{\pm} N_{\pm} \frac{d\underline{V}_{\pm}}{dt} = - \nabla P_{\pm} + m_{\pm} N_{\pm} \underline{g} \pm N_{\pm} e [\underline{E} + \underline{V}_{\pm} \times \underline{B}]$$

$$- \sum_{\ell} m_{\pm} N_{\pm} \nu_{\pm \ell} (\underline{V}_{\pm} - \underline{V}_{\ell}) \quad . \qquad 2.15$$

Here $m_{\pm}$ are the ion and electron masses, $P_{\pm}$ are the pressures, $\underline{g}$ is the acceleration due to gravity, e is the electron charge, $\underline{B}$ is the geomagnetic field and $\nu_{\pm\ell}$ are the collision frequencies with the species ℓ. The electric field $\underline{E}$ is given by

$$\underline{E} = \underline{E}_o + \underline{E}_s$$

where $\underline{E}_o$ is the external field and $\underline{E}_s$ is the space charge field created by the separation of the ions and electrons.

To simplify the expressions for flow velocities, the following approximations are made. Net acceleration is assumed to be zero so that only constant flow velocities are considered. The left hand sides of equations 2.15 are then zero. This is not unreasonable when the controlling influence is diffusion so that flow velocities change slowly with density gradients. Since the atmospheric scale height at meteor heights is large when compared to meteor train dimensions, the effect of gravity is neglected. The magnetic field is considered to be homogeneous and invariant. Assuming an ideal gas, equation 2.2 gives

$$P_+ = P_- = NkT$$

if $T_e = T_i = T_n = T$. This will not be true for heights much above 100 km early in the train lifetime. However, the electron diffusion coefficient is largely independent of temperature below 1000 K so that the higher electron

temperature has more effect on ambipolar diffusion. This may modify the shape of the ionization distribution when different dimensions are controlled by different diffusion processes as in magnetically affected trains.

The collision terms in equation 2.15 are summed over all the components ℓ with which the ions and electrons collide. The important components are the neutral atmospheric species, the meteoric ions and electrons. If no magnetic field is present the diffusion is isotropic and the electron and ion velocities of flow are equal. Consequently only collisions with the atmospheric species need to be considered. Diffusion in a magnetic field is not necessarily isotropic so that the electron and ion flow velocities are not equal. Thus electron - ion collisions should be considered if the electron - ion collision frequency ν_{+-} is of the order of the electron-neutral collision frequency ν_{-n} or ion-neutral collision frequency ν_{+n}. The cross-section of Banks (1966a) and collision frequencies derived from Kaiser et al. (1969) give

$$\frac{\nu_{+-}}{\nu_{+n}} = 4 \times 10^{-12} N_-$$

and

$$\frac{\nu_{+-}}{\nu_{-n}} = 4 \times 10^{-13} N_-$$

for 108 km, with N_- in m^{-3}. For lower heights these ratios will become smaller as the atmospheric density increases.

For a meteor with $q = 2 \times 10^{13}$ m^{-1} at 108 km $\nu_{+-}/\nu_{+n} = 6.4$ and $\nu_{+-}/\nu_{-n} = 0.6$ on the train axis after formation.

These ratios decrease both away from the train axis and as diffusion proceeds. However, they may be important for short times after train formation and should certainly be considered in overdense meteor trains. The effects of electron-ion collisions at meteor heights have not been considered theoretically, but studies have been made for heights above 150 km. Assumptions made in these studies are not valid at meteor heights, but their results may give some indication of the effect of the ν_{+-} terms. This is discussed later in this section.

In the light of the assumptions made, equations 2.15 become

$$m_{\pm} N \nu_{\pm n} (\underline{V}_{\pm} - \underline{V}_n) = - kT \nabla N \pm Ne[\underline{E} + \underline{V}_{\pm} \times \underline{B}]. \qquad 2.16$$

These may be further simplified by choosing a coordinate system (u,v,w) that moves with the velocity of the neutral wind $\underline{V}_n$ and has $\underline{B}$ in the $\underline{w}$ direction. Then equations 2.16 become

$$\underline{V}_{\pm} = -\frac{\mathbb{D}_{\pm}}{N} \nabla N \pm \mathbb{K}_{\pm} (\underline{E} + \underline{V}_n \times \underline{B}) \qquad 2.17$$

where

$$\mathbb{D}_{\pm} = \begin{pmatrix} D_{T\pm} & \pm D_{H\pm} & 0 \\ \mp D_{H\pm} & D_{T\pm} & 0 \\ 0 & 0 & D_{\pm} \end{pmatrix}$$

and

$$\mathbb{K}_{\pm} = \frac{e}{kT}\mathbb{D}_{\pm} \quad .$$

In these expressions $D_{\pm}$ are the usual isotropic diffusion coefficients already described. $D_{T\pm}$ are the transverse diffusion coefficients - those of the particles diffusing across the magnetic field - and are given by

$$D_{T_{\pm}} = \frac{\nu_{\pm n}^2}{\nu_{\pm n}^2 + \omega_{\pm}^2} D_{\pm}$$

and $D_{H\pm}$ are the Hall diffusion coefficients - arising from the $\underline{V}_{\pm} \times \underline{B}$ terms - and are given by

$$D_{H\pm} = \frac{\nu_{\pm n}\omega_{\pm}}{\nu_{\pm n}^2 \pm \omega_{\pm}^2} D_{\pm} \quad .$$

Here the $\omega_{\pm}$ are the frequencies of gyration and are given by

$$\omega_{\pm} = \frac{eB}{m_{\pm}} \quad .$$

Combining equations 2.17 with the continuity equations 2.14 now gives the diffusion equations

$$\frac{\partial N}{\partial t} = \frac{\partial}{\partial u}\left(D_{T\pm}\frac{\partial N}{\partial u} \mp K_{T\pm}NE_u\right) + \frac{\partial}{\partial V}\left(D_{T\pm}\frac{\partial N}{\partial V} \mp K_{T\pm}NE_V\right)$$

$$+ \frac{\partial}{\partial w}\left(D_{\pm}\frac{\partial N}{\partial w} \mp K_{\pm}NE_w\right) - K_{H\pm}(\nabla \times (N\underline{E}))_w \qquad 2.18$$

where E_u is the magnitude of $\underline{E}$ in the u direction and $\underline{E}$ is now given by

$$\underline{E} = \underline{E}_o + \underline{E}_s + \underline{V}_n \times \underline{B} \quad .$$

A more useful form of this equation is in a coordinate system (x,y,z) such that the y-axis corresponds to the v-axis of the previous coordinates (Fig 2.3); the meteor train is in the z-direction on an angle α to $\underline{B}$ so that $\underline{B}$ is in the x-z plane and the x-axis is perpendicular to the train. Assuming that the ionization distribution along the train is uniform there will be no density variations in the z-direction so that $\frac{\partial}{\partial z} = 0$. This assumption is discussed in section 2.8. Transforming equation 2.18 to this coordinate system gives

$$\frac{\partial N}{\partial t} = \frac{\partial}{\partial x}\left[(D_{T\pm}\cos^2\alpha + D_{\pm}\sin^2\alpha)\frac{\partial N}{\partial x} \mp (K_{T\pm}\cos^2\alpha + K_{\pm}\sin^2\alpha)NE_x\right] + \frac{\partial}{\partial y}\left[D_{T\pm}\frac{\partial N}{\partial y} \mp K_{T\pm}NE_y\right] - K_{H\pm}\cos\alpha\left[\frac{\partial}{\partial x}(NE_y) - \frac{\partial}{\partial y}(NE_x)\right] \qquad 2.19$$

which are equations (18) of Kaiser et al. (1969). Thus the diffusion of the train depends on the angle between its axis and the geomagnetic field α.

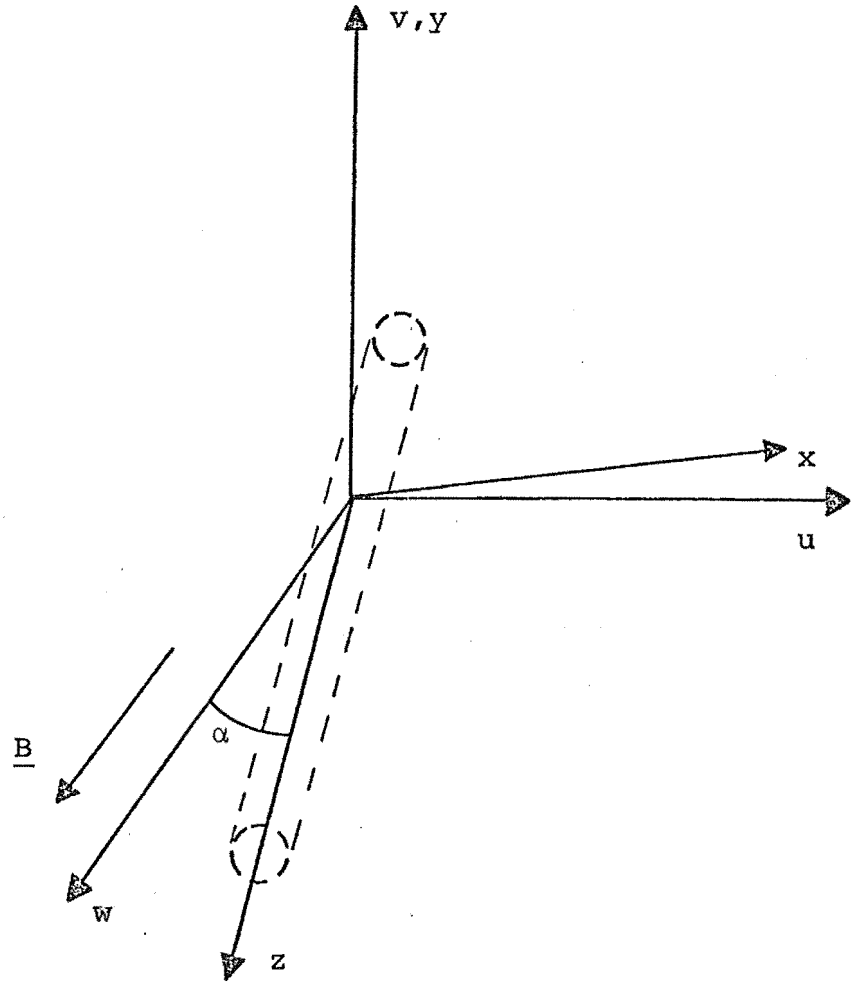

Figure 2.3: The coordinate systems

(3) Methods of Solution

There are no simple solutions to equations 2.19 for general values of α because of the anisotropy introduced by the geomagnetic field. A solution can be obtained by the use of Green's function when the meteor ionization is a small perturbation to the ambient ionization. This is not valid for the meteors studied by most radar systems. Other ways of solving equations 2.19 are: (i) perturbation methods where the meteoric ionization is a large perturbation to the ambient ionization and (ii) numerical methods.

A numerical solution was obtained by Kaiser et al. (1969). They used a Gaussian initial distribution of ions and electrons that exceeded the ambient density by a factor of three on the train axis. Meteors studied by radar typically exceed the ambient density by one to four orders of magnitude. The choice by Kaiser et al. of three times was to reduce computation time and their results are consistent with methods using larger densities. For this solution they assumed no neutral wind and no external electric field, leaving only the space-charge field. This field can then be represented as the gradient of a scalar potential Ω so that

$$\underline{E} = - \nabla\Omega$$

Solutions were obtained by a Crank-Nicholson technique which involved dividing a cross-section of the train into a mesh. Finite boundaries to the cross-section were needed to limit computation time and the following boundary conditions were used

$$\Omega = 0, \frac{\partial \rho}{\partial x} = 0 \quad \text{for the x-direction boundaries}$$

and

$$\Omega = 0, \frac{\partial \Omega}{\partial y} = 0 \quad \text{for the y-direction.}$$

Here ρ is a non-dimensional density. As a consequence of the boundary condition for Ω the results obtained differ from those of Giles (1973). Giles used a perturbation technique discussed below. Pickering (1973) repeated the

numerical calculations with a self-consistent model for the space-charge electric field. Instead of using $\Omega = 0$ on the boundaries a procedure was used to calculate Ω iteratively. This overcomes the problem of the boundary conditions affecting the final distribution. Solutions were obtained for $\alpha = 90^{o}$ so that the train is perpendicular to the magnetic field. These solutions agree with those of Giles.

Giles (1973) used singular perturbation theory to find solutions to equations 2.19. In the zeroth approximation $\nu_{-n} = 0$ was used and then ν_{-n} was used as a small perturbation for the next approximation. The potential and density were then expanded in terms of a function of ν_{-n} to obtain the outer expansion. This was not uniformly valid and another (the inner) expansion was needed that was valid where the first was not. These two expansions were then matched in the region where they overlap. The physical significance of this singularity is discussed below.

This perturbation method has been criticised by Rozhanskii and Tsendin (1977b) because the assumption $\nu_{-n} = 0$ in the zeroth approximation precludes the attainment of the closure of Hall flows. They used a method of successive approximations to solve the equations for a strong perturbation to the ambient electron density. This does not assume that $\nu_{-n} = 0$ in the initial approximation.

(4) Results

Magnetic effects become important for meteors above 95 km. Consider a field-aligned train. Diffusing electrons and ions

cross the field perpendicularly so that the transverse diffusion coefficients $D_{T\pm}$ are important. Below 95 km $D_{T-} > D_{T+}$ so that the diffusion is ion-controlled and the ambipolar diffusion coefficient is given by

$$D \approx 2D_{T+} \quad .$$

Above 95 km $D_{T+} > D_{T-}$ so that the electrons now control the diffusion and the coefficient is

$$D \approx 2D_{T-} \quad .$$

Since D_{T-} decreases as height increases and D_{T+} increases with height, the diffusion of field-aligned meteor trains is significantly inhibited above 95 km. Values of the relevant diffusion coefficients for different heights, from Kaiser et al. (1969) are shown in Table 2.10.

Table 2.10: Diffusion coefficients (m^2/s) vs height

Height(km)	D_-	D_+	D_{T-}	D_{T+}	D_{H-}	D_{H+}
75	5.10×10^{2}	0.158	143	0.158	229	7.83×10^{-5}
81	1.18×10^{3}	0.366	69.5	0.366	278	4.54×10^{-4}
83.5	2.32×10^{3}	0.720	35.7	0.720	286	1.79×10^{-3}
88	4.68×10^{3}	1.45	18.2	1.45	292	7.18×10^{-3}
93	1.21×10^{4}	3.74	7.55	3.74	302	4.64×10^{-2}
97.5	2.62×10^{4}	8.10	4.10	8.10	328	2.01×10^{-1}
102	5.74×10^{4}	17.8	2.24	17.8	358	8.80×10^{-1}
108	1.62×10^{5}	51.1	1.01	50.1	405	6.21
114	3.71×10^{5}	115	0.580	108	464	26.8

More general angles α for heights above 95 km are now considered. The numerical solutions of Kaiser et al. (1969) show that for small α diffusion is still inhibited. In this situation the ions can move more rapidly than the electrons, but are held back by electrostatic forces thus setting up a negative space-change on the train axis. A transition to more rapid diffusion is indicated by this space-charge becoming positive. The angle at which this transition occurs - the critical angle - is denoted here by α_c. The solutions show that α_c is about 1.4^o above 100 km and decreases rapidly below this height. This means that only trains that are closely field-aligned will have inhibited diffusion. Furthermore, this diffusion is isotropic, ambipolar and electron controlled.

The solutions found by Kaiser et al. (1969) for $\alpha > \alpha_c$ are affected by the boundary conditions used. Those of Pickering (1973) for $\alpha = 90^o$ were obtained by more suitable boundary conditions. These solutions show the formation of fins of ionization in the field direction. These fins could be up to 100 r_o in length, and should be formed for all angles $\alpha > \alpha_c$.

These solutions also show the formation of depletion regions in the background plasma. It is the formation of these regions that allows quasineutrality to be maintained in the fins of ionization. Clearly there is a limit to the depth of a depletion region so that for sufficiently strong perturbations the plasma density in the fins will be limited. This has been investigated more thoroughly by Rozhanskii and Tsendin (1977 a,b) and is discussed later.

The results of Giles (1973) also predict the formation of field-aligned fins of ionization. In the region of the fins the plasma is treated as a small perturbation to the ambient density so that the results are similar to Pickering (1973). Hall flows are not considered to be important in the fins, but are significant in the central column of ionization, especially when α is small. In the central region (where the outer expansion is valid) the contours of ionization density are ellipses. These ellipses are skewed relative to the field direction because of the presence of Hall flows for small $\alpha (< 8^{o})$. There is no skewness for $\alpha = 90^{o}$ because there are then no Hall currents.

Giles suggests that the positive axial space-charge influences the diffusion for radial distances less than or equal to the ion diffusion length. Inside this region diffusion is ion controlled and relatively rapid. Quasi-neutrality is maintained by electron flows down the field direction. Diffusion across the field outside this region is electron controlled and inhibited. Fins of ionization will therefore be formed that have a negative space-charge. Hall flows will not be important because of the lower density. The singularity in the solution arises from the two different regions where two different length scales operate.

The clearest and most general description of the evolution of the ionization distribution comes from Rozhanskii and Tsendin (1977a,b). The role of depletion regions in the background plasma is investigated. It is useful to introduce the quantities

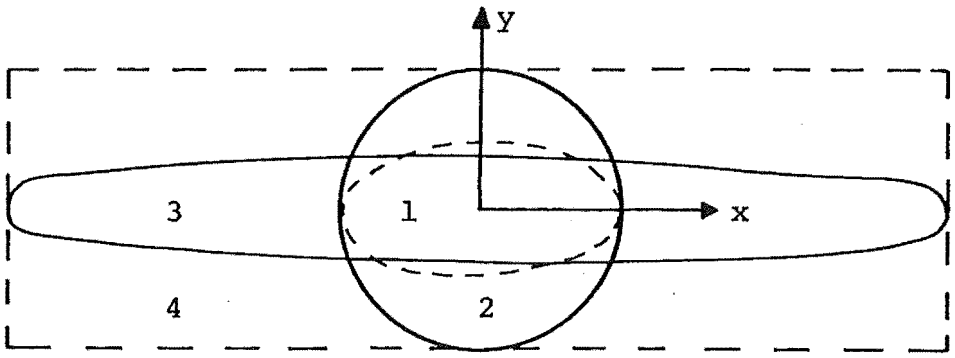

Figure 2.4: A cross-section of a meteor train showing: 1 - the ambipolar ellipse, 2 - the ion ellipse, 3 - the electron ellipse and 4 - the depletion regions in the background plasma.

$$\hat{D}_{\pm} = D_{T\pm} \cos^2 \alpha + D_{\pm} \sin^2 \alpha$$

which are the effective diffusion coefficients transverse to the train and in the plane of the train and field. The electrons and ions will, in the absence of electrostatic forces, occupy their own ellipses with dimensions given in terms of $\hat{D}_{\pm}$ and $D_{T\pm}$. They are shown in Fig. 2.4, based on Fig. 1 of Rhozhanskii and Tsendin (1977a). Quasi-neutrality will be maintained in these ellipses by a flow of ions across the field to the electron ellipse and electrons down the field to the ion ellipse (really a circle at meteor heights). These flows form the depletion regions in the background plasma. The cross-sectional area from which the background plasma can contribute ions and electrons is the product of the dimensions $\sqrt{D_+ t}$ and $\sqrt{\hat{D}_- t}$. A measure of the relative depth of the depletion regions is

$$H_d = \frac{q}{8\pi t N_a \sqrt{(D_{T+} \hat{D}_-)}} \qquad 2.20$$

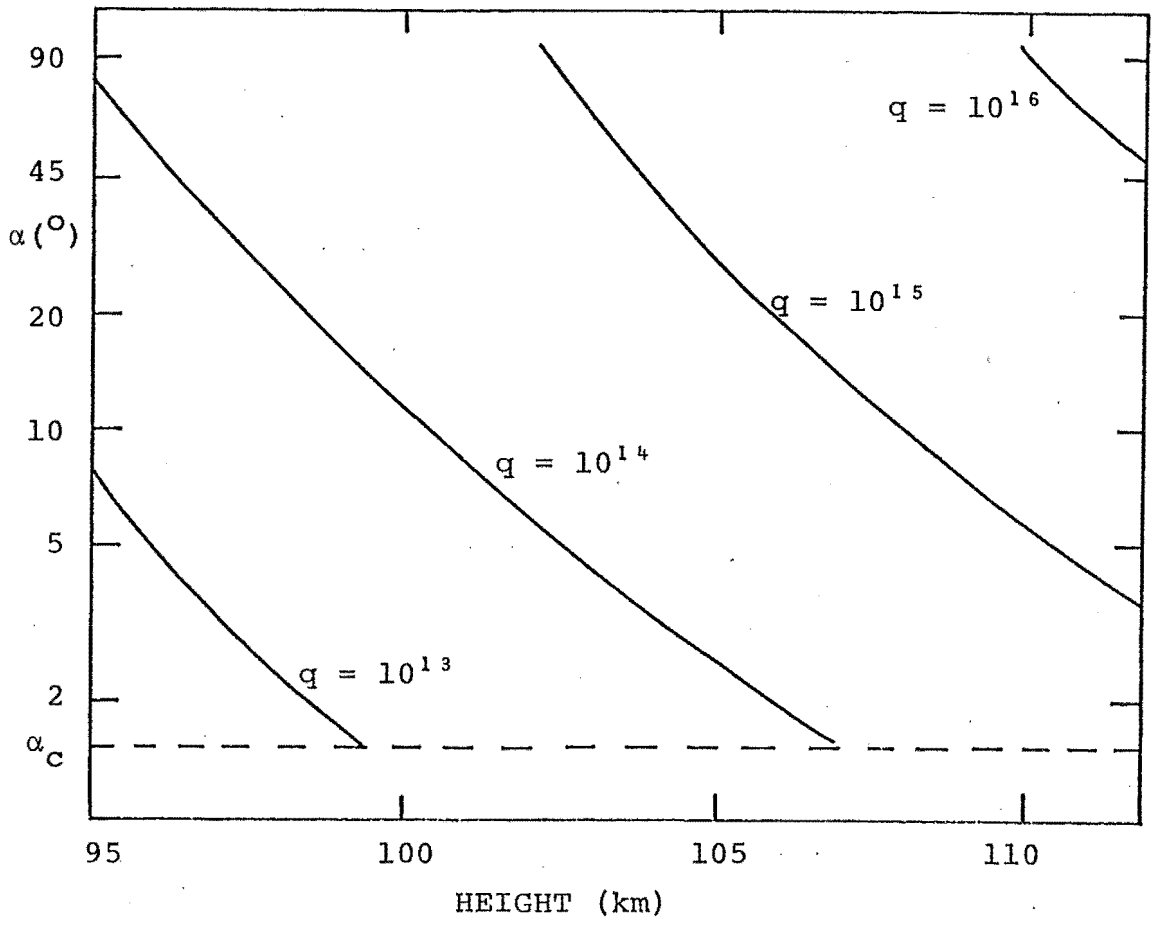

Figure 2.5: Line densities for the transition to ambipolar diffusion

where N_a is the density of the background plasma. For $H_d < 1$ the dimensions of the ionization are governed by the ellipses whereas for $H_d > 1$ the central region will diffuse under ambipolar conditions as the background plasma will be fully depleted. For $H_d >> 1$ most of the ionization will be contained in the ambipolar ellipse of dimensions $\sqrt{(4D_{T-}t)}$ and $\sqrt{(4D_{+}t)}$.

Fig. 2.5 shows the conditions under which the transition to ambipolar diffusion occurs. Values of N_a used were typical day-time values for midlatitudes from Bremer and Singer (1976). Note the logarithmic scale for α. To interpret the diagram consider a meteor with a line density of 10^{13} electrons per

metre. If this meteor occurred in a region below the line $q = 10^{13}$ (i.e. $h < 100$ km, $\alpha < 5^{o}$), then ambipolar diffusion would predominate (i.e. $H_d > 1$). Anywhere above the line the electron and ion ellipses would contain all the ionization.

In this work most meteors studied have $10^{12} < q < 2 \times 10^{13}$ m^{-1} so that according to Fig. 2.5 they will diffuse rapidly. However, Fig 2.5 is for day-time electron densities. At night these densities will decrease by at least one order of magnitude so that the lines of constant q will change by the same amount. In this case some of the larger meteors occurring below 105 km will undergo ambipolar diffusion.

The effect of Hall flow was also investigated by Rozhanskii and Tsendin. They define a second critical angle α_o such that

$$\alpha_o = \left[\left(\frac{\omega_+ \nu_-}{\omega_- \nu_+}\right)\left(1 + \left(\frac{\omega_+}{\nu_+}\right)^2\right)\right]^{\frac{1}{4}}$$

and $\alpha_o \approx 8^{o}$ above 100 km in the meteor region. The Hall current will be most important in the region where the electron and ion ellipses overlap. For $\alpha > \alpha_o$ these flows will have only a small effect on the plasma distribution. This is because any polarization of the plasma produced by the Hall flow of electrons can be easily compensated by an electron flow along the field lines.

However, for $\alpha_c < \alpha < \alpha_o$ the situation is different, particularly when $H_d >> 1$. For $H_d < 1$ the diffusion will be similar to $\alpha > \alpha_o$. The Hall flow may alter the plasma polarization in the central region giving skewed elliptical density profiles. For $H_d >> 1$, Hall flows of electrons accelerate the diffusion. Without these currents most of the ionization would be contained in the ambipolar ellipse. To compensate for the Hall flow the plasma polarization is significantly changed. New Hall currents arise across the field lines so that the ions are no longer restricted by the electric field. Rozhanskii and Tsendin predict that the transverse dimension of the ellipse will then increase from $\sqrt{(D_{T-}\ t)}$ to $\sqrt{(D_{T+}t)}$. This means that at meteor heights the central region of such a disturbance will diffuse as if there was no field present. Less dense fins of ionization will develop away from the central region in the usual manner.

For $\alpha < \alpha_c$ the diffusion will be strongly inhibited. The characteristic dimension of the ionization will then be $\sqrt{(D_{T-}t)}$.

Hitherto atmospheric winds have been neglected. Giles suggests that winds may cause the central column to move relative to the fins as the space-charge is different. Kaiser et al. (1969) showed that field-aligned trains would remain fixed to the field lines, but when $\alpha > \alpha_c$ the trains would drift with the wind. Their results for a plane slab of ionization were similar to those for a column in that a non-aligned plane would drift with the wind. Their solutions

failed to show fins of ionization. Such fins should behave similarly to a plane slab that is field-aligned and would thus be fixed to the field lines. The finite extent of the fins may allow drifts in their own plane. In this direction the ions are free to drift across the field as they are collision dominated. The electrons can diffuse along field lines to maintain quasi-neutrality. The angle at which they can no longer keep up with the ions would depend on the ion drift speed and thus the wind velocity. This angle will be $\sim \alpha_c$ for average winds above 100 km.

Electron-ion collisions may alter the diffusion processes that have been described. Pickering and Windle (1974) find that ν_{+-} terms may prevent the formation of field-aligned fins for ionization at 300 km. However, the ion behaviour is collision dominated at these heights which could change the resulting ionization distribution. Electron-ion collisions make the electrons collision dominated so that they may diffuse across the field. When the ionization density has dropped sufficiently so that these collisions are no longer important the diffusion will again be inhibited across the field. If electron-ion collisions affect meteor diffusion it is likely that they would delay the formation of field-aligned fins of ionization. When the ionization density drops sufficiently fins would be formed.

(5) Summary

Magnetic effects are expected to appear in meteor train diffusion at heights above 95 km. If the train is closely

field-aligned ($\alpha < \alpha_c$) diffusion will be inhibited. This diffusion will be ambipolar, but controlled by the electrons which can only diffuse slowly across the field lines.

If the train is at an angle to the geomagnetic field such that $\alpha > \alpha_o$, the behaviour will depend on the ionization density, height and angle α. Fig 2.5 shows where the transition takes place from separate ellipses of ionization to an ambipolar ellipse. The transition occurs when the background plasma becomes fully depleted by flows of electrons and ions maintaining quasi-neutrality in the ellipses.

For angles $\alpha_c < \alpha < \alpha_o$ and $H_d<1$ the evolution will be similar to that for $\alpha > \alpha_o$. When $H_d >> 1$ Hall flows of electrons accelerate the diffusion of the central region across the field so that the diffusion is similar to that in the absence of a magnetic field. The only difference is that an electron ellipse will be formed, its density being limited by the background plasma density at a value much less than the density of the central column.

The effect of electron-ion collisions on the evolution has not been studied. It is possible that such collisions could delay the formation of field-aligned fins.

It seems quite possible that the field-aligned fins of ionization will not drift across the field. This would occur for both $\alpha < \alpha_c$ and $\alpha > \alpha_c$. However, the fins could drift in the direction of their elongation. The central column of ionization may also drift relative to the fins.

2.7 CHEMICAL REACTIONS

(1) Introduction

The electrons freed during the meteor ablation process will eventually recombine with ions or become attached to other molecules. This leads to a reduction of ionization density and will thus reduce the reflection coefficient of the train. If the rate at which ions and electrons recombine is greater than or similar to the rate at which the effect of ambipolar diffusion reduces the reflected radar signal, incorrect values of ambipolar diffusion coefficient will be inferred.

Charge-exchange reactions that proceed rapidly in comparison with echo lifetimes may also affect the diffusion coefficient since the effective ion mass will change. These reactions may also lead to increased ionization loss by creating suitable ions for dissociative recombination reactions. The initial meteoric ions formed are O^+ and metallic ions - M^+. For an average sporadic meteor velocity of 40 km/s 76% of the ions formed will be O^+ (derived from Sida, 1969). Charge exchange reactions of O^+ are thus important.

(2) Charge Exchange

The main charge exchange reactions for O^+ ions (rate coefficients in m^3/s) are

$$O^+ + O_2 \rightarrow O_2^+ + O \qquad k_1 = 2.5 \times 10^{-17}$$

$$O^+ + N_2 \rightarrow NO^+ + \not{O}N \qquad k_2 = 2 \times 10^{-18} \ .$$

The number densities of O_2 and N_2 remain essentially constant during the reaction because they are much larger than the O^+ number density at meteor heights. Then

$$\frac{\partial [O^+]}{\partial t} = - k_1 [O^+][O_2] - k_2 [O^+][N_2]$$

and the time for $[O^+]$ to drop by a factor of exp(1) is

$$\tau = (k_1 [O_2] + k_2 [N_2])^{-1} \quad .$$

Diffusion will reduce $[O^+]$ and thus increase τ. The height at which diffusion becomes important can be estimated by calculating the time for $[O^+]$ to decrease by a factor exp(1) due to diffusion alone and comparing this time with τ. This is shown for $[O^+]$ on the train axis in Table 2.11.

Table 2.11: Comparison of diffusion and charge exchange on $[O^+]$.

Height (km)	90	95	100	105	110
τ (ms)	2	6	17	50	135
Diffusion τ (ms)	58	51	40	29	22

The effect of diffusion on τ will be small below 100 km and will increase the value of τ above this height. The transition from the dominance of O_2^+ ions to O^+ ions in

diffusion was considered in Section 2.3. As these transitions take place at similar heights, they combine to make the overall transition sharper.

One other charge exchange reaction of interest is

$$M^+ + O_3 \rightarrow MO^+ + O_2 \qquad k = 1.5 \times 10^{-16}$$

following which the MO^+ ion readily undergoes dissociative recombination ($k \sim 2 \times 10^{-13}$). The O_3 concentration is uncertain and variable, but τ will be about 20s at 80 km, using $[O_3]$ from CIRA (1972). Thus the loss rate for metal ions is much slower than the time for an underdense echo decay.

(3) Attachment and Detachment

Attachment processes are predominantly two-body and are much slower than those with third bodies present (Baggaley and Cummack, 1974). The most important attachment reactions are thus

$$O_2 + e + O_2 \rightarrow O_2^- + O_2$$

$$O_2 + e + N_2 \rightarrow O_2^- + N_2$$

$$O_3 + e \rightarrow O^- + O_2 \quad .$$

The second reaction has the shortest time constant: $\tau \sim 40$s at 80 km. This indicates that attachment will have little effect on electron density. Furthermore, Baggaley and Cummack

(1974) suggest that associative detachment may reduce the effect of attachment. The reactions are

$$O_2^- + O \rightarrow O_3 + e$$

$$O^- + O \rightarrow O_2 + e$$

and the time constants are less than 1s above 80 km. Thus any electrons lost by attachment are quickly regained.

(4) Recombination

Recombination reactions such as

$$O^+ + e \rightarrow O + h\nu$$

$$M^+ + e \rightarrow M + h\nu$$

proceed slowly in comparison with echo decay times. An estimate of the time constant for the second reaction for a transition-type meteor is $\sim 5 \times 10^5$ s. The first reaction could be expected to be the same.

Dissociative recombination appears to be the most effective loss mechanism for electrons. The important reactions are

$$O_2^+ + e \rightarrow O + O$$

$$NO^+ + e \rightarrow N + O$$

$$MO^+ + e \rightarrow M + O \quad .$$

The rates for these reactions are expected to be similar, but the charge-exchange reactions creating the molecular ions

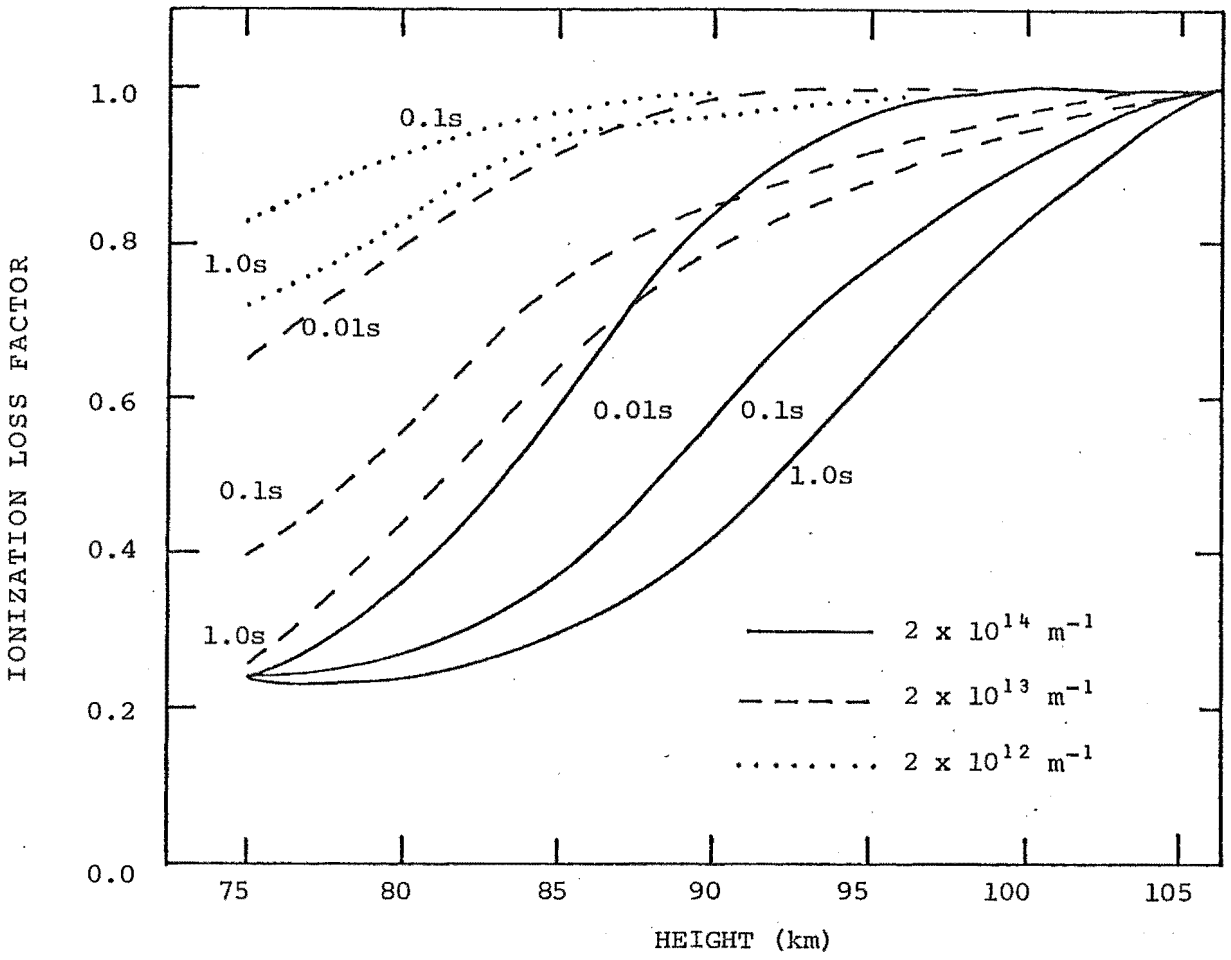

Figure 2.6: The ionization loss factor as a function of time, line density and height.

must be considered. Reactions of the M^+ ions are less important because of the low O_3 density.

Baggaley (1979a) has calculated ionization losses for various times and meteor magnitudes. He solves numerically the important reactions and includes the effect of diffusion The results, are shown in Fig. 2.6 with the calculations extended down to 75 km (Baggaley, 1979, unpublished). The ionization loss factor is the ratio of the electron line density at a certain time to the initial line density. A meteor velocity of 40 km/s has been used. Differences to Baggaley (1979a) are due to slightly different values of r_o used.

The ionization loss factor does not go below 0.24 because only metallic ions are left at this stage. The very slow loss of electrons by dissociative recombination with molecular metallic ions was not included in the calculations. Below about 90 km ionization loss will start to have an effect on durations (especially on larger meteors). This is because the greater electron and ion concentrations enable the reaction to proceed more quickly.

The effect of chemical reactions on diffusion coefficient measurements is more easily seen by calculating the effect of the ionization loss on measured D values for particular radar wavelengths. This is done in chapters four and seven where comparisons are made with experimental results.

2.8 IONIZATION PROFILE

So far it has been assumed that the initial ionization density distribution along the meteor train (referred to as the ionization profile) is uniform. Variations in the ionization profile may affect diffusion processes and reflection processes.

These variations can be classified in two groups. One is the classical ionization curve which is caused by the change in atmospheric density over the length of the train combined with the loss of meteoroid mass from ablation. The other is a more random variation over smaller length scales and is probably due to fragmentation.

Classical theory relates the ionization profile and height of maximum ionization to mass, velocity and zenith angle. See for example McKinley (1961).

Observations of the light from bright (i.e. $q > \sim 10^{15}$ m^{-1}) meteors show profiles that are in good agreement with the classical theory. The light curve is directly related to the ionization profile by the efficiency of the production of light and ionization. The light curves for faint meteors (i.e. $q < \sim 10^{12}$ m^{-1}) do not fit this pattern (Jacchia, 1955). These meteors sometimes show non-classical, rapid increases in ionization and decelerations that are larger than expected. Furthermore, the train lengths of faint meteors are shorter than those expected from the classical theory. These observations have been confirmed by television observations of faint meteors (Jones and Hawkes, 1975) who found the average train length to be 6.7 ± 0.7 km. These results are explained by Jacchia's suggestion of a fragile meteoroid structure that fragments easily. Such a model fits present experimental data better than any other (Verniani, 1969).

The model of Hawkes and Jones (1975) for the ablation of meteoroids (which involves the steady release of grains) is consistent with the fragile model. The ionization profile is expected to be steeper for faint meteors and fits the experimental data. Fragmentation is still needed to explain the more rapid variations observed.

Rapid variations in the electron density along meteor trains were measured by Rice and Forsyth (1964). Their radar experiment showed variations of up to 50% of the mean ionization with scale-lengths of less than 1 km. In a more refined experiment Jones (1969b) found that an upper

limit for ionization irregularities is 30% of the mean ionization density. In another experiment Rice and Forsyth (1963) attribute the scatter in decay times observed at three different wavelengths to irregular ionization. This scatter is not wavelength dependent at a 5% significance level. Because of this Jones (1969a) suggests that these effects are caused by small-scale wind shears. However, the number of meteors is also too small to make certain any lack of wavelength dependence.

Baggaley (1979c) presents results from a two wavelength study of 808 meteors. He found a linear relationship between a parameter that is a measure of the scatter in the ratio of decay times and a function of the wavelength difference. This function represents the difference in train length observed on the two wavelengths and is given by $\sqrt{(\lambda_1/\lambda_2)-1}$. The linear relationship is found by comparing his results with Rice and Forsyth (1963) and Greenhow (1952). This suggests that the effect seen in these experiments is caused by an irregular ionization profile.

These observed variations in the ionization profile may affect the diffusion processes and will influence diffusion coefficient measurements. There will be some diffusion parallel to the train axis which was neglected in solving the diffusion equations. The diffusion in transverse directions should not be greatly affected as the density gradient will be much greater than that along the train. The biggest effect will be in measuring diffusion coefficients from echo decay rates. It has already been shown that an irregular

ionization profile can cause a scatter in the values of diffusion coefficient deduced from echo decays (Rice and Forsyth, 1963). This is compounded by the effects of winds and wind shears in the atmosphere. These cause movement of the specular reflection point along the train and are discussed in the next chapter.

CHAPTER 3

RADAR MEASUREMENTS OF METEOR TRAINS

3.1 INTRODUCTION

In chapter 2 the behaviour of meteor train ionization was investigated. Of special interest in this work is diffusion - a process ideally suited to radar studies. Incident radar energy is scattered by electrons in the train and can be received at the transmitter site (back-scatter) or at other locations (forward-scatter).

As the ionized train diffuses the reflected signal is attenuated by phase interference effects arising from path differences across the train. When the train has a radius of the order of the radar wavelength the signal is substantially reduced. The rate at which this reduction of received amplitude occurs can then be used to find the effective diffusion coefficient in the train region.

Unfortunately, some effects will complicate the ideal situation and it is important to consider what these are and how large an influence they will have on diffusion coefficient measurements. That is the aim of this chapter in which, firstly, the basic radio reflection theory for underdense meteors is outlined and then extended to consider forward-scatter from trains that are affected by the geomagnetic field. The validity of the underdense model is also discussed. Secondly, various ways in which

atmospheric winds affect the reflection process are discussed. Thirdly, the effect of sky noise on measurements and the finite meteor velocity are considered. Finally, some aspects of measuring train heights are investigated.

3.2 MEASUREMENT OF METEOR DIFFUSION BY RADAR

(1) The Underdense Train Model

In this work only underdense-type meteors are studied. In this case it is assumed that each electron scatters the incident radio waves independently. This is a reasonable assumption if the electron line density, q, is much less than 2×10^{14} m^{-1}.

It is possible to derive an expression for the power received from the whole train by starting with the free electron scattering cross-section. McKinley (1961) gives this derivation along with modifications to the basic model. This basic model considers an infinitely long, stationary train with a diameter that is small in comparison with the radar wavelength. This can then be refined by considering the power reflected from the train as it is formed. To make the problem more tractable it is assumed that the power can be expressed in terms of Fresnel integrals. This will not be true far from the specular reflection point on the train, but the power received from these regions is small compared with that received from the first Fresnel zone.

The behaviour of the received signal can be represented graphically by the Cornu spiral (Fig. 3.6). The received amplitude is proportional to the length of the line from the point where the train begins on the spiral to the point where it ends. Generally the beginning is taken to be at $-\infty$ so that the echo amplitude increases steadily and then oscillates about a final value which is reached when the train extends to infinity in both directions. The phase of the received signal is represented by the angle between an arbitrary direction and the amplitude line.

This basic model can readily be extended to take account of the diffusion in the train. By integrating over the train cross-section, assuming a Gaussian electron density and by including the effect of the path difference across the train, the echo power is shown to decrease as

$$A = A_o \exp\left(-\frac{16\pi^2 Dt}{\lambda^2}\right) \exp\left(-\frac{4\pi^2 r_o^2}{\lambda^2}\right) \quad . \qquad 3.1$$

Here A_o is the maximum amplitude that would be received from an infinitely long train. This is reduced by the initial radius of the train and a further reduction in amplitude, as time progresses, is caused by diffusion. The echo decay time is defined as the time for the amplitude to decay by a factor exp(1) from the peak amplitude as is thus given by

$$\tau = \frac{\lambda^2}{16\pi^2 D}$$

(mentioned in section 2.4). This derivation only applies to a backscattered echo. (Forward-scatter is considered in the next sub-section). Furthermore, only stationary trains are considered in this model - moving trains are considered in section 3.3.

The decay of the underdense echo was derived by considering a cross-section of the train. In reality the problem is three-dimensional and the fact that the train is not formed instantaneously should be considered. The finite meteor velocity means that the parts of the train formed first will have had time to diffuse to greater radii than other parts. The result is the formation of a cone of ionization. However, numerical integration along the train shows that the effective average radius is equal to that at the specular reflection point.

A further effect, that has not been considered, is the change in diffusion coefficient with height. Over the length of a Fresnel zone for a typical radar wavelength of 10 m and meteor range of 300 km, the change in D_a is 20%. This will bias the measured value of D to that for a lower height. However, numerical integration by McIntosh (1969) with both D and q varying exponentially with height shows that the amount of bias is only 1-2%.

(2) Magnetically Affected Trains

Kaiser (1968) presented an expression that described the diffusion coefficient that would be measured by backscatter from an elliptical ionization distribution.

Elliptical distributions may occur in some trains, but a distribution that is a superposition of an ellipse and a circle is also expected. The behaviour in the forward-scatter case is also of interest within this work. In this sub-section the scattering properties of magnetically affected trains in the forward-scatter case are developed. Elliptical cross-sections are considered first.

Consider a set of axes (x,y) such that the x-direction is parallel to the major axis of an ellipse and the y-direction is parallel to the minor axis. Let the respective diffusion coefficients be $D_{\parallel}, D_{\perp}$ where $D_{\parallel} > D_{\perp}$. Then equation 2.1 becomes

$$N = \frac{q}{4\pi(t+k)\sqrt{(D_{\parallel} D_{\perp})}} \exp\left[- \frac{D_{\perp} x^2 + D_{\parallel} y^2}{4 D_{\perp} D_{\parallel} (t+k)} \right] . \qquad 3.2$$

Equation 3.2 describes ellipses of constant density which evolve with constant eccentricity. The constant k represents the effect of the initial configuration and would normally be expressed in terms of the initial radius. However, equation 3.2 would describe an initial distribution that was elliptical whereas the real distribution is initially circular. For this reason the initial radius is not included in this analysis. It does not contribute to the echo decay rate, but produces an initial amplitude reduction which is usually small in comparison to subsequent diffusion effects.

The reduction in echo amplitude is given by

$$S = \frac{A}{A_o} = \frac{\int_{x=-\infty}^{+\infty} \int_{y=-\infty}^{+\infty} N \exp[\frac{2\pi i p}{\lambda}] dx\ dy}{\int_{x=-\infty}^{+\infty} \int_{y=-\infty}^{+\infty} N\ dx\ dy}$$

where p is the total path difference between the point (x,y) and some origin line of zero phase (Helofson, 1951). It is now necessary to integrate over the train cross-section. This can be made easier by transforming to parametric coordinates so that

$$x = a \sin \psi,\ y = b \cos \psi \quad .$$

The eccentricity is then given by

$$e = (1 - \frac{D_\perp}{D_\parallel})^{\frac{1}{2}}$$

which is a constant. This leads to the relation

$$b^2 = a^2 \frac{D_\perp}{D_\parallel}$$

so that equation 3.2 becomes

$$N = \frac{q}{4\pi(t+k)(D_\parallel D_\perp)^{\frac{1}{2}}} \exp\left[-\frac{a^2}{4D_\parallel (t+k)}\right] \quad . \qquad 3.3$$

This means that ellipses of constant density are described by the variables a and t. Integration over all values of a and ψ will cover the cross-section of the train. ψ corresponds to an azimuth angle if the ellipse is transformed into a

circle. With the parametric coordinates the surface element becomes

$$dS = a\left(\frac{D_\perp}{D_\parallel}\right)^{\frac{1}{2}} da\, d\psi \quad .$$

The path difference p must be expressed in terms of a and ψ. Figures 3.1 and 3.2 show a train cross-section for a forward-scatter geometry with a forward-scatter angle 2ϕ. Now,

$$p = p_1 - p_2$$

$$d^2 = a^2(\sin^2\psi + \frac{D_\perp}{D_\parallel}\cos^2\psi)$$

$$\sin\delta = \frac{\sin\psi}{(\sin^2\psi + \frac{D_\perp}{D_\parallel}\cos^2\psi)^{\frac{1}{2}}}$$

$$\cos\delta = \frac{\left(\frac{D_\perp}{D_\parallel}\right)^{\frac{1}{2}}\cos\psi}{(\sin^2\psi + \frac{D_\perp}{D_\parallel}\cos^2\psi)^{\frac{1}{2}}}$$

where δ is the angle between the y-axis and the small segment, length d. Since

$$p_1 = d\sin(\theta+\delta)$$

and

$$p_2 = d\sin(2\phi - (\theta+\delta))$$

where θ is the angle between the x-axis and the transmitter direction, then

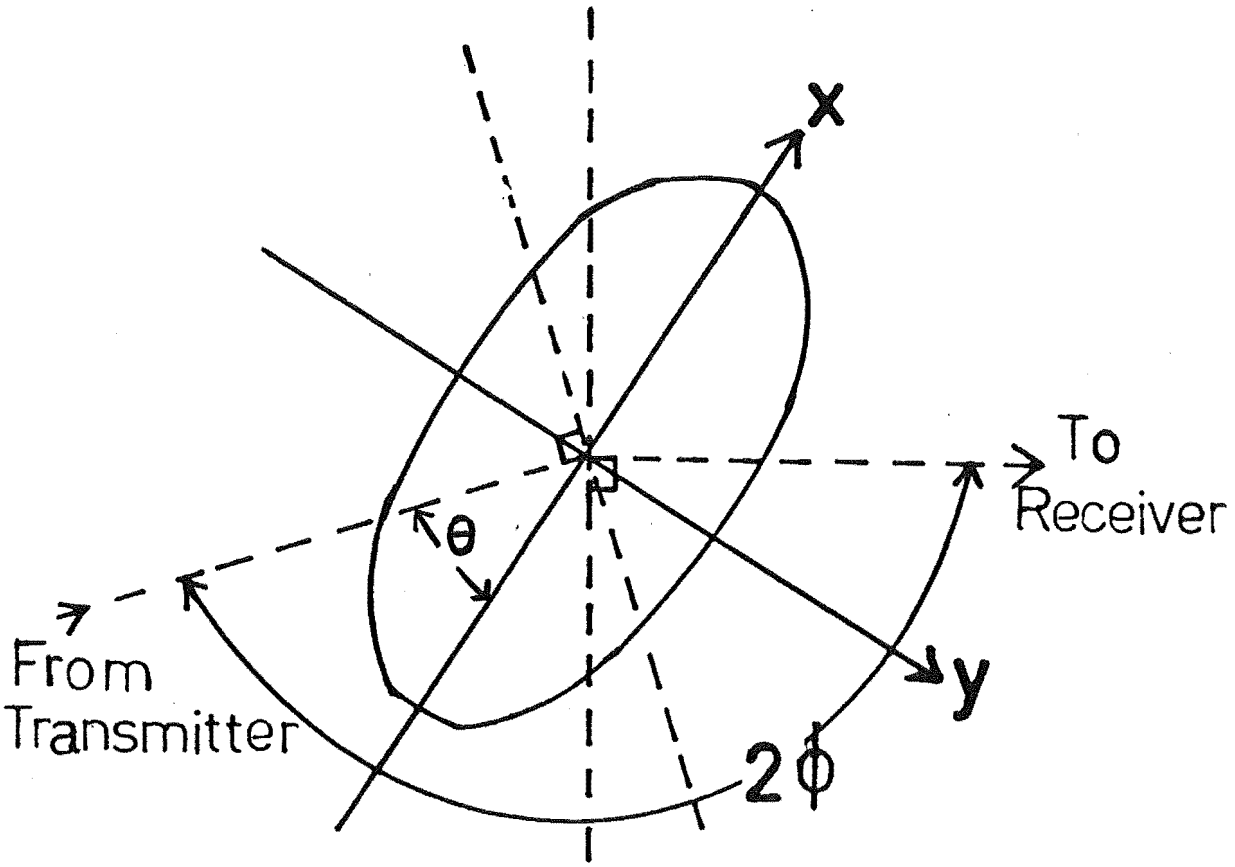

Figure 3.1: Train cross-section with forward-scatter angle 2ϕ.

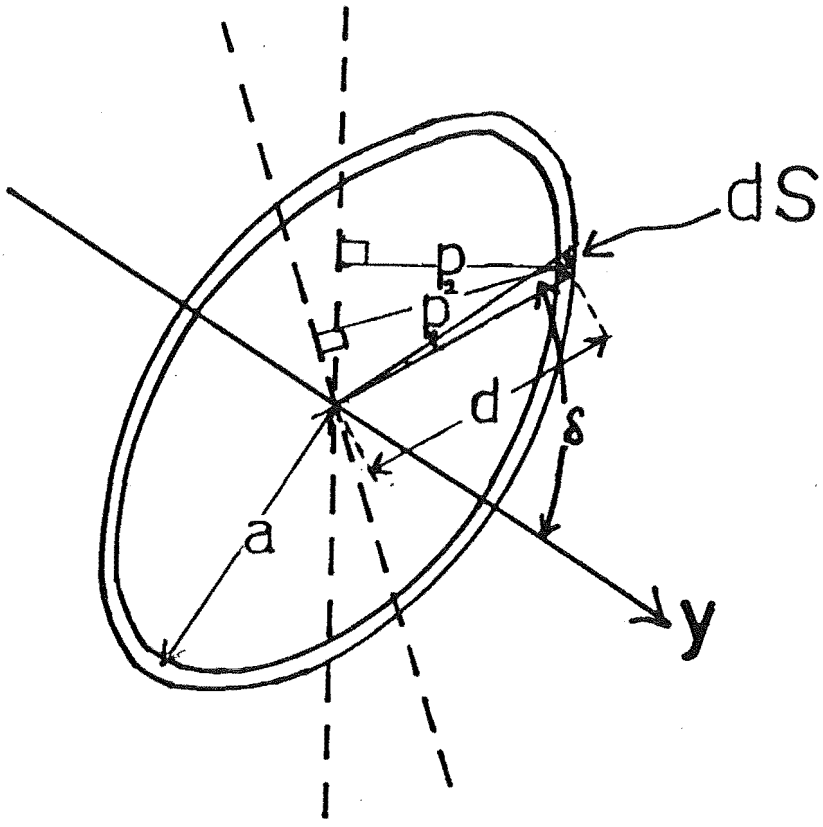

Figure 3.2: Train cross-section with path differences p_1 and p_2.

$$p = a[\sin\psi(\cos\theta + \cos(\theta-2\phi)) + \left(\frac{D_\perp}{D_\parallel}\right)^{\frac{1}{2}} \cos\psi(\sin\theta + \sin(\theta-2\phi))].$$

Finally, putting $S = I_1/I_2$

$$I_1 = \int_{a=0}^{\infty} N\, a \left(\frac{D_\perp}{D_\parallel}\right)^{\frac{1}{2}} [\int_{\phi=0}^{2\pi} \exp(\frac{2\pi i p}{\lambda})\, d\psi]\, da$$

$$I_2 = \int_{a=0}^{\infty} N\, a \left(\frac{D_\perp}{D_\parallel}\right)^{\frac{1}{2}} [\int_{\psi=0}^{2\pi} d\psi]\, da \ .$$

The evaluation of I_2 is straightforward and with equation 3.3 for N gives

$$I_2 = q \ .$$

I_1 is more difficult to evaluate. Firstly, Gradshtein and Ryzik (1965) give

$$\int_0^{2\pi} f(m\cos x + n\sin x)\, dx = 2\int_0^{\pi} f(\sqrt{(m^2+n^2)}\cos x)\, dx$$

so that the integral inside I_1 (I_1') becomes

$$I_1' = 2\int_{\psi=0}^{\pi} \exp(\frac{2\pi i a}{\lambda}\sqrt{(m^2+n^2)}\cos\psi)\, d\psi$$

where

$$m = \left(\frac{D_\perp}{D_\parallel}\right)^{\frac{1}{2}} (\sin\theta + \sin(\theta - 2\phi))$$

and

$$n = \cos\theta + \cos(\theta - 2\phi) \ .$$

Now

$$J_o(z) = \frac{1}{\pi}\int_0^{\pi} \exp(iz\cos\psi)\, d\psi$$

so that

$$I_1 = 2\pi J_o\left(\frac{2\pi a}{\lambda}\sqrt{(m^2+n^2)}\right) \quad .$$

If

$$c \equiv [4D_{\|}(t+k)]^{-1}$$

then combining I_1 and I_2 gives

$$S = 2c\int_{a=0}^{\infty} \exp(-ca^2)aJ_o\left(\frac{2\pi a}{\lambda}\sqrt{(m^2+n^2)}\right)da \quad .$$

This integral is given by Watson (1966) so that

$$S = \exp\left[-\frac{\pi^2}{\lambda^2}\frac{m^2+n^2}{c}\right]$$

$$= \exp\left[-\frac{\pi^2}{\lambda^2}(16\, D_{eff}(t+k))\right] \qquad 3.4$$

where

$$D_{eff} = \tfrac{1}{4}[D_{\perp}(\sin\theta + \sin(\theta-2\phi))^2 + D_{\|}(\cos\theta + \cos(\theta-2\phi))^2] \, .$$

Equation 3.4 agrees with that given by Kaiser (1968) for backscatter i.e. when $2\phi = 0$. It also agrees with equation 3.1 when $D_{\perp} = D_{\|}$.

D_{eff} is the diffusion coefficient that would be inferred for an echo decay from an elliptical train. Thus it is possible to predict what value of D would be observed for such trains, if the angle θ is known.

The next step is to include the effect of a circular central region that would be formed by the ion "ellipse". If N_1 is the number density of ionization for the ellipse and N_2 is that for the circle

$$S = \frac{\int_{x=-\infty}^{+\infty} \int_{y=-\infty}^{+\infty} (N_1+N_2) \exp(\frac{2\pi i p}{\lambda}) dx\ dy}{\int_{x=-\infty}^{\infty} \int_{y=-\infty}^{\infty} (N_1+N_2) dx\ dy} \quad .$$

Each integral can be divided in two and solved separately. Then

$$S = \exp[-\frac{\pi^2}{\lambda^2}(16\ D_{eff}(t+k))] + \exp[-\frac{16\pi^2 D(t+k')}{\lambda^2}] \qquad 3.5$$

where D is the diffusion coefficient for the circular distribution. The final inferred decay will depend on the method used for measuring S. For example, two points on the decay or the slope of the ln (amplitude) line could be used.

(3) Full Wave Scattering and Plasma Resonance

Poulter and Baggaley (1978) present results from a full wave scattering theory. This theory does not assume that the electrons scatter independently so that the behaviour of echoes from transition-type and overdense meteor trains can be examined along with underdense meteors.

They derive two important results for diffusion coefficient measurements. Firstly, trains in the transition region

$$2 \times 10^{13} < q < 2 \times 10^{15}\ m^{-1}$$

may show exponential decays, especially at the lower end of this range. However, the slope of this decay is a measure of βD. The factor β depends on q and is less than

unity. The physical reason for this is that although the radio wave penetrates the column of ionization and is scattered and attenuated by phase interference, the effective wavelength inside the column is increased because the refractive index for the medium of the train is less than unity. The amount by which the wavelength is changed depends on q and although the resulting decay is exponential it has a different slope leading to smaller inferred values of D.

To obtain good measurements of D it is thus necessary to obtain an estimate of q and to reject echoes with $q > 2 \times 10^{13}$ m^{-1}. This cannot be achieved by rejecting echoes with non-exponential decays: estimates of q should be made by considering the transmitter power, aerial gains and received echo amplitude for a particular experiment.

The second important result obtained from full wave scattering theory is the effect of plasma resonance. A resonant oscillation can be induced in a plasma under certain boundary conditions. If the electric vector of the incident radio wave is parallel to the train axis there is no effective boundary because of the train length. However, if the incident wave is perpendicular to the train, resonance can occur because the train has a scale comparable with the wavelength. The effect of this resonance is to increase the received echo amplitude in the early part of the echo life. The resonance rapidly decreases with time so that for the last $\sim$ 70% of the echo life decays are not affected. However, diffusion coefficients inferred from the initial decay slope may be overestimated.

To avoid overestimating D the early part of an echo decay should not be used. Plasma resonance will only occur when the electric vector of the incident waves has a component that is perpendicular to the train and the magnitude of this effect will depend on the size of the component. As train direction is not usually measured by meteor radar systems this criterion needs to be applied to all trains.

3.3 THE EFFECT OF WINDS ON D MEASUREMENTS

In the following sub-sections the effects of non-uniform winds on diffusion coefficient measurements are discussed. Many workers have derived results for various wind effects and in some cases these results appear to differ. Furthermore, they have presented the results in different ways so that comparison is difficult. The dependence of the effects on height has often not been considered. In this section the various effects that have been derived are summarised and are presented in a consistent manner. The height dependence for each effect has also been evaluated.

The important parameters describing the wind are: the wind velocity $\underline{u}_o$, the wind shear $\underline{u}_1$, the wind shear gradient $\underline{u}_2$ and the small-scale turbulent wind velocity $\underline{u}_s$. The last quantity is considered in subsection 2. Only horizontal motions are considered as there is strong evidence that vertical velocities are negligible by comparison. (Jones and Read, 1972).

Here a sinusoidal wind profile is assumed, of the same form as that used by Jones and Read (1972)

$$\underline{u}(h) = \underline{u}_o \cos\left(\frac{2\pi h}{\lambda_w}\right)\exp\left(\frac{h}{2H}\right) \qquad 3.6$$

where h is the height above some level where $\underline{u}_o$ and $\underline{u}_1$ are known. This height is expected to be that of the peak of the meteor height distribution ~ 95 km. H is the atmospheric scale height ~7km and λ_w the wavelength of the sinusoid.

Jones and Read used measured values for the root mean square (r.m.s.) wind velocity and wind shear to find λ_w and $\underline{u}_o$ so that the r.m.s. wind shear gradient $\langle\underline{u}_2\rangle$ could be calculated. They use

$$\langle\underline{u}_o\rangle = 25 \text{ m/s}$$

$$\langle\underline{u}_1\rangle = 19 \text{ ms}^{-1} \text{ km}^{-1}$$

so that $\underline{u}_o = 35$ m/s and $\lambda_w = 8.3$ km. Then equation 3.6 becomes

$$\underline{u}(h) = 35 \cos(0.76h)\exp(0.071\ h)$$

so that

$$\langle\underline{u}_2\rangle = 14 \text{ ms}^{-1} \text{ km}^{-2} \ .$$

Each of $\langle\underline{u}_o\rangle$, $\langle\underline{u}_1\rangle$ and $\langle\underline{u}_2\rangle$ will have the same height dependence as u(h) i.e.

$$\langle\underline{u}_n(h)\rangle = \langle\underline{u}_n(95 \text{ km})\rangle \exp(0.071\ h).$$

Both $\underline{u}_o$ and λ_w can vary widely from the assumed values at

different times, but they are characteristic of the 95 km level.

(1) Wind Shears

The wind shear affects meteor trains in two ways. As the train is formed the ionization is moved from its original position by the wind. By the time that the meteor has crossed the first Fresnel zone the ionization first formed has moved relatively further from its original position than the ionization formed later because of the larger wind velocity at the height. Clearly, the opposite situation can also occur. The train of ionization thus formed is often curved and has different scattering properties. A train formed in a uniform wind will be straight, but rotated with respect to the meteoroid trajectory. It will then keep this orientation and scatter normally.

The second effect of the wind shear is train rotation. This causes the specular reflection point to move along the train thus altering the apparent echo decay through three mechanisms. Firstly, the scattered power will come from a newer (or older) part of the train. For example, in the extreme case of the reflection point moving as quickly as the meteor head, no decay would be observed. Secondly, since the diffusion coefficient varies with height, a change in the measured value of D occurs so the result is some average D. Finally, if the ionization profile is not uniform along the train the scattered power will come from a section of train with a different q which will again give a different inferred value for D.

Deegan et al. (1970) give an expression for the measured value of D in terms of echo decay and wind shear. They assumed that D was constant with height and only considered near-vertical trains. Their expression can be written in terms of the error in D, ΔD, which is the difference between the value of D inferred from measurements and the real value of D at that particular height. Then

$$\Delta D = \frac{1}{1-a}\left[aD + \frac{\lambda^2 <\underline{u}_1> R}{16\ \pi^2 (1-2a)}\frac{d}{dh}(\ln q)\right] \qquad 3.7$$

where $a = <\underline{u}_1>R/V$ is approximately the ratio of the velocities of the reflection point and the meteor head, R being the echo range. In this equation the first term arises from the reflection point moving to a part of the train with a different "age". The second term results mainly from the reflection point moving to a region of the train where q is different. For a high velocity meteor ($a \to 0$) this term reduces to that found by McIntosh (1969). McIntosh suggests two models for the variation of q. In the first a classical ionization profile is assumed giving

$$\frac{d}{dh}(\ln q) = \frac{1}{H_e}$$

where the effective scale height $H_e \approx H$ the atmospheric scale height. The second model is for $H_e \approx H/6$ which agrees more closely with the expected ionization profile for faint meteors (mentioned in section 2.8).

Fig. 3.3 summarises the scatter caused in diffusion coefficient measurements by the wind effects discussed in

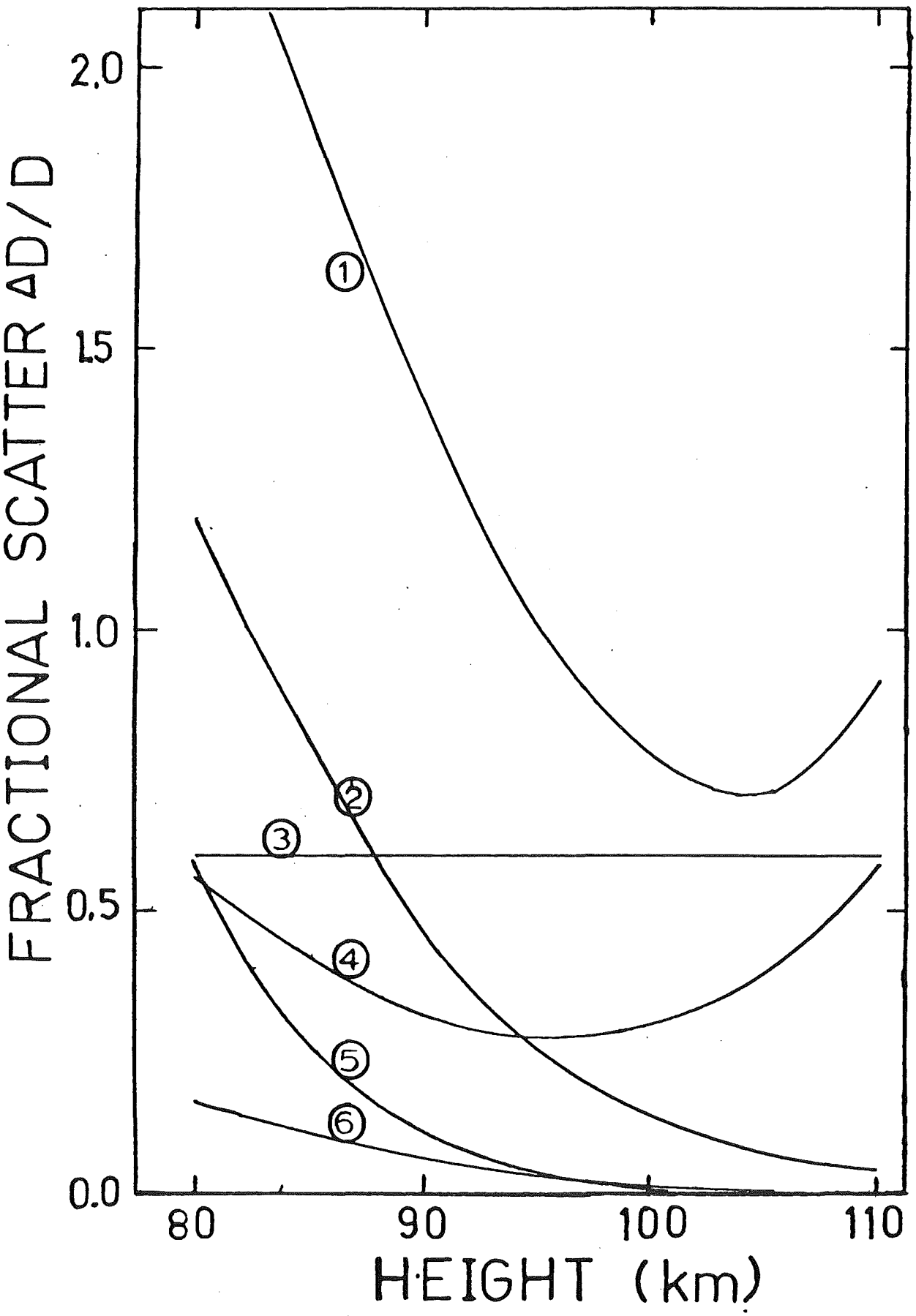

Figure 3.3: Summary of wind effects: (1) Wind shears (H_e = H/7); (2) Wind shear gradients; (3) Finite trains (upper limit); (4) Wind shears (H_e=H); (5) Small-scale wind shears (x_o << 125m); (6) Small-scale wind shears (125m << x_o < 1km). (V = 40 km/S, R = 250 km, λ = 10m).

this section. The contribution by wind shears is very large, especially for short trains, but it must be remembered that this is for the steepest part of the ionization profile.

Further work by McIntosh (1969) shows that $\Delta D/D \approx 0.6$ for "worst case" conditions. Here the change in D and q with height are considered as well as finite train lengths. This use of abruptly ending trains is probably not realistic and would increase the derived scatter. However, McIntosh concludes that this model does not fully explain the observed scatter in D.

In a computational study using a random ionization profile with tapered ends Brown and Elford (1971) found that ΔD is effectively constant with height and that wind shears could be important below 100 km. The variation of wind shear with height was not considered. These results seem to confirm the first part of the work by McIntosh.

Finally, Novotny (1978) has considered the effect of wind shears on a uniformly ionized train and takes into consideration the variation of D and r_o with height. The r_o values used are based on theory and their height dependence is thus stronger than that observed by experiment. Even so, the fractional scatter is relatively small - $\Delta D/D \approx 0.1$.

(2) Small-Scale Wind Shears

Constant wind shears along the train length have been assumed so far. In this and the next sub-section smaller scale effects are considered.

Jones (1972) has examined the effect of small-scale wind shears on both overdense and underdense meteors. Meteor trains initially scatter coherently, but the scattered amplitude decreases as the train becomes distorted by small-scale variations in the wind velocity. Jones defines a time constant, T, such that

$$T = \frac{\lambda}{2\pi \langle u_s \rangle} \qquad 3.8$$

where $\langle u_s \rangle$ is the r.m.s. value of the wind velocity and is a measure of the small-scale wind variations. For times

$$t < 0.5\ T$$

the scattering from the train is essentially coherent and the scattered amplitude is reduced by less than 5% (if diffusion is ignored). For times

$$t > 2T$$

the scattering becomes incoherent and the scattered amplitude is about 10% of the initial amplitude.

When diffusion is considered the effects are different on overdense and underdense meteors. In the overdense case, a rapid decrease in received amplitude is expected for $t > T$. An upper limit can thus be placed on u_s by examining overdense echo durations. This is only an upper limit because in practice the echoes are affected by the appearance of

secondary reflection points and ionization loss. Using the data of Greenhow (1952), Jones finds that

$$\langle \underline{u}_s \rangle < 1.6 \text{ m/s.}$$

The data of Baggaley (1966), which shows an unexpected decrease in the rate of echoes with durations greater than about 9s (λ = 10.7 m), gives

$$\langle \underline{u}_s \rangle \approx 0.19 \text{ m/s.}$$

These data were from a two wavelength experiment so that the wavelength dependence of the effect can be found. Then

$$\log\left[\frac{t_c(10)}{t_c(28)}\right] = 0.34 \pm 0.2$$

where $t_c(10)$ is the echo duration at which the cutoff occurs for a frequency of 10 MHz. Baggaley states that the expected values for two-body and three-body attachment are 0.18 and 0.3 respectively. Equation 3.8 gives a value of 0.45 for the wind effect. This indicates that three-body attachment is the most likely mechanism (as Baggaley assumed). This then provides an upper limit for u_s so that

$$\langle \underline{u}_s \rangle < 0.19 \text{ m/s.}$$

A height dependence of $u_s \propto \exp(h/2H)$ will be assumed. This may be too strong because viscosity tends to damp out shorter wavelength wind motions as they propagate upwards.

Now that an upper limit has been found for $\langle \underline{u}_s \rangle$ the effect of small-scale wind shears on underdense echo decays can be considered. Jones (1972) finds that $\langle \underline{u}_s \rangle$ will introduce scatter into measured decay times. The amount of scatter is sensitive to the scale-size of the wind variation, x_o. In terms of ΔD the scatter is

$$\Delta D \approx \frac{\lambda^2}{16\pi^2} \frac{2.0}{T} \qquad 125\text{m} << x_o < 1 \text{ km}$$

$$\Delta D \approx \frac{\lambda^2}{16\pi^2} \frac{4.1}{T} \left(\frac{x_o V \tau}{R\lambda} \right)^{\frac{1}{2}} \qquad x_o << 125 \text{ m}$$

The fractional scatter in measured diffusion coefficients for each of these scale-sizes is shown in Fig. 3.3.

(3) Wind Shear Gradients

Jones and Read (1972) examine the effect of wind shear gradients on the measurement of diffusion coefficients. These gradients will cause trains to become bent after they have formed, thus focussing or defocussing the scattered radio waves. Second reflection points will eventually be formed and are considered in the next sub-section. Earlier times are considered here.

The scatter in measured diffusion coefficients becomes

$$\Delta D \approx \frac{\lambda^2}{16\pi^2} \frac{R\langle \underline{u}_2 \rangle}{2} \quad . \qquad 3.9$$

The relative importance of wind shear gradients is shown by Fig 3.3. Their effect is most important below 90 km.

(4) Multiple Reflection Points

When trains become very distorted by the wind field new reflection points are created. Generally these reflection points will have different relative velocities so that the scattered signals interfere to give deep fading. Greenhow (1952) observed that over 70% of echoes with durations greater than 0.45s show deep fading so that the rejection of any echoes that do fade is not practical. The best way of ensuring that fading will have little effect on diffusion coefficient measurements is to exclude later parts of echo decays where fading is likely to occur.

Both Manning (1959) and Phillips (1969) find expressions for the time delay before the formation of a second reflection point. Manning has considered general wind profiles that have a constant amplitude with height, whereas Phillips considers a sinusoidal profile with an amplitude that increases exponentially with height. The most likely time for the onset of fading, from Phillips, is given by

$$T_f = \frac{0.025 \cdot 2\lambda^2}{R\, \underline{u}_o} \quad . \qquad 3.10$$

Experimentally he finds that

$$\frac{2\lambda^2}{\underline{u}_o} = 2.2 \times 10^3 \text{ km-s}$$

so that for R = 250 km

$$T_f = 0.22 \text{ s.}$$

As these data are from meteors, the appropriate height will be about 95 km so that including the height variation of $\underline{u}_o$ in equation 3.10 gives

$$T_f = \frac{55 \exp[-\frac{h}{2H}]}{R} \text{ s} \qquad 3.11$$

where h, H and R are in km. Echo decay time has a stronger height dependence than T_f so that the formation of a second reflection point during an echo decay time is more likely lower in the meteor region.

3.4 MULTIPLE WAVELENGTH STUDIES

The use of more than one radio wavelength in studying echo decays from the same train is valuable in providing information on complex processes occurring within these trains. Of particular interest is the wavelength dependence of the scatter in measured diffusion coefficients (or more directly echo decay times). The wavelength dependence of measured diffusion coefficient itself has already been mentioned in section 2.5.

The echo decay time, τ, is used in this section because it is directly measured by experiment. Most wind induced scatter in decay time ($d\tau$) is expected to be related to wavelength by

$$\frac{d\tau}{\tau} = k \cdot \tau R \underline{u}_n \qquad 3.12$$

here k is a constant and $\underline{u}_n$ is the relevant wind parameter (e.g. wind shear gradient $\underline{u}_2$). The wavelength dependence is contained in τ and there is also a height dependence. Most results are presented in terms of the logarithm of the scatter in the ratio, ρ, in the decay times on the two frequencies. Some authors use normalised decay times, removing the λ^2 wavelength dependence. This does not change the r.m.s. deviation of log ρ which becomes

$$\Delta(\log \rho) = \frac{kR}{2.3} \underline{u}_n \tau_1 \left(\frac{\lambda_1^2 - \lambda_2^2}{\lambda_1^2} \right) \qquad 3.13$$

providing $d\tau << \tau$.

Scatter due to irregular ionization, given by Jones (1969a), becomes

$$\Delta(\log \rho) = \frac{\sigma_o}{2.3} \left(\frac{\lambda_1 - \lambda_2}{\lambda_1 + \lambda_2} \right)^{\frac{1}{2}} \qquad 3.14$$

where σ_o is the standard deviation of the irregular component of the ionization line density.

Results from two wavelength experiments enable these effects to be compared as their wavelength dependence is different. Furthermore, equation 3.14 has no relationship to height whereas equation 3.13 does. This dependence is in the factor

$$f = \underline{u}_n \tau \quad .$$

τ decreases exponentially with height whereas $\underline{u}_n$ increases. The overall dependence is

$$f \propto \exp(-\ 0.071\ h), \qquad 3.15$$

where h (km) is the distance from some reference height (usually 95 km).

Two sets of data are available for examining this height dependence: those of Yu, presented by Jones and Read (1972) and those of Baggaley (1979c). These results are shown in Table 3.1.

Table 3.1: Multi-frequency results

Author	Height (km)	Δ(log ρ)		
		1	2	3
Yu	96.5	0.049	0.058	0.063
	100	0.045	0.080	0.098
Baggaley	92	0.28 ± 0.02		
	97	0.34 ± 0.01		
	102	0.26 ± 0.01		

The uncertainties shown for the data of Baggaley are one standard error of the standard deviation. These cannot

be calculated for the data of Yu because the number of echoes is not given.

The data of Yu show both increases and a decrease of the observed scatter with height. The data of Baggaley also show both increases and decreases that are significant. Neither set of data confirms the height dependence expressed by equation 3.15 or the lack of height dependence expected from irregular ionization alone.

The effect that the finite meteor velocity and electron thermalization time have on the wavelength dependence of echo decay time has already been mentioned. Both of these factors are height dependent and could thus affect the value of $\Delta(\log \rho)$.

The wavelength dependence of $\Delta(\log \rho)$ for the data of Rice and Forsyth (1963) has also been mentioned (section 2.8). Too few echoes were used to give the dependence any statistical significance. A comparison of this data with those of Baggaley for the same height is complicated by one experiment being forward-scatter and the other backscatter. This will change the values of k and R in equation 3.13 although 3.14 will remain unchanged.

A comparison of the data in terms of wavelength dependence for irregular ionization gives $\sigma_o = 0.57$ for Rice and Forsyth and $\sigma_o = 0.88$ for Baggaley. These values differ significantly so the conclusion is that no simple descriptions work. It is interesting to note that Baggaley

does find an approximately linear relationship between $\Delta(\log \rho)$ and the difference in Fresnel zone length on the two wavelengths. This supports the model for an irregular ionization profile.

3.5 OTHER EFFECTS ON D MEASUREMENTS

(1) Sky Noise

Consider the contribution of noise in signal measurements. At meteor radar frequencies sky noise is predominant because thermal noise in well designed receivers is negligible. Sky noise originates from both cosmic and earth sources and the noise power is assumed to be random and additive in this work. This would not be the case for interference.

Jones and Read (1972) consider the effect of noise on measurements of echo decay time. From this, the fractional scatter in measured diffusion coefficient $\Delta D/D$ can be derived to be

$$\frac{\Delta D}{D} \approx 2.9/S \qquad 3.16$$

where $S = A_o/\langle n \rangle$, A_o being the maximum echo amplitude and $\langle n \rangle$ the r.m.s. value of the sky noise. Equation 3.16 has been derived by assuming that two measurements (at maximum amplitude and 1/eth amplitude) have been made to determine the rate of echo decay.

For typical values of $S \sim 10$ (20 dB) equation 3.16 predicts a significant scatter in the measurements so that it is important to consider ways in which this scatter can be reduced. Clearly, this can be achieved by using more points in

the decay measurement. For the case of a pulsed radar system, more information is available if use is made of the amplitude of every received pulse that is above the noise level. Three ways of using these pulses to find D are now considered so that the most accurate way of finding diffusion coefficients can be used.

A slope of the exponential decay may be found by fitting a straight line to the natural logarithm of the amplitude of each point. This is most simply done by linear regression giving each point equal weight.

Consider a noisy signal A_n such that

$$A_n = n(x) + A_o \exp\left[-\frac{(x-1)f}{\tau}\right] . \qquad 3.17$$

where x is the pulse number

$$x = 1,2,3, \ldots N$$

f is the time interval between pulses and n(x) is the noise amplitude of pulse x. The regression line is fitted to the natural logarithm of these amplitudes so that for times

$$f\,x < 2\tau$$

$$\ln(A_n) \approx \ln(A_o) - \frac{(x-1)f}{\tau} + \frac{n(x)}{A_o} \exp\left[\frac{(x-1)f}{\tau}\right] . \qquad 3.17$$

The effect of noise increases rapidly on a logarithmic plot. The fractional scatter in D can now be derived

$$\frac{\Delta D}{D} \approx \frac{12\tau}{2SfN(N+1)(N-1)} \left\{ \sum_{x=1}^{N} \left[(2x-(N+1))^2 \exp\left(\frac{2(x-1)f}{\tau}\right)\right]\right\}^{\frac{1}{2}} \qquad 3.18$$

Fig 3.4 shows $\Delta D/D$ as a function of height for f = 1/300, S = 10 and $Nf \approx 1.4\ \tau$ which is where the signal is about twice the r.m.s. noise level. An upper limit of 0.3s has been used for Nf to avoid the effect of second reflection points. This causes $\Delta D/D$ to increase at low heights.

The slope of the $\ln(A_n)$ versus time line determines the

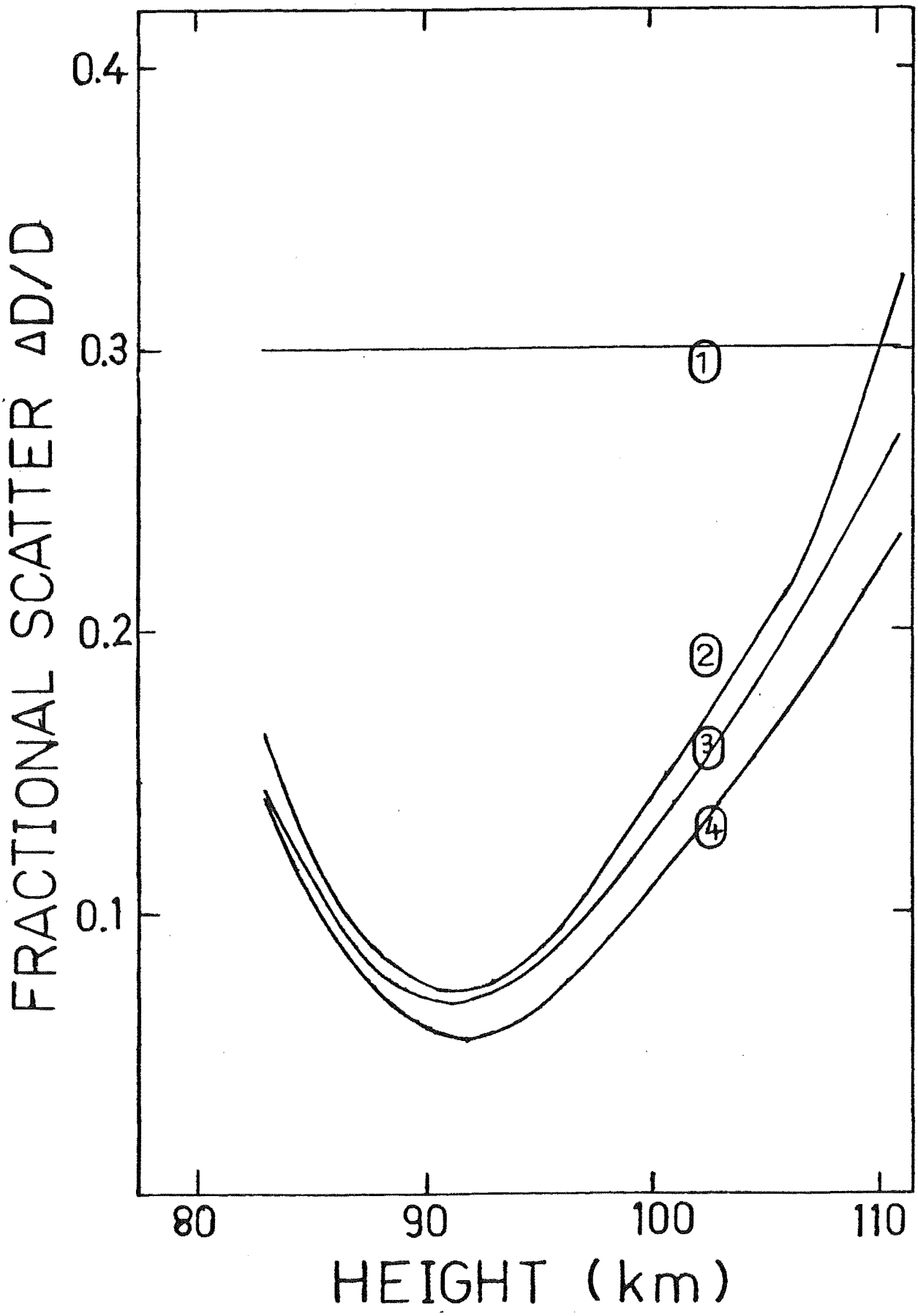

Figure 3.4: Fractional scatter (ΔD/D) due to sky noise for: (1) two points; (2) pairs of points; (3) unweighted linear regression; (4) weighted linear regression .

measured D. Noise on a point at the centre of this line will not affect the slope whereas points at each end will be most important. Furthermore, the very noisy points at the end of the echo will contribute most to the scatter in measurements. It is thus reasonable to give these points less weight in fitting the regression line.

Meyer (1975) suggests a weighting that depends on the variance of each point which, in this work, corresponds to

$$\left(\frac{<n>}{A_o}\right)^2 \exp\left[\frac{2(x-1)f}{\tau}\right]$$

for the x-th point. The fractional scatter in the measured value of D can now be found using the formula for the variance of the slope of this regression line given by Meyer. The result is shown in Fig 3.4 with the same parameters as the unweighted regression line.

By considering pairs of amplitudes and then averaging these over the whole echo, the central points will affect the slope of the lnA versus time line. $\Delta D/D$ for this method is also shown in Fig 3.4. Each pair of points was weighted equally. $\Delta D/D$ could be reduced if different weights were used.

The three methods of analysis using many amplitude points give much smaller values of $\Delta D/D$ than that using only two points. The weighted linear regression is the best method in these terms. Above 105 km, where echo decays are rapid and thus few amplitude points are measured, $\Delta D/D$ becomes much larger. It is thus necessary to decide upon a minimum number of amplitude points for finding a

decay slope. If less than this number are available the echo will not be used. This will then put a limit on the largest diffusion coefficient that can be measured. This limit will also depend on the initial echo amplitude.

A limit of five amplitude points was used in the echo analysis in this study. This will mean that $\Delta D/D$ is less than about 0.2 in the worst case. This then limits the maximum measurable D to 50-100 m^2/s for a typical range of received amplitudes.

(2) Finite Meteor Velocity

The finite meteor velocity also limits the maximum measurable value of D. When the initial radius and D become large, the only part of the train that will scatter radio waves effectively will be a short length behind the meteoroid. McKinley (1961) derives an expression for this theoretical echo ceiling by assuming that an echo will not be detected if the effective loss due to the finite meteor velocity is 40 dB. For a wavelength of 11.38m, a range of 250 km, a meteor velocity of 60 km/s (allowing for higher velocities at greater heights) and the values of D and r_o already given, the echo ceiling is 113 km. This value will vary with changes in meteor velocity and atmospheric density.

A more direct approach is used by Greenhow and Neufeld (1955). The finite meteor velocity will become important when the signal from the beginning of the first Fresnel zone has already decayed by the factor exp(1) before the

zone is fully formed. This condition is

$$V_T \leqslant 2\left(\frac{R\lambda}{2}\right)^{\frac{1}{2}}$$

which gives $D \geqslant 21\,m^2/s$ with the parameters used before. Thus if D is this large the maximum possible echo amplitude will not be reached and larger values of D will become progressively harder to observe.

3.6 HEIGHT MEASUREMENT

(1) Introduction

In Chapter 6 a system for measuring meteor train heights is described which employs an interferometer using three spaced antennas. The phases of the received signals from two of the antennas are compared with that at the third. The angles of elevation and azimuth of the reflection point can then be derived knowing the antenna spacings. A single transmitting array is used.

Because the receiving antennas are separated, each has a slightly different reflection point on the meteor train. In terms of train height this difference is much less than the measurement uncertainty. However, this separation is significant when considering the difference in the phase received by each aerial as the train forms. The effect that this has on height measurements is now investigated as other workers do not seem to have considered this problem.

One other effect that could influence the measured heights is refraction in the troposphere and ionosphere.

This is considered in the last sub-section.

(2) Fresnel Diffraction and Phase Measurement

In section 3.2 the underdense train model for radio wave scattering was outlined. If the Fresnel approximation is made the received echo phase and amplitude can be represented on a Cornu spiral (Fig. 3.6). Distance along the Cornu spiral, x, is related to distance along the meteor train, s, by

$$2s = x(R_o\lambda)^{\frac{1}{2}} \qquad 3.19$$

where R_o is the range of the specular reflection point. Both x and s are measured from this point (Fig. 3.5). If there are two separate specular reflection points (corresponding to two separated receiving antennas) each will be represented by different positions along the Cornu spiral.

Now consider a mathematical description of this. Equation 3.1 describes the initial attenuation of echo amplitude due to the initial radius and subsequent echo decay due to diffusion for a particular point on the train of age t. The received signal at a particular time A_R is then found by adding the contributions to the signal from each segment of the train over the total length that the train has at that time. Thus

$$A_R \propto q \int_{x_1}^{x} \exp\left(-\frac{4\pi^2 r_o^2}{\lambda^2}\right)\exp\left(-\frac{16\pi^2 Dt}{\lambda^2}\right) \sin\left(\chi - \frac{\pi x'^2}{2}\right)dx' \qquad 3.20$$

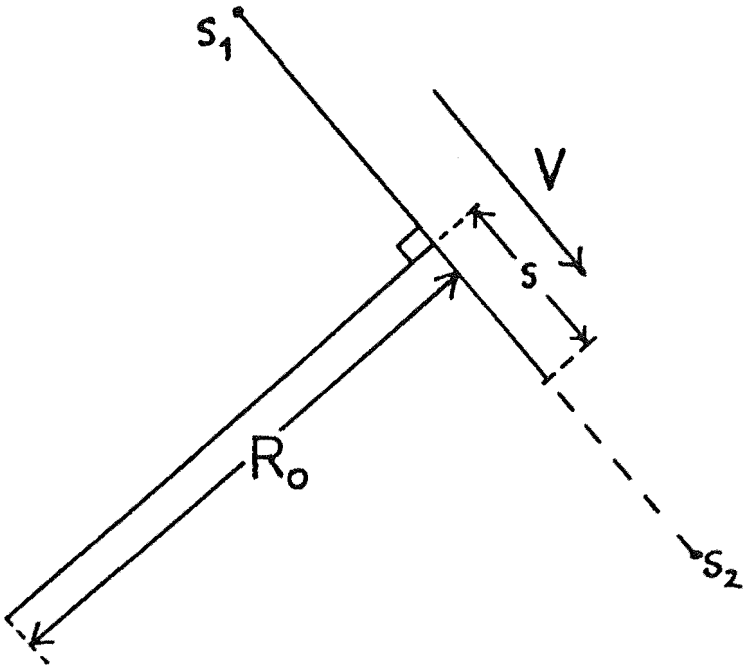

Figure 3.5: Reflection geometry

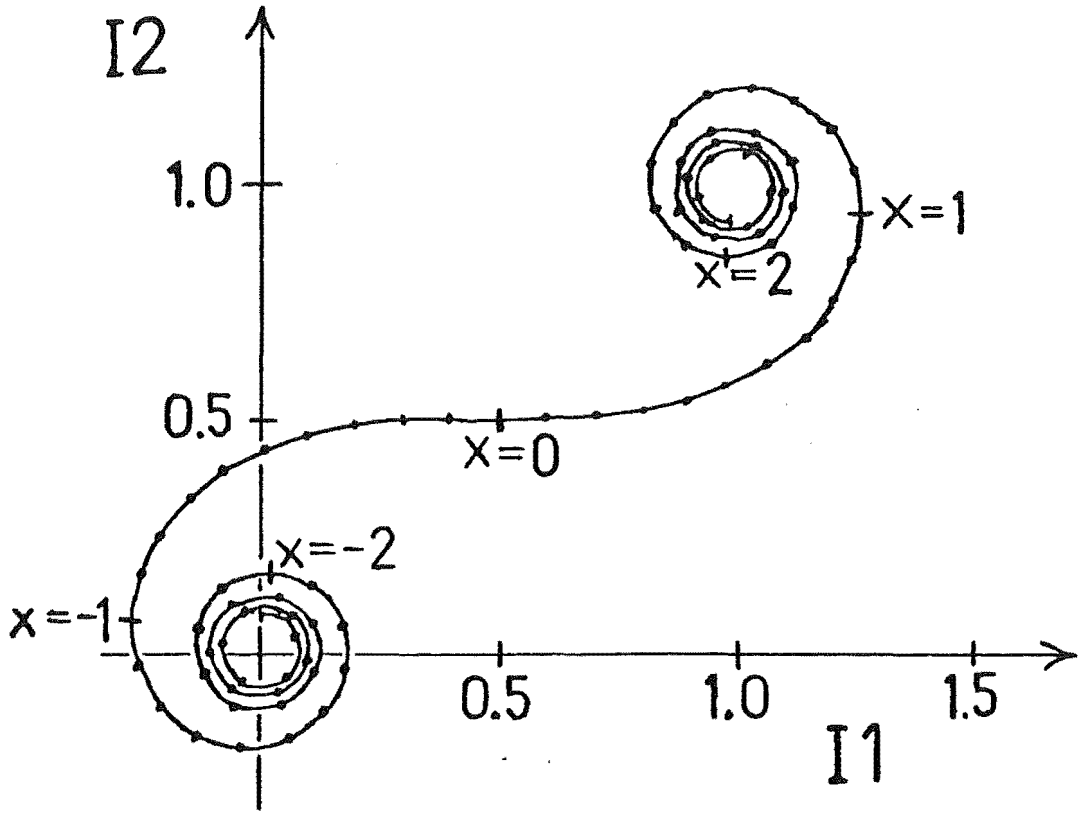

Figure 3.6: The Cornu spiral

where $\chi = 2\pi ft - \frac{4\pi R_o}{\lambda}$, f being the radar frequency. x_1 corresponds to the starting point of the train, s_1, and x corresponds to the end of the train, s, at time t. As time progresses x increases from x_1 to x_2 - the final end point. The train age t can be expressed in terms of meteor velocity V and distance along the train

$$t = (x - x') \frac{(R_o\lambda)^{\frac{1}{2}}}{2V} .$$

Equation 3.20 can be split into two integrals such that

$$A_R \alpha (I_1 \sin \chi - I_2 \cos \chi)$$

where

$$I_1 = \int_{x_1}^{x} \exp\left(-\frac{4\pi^2 r_o^2}{\lambda^2}\right) \exp\left(\frac{hD}{V}(x'-x)\right) \cos\left(\frac{\pi x'^2}{2}\right) dx'$$

$$I_2 = \int_{x_1}^{x} \exp\left(-\frac{4\pi^2 r_o^2}{\lambda^2}\right) \exp\left(\frac{hD}{V}(x'-x)\right) \sin\left(\frac{\pi x'^2}{2}\right) dx'$$

and

$$h = 16\pi^2 \frac{(R_o\lambda)^{\frac{1}{2}}}{2\lambda^2} .$$

Averaging over times that are long in comparison with the radio wave period gives the received amplitude

$$A \alpha (I_1^2 + I_2^2)$$

and the received phase

$$P = \tan^{-1}\left(\frac{I_2}{I_1}\right) .$$

A plot of I_2 against I_1 gives the Cornu spiral where the phase is the angle that a line from the origin to the point x makes with a particular direction. The length of this line represents the amplitude. Fig. 3.6 shows the Cornu spiral with no diffusion. The spiral is plotted from $x_1 = -4$ to $x_2 = +4$ for the sake of clarity. Fig. 3.7 shows the spiral for $D = 7.6\ m^2/s$, $V = 40$ km/s, $\lambda = 11.38$ m and $R_o = 250$ km (i.e. $\frac{hD}{V} = 0.2$). Fig. 3.8 shows the case $\frac{hD}{V} = 0.5$ which corresponds to more rapid diffusion (e.g. $19\ m^2/s$, V = 40 km/s) or a lower meteor velocity.

Values for these figures were obtained by numerical integration using Simpson's rule. To reduce the computing time $x_1 = -10$ was used which gave values different from $x_1 = -\infty$ by less than 0.1%. The program was checked by finding values with D constant with height and r_o. Solutions for this case have been found by Bennett (1958) for a limited range of x by the summation of series. The solutions agreed for the two methods.

An initial radius for a height of 95 km was used with the height variation found by Baggaley (1970). The maximum variation with height was used by assuming a vertical meteor train. By replacing D in equation 3.20 with an exponentially varying function of time (transformed to x-x') the effect of electron thermalization could be investigated. These results were presented in Chapter 2.

The error introduced into height measurements can be found from these diagrams by finding the difference in phase

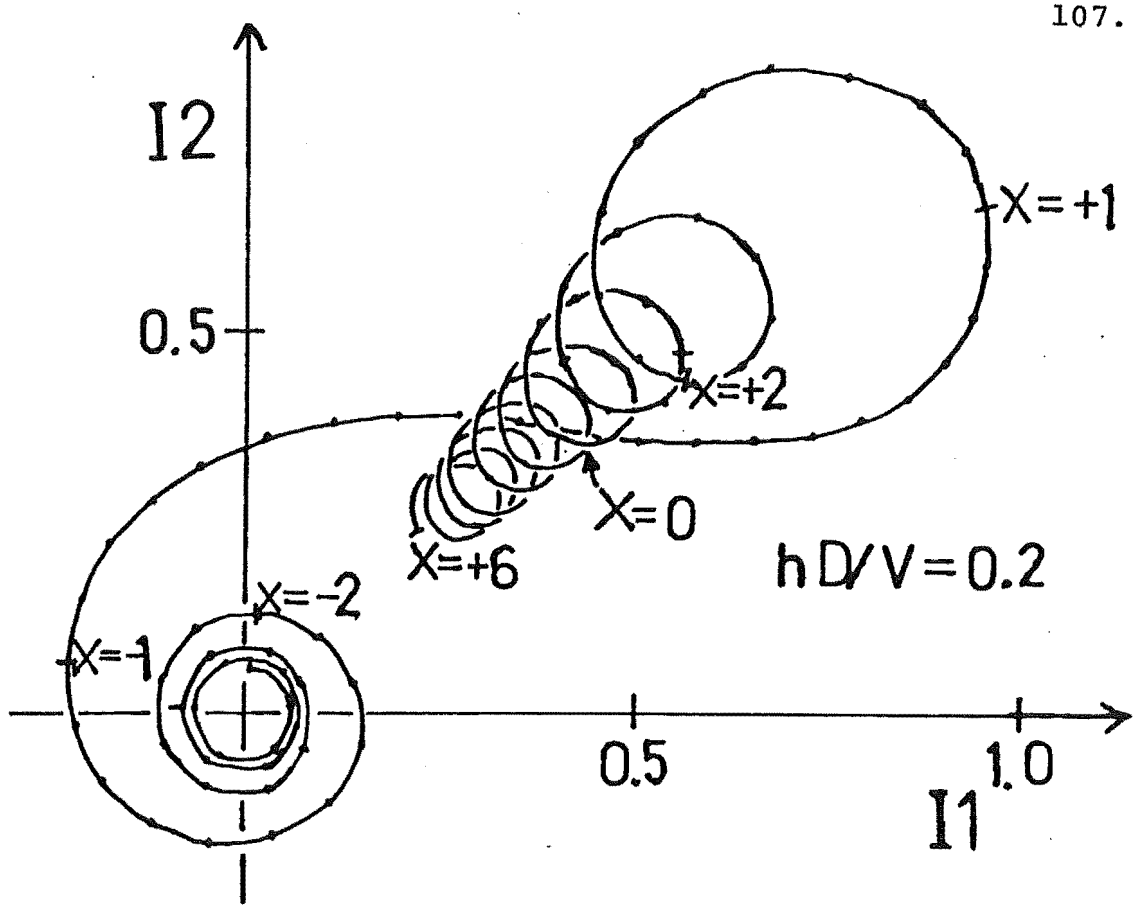

Figure 3.7: The Cornu spiral for moderate diffusion.

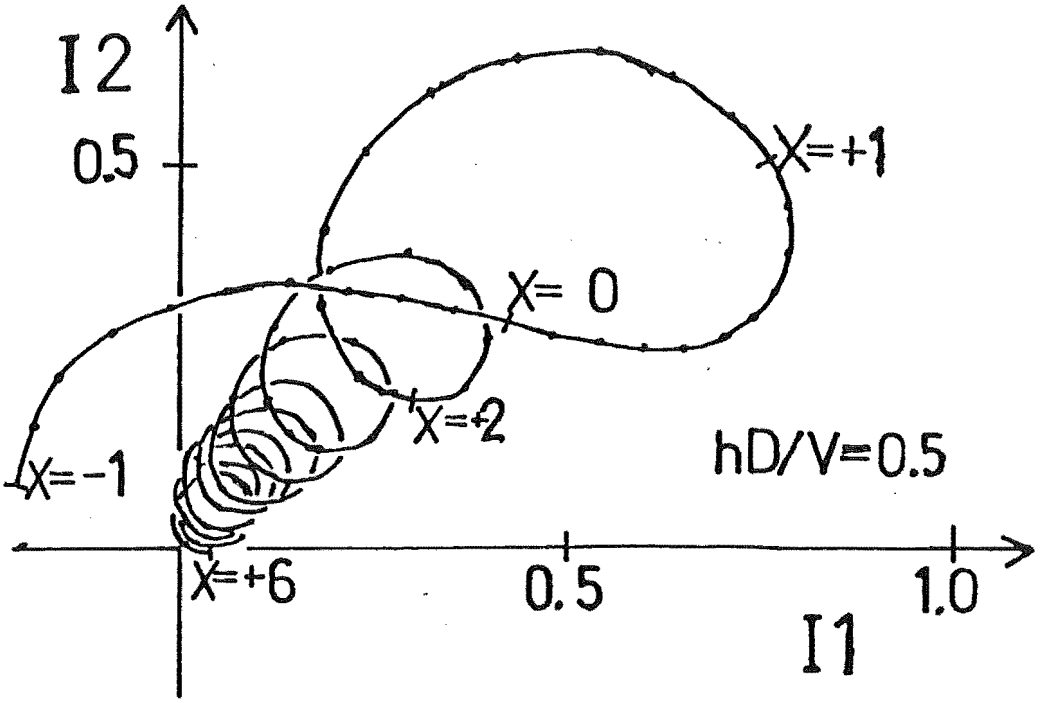

Figure 3.8: The Cornu spiral for more severe diffusion.

between two points on the spiral. A typical antenna spacing would be about seven wavelengths giving an effective antenna spacing of three wavelengths for an elevation of 25^{o}. The distance between specular points is one half of this because a common transmitting antenna is generally used. The spacing in terms of the parameter x is then

$$\Delta x = 3\left(\frac{\lambda}{R_o}\right)^{\frac{1}{2}}$$

$$= 0.02 \text{ for } \lambda = 11.38 \text{ m and } R_o = 250 \text{ km.}$$

Figs. 3.9 and 3.10 show the height error as a function of time for the meteor trains represented by the Cornu spirals in Figs. 3.7 and 3.8 respectively. Note the use of different time and height error scales in these figures. The sudden reversal of the sign of the height error in Fig 3.10 is due to the Cornu spiral crossing behind the origin. After this point the height error is always negative and increases. This is expected because the part of the train last formed will be the last part destroyed by diffusion. The initial height error is positive and decreases. This is caused by the formation of the first Fresnel zone of the train.

The effect of separate reflection points in an interferometer can cause a large scatter in heights measured from individual pulses. The ideal way to minimise this scatter would be to select pulses that occur under conditions where there is no height error. This could be done by observing the amplitude pattern. However, most pulsed meteor radar systems do not have sufficient time resolution

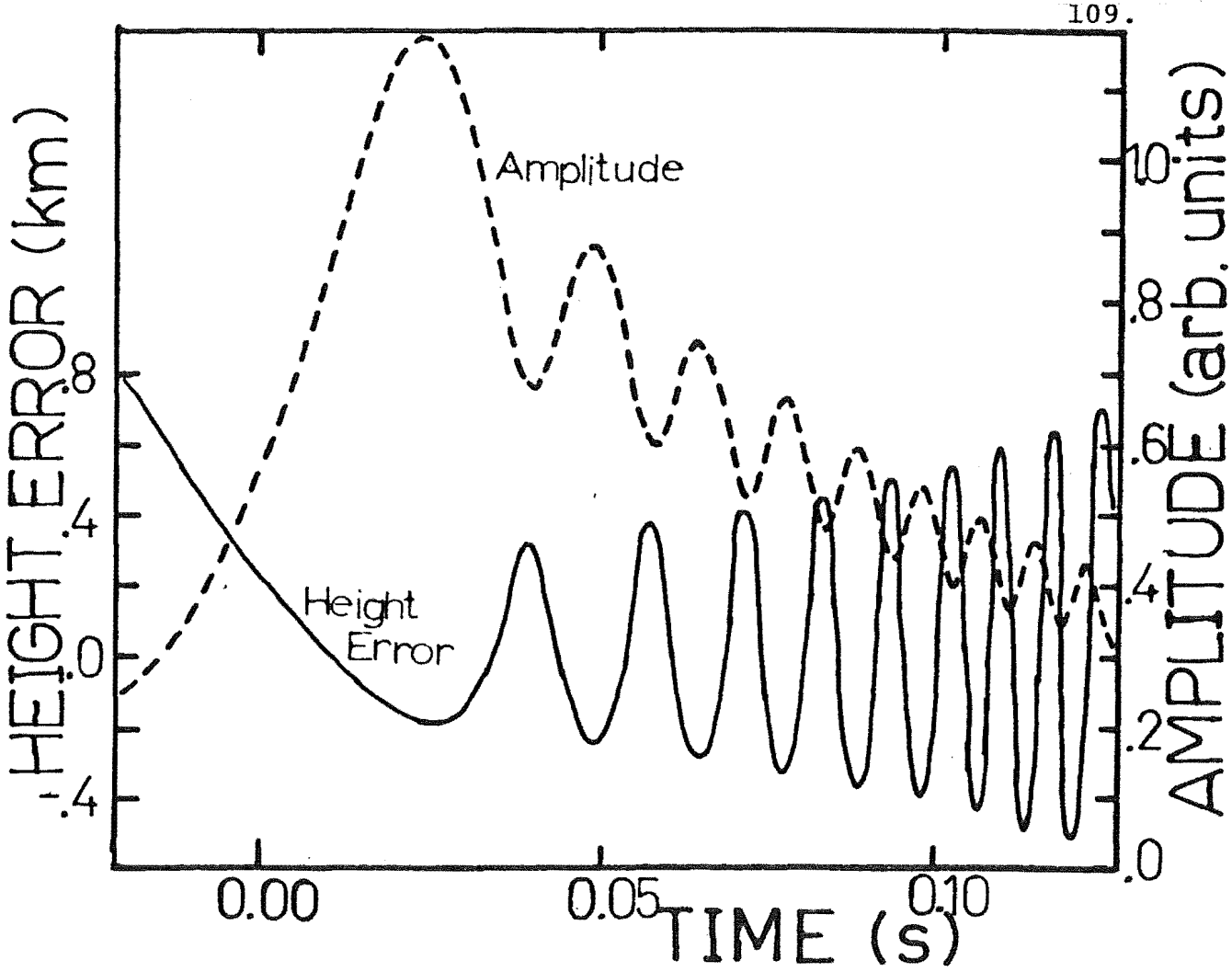

Figure 3.9: The height error due to separated reflection points for hD/V = 0.2.

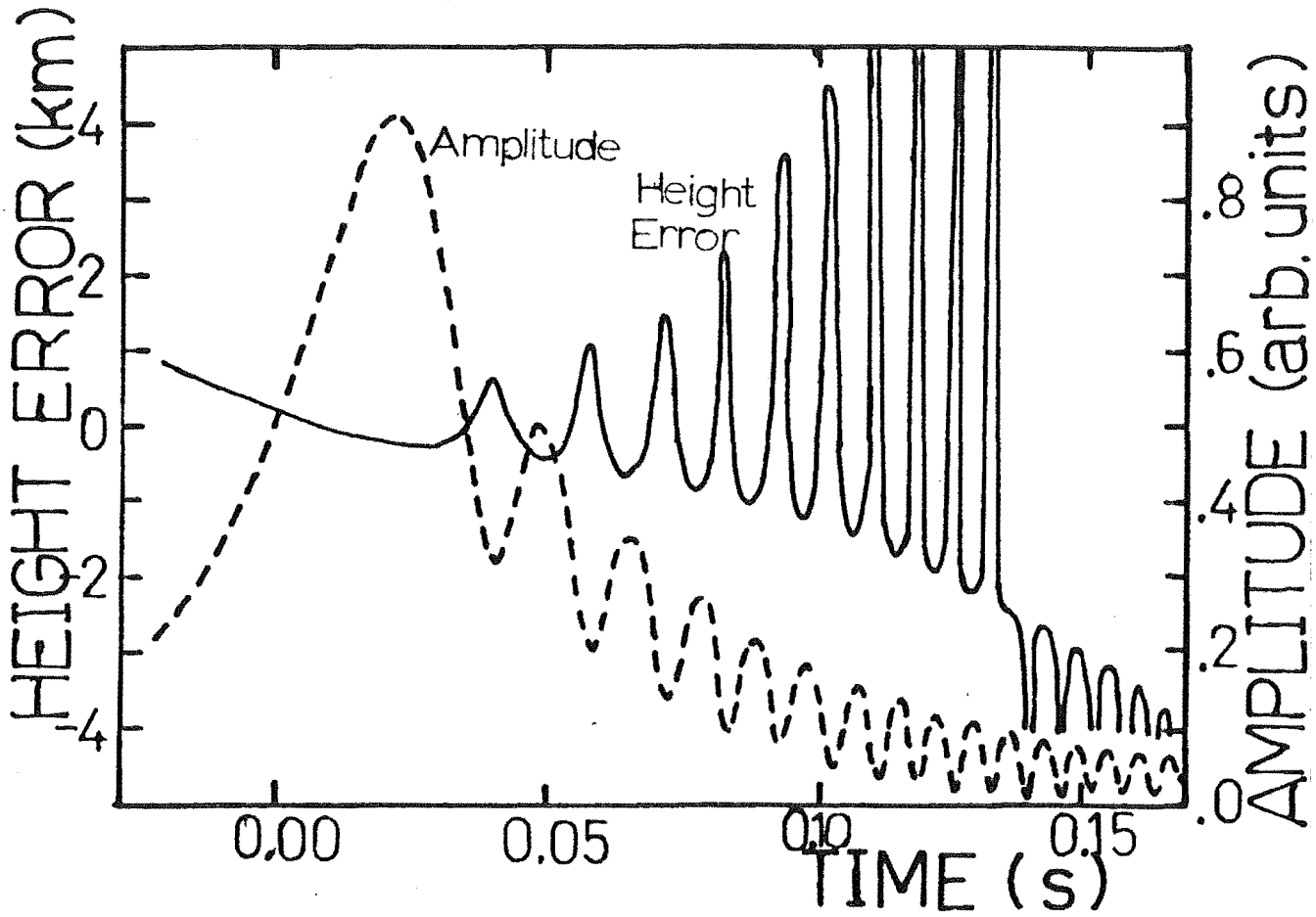

Figure 3.10: The height error due to separated reflection points for hD/V = 0.5.

to show clearly the diffraction fringes in the echo amplitude, especially for high velocity meteors. As a consequence it is not practical to select pulses that occur in favourable positions. An alternative way of minimising the scatter is to avoid pulses that occur late in the echo life and those that occur at small echo amplitudes. By these means height errors can be restricted to $\pm$ 0.3 km. The use of too few pulses will mean a greater scatter in heights because of noise variations.

Deegan et al. (1970) observed Fresnel fringes with their meteor radar system. They also saw a reduction in the expected magnitude of these fringes later in the echo life. This may be explained by fragmentation of the meteoroid. If the meteoroid fragments or releases particles that do not ablate immediately, the ionization will not be produced as if by a moving point. The ionization would be produced in a moving column up to a hundred metres long. This will not affect the size of the initial Fresnel fringes because the first few Fresnel zones will be longer than the ionizing region. Fresnel zone lengths decrease away from the specular reflection point so that later zones may have a similar length to the ionizing region. These later Fringes will then be smoothed out as there is effectively a superposition of many Fresnel diffraction patterns.

A diffuse ionizing region will also smooth out the height error arising from separated reflection points. The smoothing of the height error will result in a systematic height decrease late in the echo life.

(3) Refraction

In the present investigations radio waves between the transmitter and the target may be refracted in two ways. In the troposphere the refractive index of the air, and especially that of moist air, may cause the waves to bend. The refractive index is essentially unity above 30 km and most effect is apparent below 15 km (Unwin, 1966). In the ionosphere the ambient electron density changes the refractive index. Unlike tropospheric refraction, this refraction is frequency dependent.

(a) Tropospheric Refraction. Ideally, the effect of tropospheric refraction should be worked out by ray tracing techniques with the atmosphere stratified into layers of constant refractive index. Such an approach was used by Millman (1958) using a theoretical model of refractive index. He calculated a refraction error for 0 and 100% humidity for three elevation angles.

A simple way of estimating the error in measured elevation is to use a flat earth model and Snell's Law. This is reasonably accurate because most refraction occurs in the first 15 km whereas the heights considered are about 100 km. Then

$$n_1 \cos E_1 = n_2 \cos E_2$$

where n_1 is the refractive index at ground level and E_1 the initial beam elevation, n_2 is the refractive index at

the height of interest ($\approx$ 1) and E_2 is the beam elevation after refraction.

The refraction error (E_1-E_2) was compared with the results of Millman (1958) for n_1 = 1.00032 (Unwin, 1966) and was found to be overestimated by about 75%. The difference is probably due to the value of the refractive index used. A new value was found from Millman's results to be n_1 = 1.00023 for the worst case which could then be used to correct measurements. At typical elevation angles of 16^{o} the refraction error is 0.046^{o} which corresponds to a 0.3 km overestimate in echo height. For low elevations, heights would be overestimated by up to 0.7 km.

A correction for this effect was not incorporated in the initial data reduction, but was included in subsequent data analysis.

(b) Ionospheric Refraction. When electrons are present in the radio-wave path the refractive index is decreased. Thus a wave entering a layer of increasing electron density is bent away from the vertical in the same way as for tropospheric refraction. D-region electron densities are too small at frequencies of ~ 26 MHz to cause significant bending, but the effect may become important in the E-region.

The electron density profile in the E-region can be modelled on a parabolic form with a half width z_m = 2H where H is an effective scale height (Bremer and Singer, 1976). A value of H = 7.5 km is appropriate for equinoxal

and summer conditions while H = 4.3 km appears most suitable for winter (Whitehead, 1973). The height and density of the maximum ionization can be found from ionosonde records. Above the point of maximum density, a constant density equal to that at the maximum was assumed (Bremmer and Singer, 1976).

Although radio waves may be refracted through larger angles by ionospheric refraction than by tropospheric refraction, the effect on measured heights is not greatly increased because much shorter path lengths are involved. The refracted angle may however, be important in the calculation of the angle between the train and geomagnetic field. The angle between the transmitter direction and a perpendicular to the field direction is the off-specular angle μ.

Fig 3.11 shows the geometry for this problem. RP is the refracted ray incident on an ionized layer at an angle θ_o. The height from the base of the layer is represented by parameter z. The layer maximum is at a height h_m above the earth's surface. SP denotes the field direction and the off-specular angle is zero at point P. RS is the unrefracted path of the ray so that the off-specular angle inferred by radar measurements is $\Delta\mu$. This is also equal to the angle through which the ray is bent. AP is a tangent to the ray at P. Then from the triangles ABR and APO (O denotes the centre of the earth)

$$\Delta\mu = \theta_1 - \theta_o + \phi \qquad 3.21$$

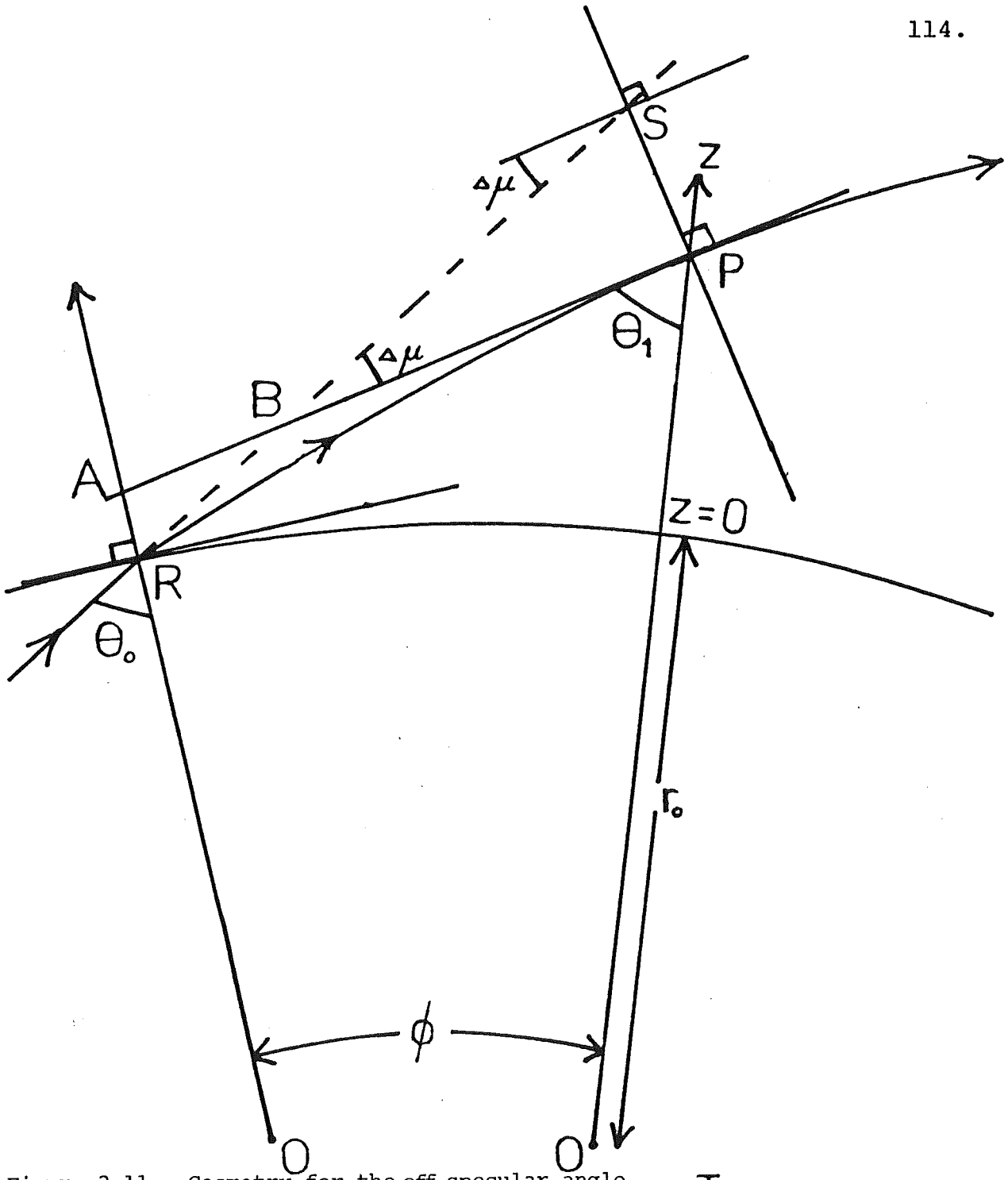

Figure 3.11: Geometry for the off-specular angle error $\Delta\mu$.

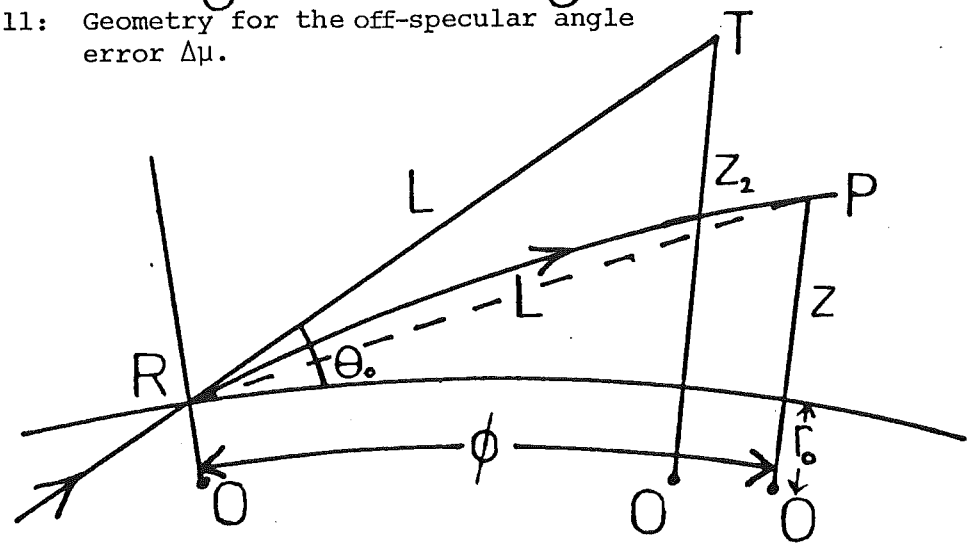

Figure 3.12: Geometry for the height error Z_2-Z

Kelso (1964) gives an expression enabling the angle ϕ to be calculated for a given z for a parabolic electron density distribution in a spherical layer. Thus

$$\phi = \frac{\sin \theta_o}{r_o\sqrt{b}} \ln\left[\frac{(\cos^2\theta_o - cz + bz^2)^{\frac{1}{2}} + z\sqrt{b} - \frac{c}{2\sqrt{b}}}{\cos \theta_o + \frac{c}{2\sqrt{b}}}\right] \qquad 3.22$$

where $b = \frac{f_c^2}{f^2 z_m^2}$, $a = \frac{2f_c^2}{f^2 z_m}$, $c = a - \frac{2 \sin^2\theta_o}{r_o}$.

ϕ can thus be found for a given height, z, in the layer.

The angle θ_1 can be found from Bouger's rule

$$\sin \theta_1 = \frac{r_o}{\mu_z(r_o+z)} \sin \theta_o$$

where the refractive index μ_z can be found from the adopted model

$$\mu_z=(1 - az + bz^2)^{\frac{1}{2}} \quad .$$

Above the point of maximum ionization no further bending will occur as a uniform ionization density has been assumed.

The error in measured height can be found from Fig. 3.12 by assuming that the length L is approximately equal to the ray path length RP. The height error, $z - z_2$, can then be found by using the triangle RPO to find L and RTO to find z_2. The height error above the maximum density continues to increase as L increases.

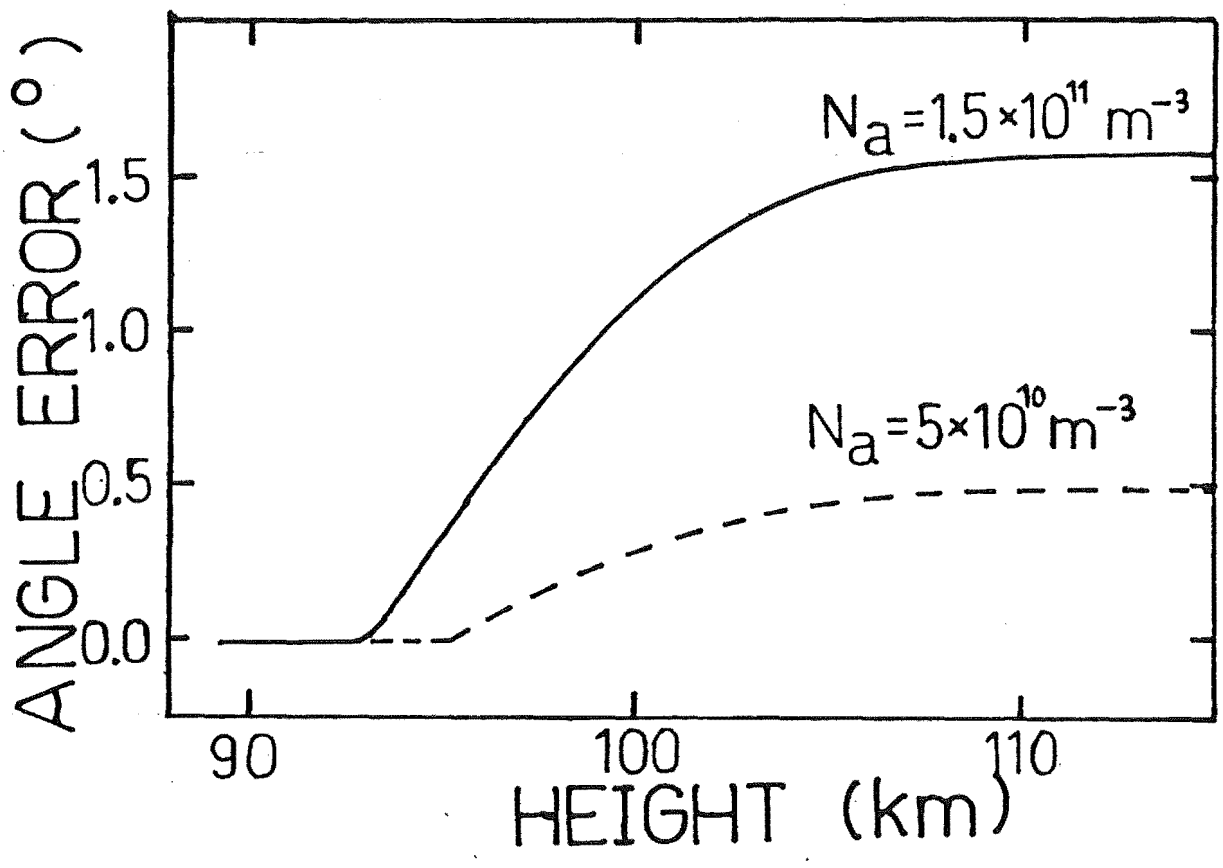

Figure 3.13: Error in off-specular angle due to ionospheric refraction.

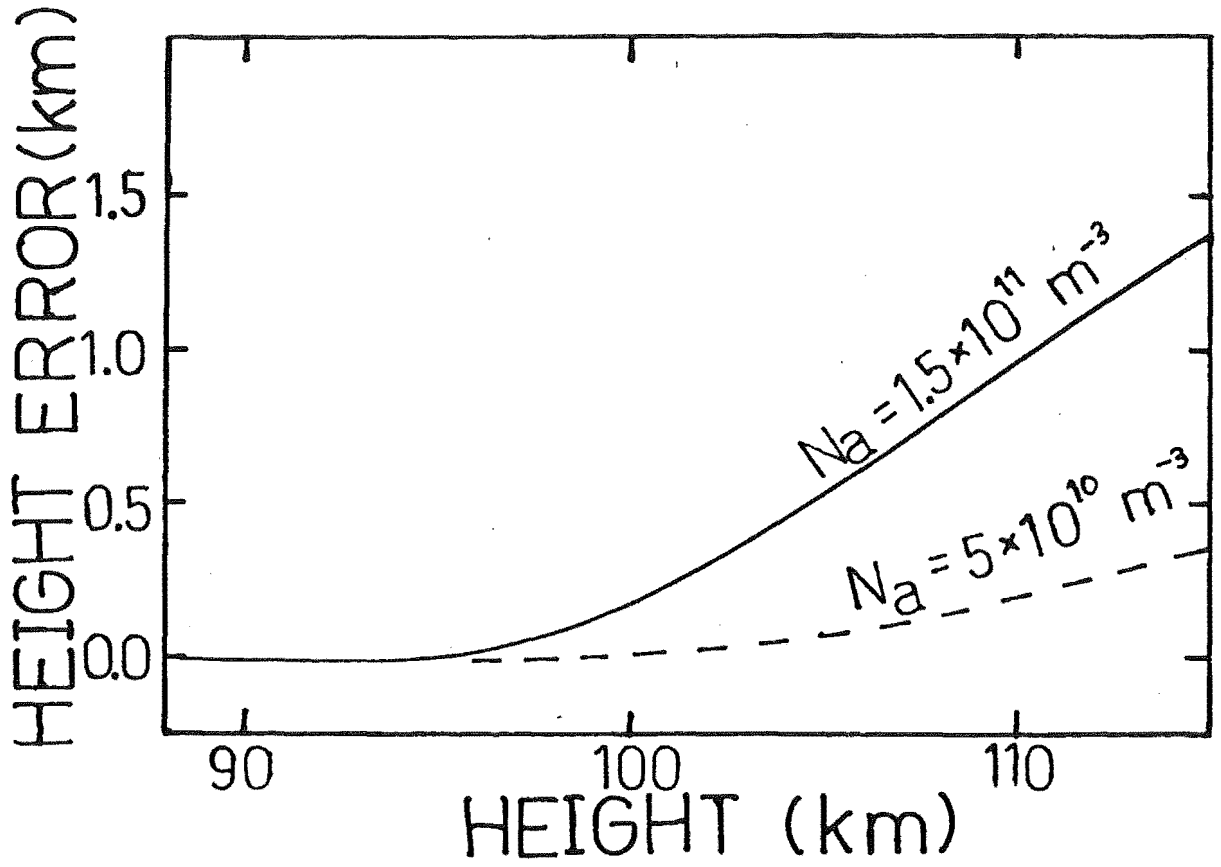

Fig. 3.14: Error in height due to ionospheric refraction.

Figs 3.13 and 3.14 show the angle error, $\Delta\mu$, and height error as a function of height for ambient electron densities, Na, of 1.5×10^{11} m^{-3} and 5×10^{10} m^{-3} at the peak of the E-region (critical frequencies of 3.5 and 2.0 MHz respectively). The calculations were for maximum heights of ionization at 108 and 110 km respectively. An incident angle $\theta_0 = 71.3^{\circ}$ was used, corresponding to an elevation of 16° at the radar.

Bending of up to 1.5° can be expected for typical mid-day electron density values.

It can be seen therefore that heights will be over-estimated by more than 1.5 km at the top of the meteor region for elevations of 16°. This will be larger for lower elevations. No attempt was made to correct for this error because of its variable nature. Its effect will systematically increase measured meteor heights above 105 km. The estimated electron densities for the times at which results were taken are discussed in Chapter 7.

CHAPTER 4

EXPERIMENTAL WORK

4.1 INTRODUCTION

Studies of meteor train diffusion add to our knowledge of the atmosphere in the meteor region (80-110 km) in several ways. For example, measured diffusion coefficients, D, enable deductions to be made about the temperature and density of the neutral atmosphere. Both diurnal and annual changes in these quantities may be inferred. Atmospheric scale heights, H, may be found from the variation of diffusion coefficient with height: H^{-1} is given by the slope of a lnD versus height plot. Diffusion coefficient measurements may also be used to deduce echo heights from echo analysis. This is useful because experimentally it is far easier to measure echo decay rates and thus D than it is to measure echo height directly. Before these methods can be used the relationship between echo decays and real diffusion must be known.

Another important aspect of meteor train diffusion is the effect that the geomagnetic field has on the evolution of the ionization distribution. Theoretical models have been proposed, but they have not been fully verified by experiment. Meteor train drift with the neutral atmosphere may be affected by the geomagnetic field. This could have important consequences for experiments that deduce neutral atmospheric winds from meteor train drifts.

In the last two chapters various effects that complicate diffusion coefficient measurements have been discussed. In this chapter these effects are summarised and a brief review is then made of experimental studies of these effects. Next, the aims of the experiment reported in this work are described and an outline of the experimental method is given.

4.2 SUMMARY OF FACTORS INFLUENCING METEOR TRAIN MEASUREMENTS

The initial radius of meteor trains have been measured experimentally: the results are given in Table 2.1. The height dependence of these results is much weaker than that predicted by theory. A possible explanation for this difference is that the meteoroids are fragile and rotating (Hawkes and Jones, 1978). Particles ablated from the meteoroid may thus travel radially outward before ablating themselves. This process may lead to a weaker height dependence of initial radius.

After the train is formed, ambipolar diffusion will control the dispersal of the ionization. The ambipolar diffusion coefficient is related to the positive ion diffusion coefficient by equation 2.3. Values of ion diffusion coefficient are presented in Table 2.5. These values are derived from laboratory measurements of the polarizability of the relevant atmospheric species.

Since these diffusion coefficients are dependent on temperature and density, the expected ~~variations in~~ diurnal and annual temperature and density variations have been

examined. The effects of these changes are additive, thus leading to diurnal variations in D of 5% at 80 km, up to 15% at 90 km and perhaps 40% or more above 100 km. Annual variations of a similar magnitude would be expected.

Since these variations increase with height, the slope of a ln D versus height line will change. This slope can be used to estimate the atmospheric scale height which would thus show a diurnal or annual variation.

D_a is dependent on the temperatures of both the electrons and positive ions in the train. The cooling processes have been investigated for neutral meteor atoms, positive ions and electrons (see section 2.5). Ions and neutral atoms cool quickly compared to echo decay times for underdense meteors (although this may not be true for larger meteors). Calculated electron thermalization times are given in Figs 2.1 and 2.2. Electron thermalization may be important above 100 km where echo decay times are similar to the thermalization time. Experiments investigating electron thermalization must be interpreted carefully. Apparent changes in diffusion coefficient with time could be caused by plasma resonance phenomena. Changes in doppler characteristics could be caused by wind shears and reflection processes as well as the "moving sphere effect". The wavelength dependence of measured diffusion coefficients may be influenced as much by the particular choice of frequencies as by thermal effects. The way in which the data is analysed may affect the results if care is not taken to remove various types of bias.

The earth's magnetic field begins to influence meteor diffusion above 95 km with the effects becoming prominent above 100 km. The diffusion of trains closely aligned with the magnetic field will then be inhibited because of the low transverse diffusion coefficient of the electrons. Trains that are not closely field-aligned ($\alpha > \alpha_c$) are expected to form fins of field-aligned ionization while diffusion in the central column is controlled by the ions. Quasi-neutrality is maintained by electrons moving down the field direction and ions moving transverse to the field. Depletion regions are thus formed in the background plasma. The finite depth of the depletion regions limits the ionization density in the fins and in the ion-controlled region. A transition to ambipolar diffusion occurs at greater densities which are shown in Fig. 2.5.

It is not clear whether ionization affected by the geomagnetic field will move with the neutral atmosphere or remain fixed to the field lines. It is likely that the field-aligned fins will not be able to drift across the field, but may drift in the field direction. The central column could probably move with the neutral atmosphere.

The loss of ionization by dissociative recombination, preceded by charge exchange reactions, is shown in Fig. 2.6. These chemical processes may begin to influence underdense meteor decay times significantly below 85 km. The loss rate depends on the ionization density and thus becomes more pronounced in large meteors.

An irregular ionization profile will cause a scatter in measured diffusion coefficients. This is compounded by wind shears moving the reflection point along the train to regions with a different ionization line density. Radio meteors appear to have shorter train lengths than predicted by classical theory, an effect which agrees with the behaviour expected from a fragile structure model. Small-scale variations in line density of up to 50% have been measured.

A model has been developed in section 3.2 to describe echo decays from magnetically affected trains. This is based on a superposition of a circular and elliptical ionization distribution. It would be possible to obtain numerical solutions for a more realistic distribution, but an analytical result is best for understanding physical processes.

Full wave solutions for the reflection of radio waves from meteor trains predict plasma resonance effects that are important in certain experiments. These effects make the interpretation of experiments measuring electron thermalization times very difficult. Furthermore, the effects may cause the overestimation of diffusion coefficients measured from echo decay times. This can be avoided by not measuring decay rates from the first part of meteor echoes.

Many wind effects will introduce scatter into measured values of D. These effects have been summarised and presented in Fig 3.3. The large scatter indicated may have been overestimated. For example, ionization changes

over the whole train length were used to find the effect of wind shears. Fig. 3.3 also clarifies the height dependence of the scatter. The effects generally decrease with increasing height, but the expected increase of wind irregularities with height tends to counteract this.

Two-wavelength studies do not resolve the problem of whether the scatter in D observed in measurements on individual trains is caused by wind effects or by irregular ionization. The scatter is probably caused by these and other factors, such as uncertainties in the measurement of D and height.

The effect of sky noise on measurements has been investigated. A weighted linear regression used to estimate the decay characteristics would be expected to give the smallest uncertainty in D. Points may be weighted by a variance estimated from the signal-to-noise ratio. The uncertainty in D from this method is smaller than that induced by winds. Decay times estimated from only two points will have a scatter of about 30% for a signal-to-noise ratio of 10.

The effect of Fresnel diffraction on interferometric height measurements has been investigated. A large scatter can be caused in height measurements during an echo life, but this can be reduced by using echo pulses near the occurrence of the maximum echo amplitude.

Refraction effects in the troposphere can be corrected in data analysis reasonably easily. Such effects cause echo heights to be overestimated. Ionospheric refraction

is more variable as it depends on the ambient electron density. This refraction can cause height errors above 105 km and can also cause errors in inferred off-specular angle measurements. Because of its variability, ionospheric refraction cannot easily be allowed for in data analysis.

4.3 PREVIOUS EXPERIMENTAL WORK ON METEOR DIFFUSION

(1) Introduction

Experimental work on meteors has already been referred to in the last two chapters. This includes: initial radius measurements; experiments to measure electron thermalization and ionization profiles and two-frequency experiments to find wavelength dependences. In this section other experimental results relating to the dependence of measured D on height and to magnetic effects are reviewed.

(2) Combined Diffusion and Height Measurements

Many workers have used combined diffusion and height data to estimate atmospheric scale heights or to compare diffusion heights with measured heights. Few people have presented these data in terms of diffusion coefficient and measured height and have at the same time made an attempt at fitting a line to the data. The way in which such a line is fitted is very important in obtaining realistic scale heights and for finding average diffusion coefficients. Fig. 4.1 summarises the D versus height measurements that have been made and that are probably free from selection effects.

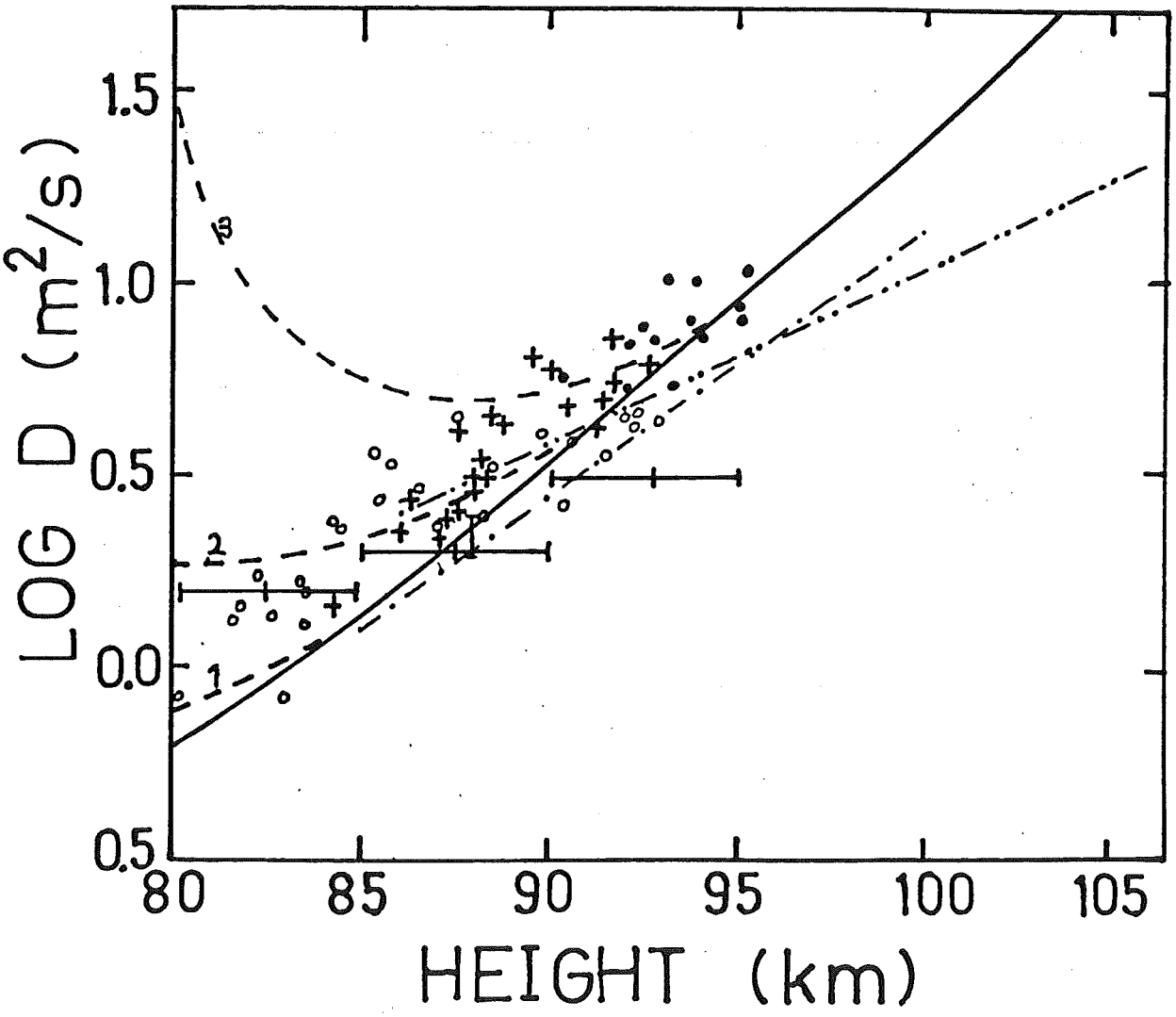

'igure 4.1: Experimental and theoretical ambipolar diffusion coefficients.

I — Closs et al (1953)

Hess and Geller (1976)

Greenhow and Neufeld (1955)

Greenhow and Hall (1961)

(E) (M) (B)
°, +, • Jones (1975) from Verniani (1973)

Theory, assuming $D_a = 2D_+$ from Table 2.5

1,2,3 Theory including chemical ionization loss
(1) $q = 2 \times 10^{12} m^{-1}$ (2) $q = 2 \times 10^{13} m^{-1}$,
(3) $q = 2 \times 10^{14} m^{-1}$.

Closs et al. (1953) found the most probable value of D for meteors during an Arietids shower to be 2 → 2.5 m^2/s. The mean height for this shower had been determined independently to be 88 km.

Greenhow and Neufeld (1955) presented results from two frequencies. Heights were measured with a split beam technique which had a systematic error of 1.5 km between the two frequencies. They observed a 50% scatter in D for a given height which was not explained by uncertainties in their height and D measurements. The effect of finite meteor velocity was apparent and differed for the two frequencies in the expected manner. Their final curves were obtained by assuming uncertainties in height only. With the large scatter observed, as well as the large uncertainties in both height and D measurements, an underestimate of D at low heights and an overestimate of D at greater heights would be expected from considering height uncertainties only. The inferred scale height of 6 km would seem to confirm this.

Weiss (1955) and Murray (1959) both presented data where echo decays were measured from a continuous-wave radar system rather than a pulsed one. Greenhow and Hall (1961) point out that this discriminates strongly against higher D values. Murray found a large spread (one standard deviation of 0.2 in log D) about the regression line of log D on height. The system height uncertainty of $\pm$ 1 km is much smaller than that of most other workers and confirms that there is an inherent spread in D. Because of the

inherent selection effect the results are not shown in Fig. 4.1.

Greenhow and Hall (1961) fit a regression line to their data by considering the uncertainties in both height and D. They do not seem to consider the effect of finite velocity which Greenhow and Neufeld (1955) found important. They observe a large scatter in D for a fixed height, but conclude that it is all accounted for by their measurement uncertainty.

In a re-analysis of their data, Jones (1970) found a scale height that agreed more closely with other observations. He also applied a correction for the finite meteor velocity and found that it had little effect on the slope of the fitted line. His derived scale height is different from that derived by Greenhow and Hall, although slightly different assumptions were made about the experimental uncertainties which account for most of this difference.

Jones (1975) derives diffusion-height data from the results of Verniani (1973). Each point in Fig. 4.1 represents a group of meteors so that the scatter is smaller than that observed for individual meteors. The three different types of point correspond to D values derived from the beginning (B), maximum ionization (M) and end (E) points of the trains.

Hess and Geller (1976) used the same radar wavelength as Verniani and conclude that selection effects will operate above 95 km. Points derived by Jones (1975) that are above this height are omitted from Fig. 4.1.

Hess and Geller also give average values of D for five height ranges. As well as selection effects above 95 km (due to the finite meteor velocity and data selection requirements) they expect bias to be introduced below 85 km due to contamination of results by trains that are not specular or are distorted by winds. The results for these data are shown in Fig 4.1 because the wind effects have not definitely been shown to be important. Again D has been averaged for each height range, a procedure which assumes that there is no uncertainty in the height measurement. The effect of this has already been mentioned.

Forti (1978) attempted to reduce the dispersion in D by correcting for wind shears. A meteor wind system with a high echo rate can be used to estimate the wind shear by building up a wind profile. Because of lack of wind information there are often two possible values for the wind shear so that two values of D are obtained. Forti selected the one closest to that expected. Such a procedure could be expected always to reduce the scatter, even if it was completely random. Furthermore, the most important term in the equation used to apply corrections was neglected - that involving the movement of the reflection point over an irregular ionization profile. The scatter in decay times could not be expected to be reduced significantly by such an analysis. As Baggaley (1979b) mentions, the conclusion arrived at by Forti that radio meteor observations can play no useful role in finding diffusion coefficients is in contrast with a large body of work, much of which has been presented here.

Fig 4.1 also shows the expected D_a values derived from laboratory measurements. Between 85 and 95 km there is good agreement with experiment, although a large scatter would be observed for individual echoes. Below 85 km there is a clear trend for the measured D value to be higher than that predicted by theory.

The dashed lines 1, 2 and 3 indicate the inferred D values if chemical effects as well as diffusion are considered for electron line densities of 2×10^{12} m^{-1}, 2×10^{13} m^{-1} and 2×10^{14} m^{-1} respectively. These lines were derived from the calculations by Baggaley (1979, unpublished) that were described in section 2.7. The ionization loss was initially assumed to be exponential so that an echo decay time for both ionization loss and diffusion could be calculated. This could then be used to modify the ionization loss decay time so that by an iterative process the final decay time was found. This was then converted to a measured D value by assuming a radar wavelength of 7.33 m - that used in recording Verniani's data.

The data of Verniani has been reanalysed by the same method as Jones (1975) and is shown in Fig. 4.2. The data are grouped according to mean line density and each symbol represents a group of meteors. A representative standard error is given. Also shown are two of the theoretical curves from Fig. 4.1.

There is no clear trend for fainter meteors to have smaller measured diffusion coefficients. More data in the

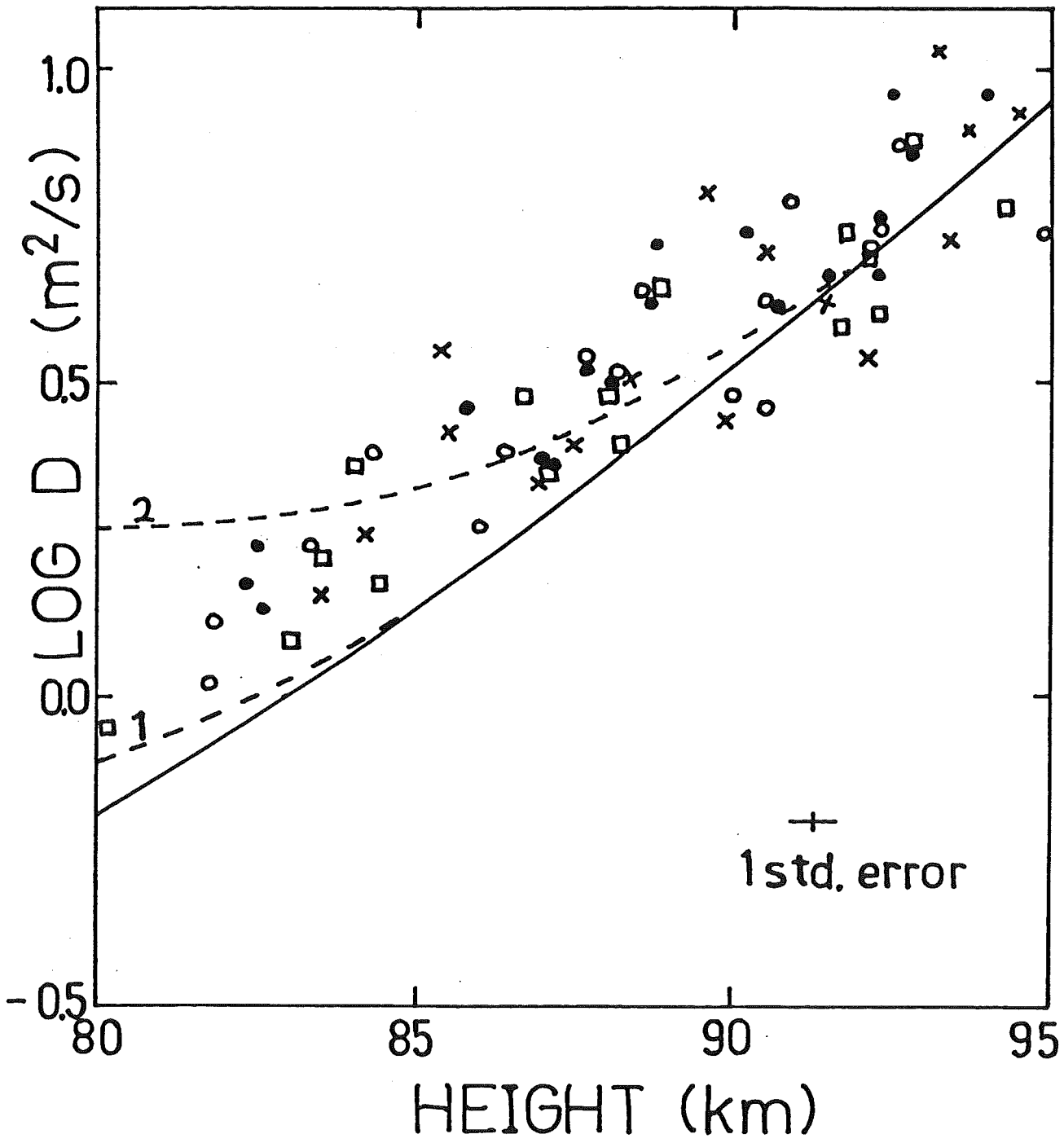

Figure 4.2: The data of Verniani grouped according to line density, q.

× $q = 6.9 \times 10^{12}\ m^{-1}$

● $q = 4.4 \times 10^{12}\ m^{-1}$

○ $q = 2.8 \times 10^{12}\ m^{-1}$

□ $q = 1.7 \times 10^{12}\ m^{-1}$

Theory, assuming $D_a = 2D_+$ from Table 2.5

1,2 Theory including chemical ionization loss (1) $q = 2 \times 10^{12}\ m^{-1}$ (2) $q = 2 \times 10^{13}\ m^{-1}$

80-82 km interval that also had a wider range of q would be useful. However, almost all points should lie between curves 1 and 2 which is the case below 85 km. Curve 3 of Fig. 4.1 has not been shown as it applies to meteors that are much brighter than those in Verniani's data. Data pertaining to such meteors would also be useful, although they would be approaching the limit for underdense trains.

It should be remembered that the method used in deriving D will affect the result. There will be a difference between D found from decay times and D found from a linear regression line fitted to the log of the echo amplitude decay, because the decay is not truly exponential.

The data are again sparse above 95 km mainly because of the finite velocity ceiling. Data can be extended to greater heights by using longer wavelengths. The height distribution for most experiments peaks at about 95 km so that sufficient echoes should be observed up to at least 105 km. The measurements of D by Greenhow and Hall and both sets of measurements by Greenhow and Neufeld are significantly less than the theoretical curve. Greenhow and Neufeld carefully removed echoes affected by the finite meteor velocity, although Greenhow and Hall do not appear to have done so.

Several ideas have been put forward as to why measured values of D above 95 km are smaller than expected. These include: the finite velocity effect (which does not apply to the data of Greenhow and Neufeld); the formation of second reflection points (which seems unlikely because of shorter decay times); selection effects in the processing of data

(which must certainly be considered and will vary with the method of analysis) and, finally, magnetic effects which are discussed in the next sub-section.

It must be remembered that all of the data in Fig. 4.1 for heights above 95 km were obtained with the same equipment, which was known to have a systematic error of 1.5 km. Because of this it would be useful to obtain results in this height region, by using a longer wavelength than 8m.

The large scatter in measured D values at a fixed height has already been mentioned. The standard deviation for this scatter is about 0.2 in log D even when height measurements are quite accurate (for example Murray, 1959). This corresponds to $\frac{\Delta D}{D} \approx \pm 0.46$. The scatter shown in Fig 3.3 is for r.m.s. values of wind effects and does account for that observed, although some effects may have been overestimated. Two-frequency experiments do not suggest that wind effects are the sole cause of the scatter so that it is quite likely to be caused by several effects such as wind, irregular ionization and measurement uncertainties (principally due to sky noise).

Before worrying about inherent scatter, the measurement uncertainties should be appraised. For example, Greenhow and Hall (1961) can attribute all of the scatter that they observed to experimental uncertainties - mainly the height uncertainty of ± 4 km.

(3) Observed Magnetic Effects

Heritage et al. (1962) found evidence that meteors produce field-aligned ionization between 100 -110 km. In

a 200 MHz experiment they found a correlation between meteor rates and the occurence of H-scatter - a rapid fading scatter signal that has a duration which is about ten times greater than those of meteor echoes. Doppler effects at the beginning of H-scatter bursts were consistent with those from meteor head echoes.

The scale sizes of the H-scatter irregularities were measured using both spaced receiving sites and spaced antennas at a single site. A large-scale length of 10 km and a small-scale of 25 m were inferred. The small-scale length was thought to be a property of the medium as it was similar to that deduced from auroral observations, while the large-scale size was attributed to the meteor.

These experiments only correlated H-scatter and meteor observations. At no stage was H-scatter known to originate from a particular meteor although previous workers had found a correlation between the onset of H-scatter and the appearance of overdense meteors at lower heights.

Watkins (1965, 1968) used a UHF radar (501 MHz) and a narrow beam aerial (half power beam width 1.6^{o}) to observe directly the effect of the geomagnetic field on meteor trains. Heights were measured from range information by assuming that signals come from the main antenna lobe where elevation was known.

Longer echo durations were observed for heights above 92 km when the angle between the transmitter beam and the perpendicular to the field direction (the off-specular angle μ) was less than $\pm 1^{o}$. Furthermore, the echo rate in this

case was about five times greater than for other values of μ. It was also found that durations for $\mu < \pm 1^{o}$ increased as height increased whereas they decreased with increasing height as expected for $\mu > 1^{o}$. This behaviour was attributed to field-aligned ionization where the diffusion was electron-controlled in the transverse direction.

Watkins et al. (1971) made a further study of geomagnetic effects, firstly at UHF with the equipment previously used by Watkins. In this case the latitude of the site was selected so that at certain observation times the Geminid meteor shower would be parallel to the field line. This enabled field-aligned trains ($\alpha = 0$) to be observed whereas only the condition $\mu = 0$ had been reached before.

Again they found that echo rates were enhanced and that echo durations were longer for $\mu < \pm 1^{o}$, but no particular effects were noticed at times when the condition $\alpha = 0$ was met for the shower. Rise times for the echoes were generally in the range 0.2 to 0.6 s which was much longer than expected.

Their second experiment involved three radar stations at VHF (31 to 36 MHz). At two of these stations, operated simultaneously, the $\alpha = 0$ condition was met for the Geminid shower at certain times, while it was never met at the third site. A negative result was obtained in this experiment as no enhancement of meteor rate was found when $\alpha = 0$. Furthermore, no effect for $\mu < \pm 1^{o}$ was observed, although in any case the wide beamwidths used would make this unlikely (as most echoes would occur for $\mu > 1^{o}$).

Fading with a frequency of 10 Hz was often noticed on echoes with durations greater than 4 s. This was attributed to the formation of second reflection points where the top of the train was fixed to the field lines while the lower part could drift. The fading rate could thus be used to derive a wind velocity of 45 m/s. The dependence of this fading rate on the angle μ was not investigated. It was mentioned in section 3.3 that such fading is often observed and is well explained by wind shears distorting the train, so that it does not necessarily indicate a magnetic effect.

Watkins et al. explained the slow rise times that were observed in terms of an increase in the reflecting area as field-aligned irregularities were formed. A transverse length of 18 m was derived from the rise times which agrees with that deduced by Heritage et al. (1962). This length was also consistent with the aspect sensitivity of $\pm 1^{o}$ which was observed in the UHF experiments of Watkins (1965,1968).

Watkins et al. (1971) concluded that the absence of an effect near the $\alpha = 0$ condition implied that the theory of Kaiser et al (1969) was not applicable to the meteors observed, which had ionization densities of 10^2 to 10^5 times the ambient electron density. The theoretical calculations used a density three times that of ambient. In section 2.6 it was mentioned why the theory of Kaiser et al. (1969) did not predict that field-aligned fins of ionization would be formed. Later work has shown that such fins should be formed.

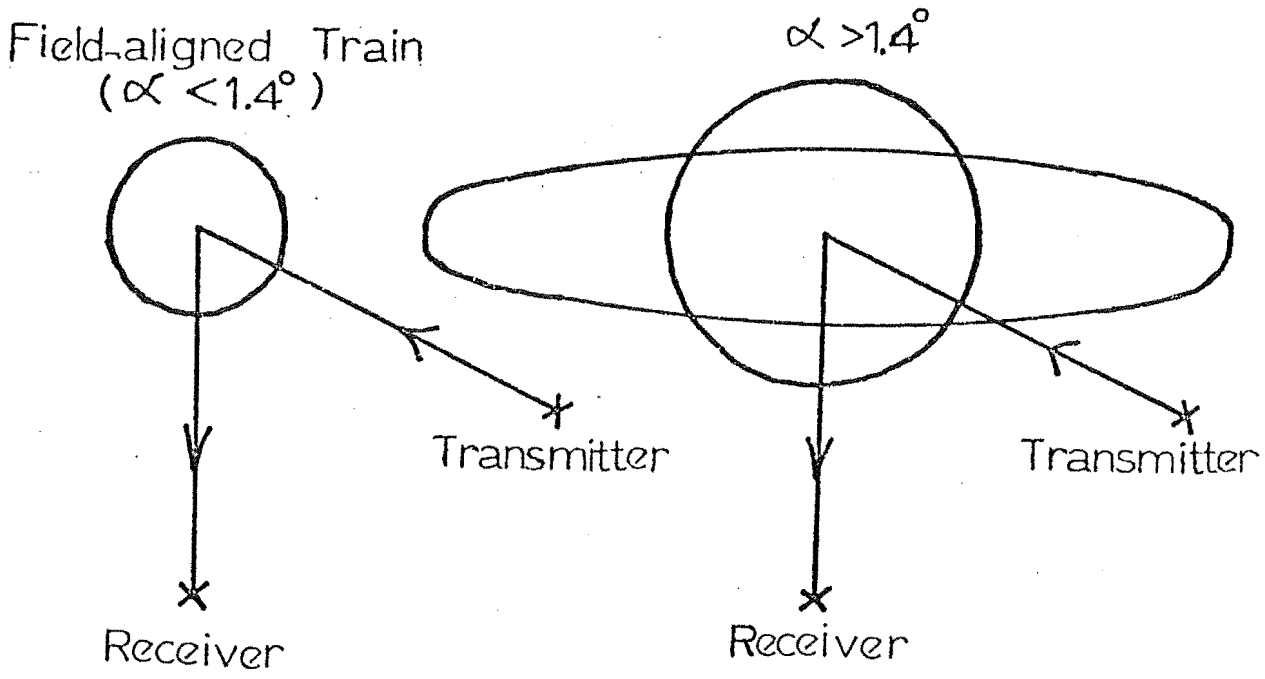

Figure 4.3: Forward-scatter from field-aligned and non-aligned meteor trains.

The results of Watkins et al. (1971) are consistent with the theory outlined in Chapter 2. Little difference could be observed between reflections from a field-aligned train ($\alpha = 0$) and from field-aligned irregularities ($\mu = 0$), by a backscatter radar system. Both will have a length scale in the direction of the transmitter that is controlled by transverse electron diffusion. Admittedly, a non-field-aligned train that is underdense will have a central column that diffuses rapidly, but in that case reflection from the field-aligned fins of ionization will dominate. However, the aspect sensitivity of the reflections for long wavelengths may give more information about the diffusion process by a comparison with the aspect sensitivity of $\pm 1^{\circ}$ observed at shorter wavelengths.

To observe directly any change in the behaviour of the train about $\alpha=1.4^{o}$, a forward-scatter experiment is needed. In this case the reflections for $\alpha<1.4^{o}$ and $\alpha>1.4^{o}$ are different. For $\alpha<1.4^{o}$ both length scales in the forward-scatter directions are the same. For $\alpha>1.4^{o}$ these length scales are different as one of the forward-scatter directions will be at an angle to the plane formed by the field and train (see Fig. 4.3). Such an experiment could, at the same time, measure train orientation by measuring the separation of the forward-scatter and backscatter reflection points. This is explained in section 5.3.

The results of Watkins (1965,1968) are also consistent with the theory outlined in Chapter 2. It must be remembered that for such UHF systems only overdense meteors will be observed (Greenhow and Watkins, 1964). In that case diffusion will be mainly ambipolar and anisotropic. Furthermore, the train will reflect as a metal cylinder, so that the interpretation of slow rise times (Watkins et al., 1971) being caused by the formation of field-aligned irregularities seems quite reasonable. The observed aspect sensitivity is also consistent with the observed length scales, but can be interpreted in another way, discussed in section 7.4.

Characteristics of underdense meteors will be different from those observed by Watkins (1968). The fins will be underdense so that the echo power will not be affected by their formation. The scale lengths of the fins will be determined by the electron diffusion coefficient in the

field direction and will be considerably larger than the length scale for the overdense train's ambipolar ellipse.

Fig. 4.1 shows a departure of observed decay times from those predicted theoretically for heights above 95 km. Magnetic effects may contribute to this. For example, consider a field-aligned train. Below 95 km the electrons have a higher transverse diffusion coefficient than the ions so that the diffusion is ion controlled and the measured diffusion coefficient is $\sim 2D_+$. Above 95 km the electrons are less mobile and the resulting diffusion coefficient is $\sim 2D_{T-}$. In the transition region

$$D \approx D_+ \approx D_{T-}$$

which would account for the difference seen at 95 km. However, the problem is more complex than this. Various values of D will be measured depending on the angle between the train and the geomagnetic field, α, and also the angle between the perpendicular to the field and the transmitter, μ. These angles will vary according to the experimental geometry so that a general analysis is not possible. A more complete analysis is presented in section 7.4.

4.4 AIMS OF THIS EXPERIMENT

From the preceding section it is clear that there are some areas where further experimental results would be valuable.

The department of Physics of the University of Canterbury, Christchurch operates a pulsed meteor radar. The operating wavelength is 11.38 m (frequency 26.36 MHz) and the peak transmitter power is 40 kW. An interferometer for height measurement is included in the system. Also available is a 10 kW transmitter operating at the same wavelength. This system is well suited for investigating some of the areas where more experimental results would be useful.

There are several geomagnetic effects that can be investigated. Firstly, with two transmitters, a combined forward-scatter and backscatter system can be operated. This enables train orientation to be established by locating the respective reflection points. This will also enable a measurement of diffusion coefficients in two directions as mentioned earlier. In order to measure trains orientated about $\alpha = 0$, the two sites need to be located on a baseline that is nearly perpendicular to the magnetic south direction. The geography of New Zealand allows a baseline separation of about 150 km in this direction which will be shown to give sufficient resolution of train orientation about $\alpha = 0$. The condition $\mu = 0$ must also occur at an elevation where the echo rate will be sufficiently high. At the Rolleston field station (43.6^{o}S, 172.4^{o}E, geomagnetic latitude -48.2^{o}, geomagnetic longitude 252.6^{o}, 34 m above mean sea level) this elevation is 16.1^{o} which is quite suitable.

With the given operating wavelength and transmitter powers, high gain aerials are needed to ensure that most echoes observed are underdense. Echo rate does not vary

with antenna gain, but the proportion of useful echoes can be increased in this way. In only one experiment has an attempt been made to measure magnetic effects on underdense meteors (Watkins et al., 1971). This was unsuccessful because no angle measurement was possible. Aspect sensitivity seen on wavelengths of 0.6 m in previous experiments can be compared with that at 11.38 m.

Furthermore, the present system also has a doppler wind measuring capability. This may enable any magnetic effects on train drifts to be assessed. Unfortunately, this system is designed to operate on a pulse repetition frequency (P.R.F.) of 300 Hz. With the need to receive two transmitter pulses simultaneously the maximum P.R.F. is 150 Hz. This reduced sampling rate will degrade the wind information.

Finally, a wavelength of 11.38 m increases the finite velocity ceiling above that relevant to previous experiments. This will enable a better determination of diffusion coefficients above 95 km. As the off-specular angle, μ, will be known for individual echoes, field-aligned trains and field-aligned ionization can be excluded from the data.

Two other effects may be examined by this system. Chemical effects may be observed for low altitudes. Ideally, line densities would be estimated from the signal amplitude and a knowledge of the antenna patterns. The use of narrow beams will make the estimates of line density less accurate than for systems using broad beams, because the change in antenna gain for a particular angle uncertainty is larger. High power systems are able to collect far more data in a

given time than the present system so that such results would carry more weight.

The effect of Fresnel diffraction on heights measured with an interferometer may also be observed. A P.R.F. of 150 Hz is usually not sufficient to resolve Fresnel fringes. A system with a P.R.F. in the range 400-600 Hz would be more suitable. The present radar cannot operate at such high P.R.F.'s, even with a single transmitter, because of power limitations and the introduction of range ambiguities. However, the fringes may be resolved for some low velocity meteors for which the height error could be examined.

Some points mentioned earlier are not amenable for study by this system. Diurnal variations of D and scale height determinations really need to be studied with a system that can operate continuously and can handle large amounts of data. The present system needs monitoring while in operation. Records are punched on to papertape which is not a suitable medium for large amounts of data because of bulk and slowness and unreliability in reading. The system has been used for wind measurements of up to ten days duration, but it was found that the echo rate in the late afternoon was marginal for good wind information. This will also apply to diffusion - height data as many echoes are needed to get statistically significant results because of the large scatter in measured D values. Thus an automatic system with a high-power radar, recording on magnetic tape is better suited to such studies.

Finally, thermalization could be studied. The difficulties in interpreting data in such studies have already been mentioned. A high power system may overcome the plasma resonance phenomena by looking at fainter meteors, so that changes in D during an echo decay could be studied. Dual frequency experiments are also more useful in these studies than the system available, but again the results would be difficult to interpret.

4.5 DESCRIPTION OF THE EXPERIMENT

The experiment uses two separated transmitters and an interferometer for receiving. The use of separated transmitters enables train orientation to be found. The backscatter signal can be used to locate the train in a particular plane. The orientation of the train within this plane can be found from the height difference ($\approx$ distance along the train) between the backscatter and forward-scatter reflection points. The second transmitter is ideally situated when a vertical train produces both reflection points at the same height. The distance between the transmitters will determine the resolution of train orientation in terms of reflection point separation. The use of forward-scatter will also enable the train cross-section to be viewed from two directions at the same time. This will enable more information to be gained about the behaviour of the ionization than can be deduced by backscatter observations alone. Narrow transmitter beams are

necessary to increase the system sensitivity and thereby maximise the useful echo rate. Wind measurements on the backscatter signal may enable effects on train drifts to be observed.

The system measures heights by using three spaced receiving antennas. Phase differences between the received signals enable angles to be found which can be converted to azimuth and elevation angles. Echo amplitudes are measured for both echoes while range and wind information is recorded only for the backscatter signal.

Trains that are parallel to the magnetic field are of most interest in the dual-transmitter observations. For Rolleston, the backscatter site, echoes in the range 330-450 km may be field-aligned. These long ranges enable a long interferometer spacing to be used without introducing height ambiguities as all echoes will come from a small range of elevations. This will reduce the height measurement uncertainty.

An echo transponder was available for calibrating the system. When triggered, the transponder returns apparent echoes with a set range delay and the receiving system records the pulses in the usual way. This information, when combined with the known location of the transponder (in the main aerial beam at a distance of 3 km), could then be used to calibrate the interferometer for that particular direction. These calibration signals, triggered by coding the transmitter P.R.F., took only a short time to record, thus enabling the transponder to be used during data collection.

The data storage medium was papertape. This could be transferred on to magnetic tape by the University of Canterbury's Burroughs 6700 computer before further processing.

CHAPTER 5

GEOMETRY OF THE EXPERIMENT

In this chapter the geometry calculations for the geomagnetic diffusion experiment are described. Firstly, the calculations for the off-specular angle, μ, are presented. μ is the angle between the transmitter beam and the perpendicular to the geomagnetic field at the reflection point. Secondly, the locus of points corresponding to possible sites for the remote transmitter is found. The calculations for determining train orientation in terms of reflection point separation are then described. Finally, a check is made to see if any known Southern hemisphere meteor showers are likely to produce field-aligned meteor trains.

5.1 OFF-SPECULAR ANGLE

Millman (1959) derives an expression for the angle between the radar beam direction and the geomagnetic field. In terms of the off-specular angle this becomes

$$\sin \mu = - \cos e \sin I - \sin e \cos I \cos \beta \qquad 5.1$$

where e is the angle between the beam (see Fig. 5.1) and the vertical direction, I is geomagnetic inclination at the reflection point and β is given by

$$\beta = 360^{o} - (B+D). \qquad 5.2$$

Here D is the geomagnetic declination at the reflection point and B is the geographic azimuth of the radar from the point directly below the reflection point, P, measured from geographic south (see Figs 5.1 and 5.2). The angle β is the angle between two planes: one is formed by the radar beam and the vertical line SP; the other is formed by the field direction and SP. The angle e is given by

$$\sin e = \frac{r}{r+h} \cos E$$

where e is the beam elevation and r is the earth's radius. The echo height for curved earth geometry is

$$h = (R^2 + 2rR \sin E + r^2)^{\frac{1}{2}} - r \qquad 5.3$$

To find μ, I and D for the reflection point must be found as well as the angle B. The reflection point can be located by the angle of elevation at the radar, E, the azimuth, A and echo range, R. The longitude and latitude of the reflection point can thus be found from these quantities.

The great circle path length between the radar and point P, c, is given by (see Fig. 5.3)

$$\cos c = \frac{r^2 + (r+h)^2 - R^2}{2r(r+h)} .$$

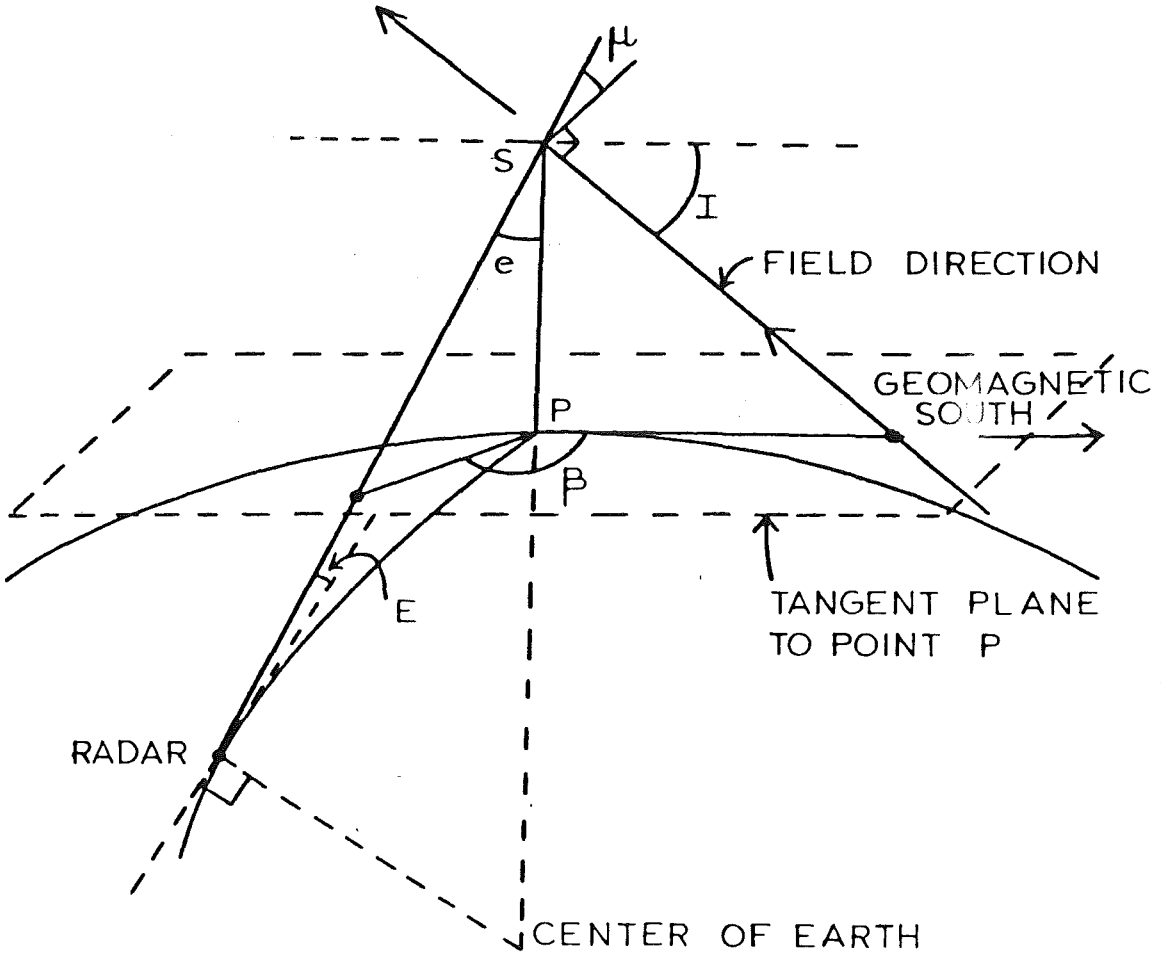

Figure 5.1: Off-specular angle geometry

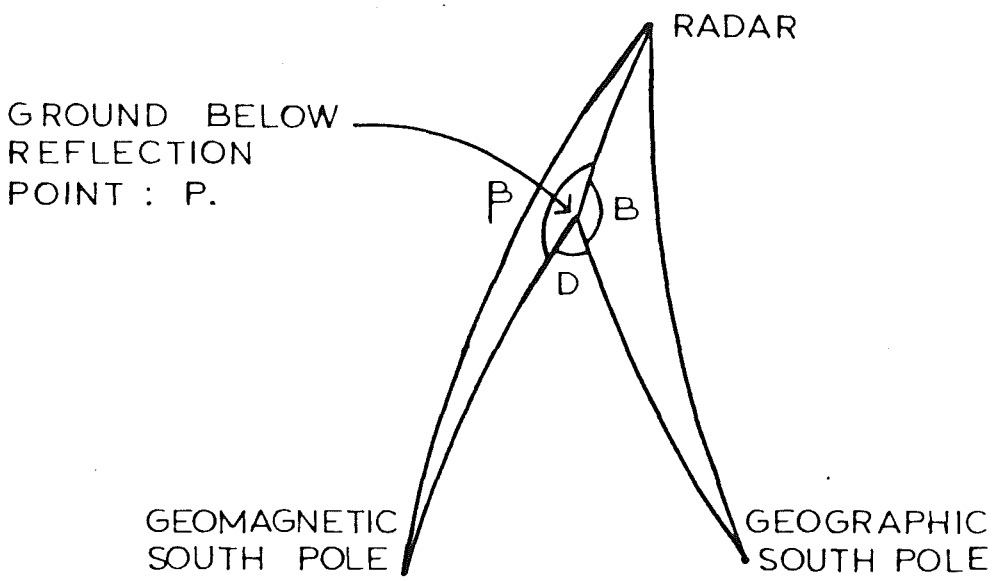

Figure 5.2: Relation between azimuth, declination and β

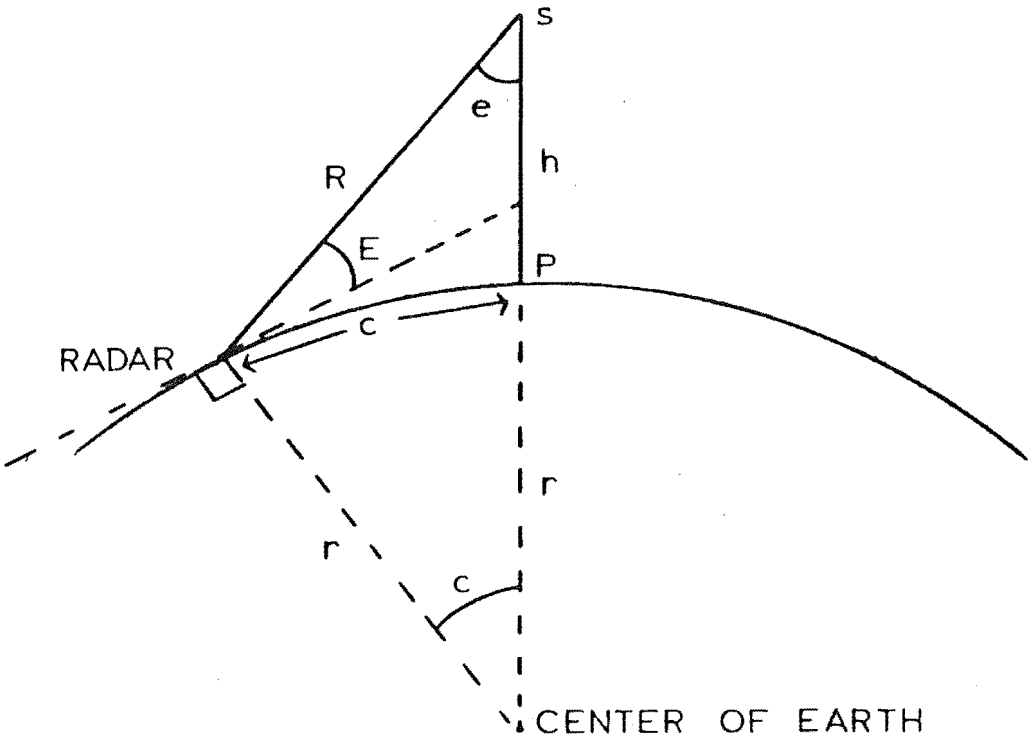

Figure 5.3: Determination of great circle path, c.

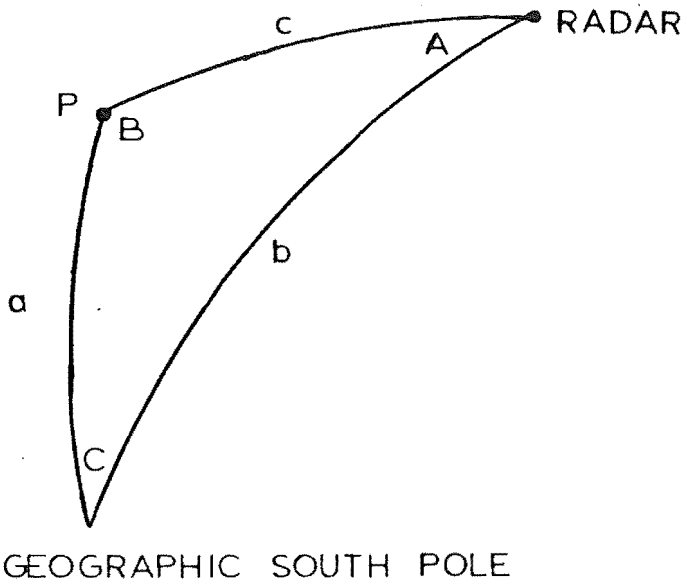

Figure 5.4: Finding colatitude and relative longitude of the point below the reflection point, P.

The latitude and longitude of the reflection point can now be found (S and P have the same values). Referring to Fig. 5.4, b is the colatitude of the Rolleston field station, a is the colatitude of P and C is the longitude difference between Rolleston and P. All lines in Fig. 5.4 are great circle paths. The quantities a and C can now be found by using spherical trigonometry.

$$\cos a = \cos b \cos c + \sin b \sin c \cos A$$

and

$$\sin C = \sin B \sin c / \sin b$$

so that the latitude and longitude of the reflection point can now be found. The angle B can also be found by using

$$\sin B = \sin A \sin b / \sin a \qquad 5.4$$

so that β can be calculated. For angles of azimuth $A < \pi/2$ or $A > 3\pi/2$ π-B must be used instead of B because the sine rule is ambiguous for these angles.

The off-specular angle can now be determined by using values of D and I for the reflection point. There are two ways of calculating these geomagnetic field values. Firstly, the International Geomagnetic Reference Field (IGRF) for, say, a 100 km height can be used. Secondly, surface values can be extrapolated to 100 km by using the difference between the ground and 100 km values of the IGRF. Table 5.1 shows the values obtained from both methods for a point near the

middle of the expected reflecting region. The IGRF values were originally for 1974, but were corrected to 1978 values by using annual variations for the surface.

Table 5.1: Magnetic field values (1978) (47^{o}S,171^{o}E,100 km a.m.s.l)

Method	Declination (^{o})	Inclination (^{o})	Source
IGRF	24.4 $\pm$ 0.1	71.5 $\pm$ 0.1	Gill, private communication
Surface values extrapolated	24.31 $\pm$ 0.05	71.62 $\pm$ 0.05	Reilly and Burrows (1973)

The values agree within the estimated uncertainties. D and I derived from the surface values were finally used.

Watkins (1971) checked magnetic inclination values for 55^{o}N, 3^{o}W by measurements on field-aligned ionization with a narrow beam, high frequency radar. Both meteor and auroral ionization were used. His measurements agreed closely with the relevant IGRF values. The extrapolated surface values differed by 0.4^{o}. Watkins suggested that this was possibly due to a local anomaly in the surface values. The close agreement between the values in Table 5.1 is thus reassuring and the values are probably reliable within their estimated uncertainties.

Values of D and I were found for several points in the area near where the condition $\mu = 0$ was met. A computer program written to calculate values of μ then interpolated

in this region by using the known values. Far away from the region where the condition $\mu = 0$ is met, the program extrapolated from these values so that μ was only accurate to within $\pm 0.5^{o}$. A grid of points for a 100 km height was calculated and contours of constant μ were drawn by hand (Fig. 5.5).

The change in inclination between 100 and 200 km, for a particular latitude, is $+ 0.044^{o}$ according to the IGRF. This means that the change between 100 and 110 km will be about 0.004^{o}. This is negligible in comparison with the uncertainty in I so that constant values of I were used over meteor region. This declination behaves in a similar way and was treated in the same manner.

The computer program was finally adopted to find μ at the reflection point of each recorded meteor. It was incorporated as a procedure into one of the data reduction programs (see Appendix 3) so that the record for each echo included the off-specular angle. This simplified subsequent data analysis.

Fig. 5.5 shows that the specular reflection region occurs for elevations near 16^{o} in the magnetic south direction. The region extends over $\pm 20^{o}$ of azimuth with little change in elevation. The off-specular angle varies much more rapidly as elevation changes. The $\mu = 90^{o}$ condition occurs for one point only - when the angle of elevation is equal to the inclination at the field station and the azimuth is in the magnetic north direction.

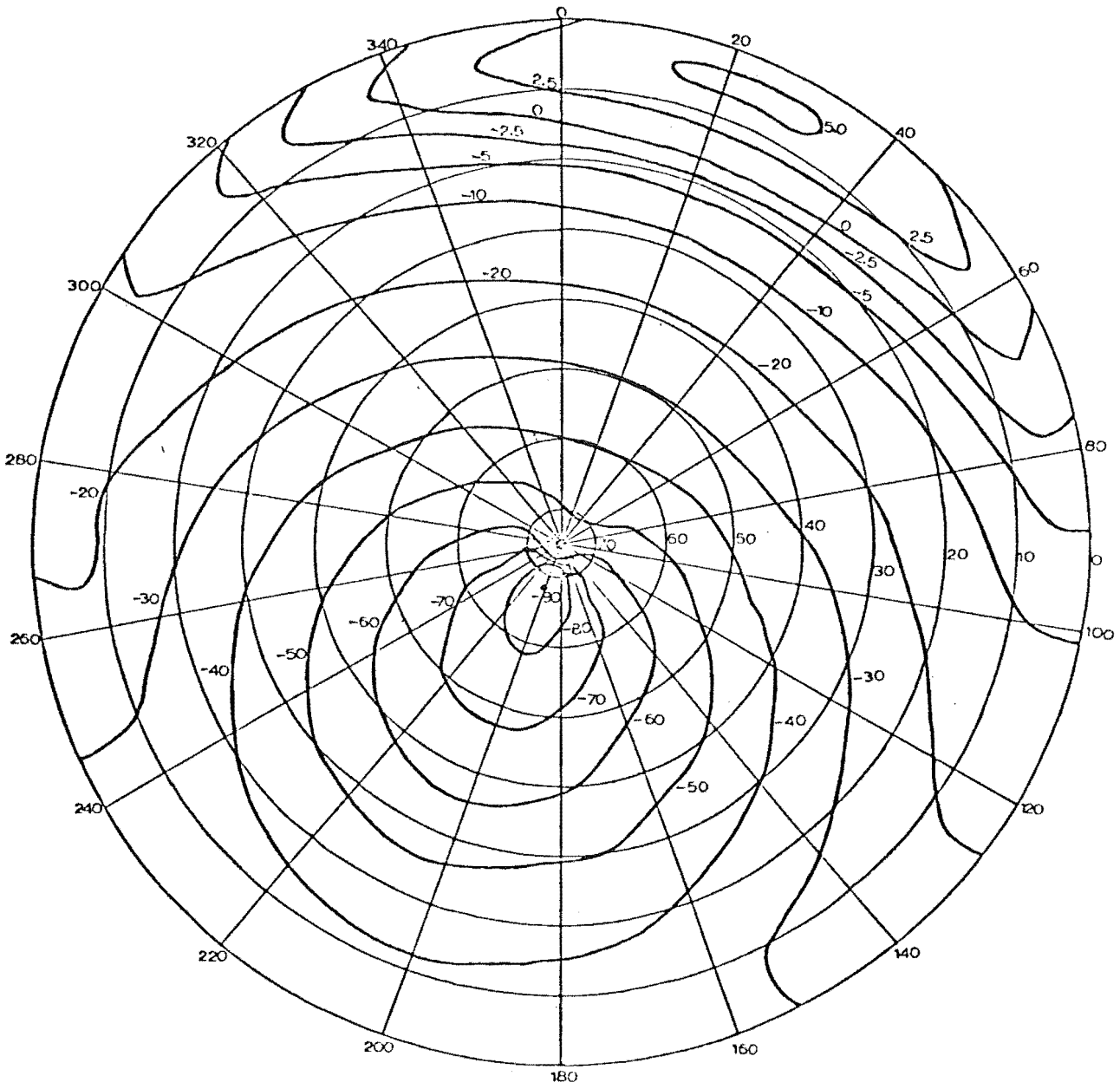

Figure 5.5: Contours of constant off-specular angle at 100 km for the Rolleston field station.

5.2 REMOTE TRANSMITTER LOCATION

The ideal location for the second transmitter is on a line where radio waves forward-scattered off a particular field-aligned meteor from Rolleston will strike the ground. The most suitable field-aligned meteor has the angle $\beta = 180^{\circ}$ (Fig. 5.1). If these conditions are met, the backscatter and forward-scatter reflection points will be at the same point on a field-aligned train.

As the site could be situated anywhere on the line defined above, the aim of this section is to plot this line on a map so that a suitable site can be selected. The longest possible transmitter separation is desirable to maximise the resolution of the system.

The calculations presented here are for a 100 km height, $\beta = 180^{\circ}$ and $\mu = 0$. An iterative method of calculation was adopted to find the angles of elevation and azimuth to satisfy the above conditions. A choice of azimuth and elevation defined a reflection point and thus values of I and D so that β and μ could be found. This was repeated until the final values of azimuth, A, and elevation, E, were found to be

$$A = 22.54^{\circ}, \quad E = 16.1^{\circ}$$

giving R = 332 km, $\beta = 180.0^{\circ}$ and $\mu = -0.03^{\circ}$ for an assumed earth radius of 6368 km. Considering Fig. 5.6, all lengths can now be found. The figure DSMC is a plane because $\beta = 180^{\circ}$. M is the point where an extension of the meteor

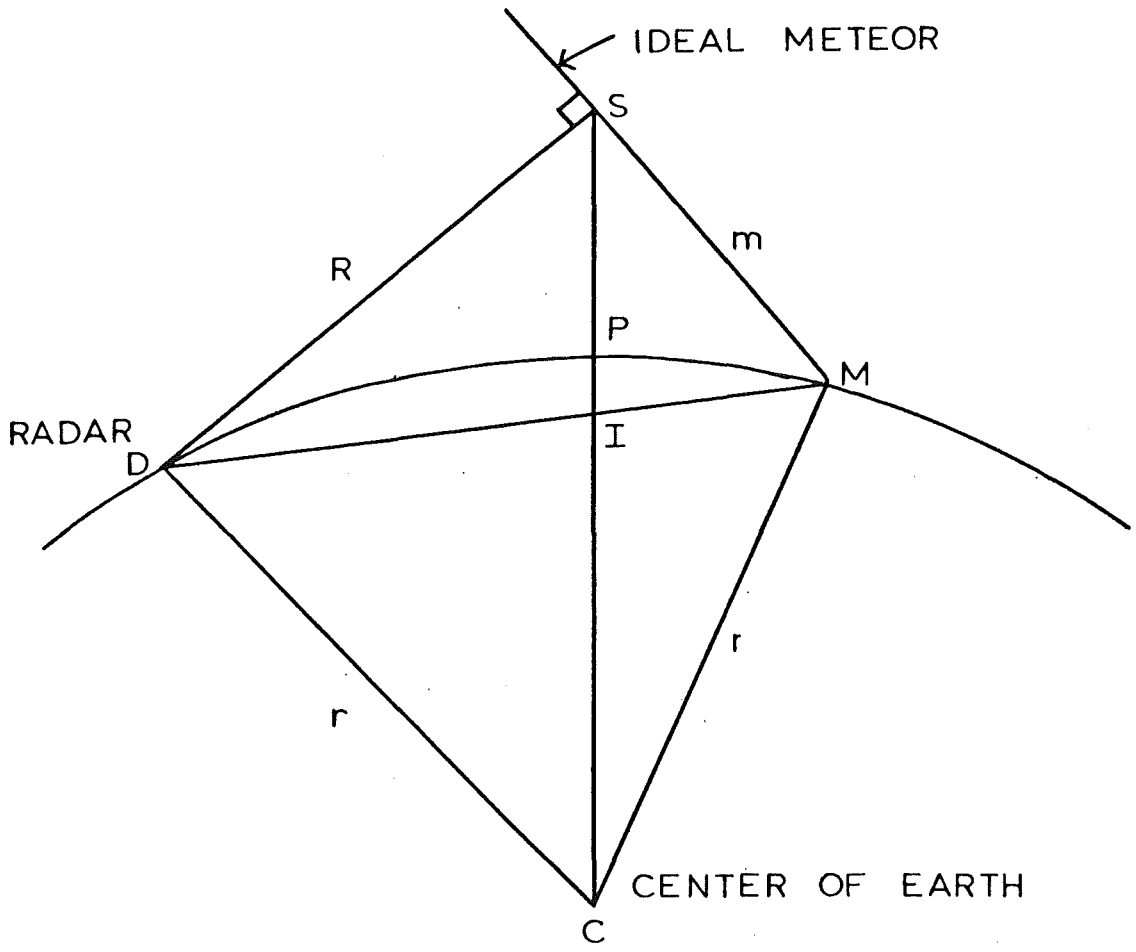

Figure 5.6: Backscatter geometry for the ideal train

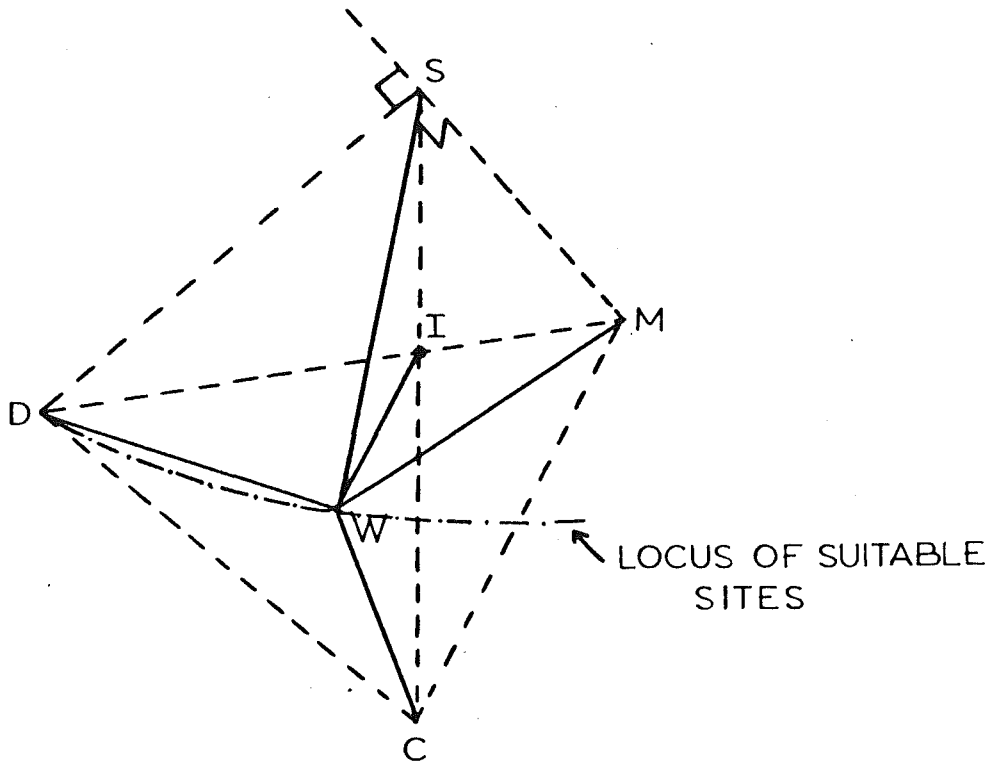

Figure 5.7: Forward-scatter geometry

path meets the earth's surface.

Fig 5.7 introduces the second transmitter site W. The position of W is anywhere on the line of possible transmitting sites. Once one parameter, for example the length MW, has been set, W is well defined, because of the right angle MSW. All lengths can then be found. The lengths DM, MW and DW can all be used to find great circle paths between these points and then the longitude and latitude of W can be found.

First it is necessary to relate the parameter MW to DW in terms of the known lengths from Fig. 5.6 so that the triangle MWD can be solved. Simple geometry enables SW to be calculated so that in Fig. 5.8, which shows one triangle (SCW) from Fig. 5.7, all lengths are known except WI, which can thus be found in terms of MW. Then referring to Fig. 5.9, DW can be found in terms of the other sides, all of which are now known. With the use of the previously calculated values for Fig. 5.6 this then gives

$$DW^2 = 0.842\ MW^2 - 1.023 \times 10^{11} \quad . \qquad 5.5$$

This equation can be checked by putting MW = DM which should give DW = 0. The result, DW = 800 m, is due to round-off errors in the calculations. An 800 m uncertainty in the site would not be important.

The lengths DW and MW are related to their respective great circle paths GDW and GMW by

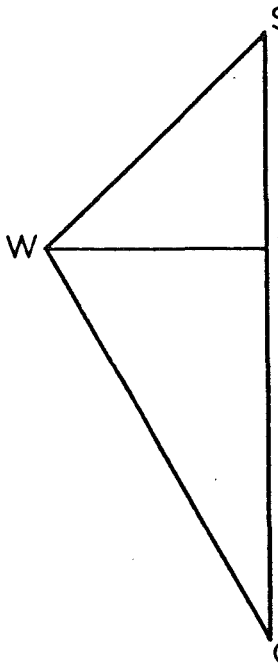

Figure 5.8

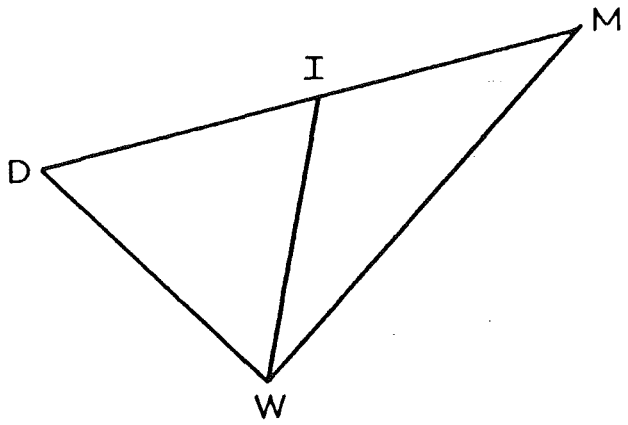

Figure 5.9

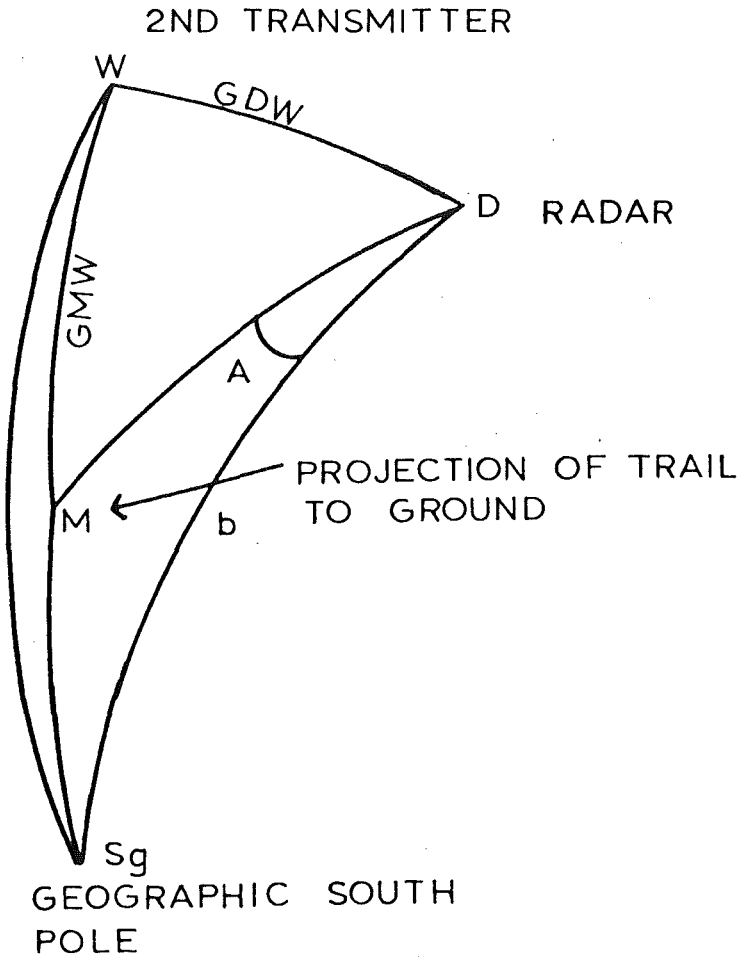

Figure 5.10: Great circle paths used in finding the locus of possible transmitting sites

$$\cos(GDW) = 1 - \frac{DW^2}{2r^2} \quad , \cos(GMW) = 1 - \frac{MW^2}{2r^2} \qquad 5.6$$

The great circle triangle DMS_g in Fig 5.10 can be solved completely as the great circle path DM can be found, the azimuth of M from D is known, as is b - the colatitude of Rolleston. Then for a particular choice of GMW, GDW can be found by using equations 5.5 and 5.6. The angle WDM can then be found using spherical trigonometry so that the angle WDS_g can be found. There is then sufficient information to solve the great circle triangle WDS_g so that angle WS_gD gives the longitude of W relative to D, and the length WS_g is the colatitude. This process can be repeated for further choices of GMW so that a locus of possible sites is obtained.

Fig 5.11 shows the locus of suitable sites where it crosses the main road on the West Coast of the South Island of New Zealand. The final choice of a site was made after investigating the availability of an electricity power supply and suitable land. The chosen site is marked on Fig. 5.11 and is about 10 km from the ideal line. The area was clear and flat. A hill 3 km to the south of the site had a maximum elevation of 6^o which would not interfere with the transmitted beam at 16^o.

5.3 TRAIN ORIENTATION

The aim of this section is to find the train orientation with respect to the geomagnetic field (angle α). This can be

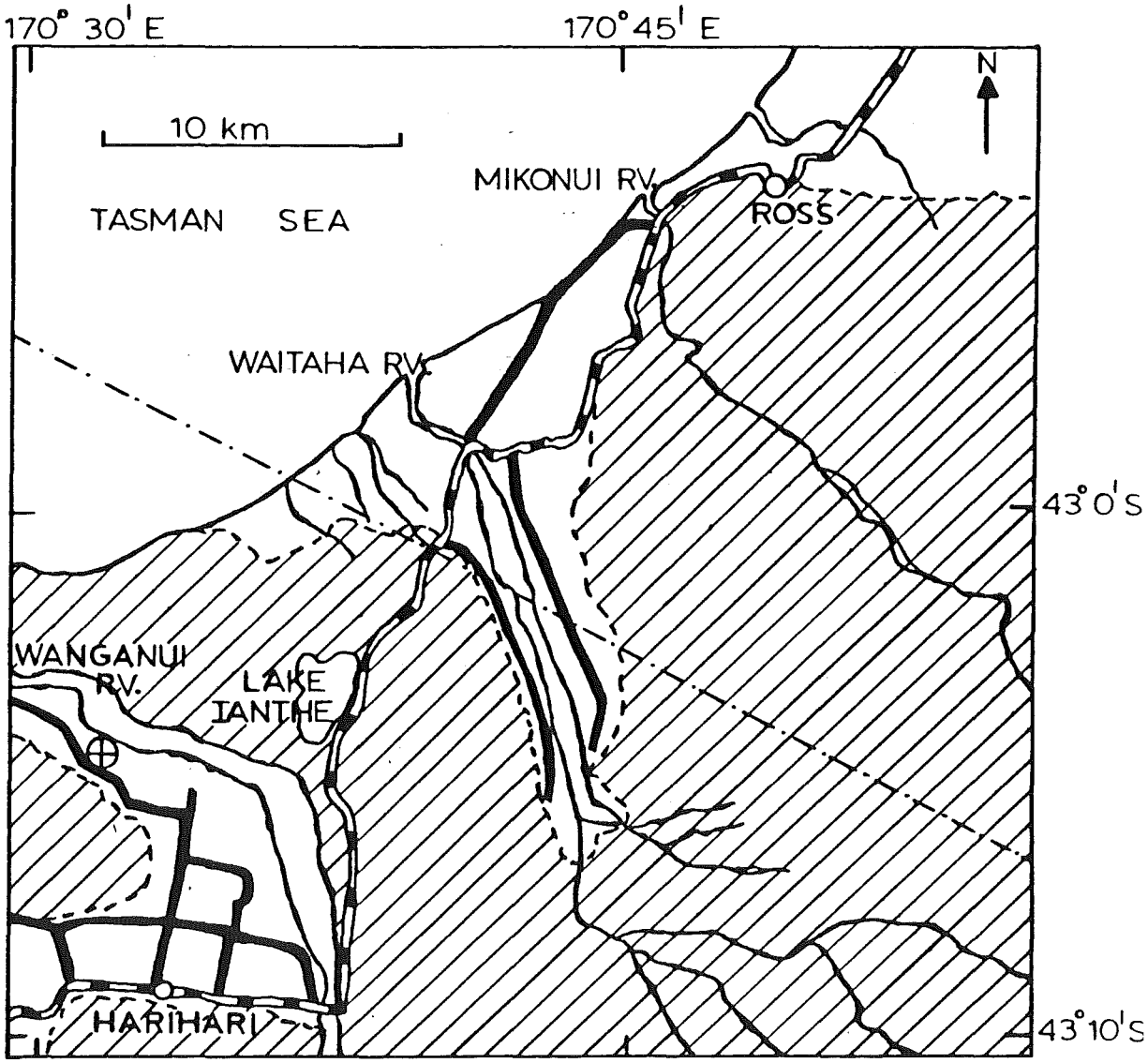

Native bush

Main Road

Town

River

Locus of ideal transmitter sites

Selected site for remote transmitter

Figure 5.11: The remote transmitter site

found from the angular separation of the backscattered and forward-scattered reflection points on the train, ε, together with the range, azimuth and elevation of the backscattered signal and the location of the remote transmitter. The calculations were done in three stages. First, an expression for the angular separation, ε, was found in terms of the measured quantities. Secondly, the angle between the train and a perpendicular train, η, was found in terms of ε and the other known quantities. Trains described as perpendicular are orientated so that a vertical line (towards the earth's centre) through the backscatter reflection point is in the plane formed by the transmitter and meteor train. An extension of such a train would pass through the zenith of the transmitter site. Finally, the angle η was related to the angle α between the train and the field direction.

(1) Angular Separation

Fig. 5.12 shows the geometry for finding the angular separation of the reflection points, ε. D,M and L lie on the plane tangent to the earth's surface at the receiving site. JM and KL are perpendiculars to this plane from the backscatter and forward-scatter reflection points respectively, constructed so that DJK is a right angle. Also shown are the respective elevations and azimuth difference of the reflection points, and the backscatter range, R. In Fig 5.12

$$ML^2 = R^2 \cos^2 E_1 + DK^2 \cos^2 E_2 - 2R.\ DK \cos E_1 \cos E_2 \cos A$$

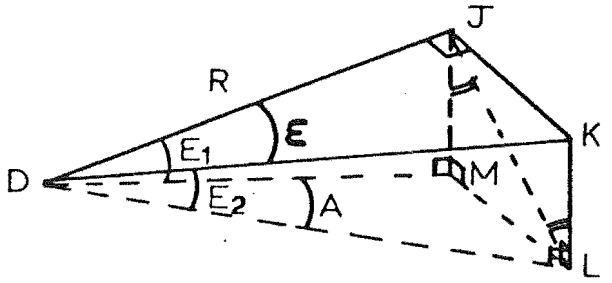

Figure 5.12: Determining the angular separation of the reflection points

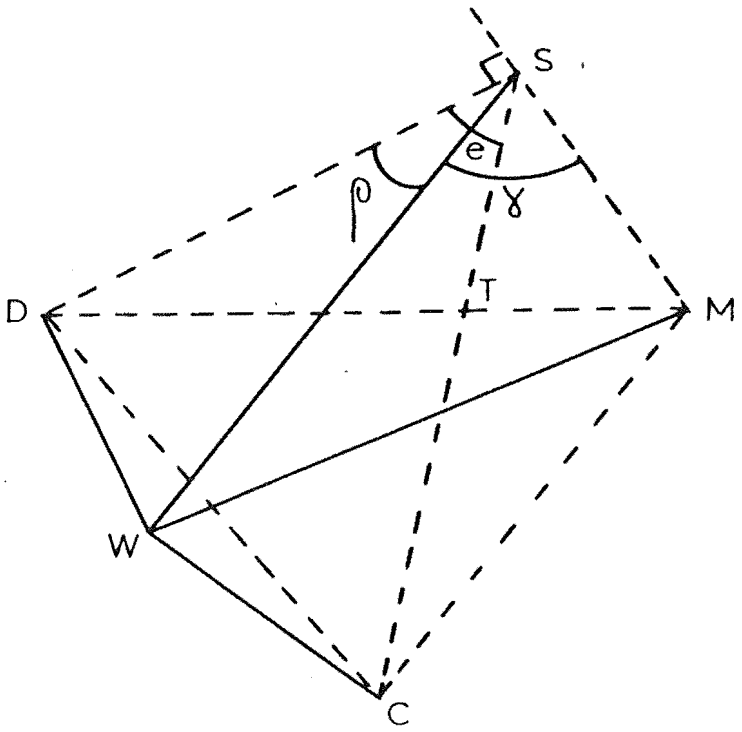

Figure 5.13: Forward-scatter geometry for a perpendicular train

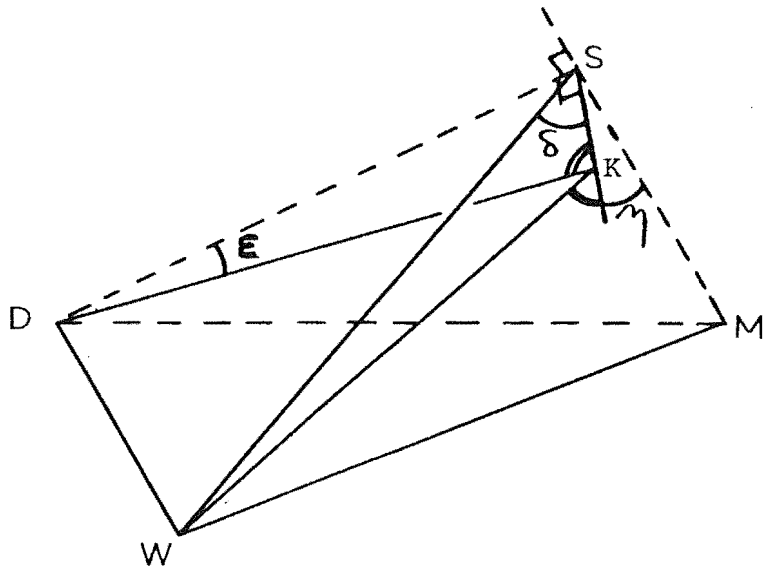

Figure 5.14: Forward-scatter geometry for a train at an angle η to a perpendicular train.

and

$$JL^2 = ML^2 + R^2 \sin^2 E_1 .$$

Also,

$$M\hat{J}L = J\hat{L}K$$

$$= \cos^{-1} (R \sin E_1/JL)$$

and

$$JK^2 = DK^2 - R^2$$

$$= ML^2$$

which gives

$$R^2 - R.DK(\cos E_1 \cos E_2 \cos A + \sin E_1 \sin E_2) = 0 .$$

With

$$R = DK \cos \varepsilon,$$

and neglecting the trivial solution R = 0,

$$\cos \varepsilon = \cos E_1 \cos E_2 \cos A + \sin E_1 \sin E_2 . \qquad 5.7$$

The maximum length of trains expected is about 8 km which means a maximum angular separation of $\varepsilon \sim 1.4^{\circ}$ for the minimum range used of 330 km. This is shown to correspond to a train inclined to a perpendicular train by $\sim 7^{\circ}$. The observed azimuth difference will then be about 0.2°. This difference is comparable to the azimuth measurement uncertainty (see section 7.3). If this were not the case, train orientation could be determined directly from E_1, E_2 and A. The use of ε enables a far more accurate determination of orientation to be made. As the azimuth difference, A, will be barely resolvable, the first term in equation 5.7

will serve only to introduce random errors into the determination of ε. It was thus decided to use the simplified expression

$$\varepsilon = E_1 - E_2 .$$

This will be effective since the elevation difference is much larger than the azimuth difference because near-perpendicular trains are being observed. Furthermore, the interferometer used in the height measurement has a smaller uncertainty for the elevation angle than for the azimuth angle (section 7.3).

(2) Inclination to Perpendicular Trains

Consider Fig. 5.13 which is similar to Fig. 5.7, but now W is the selected site for the second transmitter. The train MS is perpendicular in the sense used here in that D,S,M,I and C all lie in one plane. The length DW can be found from the known positions of the two transmitter sites by using great circle paths in the same way as in section 5.2. The result is

$$DW = 162200 \text{ m} .$$

The azimuth of the line DW from geographic south was found in a similar way to be 110.65°. The angle $\hat{MDW}$ could then be found from the echo azimuth by

$$\hat{MDW} = 110.65^{\circ} - A .$$

This assumes that the angle between the great circle paths is equal to that between the straight lines DM and DW. A trial calculation showed that there was a difference of 0.02°

between these angles which is much less than the uncertainty in the measurement of A. For a particular range, azimuth and elevation, the lengths SW, MS and the angles ρ and γ can now be found using

$$MS = r \cos E - (r^2 \cos^2 E - h[2r + h])^{\frac{1}{2}}$$

$$DI^2 = R^2 + h^2 - 2Rh \cos e$$

$$SW^2 = r^2 + (r+h)^2 - \frac{r+h}{r} [2r^2 - DI^2 - DW^2 + 2 \cdot DI \cdot DW \cos (110.65 - A)]$$

$$MW^2 = DW^2 + R^2 + MS^2 - 2 \cdot DW(R^2 + MS^2)^{\frac{1}{2}} \cos(110.65-A).$$

Finally,

$$\cos \gamma = \frac{SW^2 + MS^2 - MW^2}{2 \cdot SW \cdot MS}$$

$$\cos \rho = \frac{R^2 + SW^2 - DW^2}{2 \cdot R \cdot SW} .$$

Fig 5.14 introduces the second reflection point, K. Radio waves are forward-scattered from meteor trains in a cone and at an angle to the train equal to the incident angle. These equal angles are shown at point K in Fig. 5.14. For a given value of ε the angle δ needs to be found. The desired angle η can then be found from δ, ρ and γ. By relating the triangles in Fig 5.15 and Fig 5.16 through the side KS and the angle $90^{o}-\varepsilon$

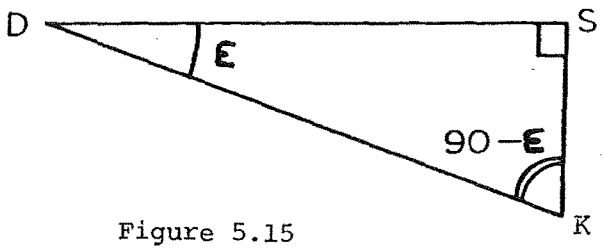

Figure 5.15

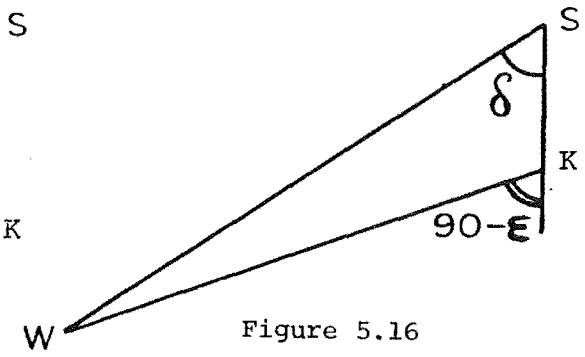

Figure 5.16

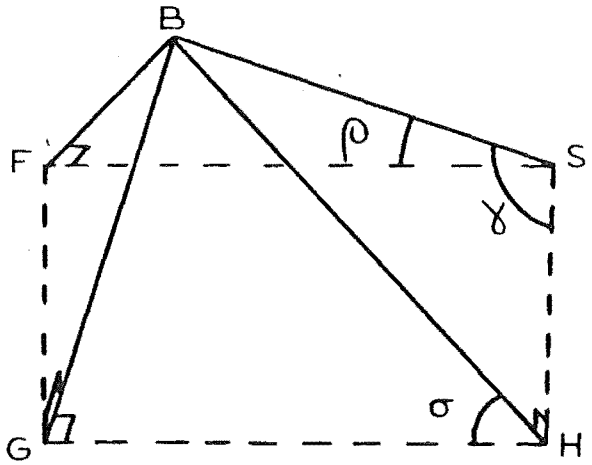

Figure 5.17

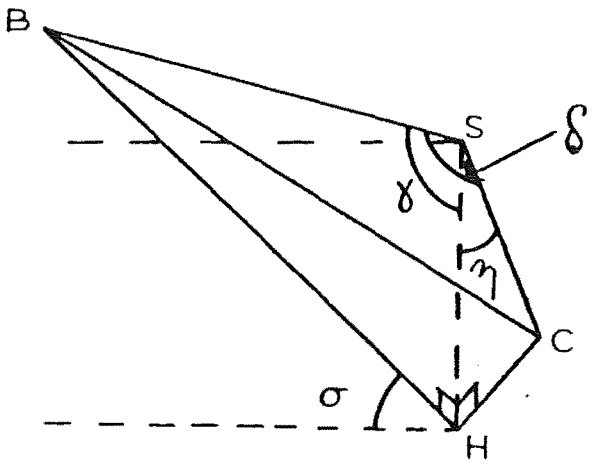

Figure 5.18

$$\cos\delta = \frac{\sin\varepsilon[DS\cos\varepsilon + (SW^2 - DS^2\sin^2\varepsilon)^{\frac{1}{2}}]}{SW} \quad . \qquad 5.8$$

The ambiguity in finding δ was removed by considering Fig. 5.16 which shows that δ must be acute. Equation 5.8 was checked for angles $\varepsilon < 0$ (when the forward-scatter reflection point is above the backscatter one) and obtuse values of δ were obtained, as required by the geometry.

The final step is to relate η to δ, ρ and γ. Fig. 5.17 was constructed by dropping the line BG such that it is everywhere perpendicular to the plane SFGH. SH corresponds to the perpendicular train, SF is the backscatter direction and BS is the direction of the remote transmitter. Lines BF and BH are then drawn at right angles to SF and SH respectively and SFGH is then a rectangle. The angle σ is then related to ρ and γ by

$$\cos\sigma = \cos\rho/\sin\gamma \quad . \qquad 5.9$$

In Fig. 5.18 the train SC is introduced at an angle η to the perpendicular train. Now

$$BC^2 = BS^2 + CS^2 - 2\,BS\cdot CS\cdot\cos\delta$$

$$= BH^2 + CH^2 - 2BH\cdot CH\cdot\cos(90^{\circ}-\sigma),$$

but

$$SH = BS\cos\gamma = CS\cos\eta = BH\tan\gamma = CH\tan\eta.$$

Including equation 5.9 finally gives

$$\cos \eta = \frac{\cos \gamma \cos \delta + [(\cos^2 \delta + \sin^2\rho)(\cos^2\gamma - \sin^2\rho)]^{\frac{1}{2}}}{\sin^2\rho} \qquad 5.10$$

A check of this equation for $\varepsilon < 0$ confirms that it holds for general angles. Unfortunately, equation 5.10 does not give the sign of η because the cosine function is even. Examination of Fig. 5.14 shows that when $\eta = 0$, $\delta = \gamma$. If η is defined to be positive for positive azimuths (west of south) then $\delta < \gamma$, and $\eta < 0$ if $\delta > \gamma$.

A computer program was written to calculate η so that the dependence of η on different parameters could be examined. This program was later modified and used as a procedure to find η for individual echoes.

Fig. 5.19 shows the relationship between train orientation and the angular separation of the reflection points for a height of 100 km, a range of 350 km and a geographic azimuth, measured from geographic south (positive towards the west), of 22.5°. This relationship is nearly linear. A perpendicular train ($\eta = 0$) corresponds to a reflection point separation of $\sim 0.26^{\circ}$. The azimuth of 22.5° corresponds to that for an ideal field-aligned train and the offset in ε, ε_0, is due to the remote transmitter not being on the ideal locus of points calculated in the previous section. The variation of the offset ε_0 is shown in Fig 5.20 as a function of echo azimuth. The most common azimuths lie in the range $14^{\circ} < A < 31^{\circ}$ because most transmitted power was directed there to observe meteors where the specular condition $\mu = 0$ was met. This range of azimuths is shown in the figure. The change in ε_0 with azimuth means that the choice

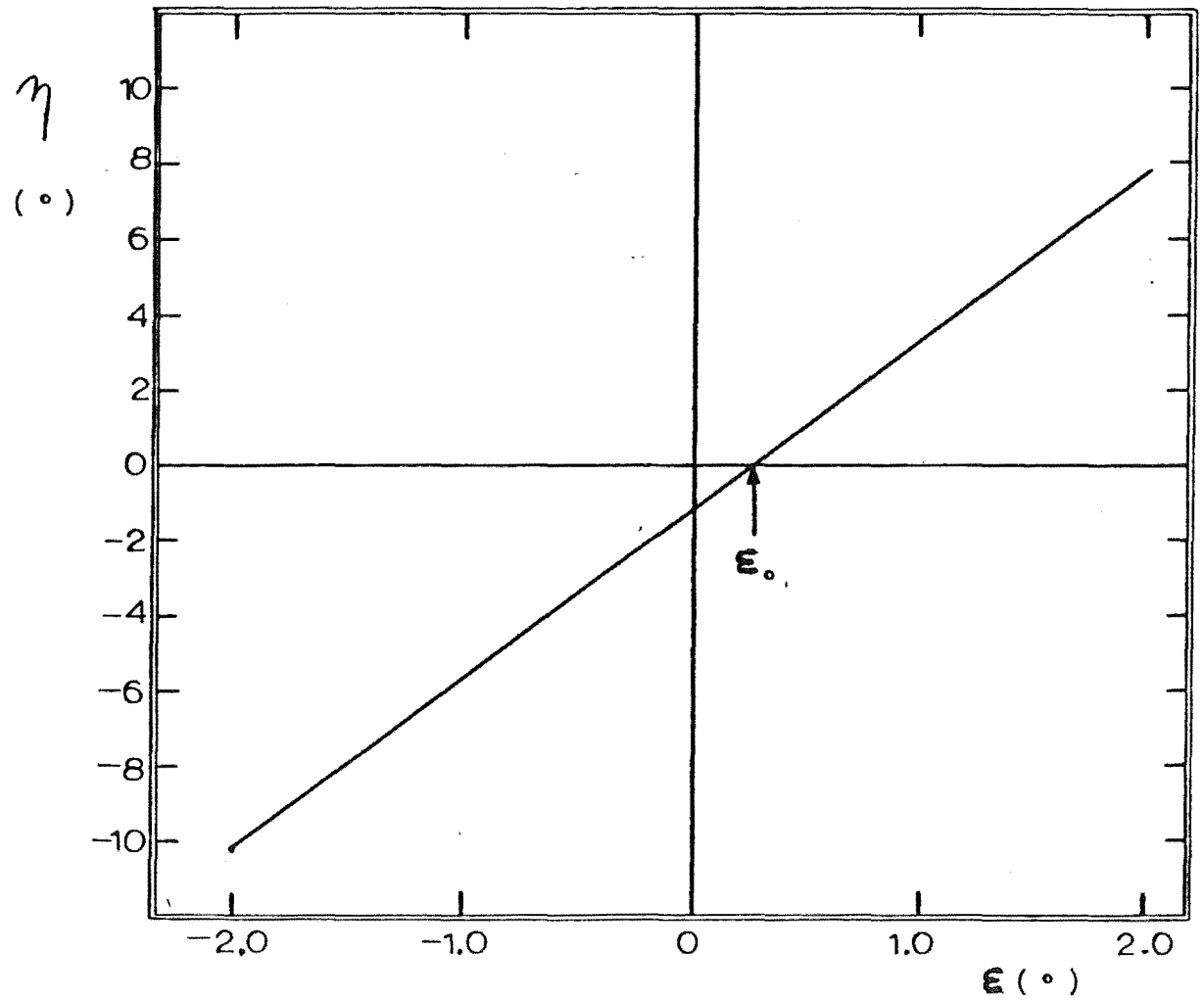

Figure 5.19: The dependence of train orientation on the angular separation of the reflection points for R = 350 km, h = 100 km, A = 22.5°.

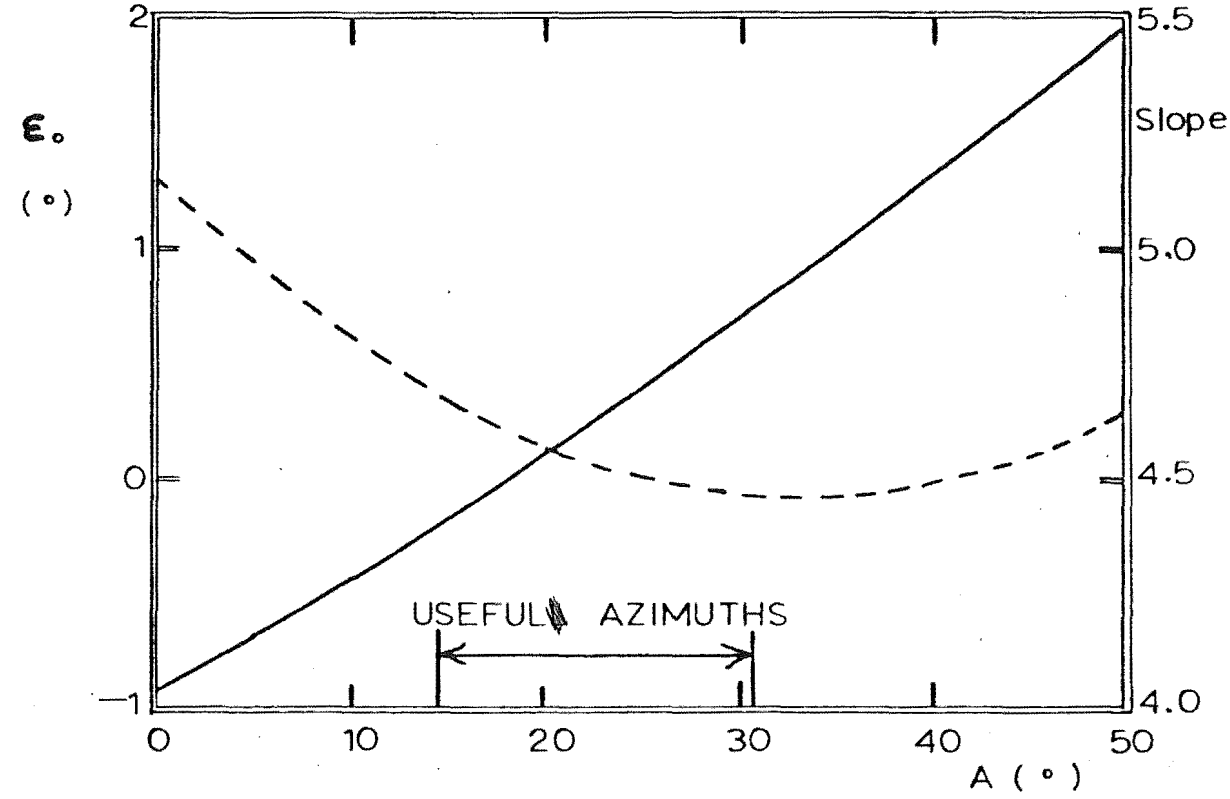

Figure 5.20: The dependence of ε_0 (——) and slope (---) on the azimuth of the reflection point.

of the remote transmitter site was not critical - trains with $\eta > 0$ will not be discriminated against as strongly as Fig. 5.19 might suggest.

The slope of the line in Fig. 5.19 is inversely related to the angular resolution of the system. The dependence of this slope on azimuth is also shown in Fig. 5.20. There is a broad maximum in resolution, for the fixed baseline, at 33^{o}. This corresponds to the maximum forward-scatter angle when both transmitters are symmetrically situated with respect to the reflection point. The change in resolution over the useful azimuth range is not important.

(3) Inclination to the Earth's Magnetic Field

The aim of this sub-section is to relate the angle, η, at which a train is inclined to the perpendicular train to the angle between the train and the field direction, α.

In Fig. 5.21 MPLN is a plane tangent to the earth's surface at point P. S is the backscatter reflection point; SM is the direction to the receiving site (note that M is not the site location); SL is a perpendicular train and SN is a train at an angle η to the perpendicular train. The angles e and η define the angles ν and $\mathcal{H}$. By use of all triangles in Fig. 5.21 these angles are related by

$$\sin \nu = \cos \eta \sin e \qquad 5.11$$

and

$$\cos \mathcal{H} = \cos \eta \cos e / \cos \nu. \qquad 5.12$$

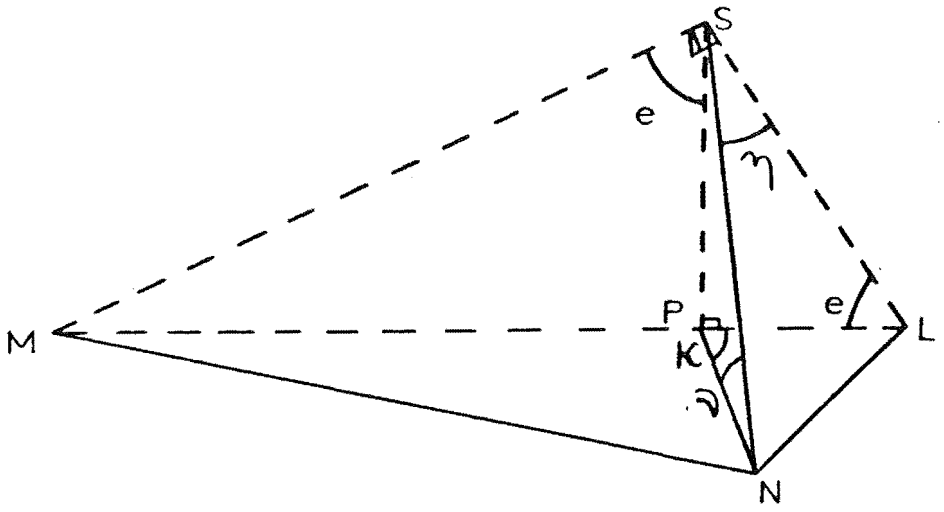

Figure 5.21

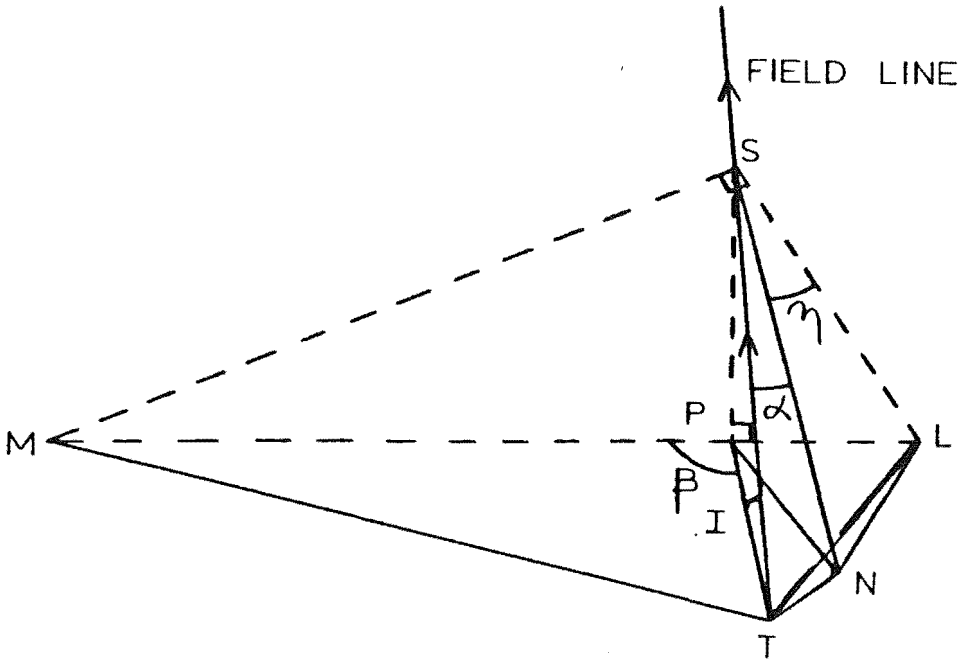

Figure 5.22: Train orientation with respect to the geomagnetic field

Fig. 5.22 is the same as Fig. 5.21 except that the field direction ST has been added. The required angle, α, is indicated and can be found by using the relations

$$NT^2 = PT^2 + NP^2 - 2.PT.NP \cos(180 - \beta - \mathcal{H})$$

$$= ST^2 + NS^2 - 2.ST.NS \cos \alpha$$

and

$$PS = PT \tan I = NP \tan \nu = ST \sin I = NS \sin \nu$$

which give

$$\cos \alpha = \sin I \sin \nu - \cos I \cos \nu \cos(\beta + \mathcal{H}). \qquad 5.13$$

Equation 5.13 requires that $\mathcal{H} < 0$ if $\eta < 0$ which is not true for $\mathcal{H}$ found from equation 5.12 and so must be evaluated carefully during analysis.

Equation 5.13 enables α to be found for individual echoes by using the procedures developed in section 5.1 and sub-section (2).

5.4 METEOR SHOWER DIRECTIONS

Watkins et al. (1971) used the Geminid shower meteors to see if there was any observable geomagnetic effect on underdense meteor rates and durations for $\alpha = 0$. Unlike their system, the present system can measure train orientation so that sporadic meteors can be employed for this purpose. However, if a shower meteors were field aligned this would greatly enhance the number of meteors observed by both transmitters and so

shower periods would be a very fruitful time in which to record data.

Fig. 5.23 is a view of the celestial hemisphere centered on the receiving site and viewed from the west. The transmitter beam is shown as well as a great circle path on the celestial sphere at right angles to the transmitter beam. A meteor must have its radiant point in this area to be observed by the backscatter system. The path of a perpendicular train (in the sense used here) is also shown. This train will be field-aligned for A = 22.5^{o} (when $\beta = 180^{o}$). Fig 5.24 is the same celestial hemisphere viewed from the east. The radiant point may be located from the great circle triangle formed by the South Celestial Pole (S.C.P.), the zenith and the radiant point. The sides of this triangle are: the colatitude of the receiving site ($90^{o}-\phi$); the co-declination of the radiant point ($90^{o}-\delta$) and the transmitter beam elevation, E. The declination of the radiant point, δ, can be related to the other known quantities by

$$\sin \delta = \sin \phi \cos E - \cos \phi \sin E \cos A \qquad 5.14$$

and the hour angle of the radiant point, H, can be found from

$$\sin H = \sin A \sin E/\cos \delta. \qquad 5.15$$

For an elevation of 16^{o} at the Rolleston site and in the

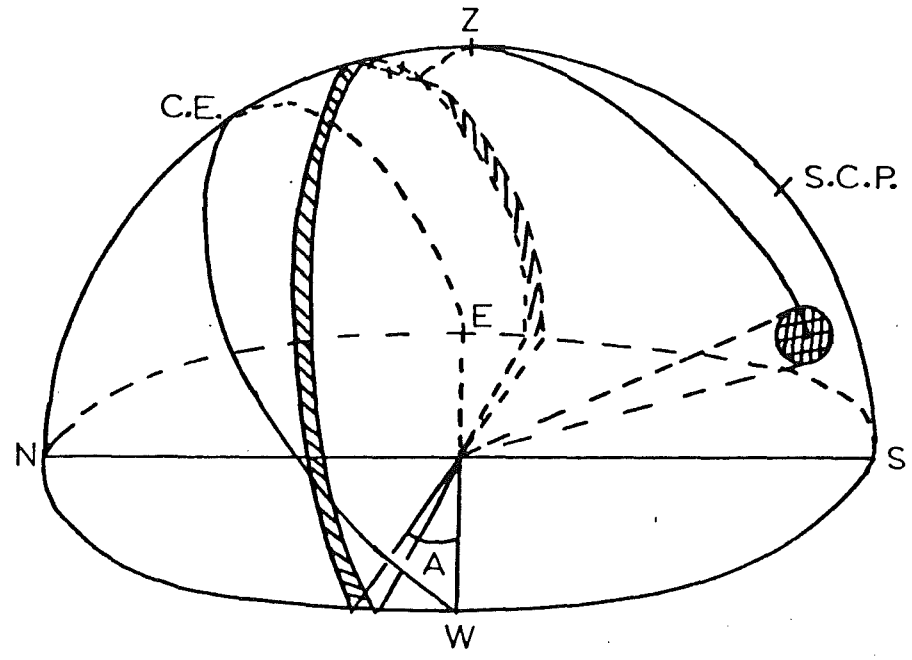

Figure 5.23: Celestial hemisphere viewed from the west with a perpendicular train

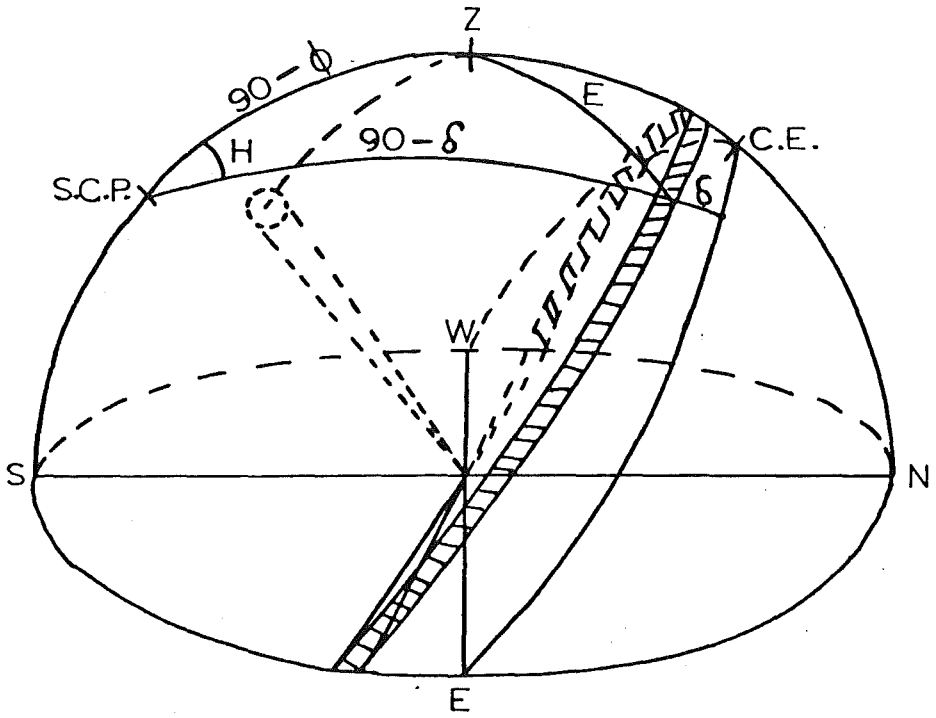

Figure 5.24: The celestial hemisphere from the east

magnetic south direction the results are

$$\delta = 28.6 \pm 0.6^{o}S$$

$$H = 7 \pm 2^{o}$$

where the uncertainties indicate the range of δ and H for the azimuth range of 8^{o}.

Ellyett et al. (1961) have identified the main southern hemisphere meteor showers. Two of these showers occur near the required declination and their relevant details are given in Table 5.2.

Table 5.2: Meteor showers

Name	Declination	Right Ascension	Date
Pisces Australids	$27^{o}S$	331^{o}	July 21-26
Puppids	$28^{o}S$	320^{o}	July 25-30

To determine whether these showers are ever within $\pm 1.5^{o}$ of being field-aligned, δ and H were found for $\alpha = \pm 1.5^{o}$. Figs 5.25 and 5.26 are celestial hemispheres where the path of a meteor with $\alpha = 1.5^{o}$ is shown. The hour angle, H', and declination, δ', need to be found for this meteor. Fig. 5.27 shows part of the celestial hemisphere from Fig. 5.25. The lengths p and q and the angle r can be found in terms of E, ϕ and A. Fig. 5.27 shows a triangle from Fig. 5.26. Knowing p,q and r, the hour angle and declination can now be found.

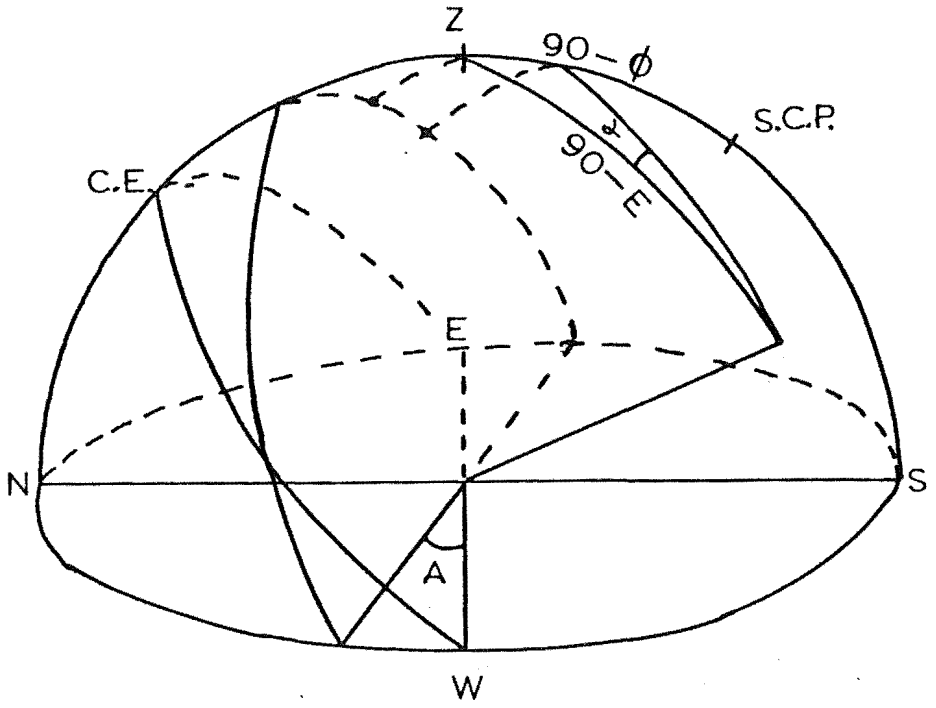

Figure 5.25: Celestial hemisphere with a field-aligned train and a train at an angle α

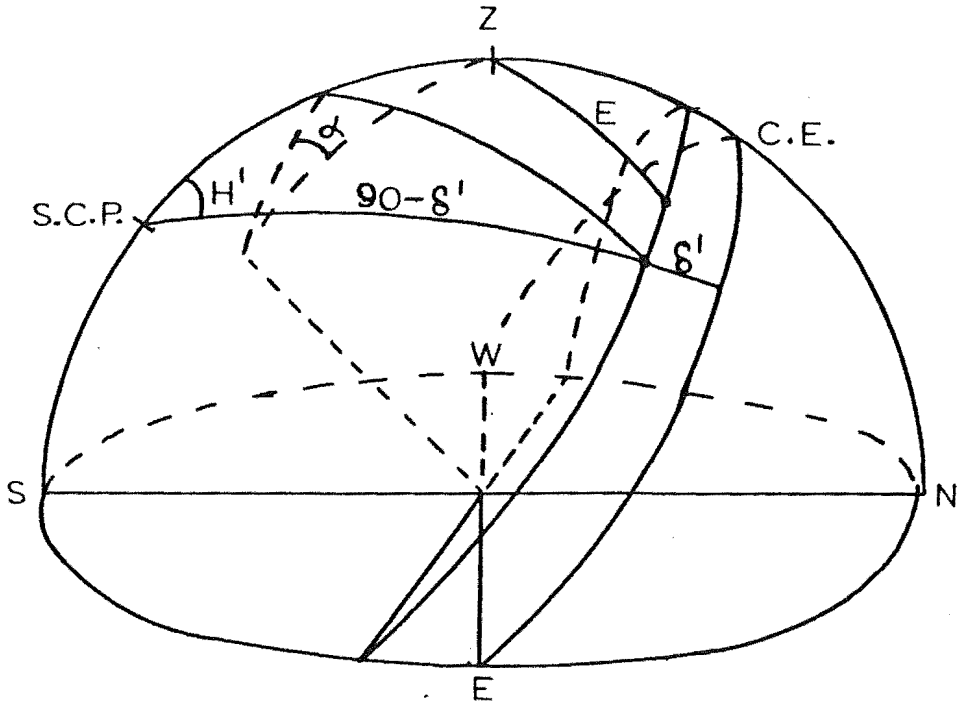

Figure 5.26: The same celestial hemisphere as above, viewed from the east

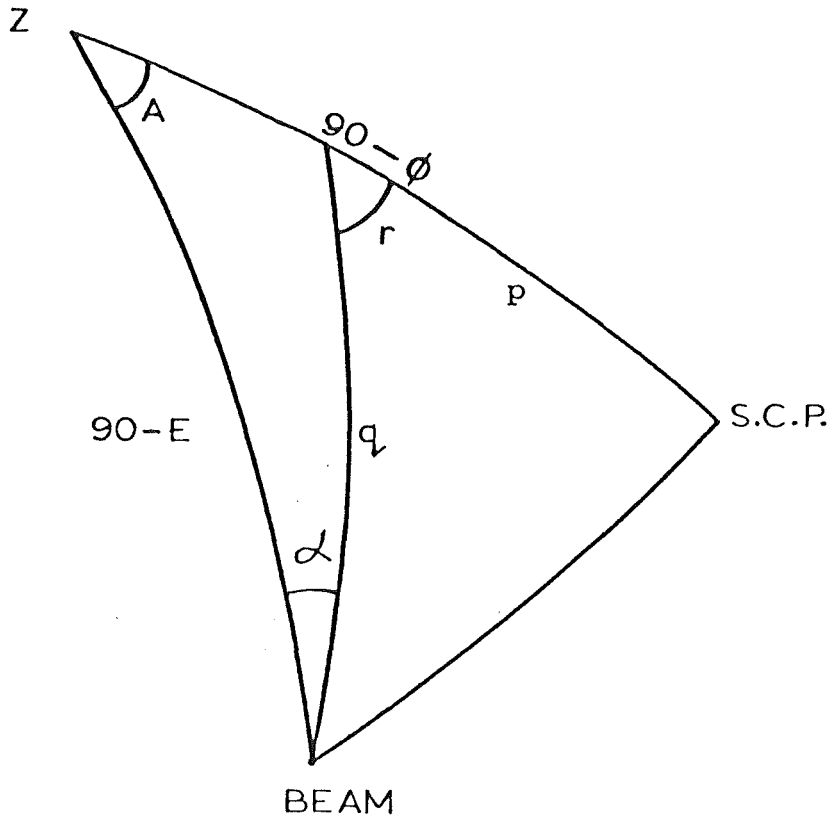

Figure 5.27

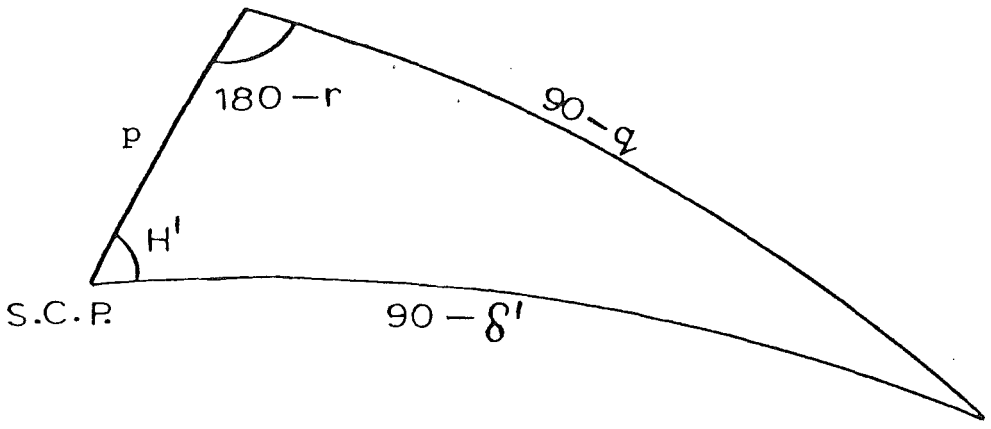

Figure 5.28

For

$\alpha = +1.5^{o}$ $\delta' = 28.1^{o}S$ $H' = 5.3^{o}$

and

$\alpha = -1.5^{o}$ $\delta' = 29.1^{o}S$ $H' = 8.5^{o}$.

It thus appears that Pisces Australids will not quite reach the field-aligned orientation, but Puppids probably will. Ideally, corrections need to be made for the earth's rotation and for gravitational attraction. Furthermore, there is a spread of radiant points in a given shower of up to ten degrees (Lovell, 1954). This spread depends on the age of the particular shower.

It is now useful to calculate the time at which the Puppid shower meteors will be field-aligned. This time is 28 minutes (7^{o}) before the transit of the shower radiant point. The field-aligned time was then found to be 0108 hours New Zealand Standard Time on July 25 and 0048 hours on July 30.

This shower is not very strong in comparison with the major showers and there may be little change to the mean sporadic rate. However, the number of field-aligned meteors at this time could be considerably higher than normal.

CHAPTER 6

SYSTEM DESIGN AND DESCRIPTION

6.1 INTRODUCTION

The radar system uses two pulsed transmitters operating at 26.36 MHz and an interferometer which consists of three receivers and a data processing system. Apart from the remote transmitter which is located on the West Coast and was mentioned in Section 5.2, this system was used and described by Poulter (1978). Some modifications have been made to enable two transmitters to be used and the nature of the problem meant that a different interferometer design was desirable.

In this chapter the transmitters and their respective transmitting antennas are described. The interferometer is also described and factors considered in its design and tests of its performance are presented. Finally, modifications to the data processing system are described.

6.2 THE REMOTE STATION

(1) The Transmitter

A 27.12 MHz pulsed transmitter, housed in a caravan, was available in the department for the experiment. This was retuned to the operating frequency of 26.36 MHz. A crystal for this frequency was added to the Colpitts oscillator in the first stage to improve the frequency stability.

Frequency stability was very important because changes in frequency would lead to changes in the phase measured by the receiving equipment. This is probably caused by an extra i.f. amplifier in the reference channel of the equipment. The transmitter frequency was measured over the temperature range 10 to 40°C and was found to vary by 400 Hz, however, the maximum variation after the transmitter had warmed-up was less than 100 Hz, even with ambient temperature variations of 10°C. The corresponding height error due to errors in measured phases is ≈ 25 m which was considered to be satisfactory in that it was much smaller than expected measurement uncertainties. Thus there was no need to enclose the crystal in a temperature-controlled oven.

A pulse repetition frequency (P.R.F.) of 150 Hz was used as this enabled the backscattered and forward-scattered signals to be distinguished unambiguously at the receivers. It was necessary to trigger both transmitters with a constant time difference for the received pulses to be distinguished. This was achieved by timing the triggering of both transmitters from the 50 Hz national mains power supply. The electricity supply throughout the South Island of New Zealand is on a common grid so that the phase difference between the supply at Rolleston and that at the remote site should be constant. The timing of the local transmitter could be adjusted so that each transmitter was triggered at a suitable moment.

Initially, the P.R.F. was locked to the mains supply by a phase locked loop that also tripled the frequency to 150 Hz. This smoothed out short-term variations in the

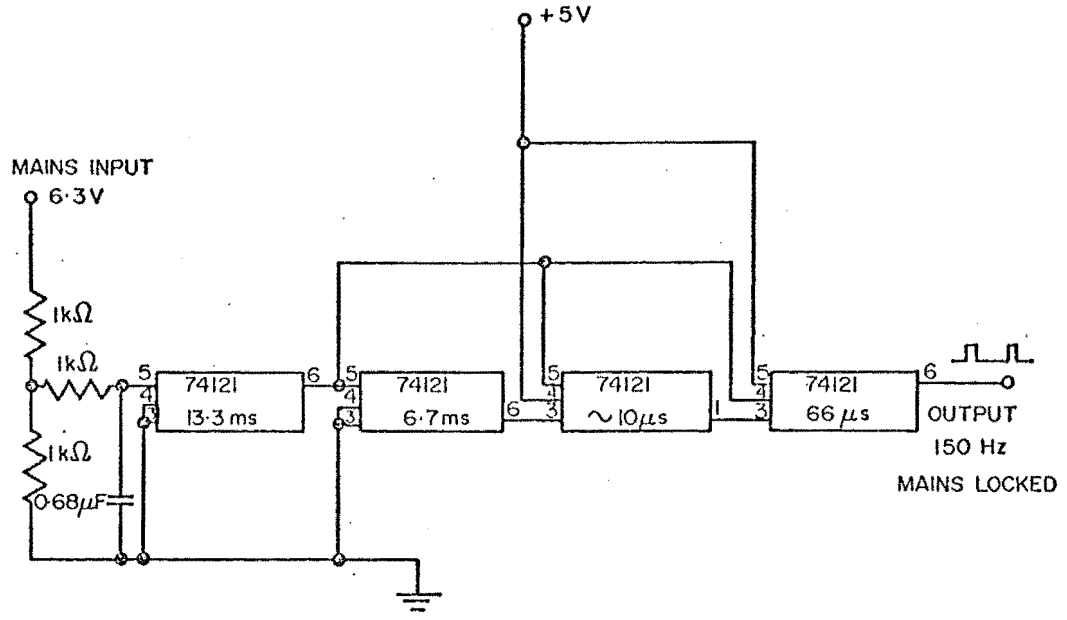

Figure 6.1: Mains locked transmitter trigger.

mains frequency. Unfortunately, this system was very susceptible to noise on the input which caused it to loose the lock with the mains frequency temporarily. It was replaced with the circuit shown in Fig 6.1 which consists, basically, of four monostable multivibrators. The input to the first monostable is a schmitt trigger, so that this monostable is triggered off the same point on each mains cycle. The first two monostables are timed accurately to 13.3 and 6.7 ms respectively. Their outputs are combined in the last two monostables to give a final output of rectangular ~~square~~ pulses of adjustable length at 150 Hz locked to the mains frequency. A pulse width of 66 μs was used to agree with the local transmitter, giving a duty cycle of 1%.

The triggering circuit worked well. The drift in the monostable timing was of the order of a few tens of micro-seconds. A larger effect, caused by variations in the mains frequency was a jitter between pulses of up to 80 μs. Such jitter prevents an accurate range measurement from being made on the forward-scattered signal, but this was not necessary for determining train orientation (see section 5.3). For small separations of the reflection points the difference in ranges is very small anyway. The jitter of 80 μs did not create any difficulties in receiving the two signals as timing variations due to the different echo ranges are as large as 3 ms.

A drift with a period of hours in the relative timing between the transmitters was also noticed which was up to 300 μs in length, but could be corrected by the operator. The adjustment was easily made during persistent echoes received from both transmitters, but could also be made, with more difficulty, on underdense decays. This slow drift may have been caused by variations in the phase difference between the mains at each transmitter site as loading conditions changed. The drift was not observed when both transmitters were operated from the same site; it tended to be in the same direction at the same time each day and it did not usually begin until about 0700 hours. These facts suggest that changes in the mains phase between Rolleston and the remote site are the origin of the drift.

Some of the remote transmitter's power supplies were rebuilt to give more reliable operation at the remote site.

These included the high voltage supply for the last amplifier in the driver stage and the bias supply for the screen of the valve in the final amplifier. A defective winding of the transformer for the final amplifier high voltage supply was replaced with a new winding. The new winding had been designed to produce half of the original voltage so that a voltage doubler was needed in the final power supply circuit. The original 866A rectifier valves were replaced with stacks of fifteen IN 4007 solid-state diodes along with suitable parallel resistors and capacitors to compensate for the different characteristics of the individual diodes.

A controller was built by a technician in the Department of Physics to enable the transmitter to be switched on and off with a time switch. This meant that the transmitter could be left unattended for long periods. Because of some initial warm-up problems, the valve heaters were wired so thatthey were on continuously. The controller turned on the bias supplies, the driver high voltage supply and the final amplifier high voltage supply in separate stages. There was a pause of about one minute between each stage. There were two fault detectors: a current overload in the final amplifier high voltage supply and a r.f. detector. If a fault was detected the controller would switch off the high voltage supply for one minute before trying again. This would be repeated up to a maximum of twice and then, if the fault was still present, the high voltage supplies to both the driver and final amplifier were switched off. The time clock was set so that the transmitter would stop and restart in

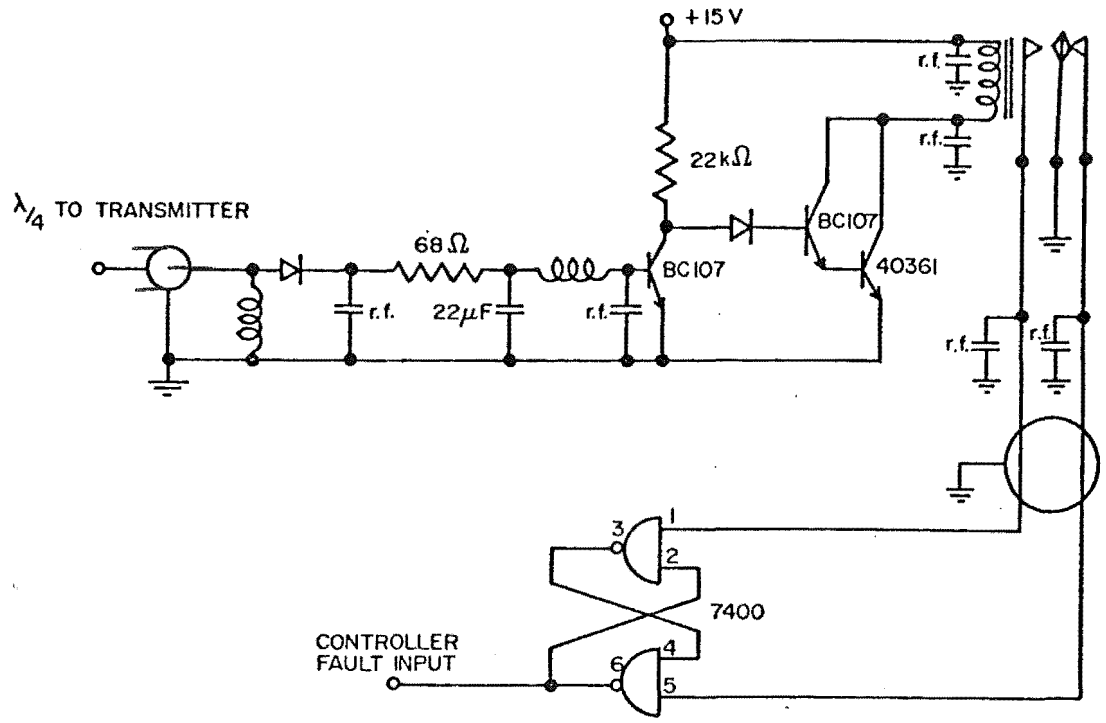

Figure 6.2: The r.f. detector

the middle of each run as a precaution against the transmitter stopping if more than three faults had occurred during the first part of the run.

The circuit for the r.f. fault detector is shown in Fig. 6.2. The detector was mounted at the end of a quarter -wavelength of coaxial cable connected to the transmitter output and would indicate a fault (by a low level at the controller) if no r.f. signal was present after the final screen supply was turned on (this supply was switched with the final amplifier high voltage supply). The termination of the quarter-wavelength was one turn of wire which was effectively a short-circuit

so that the end at the transmitter was effectively an open circuit thus ensuring no loading of the transmitter output. A relay was included to reduce the amount of r.f. signal entering the controller. This r.f. signal interfered with the switching logic in the controller at times. The two NAND gates (7400) acted as a flip-flop so that the noise from the relay contacts was also prevented from entering the controller circuits.

The final amplifier used a single English Electric C1149 pulse tetrode that was biased off and was driven by the pulses from the driver. The peak output power was estimated from the average power input to the final amplifier to be 10 kW. The output from the final amplifier was unbalanced, enabling the r.f. detector to be coupled through a coaxial cable. The power was fed to the antenna through a 50Ω impedance coaxial cable as far as the wall of the caravan in which the transmitter was housed. A 4:1 impedance step-up balun was then used to connect with an open-wire line which was connected by a quarter-wavelength matching section to the antenna.

(2) The Antenna

The choice of a suitable antenna was influenced by two factors: the power gain necessary to give the overall system enough sensitivity to record underdense meteors and the need for an easily transported antenna that was not difficult to erect. A yagi antenna or a stack of several yagi antennas would not be suitable because of their

weight and complexity (a pole is needed to support each element).

The non-resonant rhombic antenna was considered to be suitable because of its power gain, light weight and simplicity of construction. It is basically a long-wire antenna. The main lobe voltage pattern for a long wire is shown on one leg of the rhombic in Fig. 6.3. As the leg length is increased, the main lobe directions become closer to the wire direction. By choosing a particular half apex angle, ψ, the lobes not in the direction of propagation and on opposite sides of the rhombic cancel. This ideally leaves only the forward and back lobes. In practice, the long-wire radiation pattern is not so simple and the cancellation is not complete, leaving many side lobes. If the forward end of the rhombic is terminated by a suitably matched resistor, no transmitted power is reflected from that end. This termination procedure, in the ideal case, removes the back lobe.

As plenty of space was available at the remote transmitting site a design for maximum output was used. The method of Bruce et al. (1935) was followed in the design. For maximum gain, the desired wave angle (that is, the elevation angle at which maximum gain is desired) is equal to the angle ψ in Fig. 6.3. In this case the desired wave angle is 16^{o}. The length of each leg, l, is then

$$l = \frac{\lambda}{2 \sin^2 \psi}$$

$$= 6.58\lambda \text{ for } \psi = 16^{o} \quad .$$

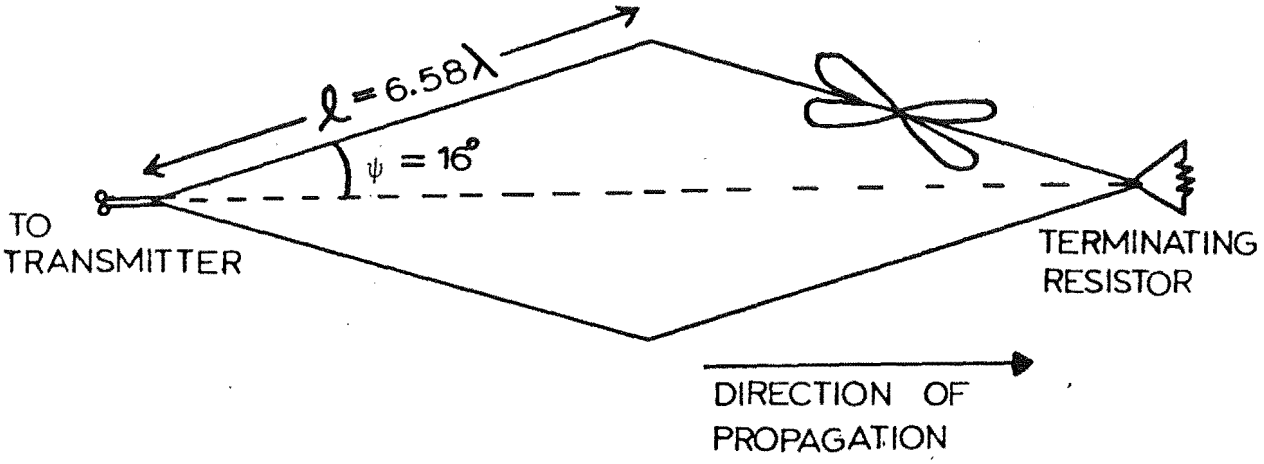

Figure 6.3: The rhombic antenna

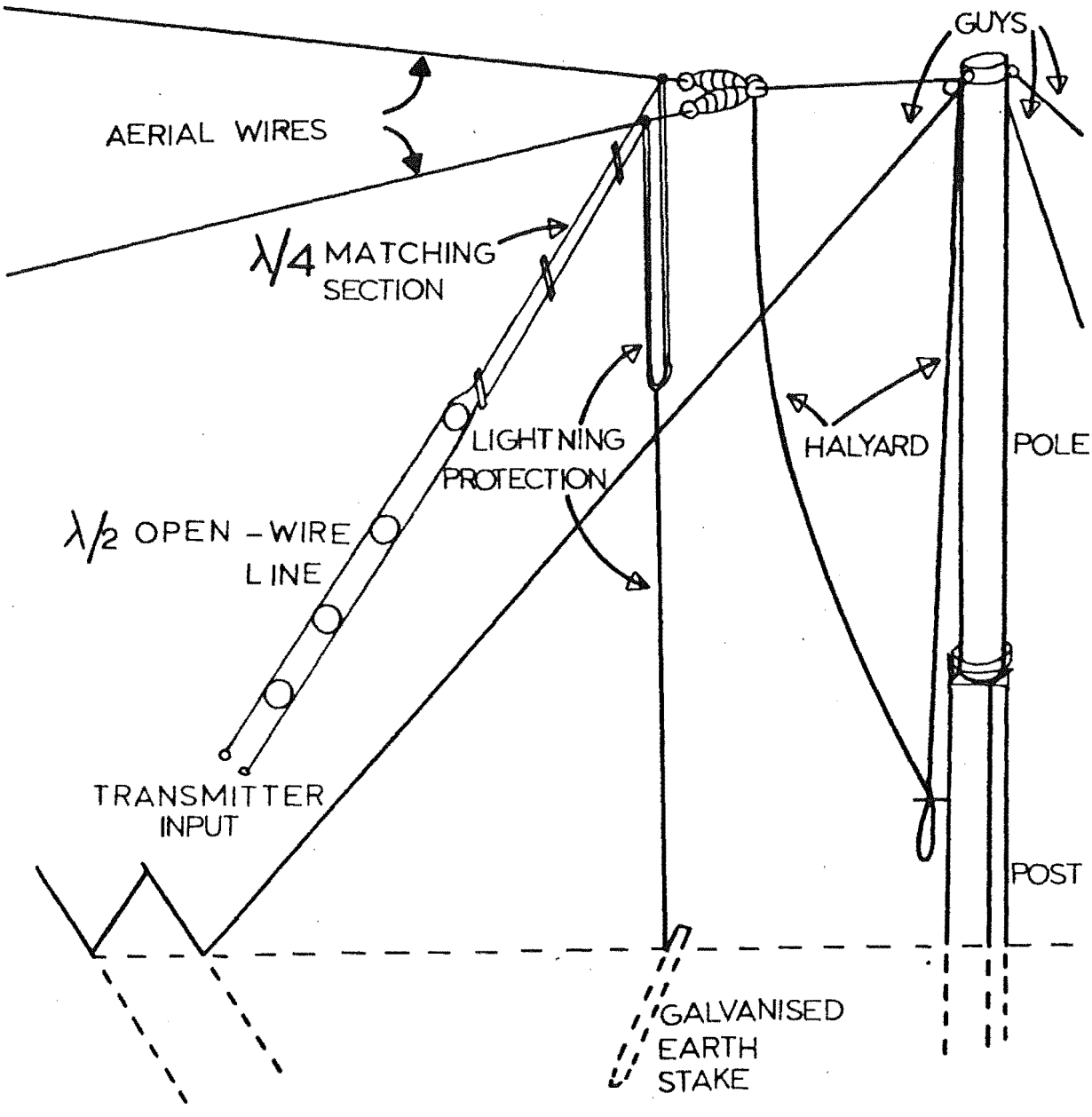

Figure 6.4: Construction and feed arrangements for the rhombic.

The height of the antenna above the ground, H, is then given by

$$H = \frac{\lambda}{4 \sin \psi}$$

$$= 0.91 \lambda$$

$$= 10.3 \text{ m for } \lambda = 11.38 \text{ m.}$$

The final rhombic design used is shown in Fig. 6.3. It is interesting to note that although this antenna will give the maximum power possible at a wave angle of 16^{o}, its maximum gain is not at 16^{o}. It will have more gain at a wave angle slightly greater than this. A design having maximum gain at 16^{o} would have less gain at 16^{o} than the design shown.

Tables given by Bruce et al. (1935) indicate that this design will have a major side lobe at an angle of 17^{o} to the direction of propagation. Rhombic antennas can be designed to minimise side lobes at the expense of power gain, but it was considered more important to maximise the power gain in this case. The effect of side lobes in determining echo positions is considered in section 6.4.

The power gain of a non-resonant rhombic with a leg length of 6.58 wavelengths was estimated from the A.R.R.L. Handbook (1970) to be 14 dB relative to a half-wavelength dipole in free space. This includes the effect of power loss in the termination. The power gain, relative to an isotropic radiator, for a rhombic antenna above ground of good conductivity is then about 22 dB.

This power gain could be increased further by using more than one antenna in an array. The physical size of the rhombic means that the smallest centre separation (by sharing a supporting pole) is 3.8λ. The array factor for two antennas, fed in phase, with this separation will have a null at 7.6^{o}. The half power beamwidth of the single rhombic is, from measurements, $\pm\ 7^{o}$. This means that the already narrow beam would be narrowed further if an array of two rhombics were used. Not much would be achieved by using an array because of the fine structured beams that would result. The simple feed arrangements for single antennas are also clearly an advantage.

The system sensitivity can be estimated from the aerial gains and other known quantities. For forward-scatter, the received power (expressed in watts) is given by McKinley (1961) to be

$$P_R = 5 \times 10^{-32} \frac{P_T\ G_T\ G_R\ \lambda^3\ q^2\ \sin^2\gamma}{R_1\ R_2 (R_1+R_2)(1-\sin^2\phi\ \cos^2\beta)} \qquad 6.1$$

where P_T is the transmitter power, G_T and G_R are the transmitting and receiving antenna power gains, q is the electron line density, γ is the angle between the electric vector of the wave incident on the train and the line of sight to the receiver, R_1 and R_2 are the forward-scatter ranges, ϕ is the forward-scatter angle (half of the angle between the lines of site to the receiver and transmitter) and β is the angle between the train and the phase of propagation of the radio waves.

For the geometry of this experiment typical values are

$\gamma = 62^{o}$, $\phi = 14^{o}$, $\beta \geqslant 85^{o}$, $R_1 = 3.3 \times 10^{5}$m,
$R_2 = 3.6 \times 10^{5}$m.

The recieving antennas have a power gain of 20 db relative to an isotropic radiator (see section 6.4) so that

$$P_R = 1.11 \times 10^{-37} q^2 \quad .$$

The minimum measurable echo has a peak amplitude of 8μV which, with a receiver input impedance of 50Ω, gives a minimum detectable line density of

$$q = 3.4 \times 10^{12} \ m^{-1} \quad .$$

This appears to be a satisfactory sensitivity since it is nearly six times less than the line density where measured diffusion coefficients start to become affected by q (2×10^{13} m^{-1}).

Four 7.6m aluminium pipes of about 10 cm diameter were used as the supporting poles for the rhombic. To obtain the optimum height these were placed on wooden posts which were buried so that their tops were 2.7 m above the surface and so that they provided a firm base for the aluminium poles. The aluminium poles sat in metal rings on the wooden posts (see Fig 6.4) and were each supported by three nylon guy ropes. These ropes were fastened to

pairs of metal fencing standards. Pairs of standards were necessary as single standards could work loose. The antenna proved very convenient and could be erected by one person.

The terminating resistor for a rhombic antenna needs to be about 800 Ω for optimum operation (A.R.R.L., 1970). The termination was made from sixteen pairs of 100 Ω, 2 W carbon resistors connected in series. This gave a rated power of nearly two thirds of the average transmitter power output - a factor of two greater than the power to be dissipated. The resistors were housed in a "tufnol" container that was suspended from the halyard and connected directly to the end of the antenna. This container was open at the bottom to prevent a build-up of moisture. Some signs of overheating were observed because the resistors were enclosed, but this was not serious. Measurements with an admittance bridge showed the termination to have a resistance of 813 Ω and a capacitance of 0.7 pF at 26.36 MHz.

Bridge measurements on the input to the antenna showed that it had a resistance of 700 Ω and a capacitance of 1.5 pF at the operating frequency. The balanced output from the transmitter had a 200 Ω impedance (after the 4:1 impedance step-up balun) and a quarter-wavelength matching section was used to match the two. This was constructed of two parallel lengths of 6.4 mm brass tubing held 7 cm apart with "tufnol" spacers and had an impedance of 370 Ω. The matching section was suspended from the antenna and was connected to the transmitter caravan with a half-wavelength of open wire line (see Fig. 6.4).

Final matching was achieved inside the caravan by using two capacitive matching stubs of coaxial cable, connected to the ends of the open wire line. These were trimmed until the line was purely resistive when measured by the r.f. bridge.

Some protection against lightning was provided by two half-wavelength pieces of 12 mm aluminium tubing. These were bent into "u" shapes and were trimmed so that an open circuit was measured at the open end of each. One of these sections was connected to each end of the aerial and a copper wire was run from the base of each to an earthing stake. These sections were installed on the advice of the local electricity supply authority who experienced problems with lightning every spring. The transmitter suffered no damage from lightning during its operation.

The antenna was first erected at the Rolleston field station so that the system could be tested. A check was made of the radiation pattern at this time. A continuous wave (C.W.) transmitter was placed in a van to which was attached a telescopic pole that was raised and lowered with compressed air. A half-wave dipole mounted on top of this pole served as the antenna for the test transmitter. The van was driven to known locations and the transmitter was operated while measurements were made on the signal received by the rhombic antenna.

Kraus (1950) gives the expression

$$r \geqslant \frac{2a^2}{\lambda}$$

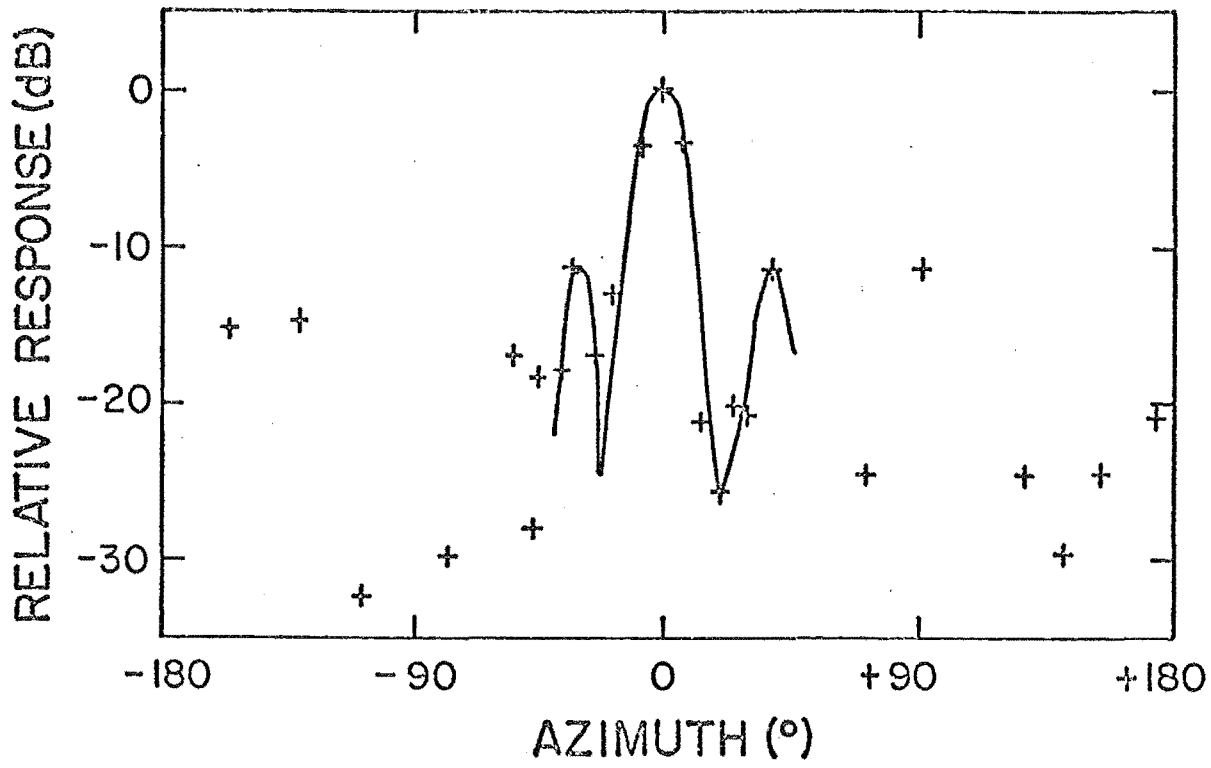

Figure 6.5: The rhombic radiation pattern.

for estimating the minimum distance, r, of a test transmitter from an antenna in order to measure the true far-field radiation pattern. a is the maximum antenna dimension as viewed from the test direction. For the rhombic

$$r \geqslant 3.3 \text{ km}$$

for the most unfavourable angle of 90° to the main beam.

The signal measurements were made with the reference receiver described in section 6.4. The receiver video output was measured with an oscilloscope. The van location was then used to find the relative azimuth angle and distance of the test transmitter so that the antenna radiation pattern could be constructed.

Fig. 6.5 shows the results. The azimuth angles are relative to the expected propagation direction. The points

are not close enough to resolve the fine structure of the side lobes, but the main beam and nearest side lobes have been outlined.

The condition for r was met for most azimuths except those near $\pm$ 90°. This may have caused the large amplitude observed at A $\approx$ + 90°. The front to back ratio is about 20 dB which shows that the terminating resistor is effective. All side lobes are at least 10 dB below the main lobe. The half-power beamwidth is 14°.

The antenna was orientated at the remote site with a theodolite. Two methods were used. A theodolite compass, together with the known magnetic declination for the site, was used to align the antenna 2° east of geographic south. This direction was calculated (from the angle $\hat{DWS}$ in Fig. 5.13) to give a volume of intersection with the local transmitter beam that was in the specular reflection region. This alignment was then checked by measuring the angle to a known landmark. The measurements agreed within the estimated uncertainty of 0.2°.

6.3 THE LOCAL RADAR

(1) The Transmitter

The local transmitter has been described by Wilkinson (1973) and Poulter (1978) and is not described again in detail here. It is a pulse transmitter with a peak power of about 40 kW. The final amplifier uses four English Electric C1149 pulse tetrodes and has a balanced output with an

impedance of 600 Ω.

The frequency of 26.36 MHz is obtained by mixing the frequencies 24.74 MHz and 1.62 MHz produced by two crystal controlled oscillators. These oscillators also provide reference frequencies for the receivers so that the system is phase coherent. This phase coherence was originally needed for doppler measurements of meteor train drift, used to determine atmospheric winds. The temperature stability of the oscillator frequencies was checked. It was found that the higher frequency was 24.745 MHz. The oscillator could not be tuned to 24.740 MHz so a new crystal was obtained. This operated at 24.741 MHz in the original circuit, but stable operation at 24.740 MHz was obtained in the transistor oscillator shown in Fig. 6.6. A frequency change of 800 Hz was measured over the temperature range 21 to 34^{o}C. The maximum variation under stable conditions was 50 Hz. The corresponding variation for the 1.62 MHz oscillator was 20 Hz. During data recording runs, the valve heaters were always switched on at least thirty minutes before collecting results. Usually, this warm-up time was much greater.

The transmitter was triggered by pulses from the receiving equipment. A 66 μs pulse length was used and a P.R.F. of 150 Hz (mains locked) was used for the two-station operation. Later runs without the remote station were completed with a P.R.F. of 300 Hz. The transmitter cannot sustain a P.R.F. of 300 Hz at full power and so Poulter (1978) used a system that doubled the P.R.F. from 150 Hz for 0.8s when a

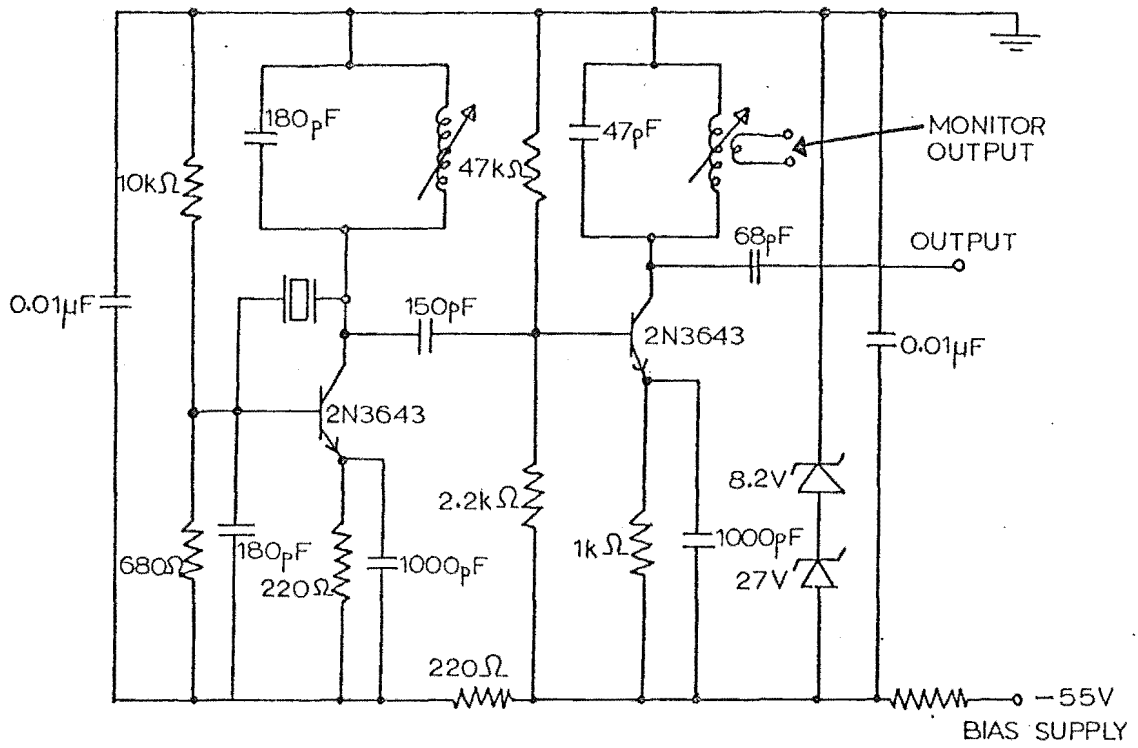

Figure 6.6: The 24.74 MHz transistor oscillator

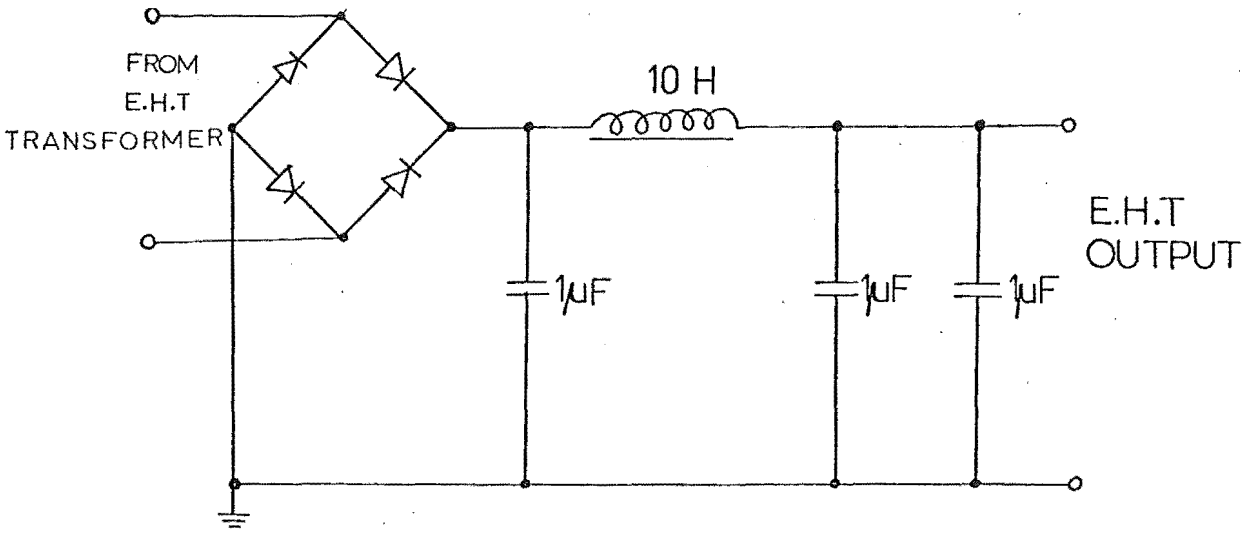

Figure 6.7: The final amplifier high voltage power supply

meteor was detected. Unfortunately, this caused the transmitter output power to decrease for fifteen pulses, due to the high voltage supply dropping before stabilising. This would affect diffusion coefficient measurements if these initial pulses were not excluded from the analysis.

This problem was corrected by replacing the original 5.4 kΩ resistor in the final amplifier high voltage supply with a 10 H inductor (see Fig. 6.7). As a check of the output power, stray radiation from the transmitter was displayed on an oscilloscope. This was photographed with a time exposure as the P.R.F. was doubled. The oscilloscope was used in a single sweep mode and was triggered by the logic signal that doubled the P.R.F. This means that the first pulse in the photograph was the first at 300 Hz and would also be the first recorded by the system.

The results are shown in Fig. 6.8 and Fig. 6.9. Fig. 6.8 was taken when the 5 kΩ resistor was shorted out of the circuit. The droop, although reduced, was still present. Also noticeable is a 50 Hz ripple which indicates that the filtering is inadequate. Problems were experienced with the rectifiers with this arrangement as they were not protected from short period current surges. Fig. 6.9 was taken with the 10H inductor in place. The small variations are probably due to changes in the stray radiation rather than changes in power output. No droop in the output power is noticeable.

A further check of the output power was made by triggering the system from aircraft echoes. Fig. 6.10 shows two such

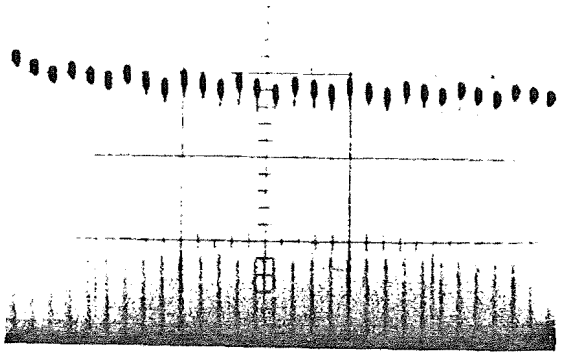

Figure 6.8: Transmitter output without 10H inductor

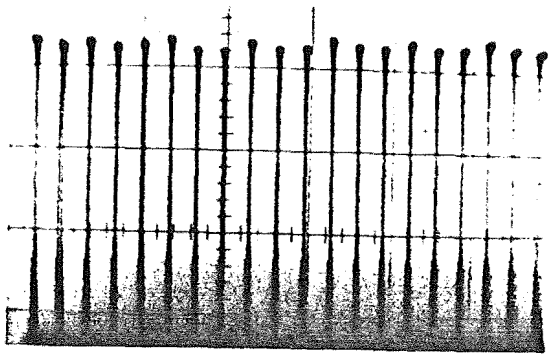

Figure 6.9: Transmitter output with 10H inductor in power supply

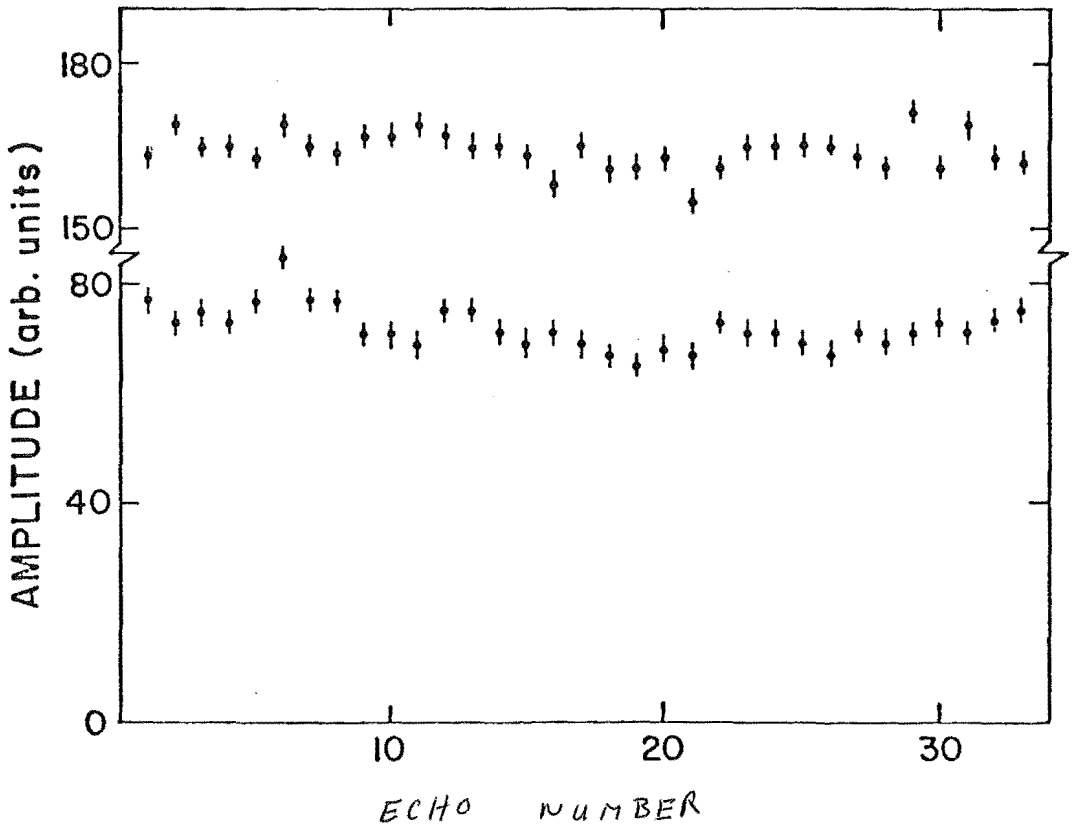

Figure 6.10: Aircraft echoes as a check of transmitter power output

echoes. The small variations in amplitude in this case may be accounted for by sky noise although some structure appears to be present. The uncertainty bars indicate the magnitude of the estimated sky noise at the time. The gradual reduction in received amplitude was due to the decreasing signal from the aircraft as it moved. The smaller echo was recorded 28 s after the larger one.

(2) The Transmitting Array

The eight element yagi antennas used by Poulter (1978), were available for the transmitting array. The need for a high gain antenna to increase the system sensitivity was mentioned in section 4.5. An array of four yagis fed in phase was used. Poulter made radiation pattern measurements on a single yagi: these were used to find the theoretical pattern for an array of four yagis. This was done by computer so that the effect of antenna spacing could be easily observed. The final radiation pattern for an array is the product of the individual antenna radiation pattern and the array factor. The ideal spacing of the antennas places nulls of the array factor on the maxima of antenna side lobes. A spacing of 1.5 wavelengths between each antenna was found to be most suitable. Fig. 6.11 shows the theoretical pattern for the array. Azimuth is measured from the expected propagation direction.

The transmitting array radiation pattern was measured in the region of the main beam by the method described in section 6.2. For this array the minimum distance of the

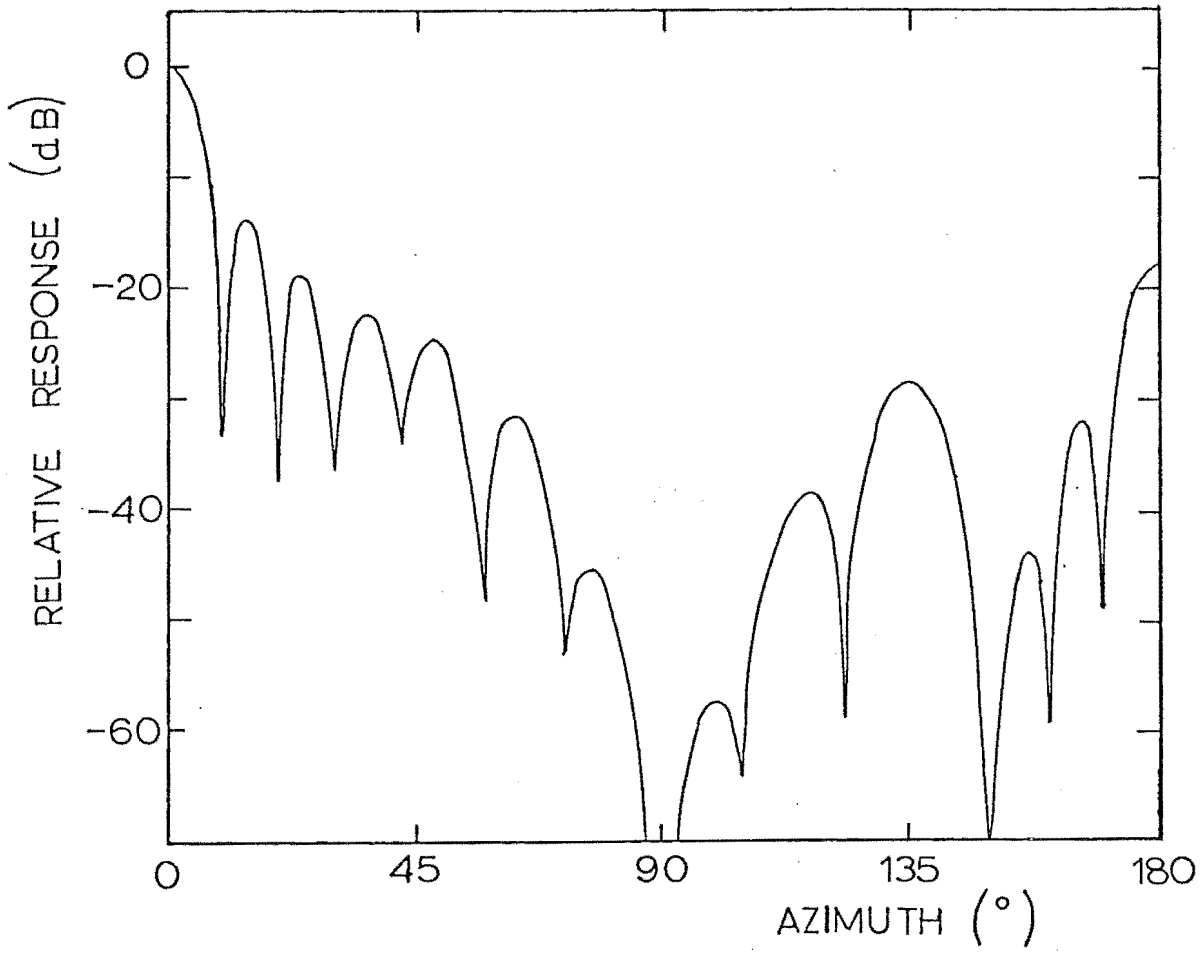

Figure 6.11: The theoretical radiation pattern for the transmitting array

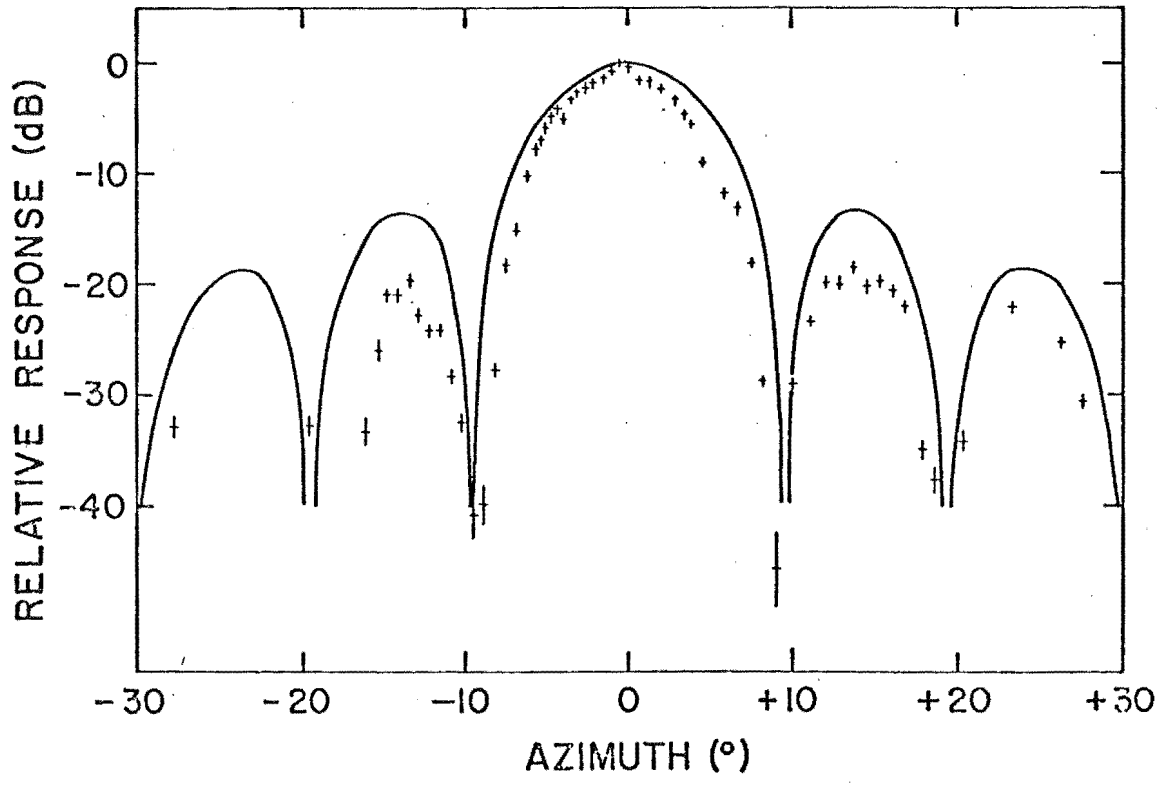

Figure 6.12: Theoretical and measured radiation patterns for the transmitting array.

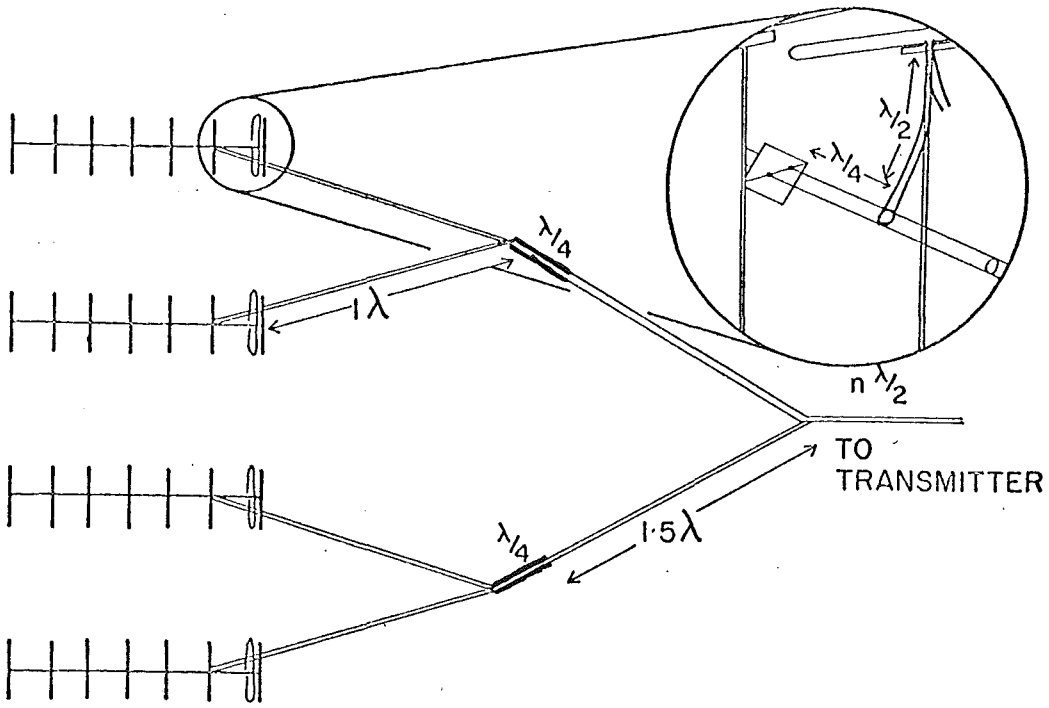

Figure 6.13: Transmitting array construction and feed arrangements.

test transmitter, r, is 570 m which was always exceeded. The theoretical and measured values are shown in Fig. 6.12. The beamwidth to the half-power points was 14^{o}.

The antennas were constructed in the way described by Poulter (1978). The feeding arrangements were also similar and are shown in Fig. 6.13. Each folded dipole was fed by two coaxial cables with an electrical length of one half of a wavelength. Capacitive matching stubs were used at each driven element to cancel the inductance of the element. These were trimmed to give a pure resistance at the end of the half-wavelength coaxial cables. These

cables were connected to an open wire line which was one wavelength long. The open wire lines were connected in pairs to quarter-wavelength matching sections. These were constructed from 12 mm diameter aluminium tubing and their spacing was adjustable. The necessary impedance transformation was from 100Ω (the input impedance of each antenna at 26.36 MHz was ~ 200Ω) to 1200Ω (so that the transmitter would "see" a 600Ω load). This meant a section impedance of about 330 Ω which was achieved with a tubing spacing of 10 cm.

The matching sections were connected by 1.5 wavelength open-wire lines. Before this connection was made, the sections were adjusted to have equal impedances to within $\pm$ 2%. A capacitance of ~ 2 pF was measured which was considered to be quite acceptable, thus eliminating the need for compensation with inductors.

The final connection to the transmitter was made with an open-wire line that was an integral number of half wavelengths long. The impedance of this line was about 550 Ω which meant that an arbitrary length would not give a good match.

The antennas were initially aligned by theodolite, the reference direction being obtained from a prominent landmark. The measurements of the antenna pattern (mentioned above) confirmed that it was orientated to within 0.5° of the desired direction. The reasonable agreement with the theoretical pattern confirms that the antenna phasing was correct.

The minimum detectable line density can be calculated in the same way as for the remote station. Equation 6.1 simplifies for backscatter because $\gamma = 90^{o}$, $\phi = 0^{o}$ and $R_1 = R_2$. For a minimum range of 330 km, the minimum detectable line density is

$$q = 8.8 \times 10^{11} \text{ m}^{-1} \quad .$$

This means tha the local station can theoretically detect a meteor with one quarter of the line density of that detected by the remote station.

6.4 RECEIVING AND DATA PROCESSING EQUIPMENT

(1) Interferometer Design

The interferometer consists of three spaced antennas (each an eight element yagi, horizontally polarized, with a gain of 20 dB over isotropic) positioned as shown in Fig. 6.14. The angles γ and β can be measured by comparing the phase of the radio waves recieved at antennas 2 and 3 with that at the reference antenna 1. These angles are related to the elevation, E, and azimuth, A, of the reflection point by (see Fig. 6.15)

$$\sin \gamma = \cos E \sin A \qquad 6.2$$

$$\cos \beta = \cos E \cos A \qquad 6.3$$

where A is measured relative to the line of antennas (1) and

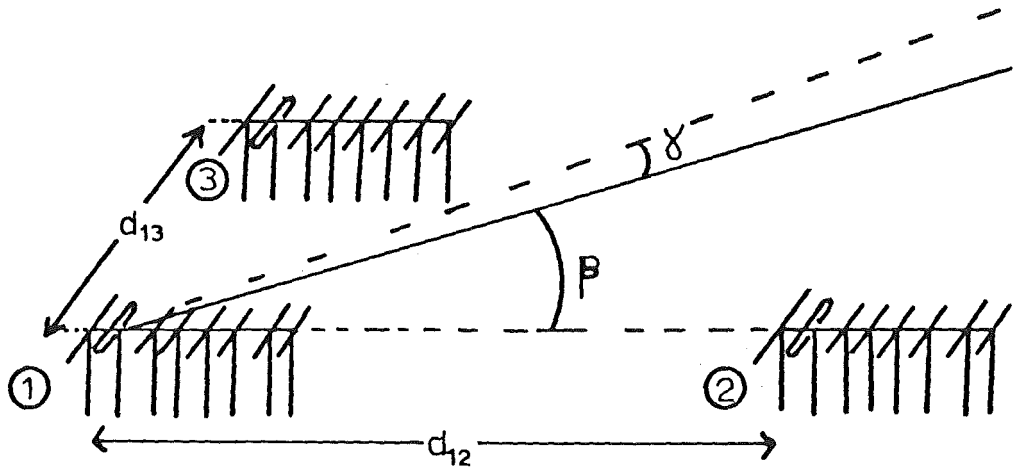

Figure 6.14: The interferometer layout

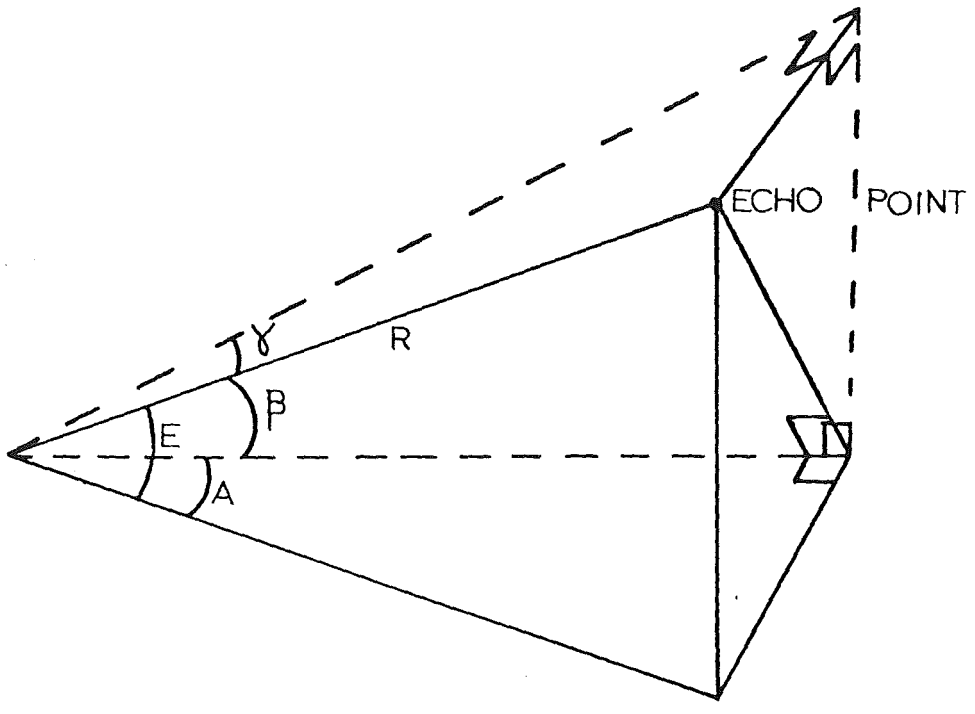

Figure 6.15: Angles measured by the interferometer

(2) and is positive to the west. If the echo range is also measured, the height of the reflection point can be found. In this sub-section the antenna spacings are calculated so that ambiguities in the echo location are largely avoided.

(a) The Spacing d_{13} The choice of d_{13} is a compromise: for small spacings mutual coupling between antennas could become important and the uncertainty in the angle measurement will be larger whereas with large spacings accuracy is improved, but echoes will not be located unambiguously.

The condition for no ambiguity in echo location is

$$\frac{2\pi d_{13}}{\lambda} (\sin \gamma_{max} - \sin \gamma_{min}) \leqslant 2\pi \quad .$$

For a range of positive and negative azimuths this reduces to

$$d_{13} \leqslant (2 \sin \gamma_{max})^{-1}$$

where d_{13} is expressed in units of a wavelength. Combining with equation 6.2 gives

$$d_{13} \leqslant (2[\cos E \sin A]_{max})^{-1} \quad .$$

The most unfavourable situation is then at low elevations and large azimuths. The lowest elevations encountered will be about 7^{o} (see the design of d_{12}). The aim now is to find the smallest necessary unambiguous azimuth range. The

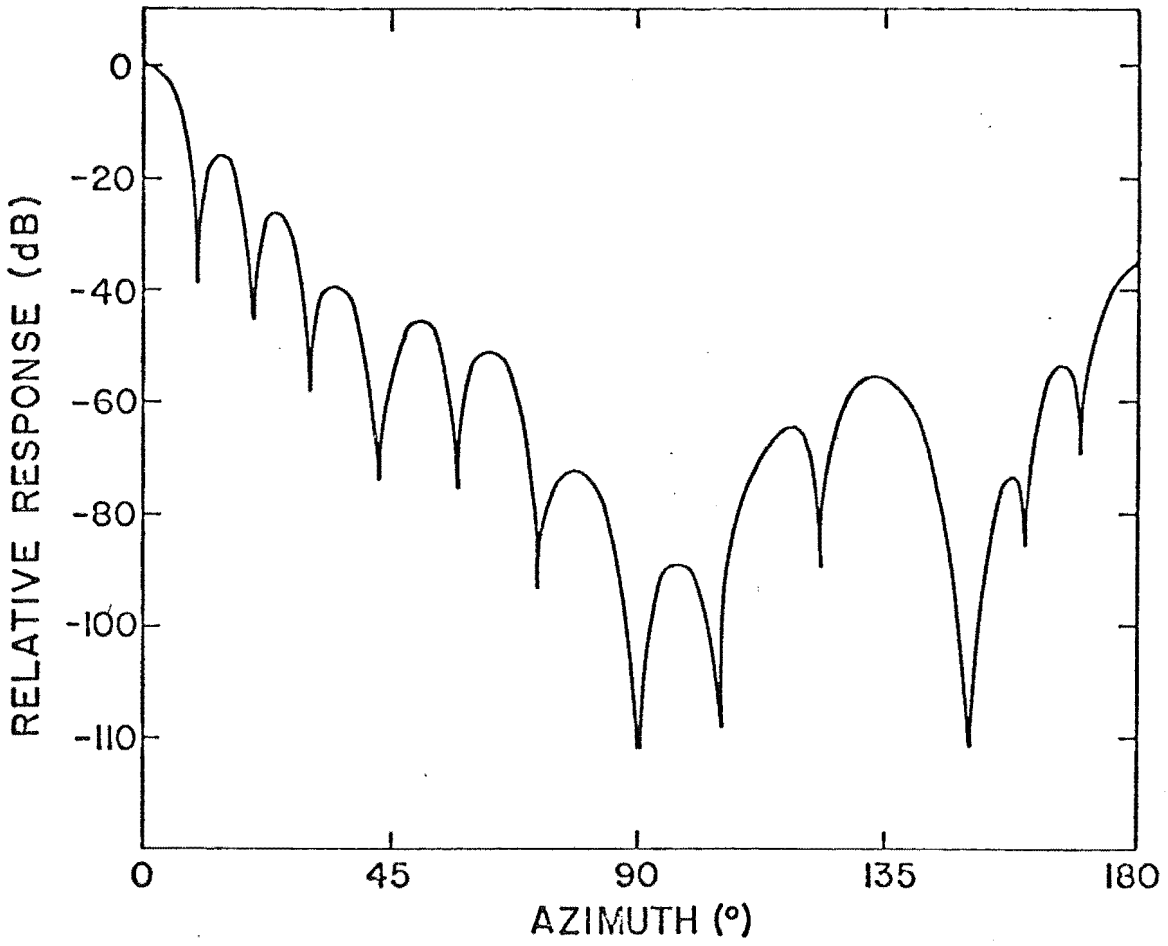

Figure 6.16: Combined transmitting and receiving antenna radiation patterns.

maximum azimuth at which echoes are located is determined by the combined transmitting and receiving antenna radiation pattern, shown in Fig. 6.16. The azimuth range needs to embrace the first few side lobes to keep the number of ambiguous echoes to an acceptable level. For the first side lobe

$$d_{13} \leqslant 1.48\ \lambda$$

and for the second

$$d_{13} \leqslant 1.02\ \lambda \quad .$$

Mutual coupling may become important for spacings of about 1λ so a final spacing of 1.5 λ was used which embraced the first side lobe, but not the second. Poulter (1978) found mutual coupling to be negligible with a 1.4 λ spacing.

The number of echoes likely to be detected in a side lobe depends on the width and relative amplitude of the lobe. The most important side lobe will be the one centred at 23° as echoes in the first side lobe can be located unambiguously. An estimate of the number of echoes detected can be made by measuring the area under the side lobe in the combined radiation pattern, expressed in terms of $(G_T\ G_R)^{\frac{1}{2}}$. The result for this system is that at most 5.6% of echoes could occur in the second side lobe.

The remote transmitter rhombic antenna pattern will have larger side lobes than the local one. However, these echoes will only be analysed if they occur in conjunction with a backscatter echo and so the same probability of their occurring in side lobes applies.

The position of the two antennas (i.e. 1 and 3) relative to the receivers meant that their respective transmission lines (open wire lines spaced by 7.6 cm with an impedance of 550 Ω) ran parallel for about ten wavelengths. These lines were supported on common poles and were separated by 2.0 m. The effect of interference between these lines (cross talk) was investigated. The lines were twisted (one

turn in three wavelengths) to minimise the cross talk. The magnitude of the effect, for untwisted lines, can be found theoretically by finding the magnetic flux crossing one transmission line because of a signal in the other. For the given construction the induced signal was calculated to be 76 dB below the other.

The cross talk was measured by disconnecting one antenna and connecting that end of the line to a signal generator (see Fig. 6.17). The receiver end of this line was then terminated with a 50 Ω load. The induced wave was then measured by connecting the other line to the reference receiver. It is important to have the signal generator at the far end of the line so that the induced wave will travel towards the receiver. In the other case the induced wave will travel to the antenna and only reflections will be measured at the receiver. The measurements showed that the induced signal was 83 $\pm$ 1 dB below the signal in the other line. This is 7 dB more isolation than expected and may have been due to the twisting of the lines. The two investigations show that the degree of cross talk between these parallel transmission lines is negligible.

(b) <u>The Spacing d_{12}</u> The largest possible spacing d_{12} is desirable as the angle β contributes most to the height measurement uncertainty as small azimuths are used. Again there is a condition for no ambiguity

$$\frac{2\pi d_{12}}{\lambda} (\cos \beta_{max} - \cos \beta_{min}) \leqslant 2\pi$$

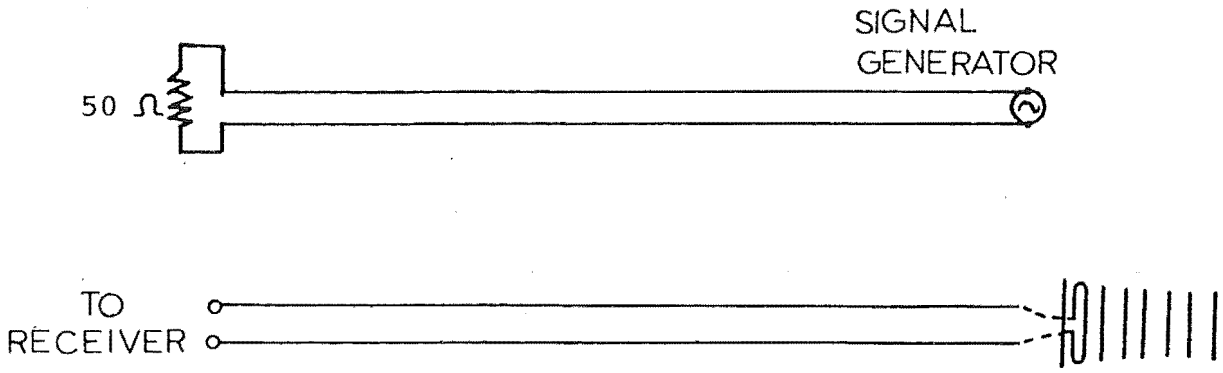

Figure 6.17: The cross talk measurement

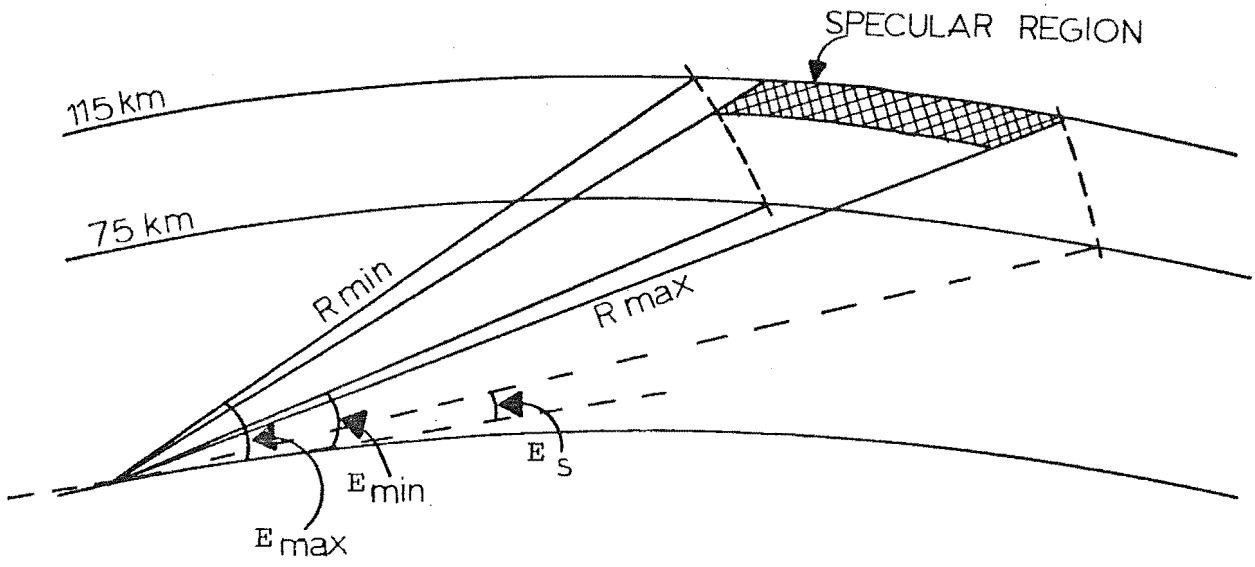

Figure 6.18: Possible elevations for measured meteors

which becomes

$$d_{12} \leqslant ([\cos E \cos A]_{max} - [\cos E \cos A]_{min})^{-1} \quad .$$

The size of d_{12} can be increased by using the smallest range of azimuths that is practical. The range $\pm 8^{o}$, embracing the main transmitter beam, was used. This means that echoes at greater azimuths may have ambiguous heights, but they can be excluded from the analysis because A is known unambiguously.

The possible elevations from which echoes can be received depends on the meteor height distribution and the echo ranges used. Data is recorded in this system on paper tape. This is not a good storage medium for large amounts of data, so it is desirable to maximise the proportion of specular echoes (i.e. with $\mu = 0^{o}$). This can be achieved by restricting the ranges in which echoes can be recorded. More precise range restrictions can be applied in subsequent computer analysis.

Echoes that are within 1^{o} of being specular will be in the elevation range

$$14.5^{o} < E < 17^{o}$$

for heights between 100 and 110 km where magnetic effects should be observed. The ranges R_{min} and R_{max} in Fig. 6.18, for useful specular echoes are then 320 and 400 km respectively. Normally, echoes would not be observed above 110 km because

of the finite velocity ceiling, but if diffusion is inhibited by the earth's magnetic field this ceiling will be raised. In practice, a maximum range of 450 km was used.

The widest span of possible echo elevations will occur for the shortest echo range. By assuming that all meteor echoes occur in the height span 75-115 km, the maximum and minimum values of E can be calculated for the minimum range. Poulter (1978) using a very similar antenna system found only 2% of sporadic meteors outside of this span. The smallest possible elevation, E_s, is obtained by using the longest range and is 7^o.

The condition for no ambiguity now becomes

$$d_{12} \leqslant 22.03\ \lambda \quad .$$

A value of $d_{12} = 20\ \lambda$ was finally used, allowing for a slightly larger unambiguous height range at the shortest echo range. Having decided upon d_{12} it was possible to construct a diagram showing the unambiguous height range as a function of echo range (see Fig. 6.19). The shaded area indicates where the height determination is ambiguous. The choice of 20 λ meant that the minimum useable range was about 300 km, embracing 98% of echoes, but a minimum range of 335 km would extend the resolvable height range to 70 → 120 km.

(c) <u>The Height Uncertainty</u> The uncertainty in the angles measured by the interferometer is related to the uncertainty in the phase measurement (for small uncertainties) by

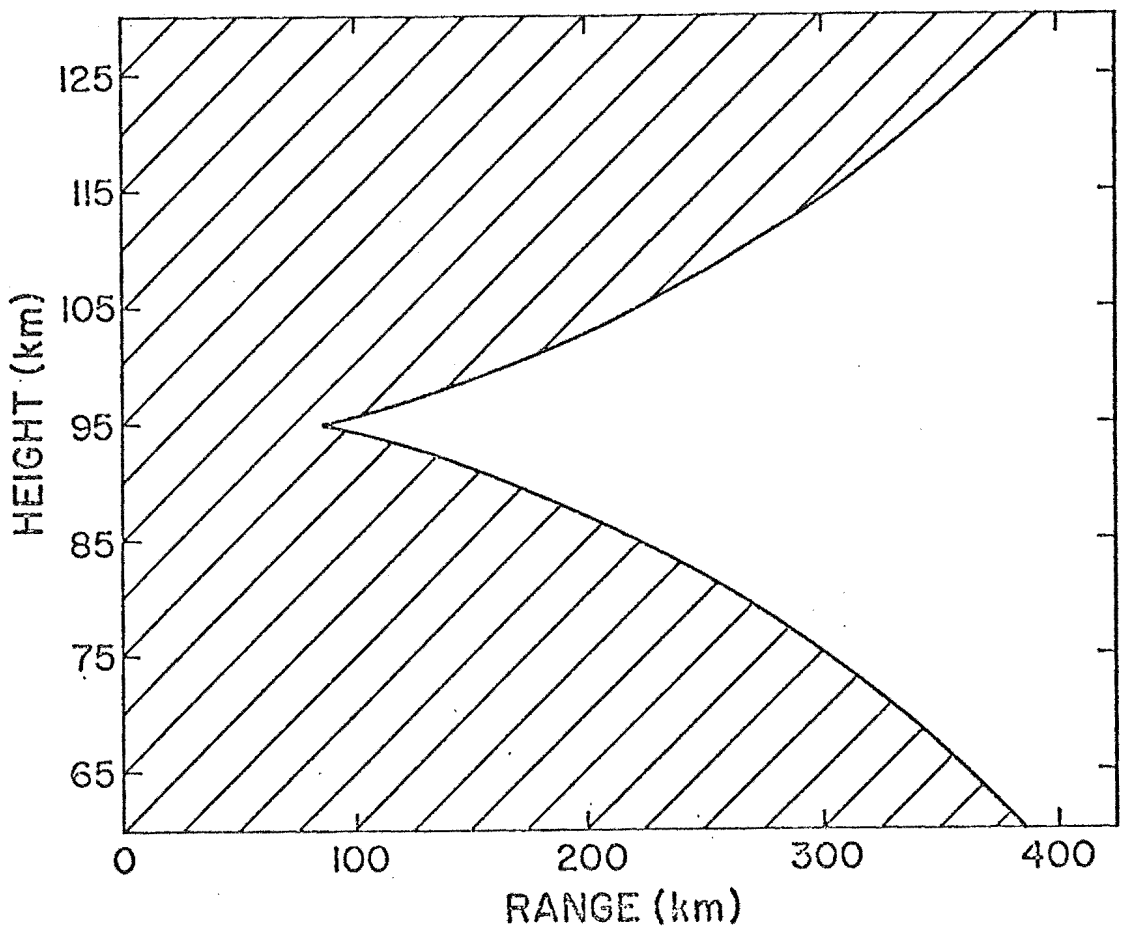

Figure 6.19: The region of ambiguous height measurement (shaded).

$$\Delta\beta = - \frac{\Delta\phi_{12}}{2\pi d_{12} \sin \beta}$$

$$\Delta\gamma = \frac{\Delta\phi_{13}}{2\pi d_{13} \cos \gamma}$$

where $\Delta\phi$ is the uncertainty in the phase measurement. The phase uncertainty is principally caused by noise on the signal being measured and can thus be related to the signal-to-noise ratio, S, by

$$\Delta\phi = \frac{\sqrt{2}}{S} \quad .$$

The factor of $\sqrt{2}$ arises because two noisy signals are being compared.

However, the standard deviation of the measured phases can be calculated during the analysis thus giving an estimate of the height uncertainty for each echo. Only phases measured near the maximum amplitude of the echo are used in its location because of the effect of Fresnel diffraction on phase measurements (discussed in section 3.6). This means that from three to five phase measurements are used to locate an echo. To avoid underestimating the standard deviation of the measured phases Bessel's correction was applied.

The final expression for the height standard deviation, derived from the standard deviations of the range and phase measurements, is

$$\Delta h = \Delta R \sin E + \frac{h \sin A \cot E \, \Delta\phi_{13}}{2\pi \, d_{13} \sin E} + \frac{h \cos A \cot E \, \Delta\phi_{12}}{2\pi \, d_{12} \sin E}$$

where ΔR is the standard deviation of the measured range values. The height standard deviation is a measure of the spread in heights found from individual phase measurements on a single train, i.e. measurements on individual pulses. The reliability of the average height is the standard error of the height which is

$$h_{s.e.} = \frac{\Delta h}{\sqrt{N}}$$

where N is the number of phase measurements.

(d) Antenna Construction The method used in constructing the interferometer was the same as that used by Poulter (1978). Each receiving antenna was an eight element yagi, the same as used in the transmitting array and the transmission lines were similar. Half-wavelength coaxial cables linked the antennas to open-wire lines. Again capacitive matching stubs were used on the driven elements of each antenna. The open-wire lines were an integral number of half-wavelengths long. The impedance at the receiving end of these lines was about 200 Ω and purely resistive. A 4:1 impedance balun was used to connect each line to 50 Ω coaxial cable. These cables were connected directly to the receiver inputs.

The gain of each antenna was checked regularly by connecting each, in turn, to that receiver used by antenna 1 which was the phase reference receiver and contained the amplitude detector. The receiver video output was then used to measure the signal received from the echo transponder (see sub-section (3)). The antenna gains were found to agree within 1.5 dB when operating correctly.

The ground over the area of the interferometer was level to within about 1 m. This corresponds to 0.25^{o} in elevation over the distance d_{12} where the variation occurred. However, the point of zero elevation is determined by the position of the echo transponder. This was at a distance of 3 km and its antenna was mounted at the same height as the receiving array. A topographical map showed that the

ground over this distance sloped downward by 8 m which corresponds to an elevation of -0.15^{o}, thus giving a systematic height error of 0.9 km at a 350 km range. This was corrected for in the data analysis. Earth curvature of 0.7 m over this distance was neglected, but, of course, a curved earth model was used in all the echo geometry calculations.

(e) Tests of the Phase Measurements The phase detectors and antennas had been modified since the previous phase testing undertaken by Poulter (1978). To verify that the system still worked, the portable C.W. transmitter used in the antenna measurements was taken to known locations in the region of the main transmitter beam. For the maximum azimuth of 17^{o} measured, the minimum distance, r, to measure a far-field pattern, was 800 m which was always exceeded. The system was checked in two ways. An X-Y recorder was connected to the cos ϕ and sin ϕ video outputs from the phase detectors. The mobile testing transmitter power was gradually increased so that the recorder drew a line on the chart. A straight line would indicate that the phase response was linear with input amplitude. Fig. 6.20 shows the results for ϕ_{12} and ϕ_{13} for one location of the mobile transmitter. The different paths traced as the amplitude increases and decreases was found to be due to hysteresis in the chart recorder. The slight curve in the phase response at small amplitudes is due to the small input signal to the limiting amplifiers in the reference channel. The output of these

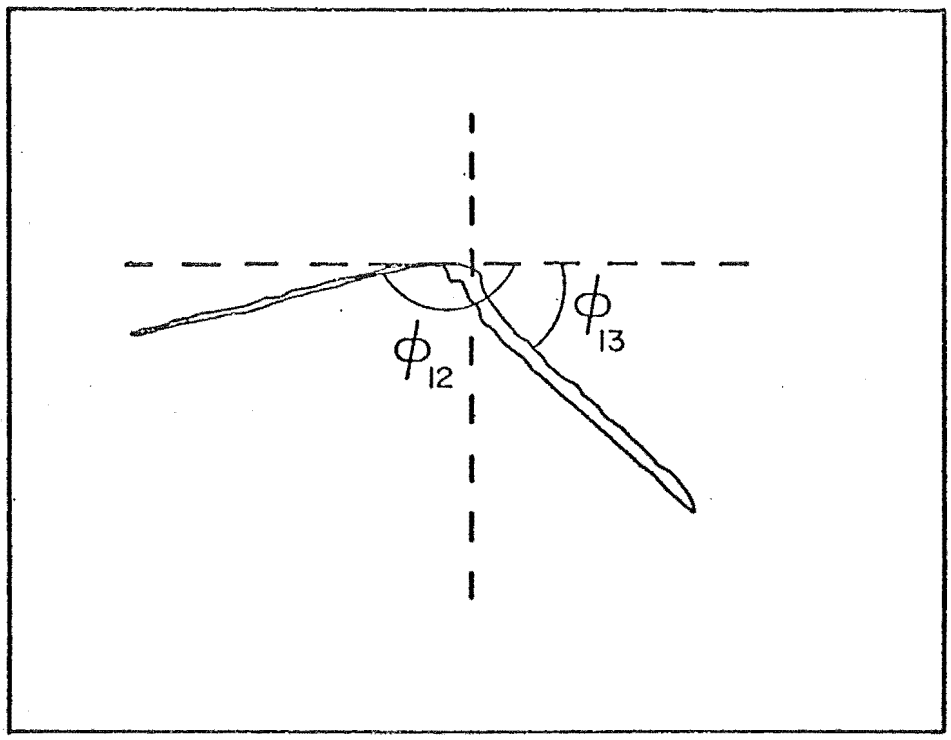

Figure 6.20: Test of the linearity of phase detector response (a tracing of the actual record).

amplifiers is used as the phase reference and does not limit until the input signal is sufficiently large. This problem was corrected in the analysis by not measuring phases from pulses whose amplitudes were too small to limit the output.

The second check involved triggering the system off the C.W. signal and analysing the measured phase angles. This had the advantage of testing the whole system. For this geometry the phase angles are given by

$$\phi_{12} = 2\pi\, d_{12} \cos A + \Delta\phi_{12} \qquad 6.4$$

$$\phi_{13} = 2\pi\, d_{13} \sin A + \Delta\phi_{13} \qquad 6.5$$

where $\Delta\phi_{12}$ and $\Delta\phi_{13}$ are the differential phase offsets. The

azimuth, A, is measured from the propagation direction, values to the west being positive. The phase angles are shown plotted against the cosine and sine of the azimuth in Fig. 6.21 and Fig. 6.22 respectively. Also shown are the determinations of the differential phases by the echo transponder. These were obtained 1.5 hours before the phase measurements were made and while the equipment was warming-up. Phase drifts of about 10^{o} were often recorded under these conditions so that the apparent disagreement between the transmitter phase measurement and the transponder is explained. The method of calibration, phase drifts and the differential phases are discussed in sub-section (3).

The phase variation ϕ_{12} is linear for positive (west of south) and negative azimuths. Phase drifts that could occur during the measurements were checked by repeating the first measurement half way through the run. A drift of 2^{o} in ϕ_{12} and 0.6^{o} in ϕ_{13} had occurred which does not explain the difference in slopes. A linear regression analysis gave

$$d_{12} = 20.3 \pm 0.5 \ \lambda \text{ for } A > 0$$

and

$$d_{12} = 17.2 \pm 0.8 \ \lambda \text{ for } A < 0 \quad .$$

The difference in slopes could be caused by irregular ground reflections. These would not be expected to behave in the same manner for elevations of 16^{o} as they did at zero elevations so the difference observed may not be important. A check of this would be to compare the meteor height distribution

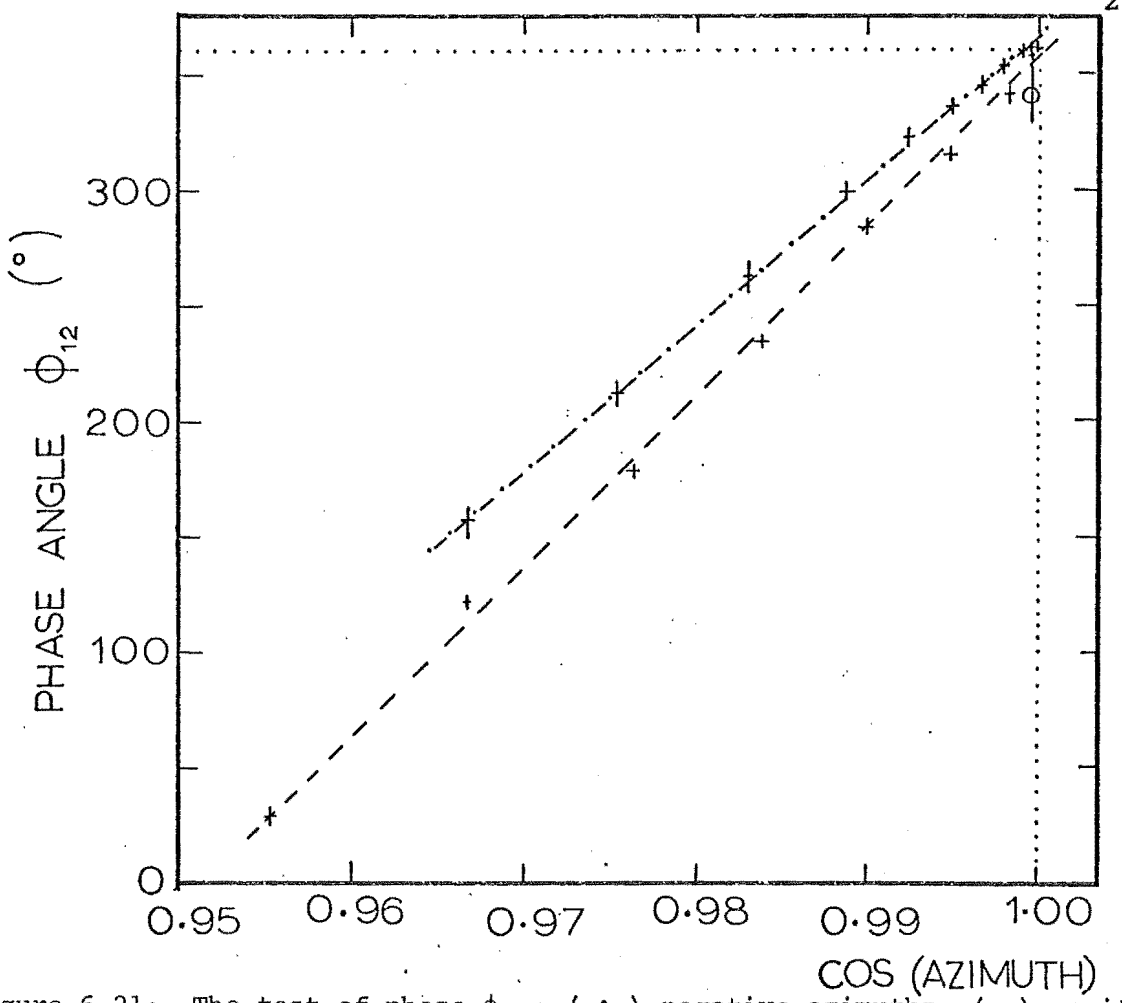

Figure 6.21: The test of phase ϕ_{12}: (-•-) negative azimuths; (--) positive azimuths and (ϕ) transponder.

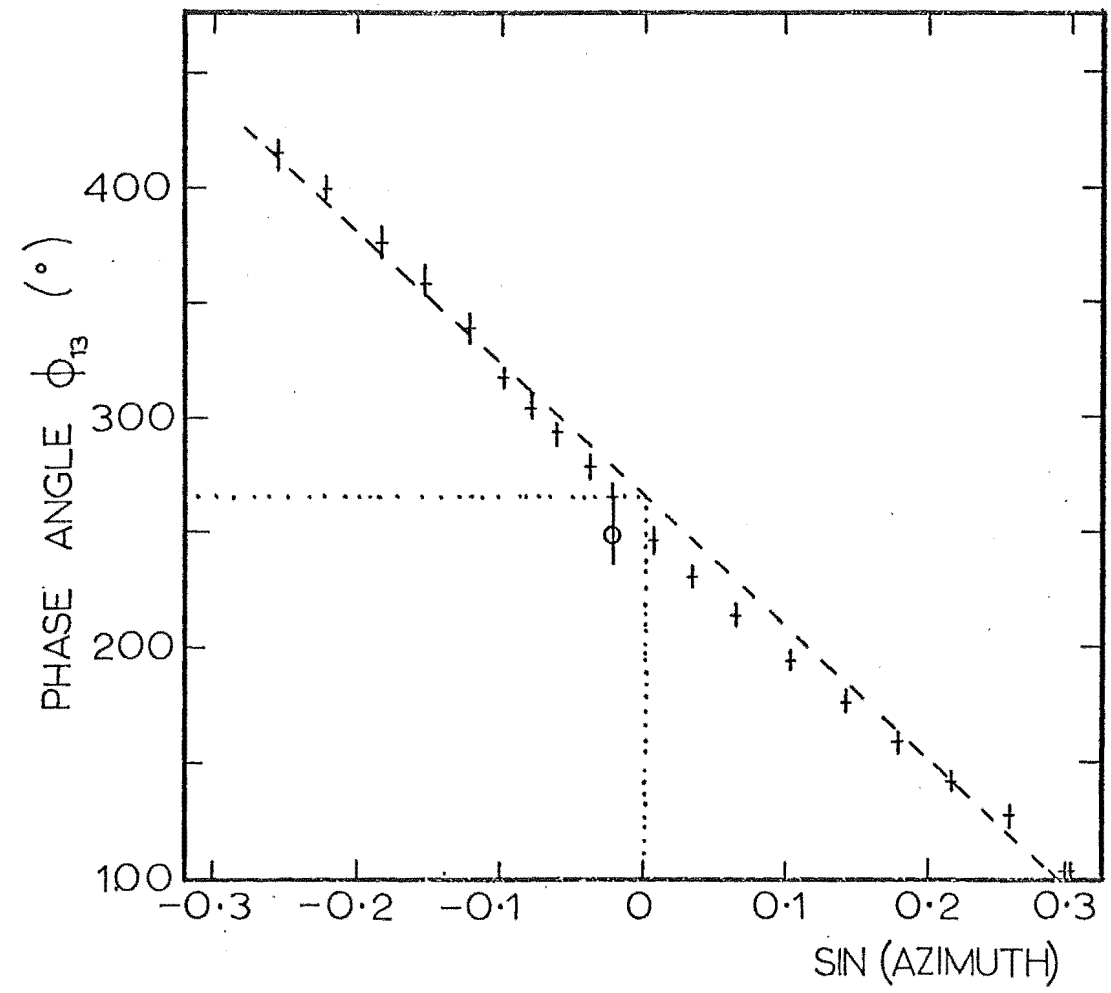

Figure 6.22: Test of phase ϕ_{13}: (ϕ) transponder differential phase.

for positive and negative azimuths (see section 7.3).

The ϕ_{13} phase shows only a slight variation from linear behaviour. The antenna spacing inferred from a linear regression analysis is

$$d_{13} = 1.61 \pm 0.05 \ \lambda \quad .$$

This does not agree with the physical spacing of 1.5 λ which indicates that there may be some coupling between the antennas. A value of 1.6 λ was used in the analysis which could therefore introduce a systematic error of 7% in measured azimuths. This would introduce only a small uncertainty into the height measurement as azimuths of less than 8^{o} are used.

(2) Signal Processing

The signal processing equipment was basically that described by Poulter (1978) with some modifications. The main changes were to enable the system to record the signals from two transmitters operating at the same time and were confined to the logical control. A brief description of the system is given here and the modifications are described in more detail.

(a) General Description Fig. 6.23 is a schematic diagram of the system with most of the logical control omitted. The r.f. signals from the three antennas of the interferometer are fed into r.f. amplifiers. The reference

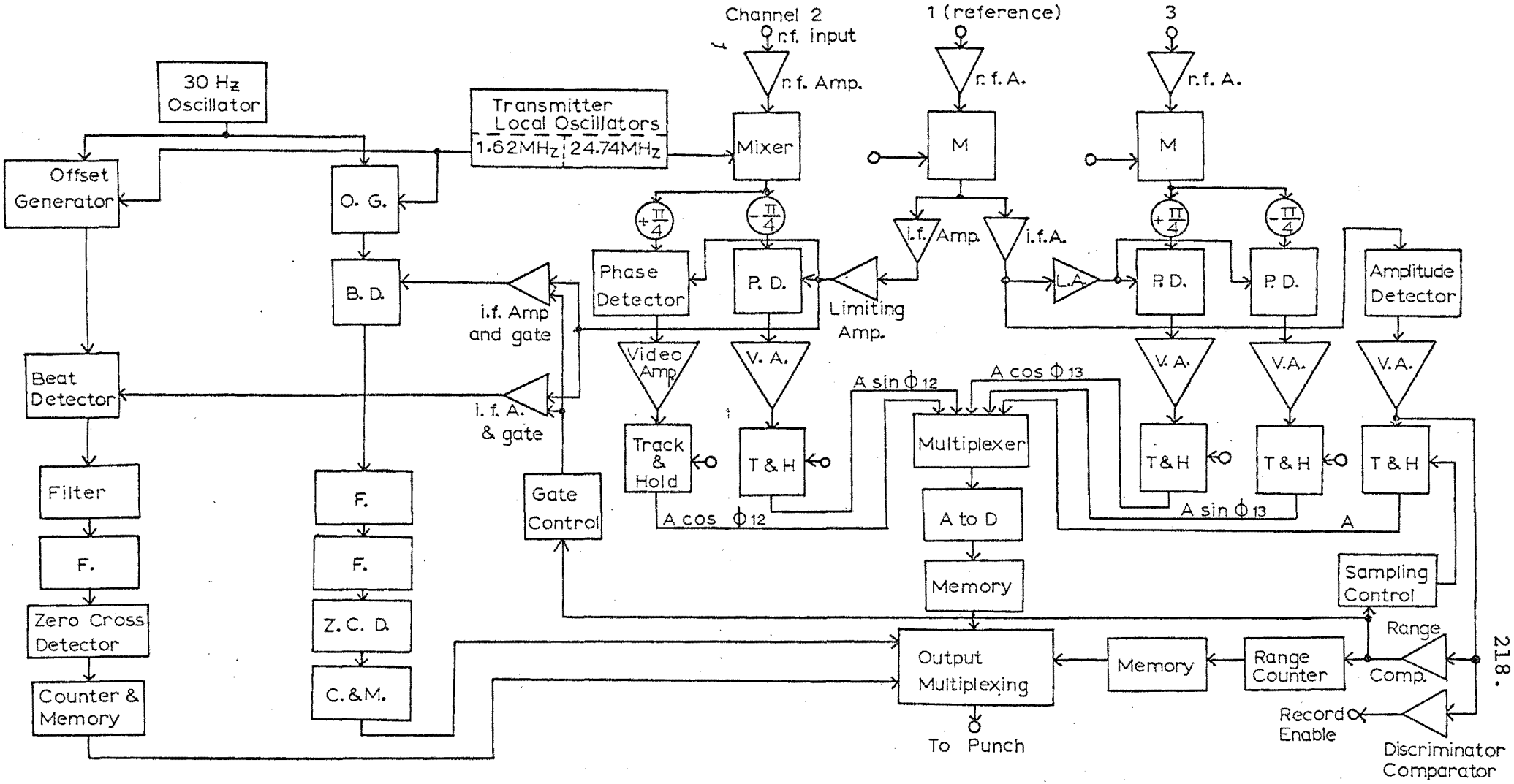

Figure 6.23: The receiving and data processing system.

amplifier has a little more gain than the other two channels as it has to drive two i.f. amplifiers. Each amplified signal is mixed with the 24.74 MHz signal from the transmitter to give a phase coherent i.f. of 1.62 MHz. This is further amplified in the reference channel in two parallel i.f. amplifiers. A part of the signal from one amplifier is taken to an amplitude detector. The video output of the amplitude detector is then amplified and passed to its track and hold circuit.

The remaining i.f. signals then pass to limiting amplifiers so that they can be used as reference signals for the phase detectors. The fact that these amplifiers do not limit for very low signals has already been mentioned. The output of one limiting amplifier also passes to the doppler circuits, described below.

The i.f. signals from the other two channels are each phase shifted by $+\pi/4$ and $-\pi/4$. These signals then pass to the four phase detectors which give outputs $a(t)\cos\phi_{12}$, $a(t)\sin\phi_{12}$, $a(t)\cos\phi_{13}$, $a(t)\sin\phi_{13}$ where $a(t)$ is the time-varying signal amplitude. Care needs to be taken in setting up the equipment that each pair of phase detectors has equal gain so that the amplitudes $a(t)$ cancel to give $\tan\phi_{12}$ and $\tan\phi_{13}$ in the final analysis. Each of the four video outputs from the phase detectors are amplified and passed to track and hold circuits.

The amplitude video output is also passed to two signal comparators. One is set for echo detection and is the input to a meteor echo discriminator. This tests pulses for

width and the correct P.R.F. If two signal pulses meet these conditions the system will begin to record an echo. Should an echo end before the recording is complete, an end-of-echo detector is triggered which inserts dummy values into the memories until the recording cycle is complete. This is necessary because the memories are static shift registers. The dummy values ensure that the initial useful values are moved to the end of the shift registers ready for feeding to the output multiplexing when the punchout cycle begins.

The other signal comparator is used to obtain square pulses for timing. The output is passed to the range counters, doppler circuits and analogue-to-digital converter (A/D) sampling control. At the beginning of the transmitter trigger pulse the echo range counters begin counting the number of cycles of a 1.62 kHz square wave. This frequency is halved at the beginning of the received pulse and is continued until the end of the received pulse. This ensures that the centre of the pulse is found, independently of pulse amplitude. A correction has to be made for half of the width of transmitted pulse and for time delays in the receiver circuits. The counts are stored in the range memories which are static shift registers. The range words need to be 12-bit to give sufficient range measurement accuracy and are punched on to paper tape as pairs of 6-bit words.

The range comparator level determines whether or not a pulse is sampled. Normally this level would be set just above the noise level. The discriminator comparator is set

higher than this so that once an echo has been detected, it is sampled nearly to the noise level.

The pulses from the range comparator pass to the A/D control where they trigger an adjustable monostable. This enables the time at which the track and hold circuits "hold" to be adjusted so that the peaks of the video pulses are sampled. There are five pulses to sample (four phases and one amplitude) so that this adjustment is a compromise. The setting of the range comparator level also affects this timing so that readjustment is necessary if the range comparator level is adjusted too far.

The multiplexer passes the output level from each track and hold circuit, in turn, to the A/D converter. The digitised output is then stored in static shift registers until they have been filled.

The doppler circuit has two channels which are offset from the transmitter i.f. by $\pm$ 30 Hz. This avoids the discrimination against low velocity measurements which occurs because the beat frequency for low velocities is small and thus takes longer to measure. As the measurement time available is limited to the echo lifetime, the lower doppler frequencies are less likely to be measurable and so there is a bias against lower wind velocities. This was quite evident in studies that did not use frequency offsets (e.g. Wilkinson, 1973).

The doppler circuit has a 30 Hz oscillator, the output of which is mixed with the i.f. signal from the transmitter local oscillator to produce two shifted frequencies. The

output is amplitude modulated and needs to be actively filtered before being passed to the beat detectors. The input to the beat detectors from the received signal is first gated and amplified. The gating reduces the amount of noise admitted to the beat detectors by cutting out all of the noise between pulses. The gate is controlled by the logic; timing is taken from the preceding pulse from the range comparator.

The beat detectors are phase detectors that effectively sample the doppler frequency. The sampled output is filtered by active filters in series and is then passed to zero crossing detectors. The time interval between zero crossings is counted at a 5 kHz rate and the number of counts is stored in static shift registers.

When the memories of both doppler channels, the range circuit and phase and amplitude circuits are full, the system stops recording and switches to a punch out routine. The contents of each set of shift registers are clocked out in turn through the output multiplexing to the punch drivers. The timing of the output is controlled by the paper tape punch which takes about three seconds to punch a complete echo. The recording sequence takes about 0.6 s.

Three other pieces of information are punched out for each record. The time is punched from an internal clock that can be reset by the operator. This output can be translated in the analysis to time in days, hours, minutes and seconds. The last significant bit of the first character of data is set when the echo transponder is

triggered. This enables the calibration echoes to be distinguished in the analysis. The bit is reset when the calibration echo has been punched. Finally, a bit is set by the double echo detector when echoes from both transmitters are present.

A P.R.F. of 150 Hz was used for the two-station operation. This rate was mains locked and was used to trigger the local transmitter, as well as some circuits in the processing equipment. The mains locking device is described below. A P.R.F. of 300 Hz was used for single transmitter runs. A 150 Hz rate was used until an echo was detected when the P.R.F. doubled.

(b) Modifications One modification was made to the linear circuits to improve the performance of the phase detectors. Some breakthrough of the reference signal was measured on the output of the phase detectors when the input signal was absent. This meant that a vector of constant phase was being added to the phase detector output so that for most phase angles the detector response was not linear (see Fig. 6.24). The error in the measured phase was greatest at small amplitudes. In the modified circuit (Fig. 6.25) the breakthrough signal could be balanced out with the 50 kΩ potentiometer. (In the following circuits all resistances are in ohms and all capacitances are in microfarads, unless otherwise shown). This balancing reduced the error signal to a level such that the non-linearity in the phase response was due to the limiting amplifiers not giving a limiting output signal.

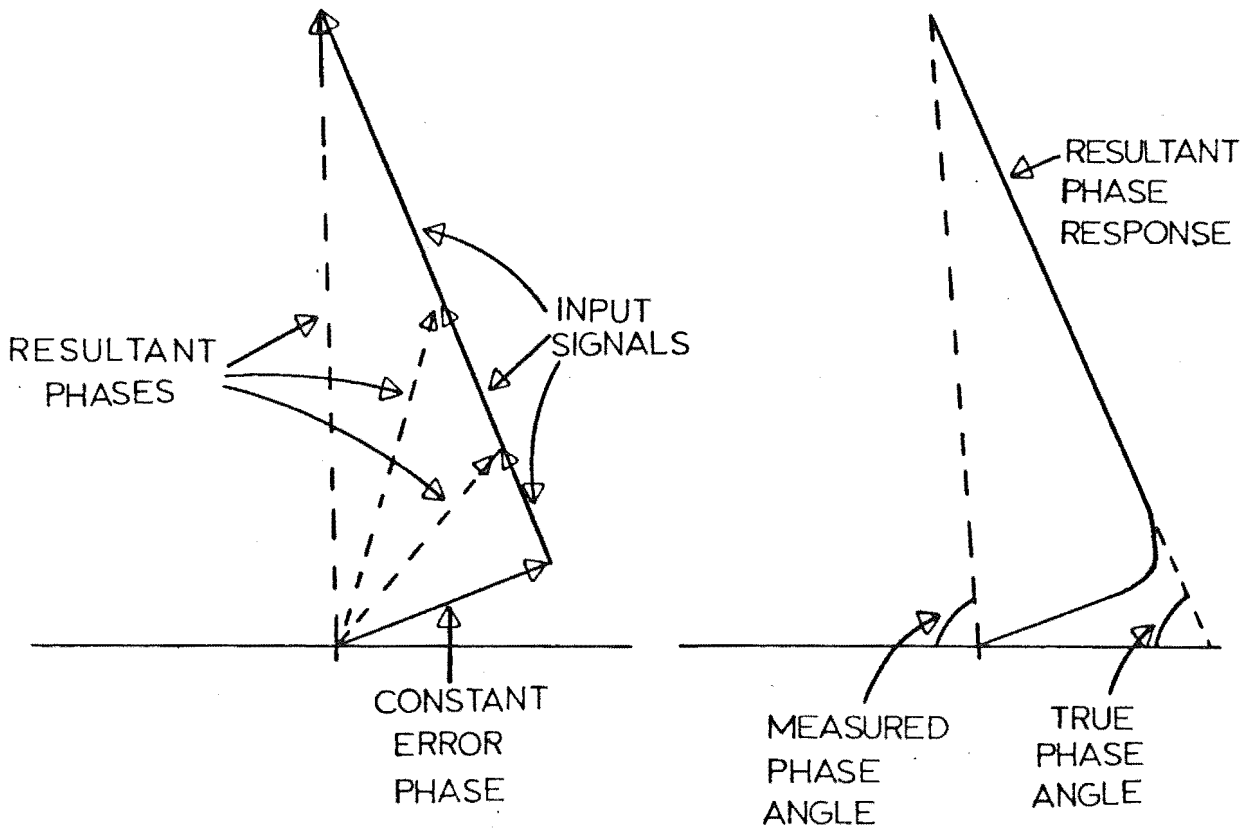

Figure 6.24: The effect of carrier breakthrough on phase detector response

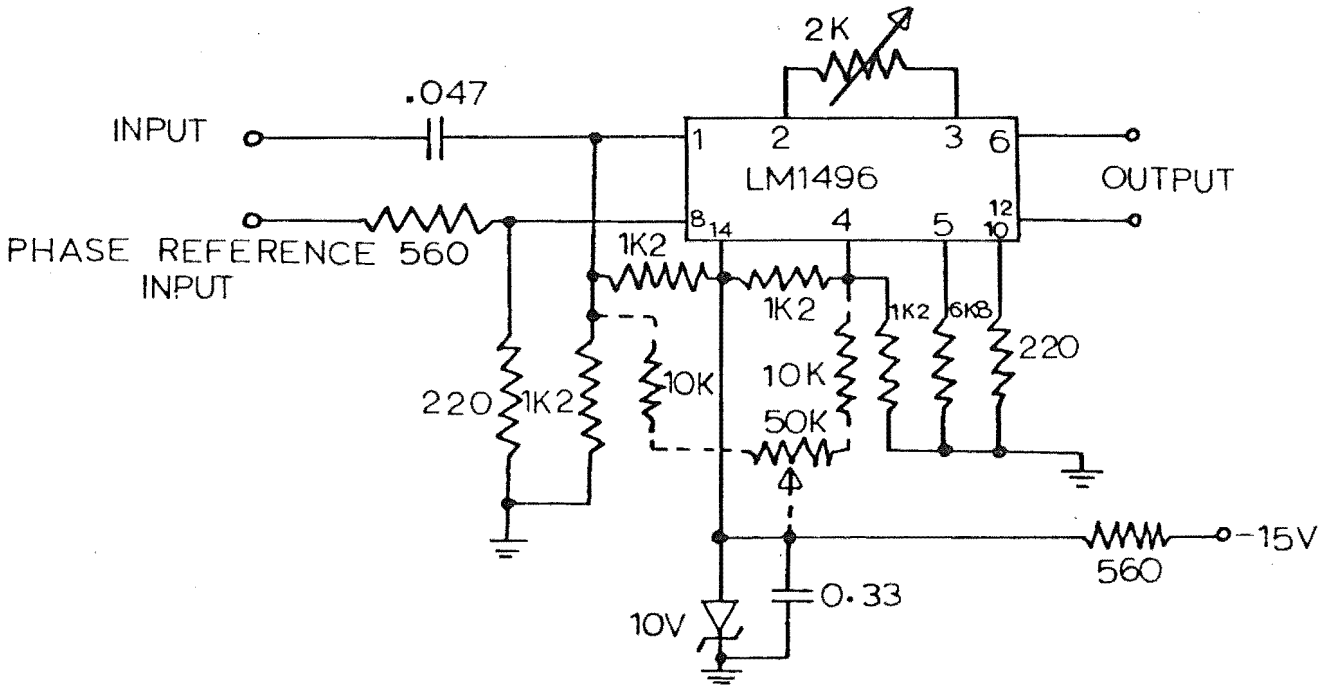

Figure 6.25: The modified phase detector circuit

The number of measured phases and amplitudes for each echo was increased. Originally fifteen pulses were measured for phase and amplitude and a further 125 for amplitude alone. The number of phase measurements was increased because two signals were being measured. An increase to 60 phase measurements was made in the hope of achieving greater accuracy. The variations in the phases due to Fresnel diffraction defeated this aim (see section 7.3). However, the additional phases did ensure that the two received echoes, which could reach maximum amplitudes at different times, would be measured about their maxima. The original 150 amplitude measurements were increased to 160. A large increase was not necessary because, although two signals were being measured, the P.R.F. was only 150 Hz, which meant that the overall sampling time was about the same - 0.5 s. Longer sampling times for amplitude are not useful for decay measurements because of the formation of second reflection points on the train as it becomes distorted by the atmospheric winds.

The new system now measures a total of 400 words of phase and amplitude. This meant that the number of shift registers had to be doubled and some minor changes to the counters in the A/D and output multiplexing had to be made.

Fig. 6.26 shows the range gating and blanking circuits. The circled figures indicate the location of the particular integrated circuit on the circuit boards. Five monostables are triggered by the P.R.F. C.P.T. refers to the command pulse train that triggers the echo transponder and is not

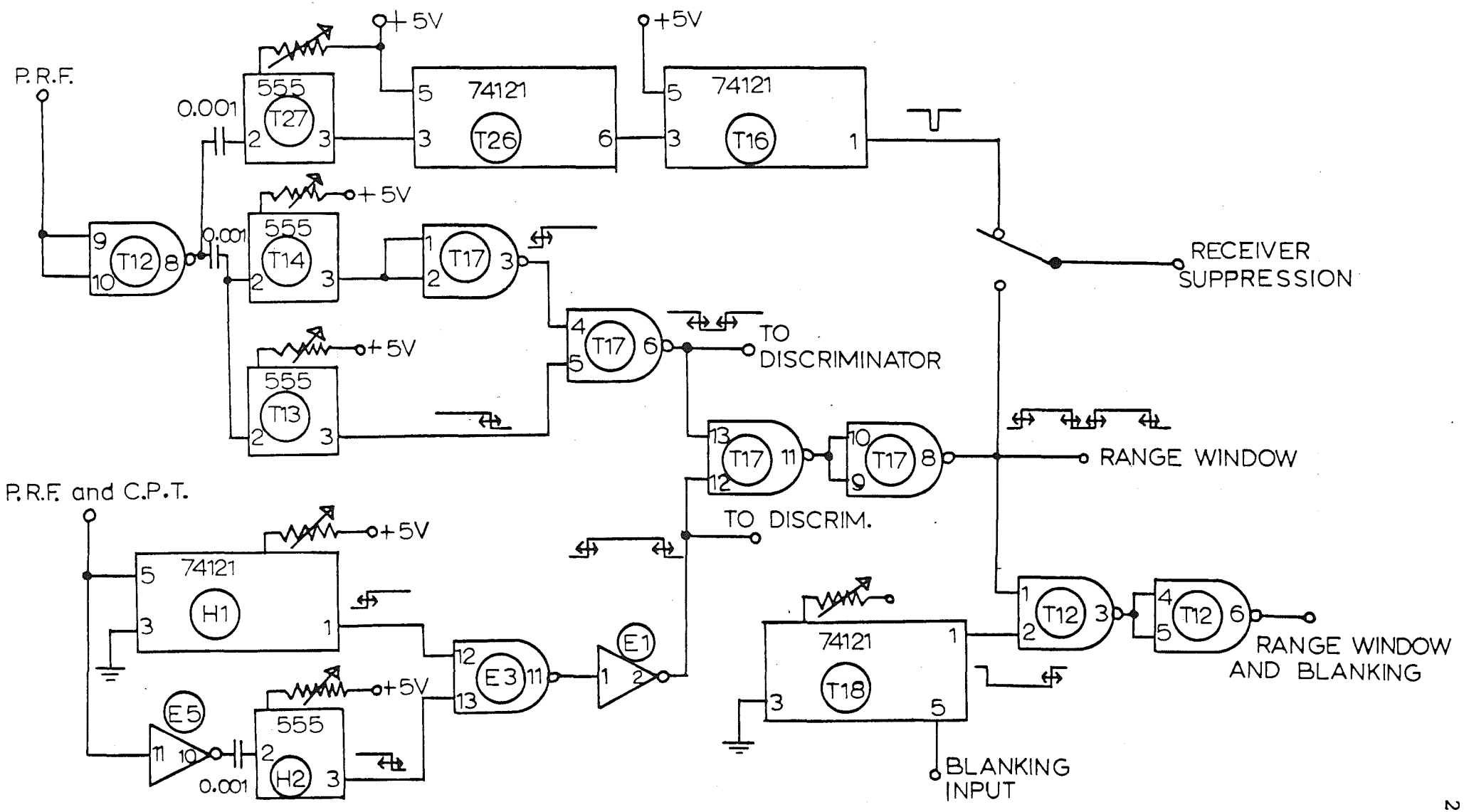

Figure 6.26: The range gating and blanking circuits

important in this context. Four of these monostables produce adjustable pulse edges that are combined to give the range windows. This allows control over the minimum and maximum ranges measured as well as enabling the operator to blank out an intermediate range region to omit unwanted signals such as auroral echoes. When two transmitters were being operated the first window would receive the backscattered echo while the local transmitter triggering was adjusted so that echoes from the remote transmitter fell in the second window. In the 300 Hz mode, the range window was reduced to less than 3.3 ms so that it was re-triggered by every P.R.F. pulse. The range windows were used to gate the input to the discriminator comparator and could also be used to suppress the receivers. This enabled the system to be used with the remote transmitter at a nearby location.

The fifth monostable triggered two further monostables which produced a 100 μs suppression pulse that was applied to the receivers if the range windows were not being used for transmitter suppression. The use of two monostables for the timing allowed the first to be retriggered while the second was still delaying the preceding pulse. This meant that the circuit could be used for 150 Hz and 300 Hz operation without adjustment.

The blanking monostable, T18, was triggered by the trailing edge of pulses from the range comparator. Its delay length was adjusted to about 3 ms and its output was combined with the range windows. This composite signal was

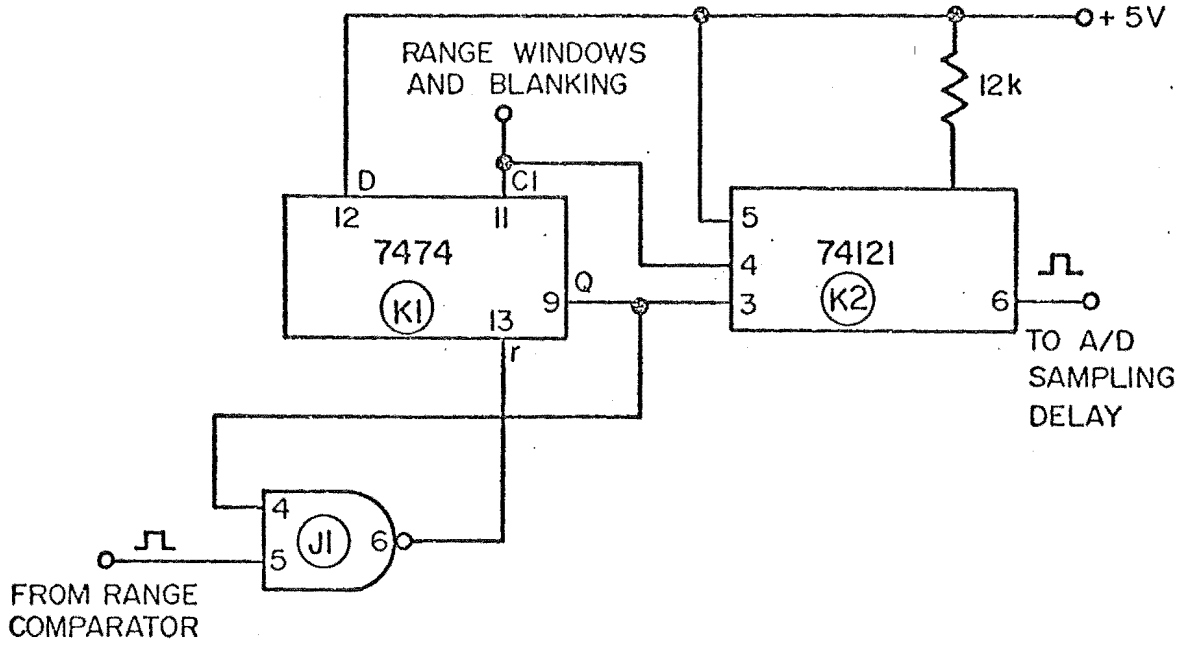

Figure 6.27: The A/D sampling control

used to blank the range comparator so that after a pulse was measured, no more pulses could be recorded for 3 ms. In the two station operation the remote station echo pulse would then be recorded while for a single transmitter at 300 Hz the next local pulse was measured.

{The use of NAND gates as inverters in some circuits was necessary because of availability of components already on the circuit boards. The NAND gates are all 7400s and the inverters are 7404s.}

Fig. 6.27 shows the A/D sampling control. This circuit makes the A/D sample in each range window whether or not a pulse is present. This means that the received echoes can be distinguished in the analysis by taking odd and even numbered amplitude measurements. In the unmodified equipment the range comparator pulse was applied directly to the A/D

circuit. Here the flip-flop (K1) output Q is set high by the first positive edge of the range window transferring the high D level to Q. This enables the NAND gate J1 so that a range comparator pulse can enter and reset the flip-flop. This disables J1 so that the transmitted pulse is really a spike. This does not matter because the function that it performs is complete before the pulse is terminated.

The monostable K2 is not triggered by the positive edge of the range window, but is triggered by the negative edge produced when the flip-flop is reset. This then causes the A/D to sample in the usual way. The negative edge of the range window does not occur if a pulse is present because this signal is combined with the after-pulse blanking. The negative edge thus occurs at the end of the first pulse and does not trigger K2 because it is already triggered. This means that the delay of K2 has to be longer than the pulse and it was set to 200 μS. This does not affect later circuits as only the positive edge is used.

If a pulse is not present in the range window, the negative edge of the range window triggers K2. This causes the A/D to sample on noise. The correct operation of this circuit depends on suitable settings of the range windows and blanking length.

Now that the recorded pulses can be distinguished there remains the problem of which pulse occurred first. This was overcome by modifications to the meteor echo discriminator so that when an echo was detected, the "go" condition would not occur until the local transmitter was

triggered. This meant that odd numbered amplitudes corresponded to the backscattered pulses.

Fig. 6.28 shows the discriminator. Pulses that are large enough to be sampled by the comparator trigger the monostable F1 which is set to 50 μs. The diode, resistor and capacitor, together with the buffer E1, delay the arrival of the pulse at pin 5 of E2 so that pin 9 has time to reach a low level. Thus E2 is not enabled until 50 μs later and then only if the pulse is still present and is inside a range window.

If the pulse had a suitable width the monostables A4, F2 and H3 are triggered in turn so that if another pulse appears one P.R.F. cycle later the output of E2 (pin 8) will go low. This sets Q of flip-flop K1 thus enabling gate J1 when the transmitter is next triggered. This pulse begins the data recording sequence. At the same time, flip-flop B4 is set so that E2 is disabled. This prevents further pulses from entering the discriminator until the "punch complete" signal resets this flip-flop. The "go" condition also changes Q of K1 to low so that no further P.R.F. pulses can enter the system. Finally, the "go" pulse triggers monostable F3 which changes the output to 300 Hz for 0.8 s. This output to the P.R.F. switch enables the operator to control whether or not the P.R.F. will double during a particular period of data collection.

Pulses from the range comparator are used for triggering blanking pulses, the A/D sampling, the end-of-echo detector,

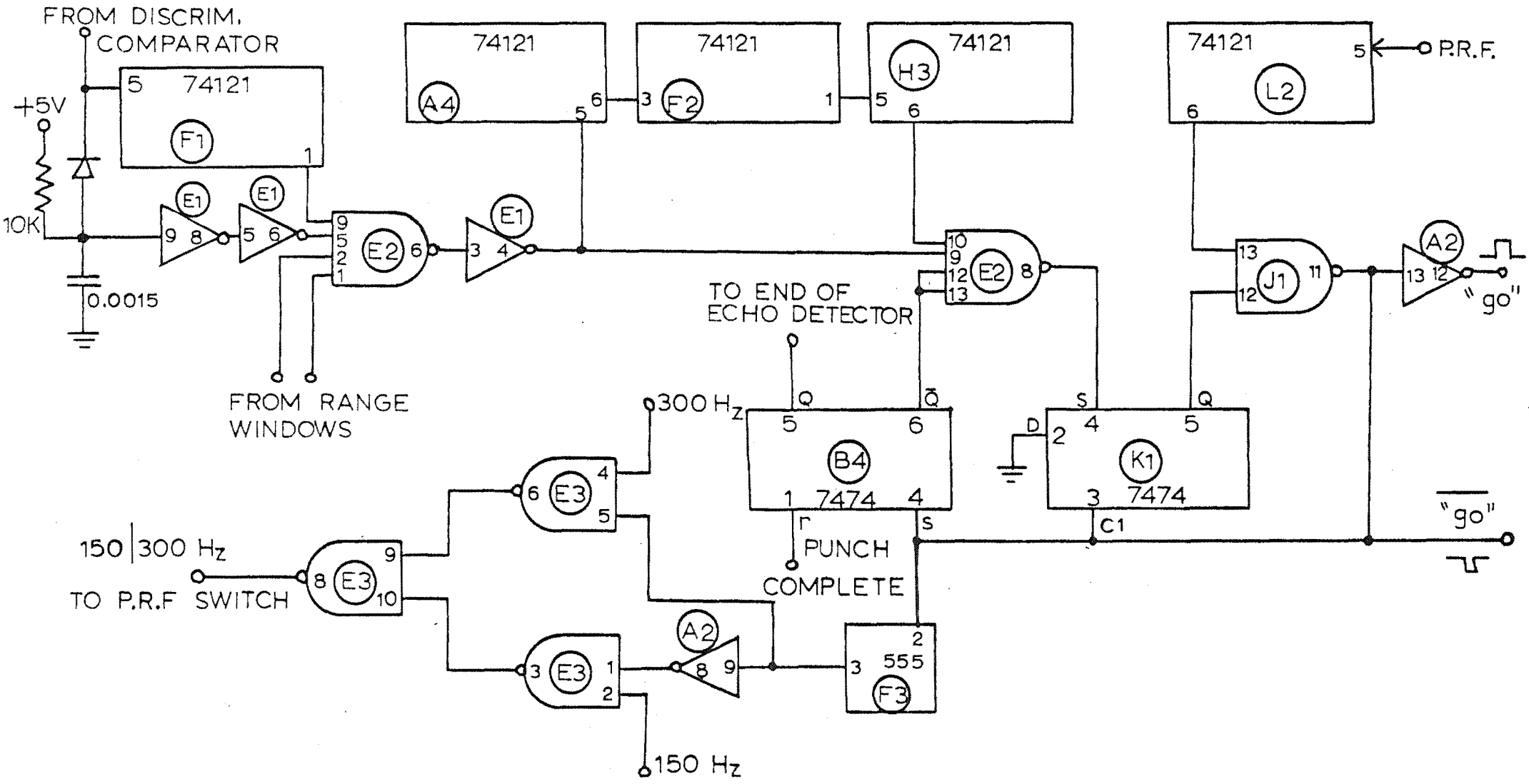

Figure 6.28: The meteor echo discriminator

the range counters and the doppler i.f. gating. For two station operation the pulses from the second transmitter need to be prevented from triggering the range counters and doppler gate. As the system is not phase coherent with the remote transmitter, the doppler output would be meaningless. The remote transmitter triggering time is not sufficiently accurate for range values to be useful and these remote site reflection point ranges are not needed for this experiment. The pulses were prevented from reaching these circuits by a NAND gate that was held open for 3.3 ms by a monostable triggered by the P.R.F. signal.

A circuit was built to detect when pulses had been sampled in both range windows at the same time. This simplified the later analysis in that the program did not have to search for double echoes unnecessarily. Pulses from the range comparator trigger monostable T23 (Fig. 6.29) if they are inside the range windows. This monostable is necessary to produce sufficiently sharp edges for the clock input of flip-flop $T25_1$. The flip-flops T25 count the number of pulses between local transmitter pulses. Gate T28 is only enabled if two pulses occur in one P.R.F. cycle. If this is the case, the Q output of flip-flop $T29_1$ is set high. This can only occur during an echo recording sequence so that pulses above the range comparator threshold, but below the discriminator comparator level, do not get detected. Flip-flop $T29_2$ stops the counting process when all shift registers have been filled. This is necessary to immunise the detector from noise spikes created by the paper tape punch motor

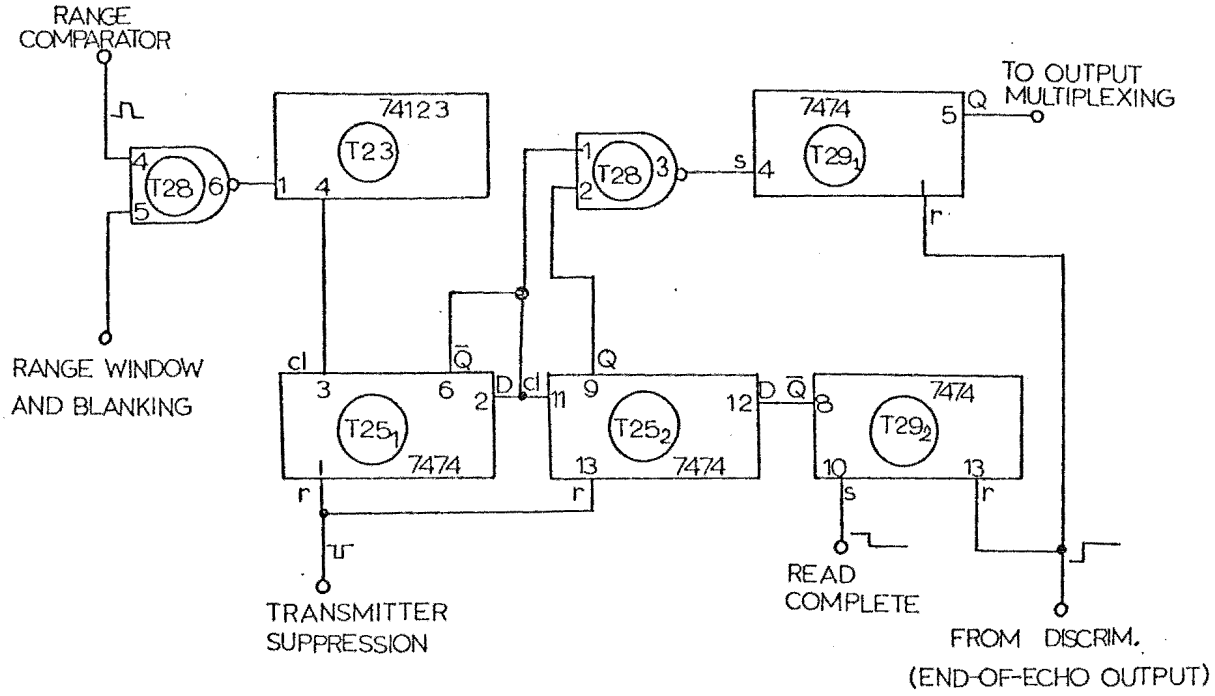

Figure 6.29: The double-echo detector.

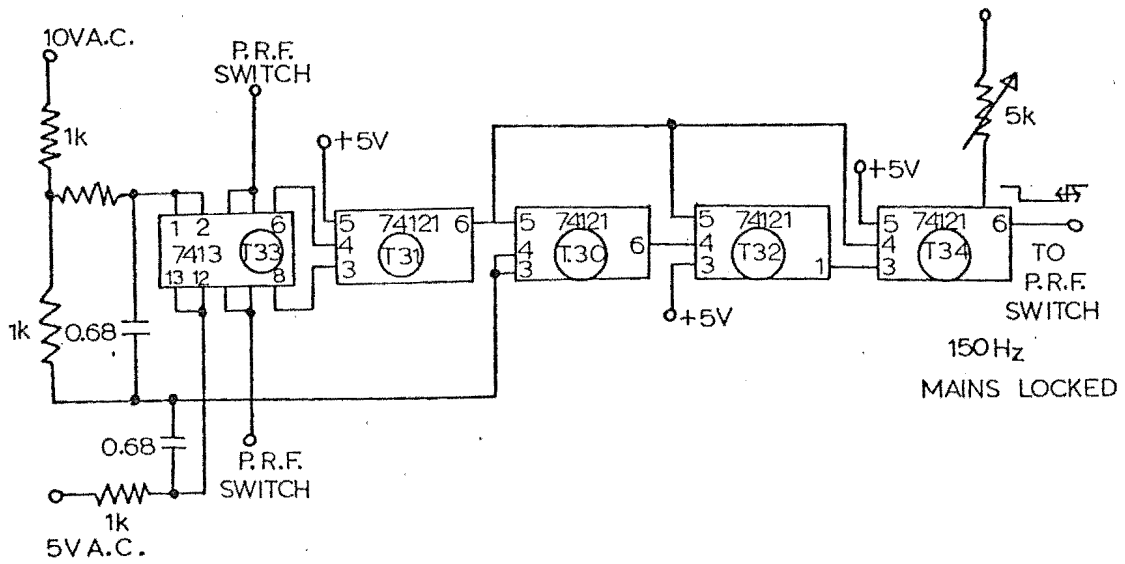

Figure 6.30: The local mains locking device

starting. The detector indicates a double echo if two pulses occurred above the range comparator level in any one P.R.F. cycle during an echo recording sequence.

The mains locked transmitter trigger was very similar to that described for the remote transmitter. Adjustment of the timing relative to the mains phase was achieved by adjusting the delay length of the final monostable T34 (Fig. 6.30). This did not quite give an adjustment over 360^{o} of the P.R.F. cycle. To obtain a complete range, a different input circuit was used. T33 is a dual NAND gate with schmitt trigger inputs. Two opposite phases from a power supply transformer were voltage divided and filtered. These were each applied to one of the NAND gates. The other gate inputs were taken to the P.R.F. switch which earthed one or the other. This provided a 180^{o} phase shift so that the full 360^{o} range could be obtained. The transmitter was triggered by the positive edge of the P.R.F. pulse. Note that the NOT output could not be used to obtain the 180^{o} phase shift as it provides an adjustable negative edge.

(3) Calibration

Equations 6.4 and 6.5 relate the measured phase angles to the azimuth of a signal at ground level. In the general case

$$\phi_{12} = 2\pi d_{12} \cos \beta + \Delta\phi_{12} \qquad 6.6$$

$$\phi_{13} = 2\pi d_{13} \sin \gamma + \Delta\phi_{13} \quad . \qquad 6.7$$

To find β and γ, the differential phase offsets $\Delta\phi_{12}$ and $\Delta\phi_{13}$ need to be known. These offsets originate from differences in electrical lengths of transmission lines and matching stubs and phase delays in receivers between the three channels. Those delays due to transmission lines are constant, but those in the receivers change with receiver tuning and were found by Poulter (1978) to be temperature dependent.

The differential phases can be found from the phase tests described in sub-section (1). Referring to Figs. 6.21 and 6.22, $\Delta\phi_{12} = 360^{o}$ and $\Delta\phi_{13} = 265^{o}$. These figures also show the differential phases found from the echo transponder, but at an earlier time as the equipment was warming-up. Regular calibrations are necessary because of these short term changes so that $\Delta\phi_{12}$ and $\Delta\phi_{13}$ values can be updated by the analysis program. This could be achieved by using the echo transponder, situated in the main transmitter beam at a distance of 3 km, schematically shown in Fig. 6.31. The receiver, discriminator and logic control were designed to minimize power consumption. All logic was of the C.M.O.S. type and was powered by two penlight dry cells. Current requirements were low so that these batteries lasted for their shelf life.

The transponder was activated by a train of 200 Hz pulses from the local transmitter which turned on the crystal controlled oscillator and the final amplifier for one second. The output of the oscillator was then gated by 66 μs pulses from the logic control. These gating pulses were produced

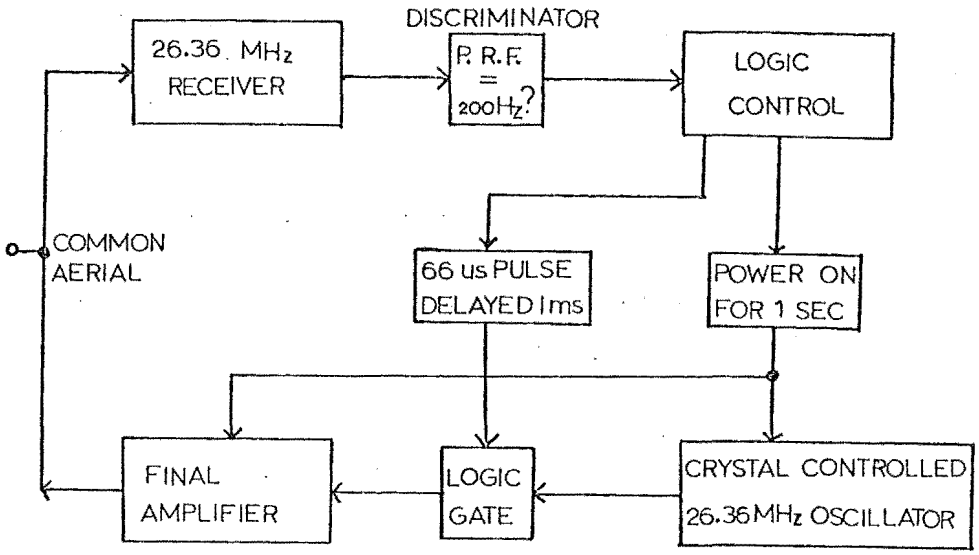

Figure 6.31: Echo transponder functional layout

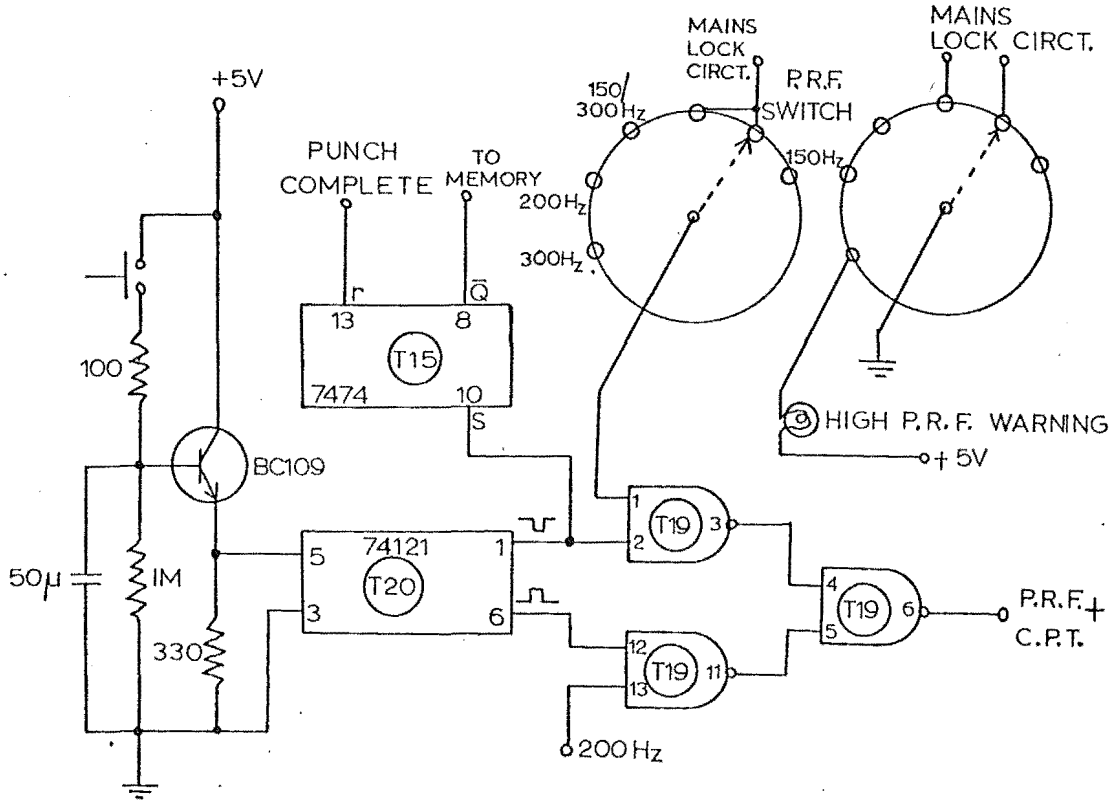

Figure 6.32: The transponder trigger and P.R.F. switch

1ms after any received pulse so that the artificial echo produced had a convenient range value at the main radar site 3 km away. The transmitter was powered by two 9 V dry cells in series which lasted for their shelf life.

The frequency stability of the transponder oscillator is as important as that of the main transmitters for absolute height measurement. In terms of finding a height difference this stability is not important. A test of the frequency stability over the temperature range 0 to 50^{o}C gave a variation of 160 Hz which is quite satisfactory.

Fig. 6.32 shows the triggering circuit for the transponder. Depressing the push button triggers monostable T20 for about 50 ms. The associated timing circuit prevents retriggering for five seconds thus preventing any further change in the P.R.F. (apart from doubling to 300 Hz) while a calibration echo is being recorded. The output of this monostable changes the P.R.F. to 200 Hz for about ten pulses - referred to as the command pulse train (C.P.T.). This monostable also sets flip-flop T15 so that the calibration echo can be distinguished from normal echoes by the paper tape record. The computer analysis program can then update the differential phases calculated from the calibration echo. T15 is reset when punching is complete.

In practice the transponder was not located directly in front of the antennas, but was 1.3^{o} to one side. Corrections were made to the differential phases during the analysis so that they would apply to the position directly in line with antennas 1 and 2.

For the final set of results which involved transmitting in both the magnetic south and geographic west directions, only one transponder was available. The system was initially calibrated by taking the transponder to a position in line with the west interferometer and then to the south one so that the difference in differential phase could be found. This was assumed to be constant as it originates from differences in transmission line lengths.

CHAPTER 7

RESULTS

7.1 INTRODUCTION

Three different sets of results were obtained. The first set was recorded with two transmitters, but without all of the modifications to the signal processing equipment that have been described in section 6.4. It was hoped to separate the two recorded signals by comparing the received amplitudes, punching data on cards and using these as an input to an analysis program. The two signals could be distinguished successfully, but it was not possible to determine unambiguously which was due to the local transmitter so recorded meteors giving two signals were omitted in later analysis. This set of data was recorded with the meteor echo discriminator at a higher detecting threshold than for the two later runs. The threshold was lowered for these runs to increase the system sensitivity as it was found that echoes with smaller amplitudes still had a satisfactory signal to noise ratio of at least 20 dB. These first data were collected on twenty random days during the period June 26 to August 8, 1978. The recording time was usually of about five hours duration between 0500 hours and 1000 hours local time as the aim was to record data when the meteor rate was near its diurnal maximum. In this time 1844 echoes that could be used for further analysis were recorded.

The second set of data was mainly recorded with two transmitters and with the signal processing equipment fully modified so that the two echoes could be unambiguously distinguished. The last five days were recorded with only the local transmitter so that a P.R.F. of 300 Hz could be used which increased the echo height ceiling set by the number of pulses needed to fit a regression line to the echo decay. These data were recorded on 32 days in the period September 18 to December 9, 1978. The recording time averaged four hours, usually between 0600 hours and 1100 hours and 4738 echoes met the initial selection criteria.

The third set of data was collected primarily to study atmospheric winds and not for this work. It was collected on alternate hours with separate receiving and transmitting antennas in the geographic west and magnetic south directions so that magnetic effects could still be examined. Originally a continuous run for fourteen days was planned, but recording was restricted to twelve hour intervals at night because of the prevalence of reflections from sporadic -E layers during the day. These data were collected from March 21 until April 3, 1979. The different interferometer antenna spacings used for these recordings meant that slight changes to the analysis programs and selection criteria were necessary as well as a need to incorporate the differential phase calibration for the west direction. 5484 echoes were recorded in the southerly direction and 4687 in the west.

In this chapter the method of analysis for these data is described along with the selection criteria that have

been applied. The general characteristics of each set of data is presented in various frequency distributions and comparison of these with other work verifies that the system is operating correctly. Phase variations on some selected echoes are examined and an attempt is made to see if plasma resonance effects are important. Magnetic effects on measured diffusion coefficients for both two-station and backscatter echoes are then examined. The variation of measured diffusion coefficient with height is discussed in relation to a model of ambipolar diffusion, magnetic effects and the effect of chemical reactions.

7.2 METHOD OF ANALYSIS AND SELECTION CRITERIA

The first step in the analysis was to transfer the information from paper tape on to magnetic tape with the University of Canterbury's Burroughs 6700 computer which was also used for all subsequent data processing. The next step involved reading the information from magnetic tape, sorting out individual meteor echo records, processing them to a limited extent and creating new data files again stored on magnetic tape.

The meteor data output to paper tape had gaps of sixteen characters between each echo. The sorting program (Appendix 1) searched for the end of these blank characters and then processed the following record. The paper tape reader occasionally inserted or skipped characters so that the sorting procedure would not find the true start of the record. In this case it would search for sixteen blank characters and thus regain synchronization with the input records.

Each echo was numbered for each data file that was created and echoes could be further distinguished by the echo time and name assigned to the data file. Echoes for which the double echo detector had been set were distinguished by a bit on the paper tape record, as were calibration echoes.

The phase values measured from pulses above a certain amplitude threshold were averaged for calibration echoes. The average values were printed so that suitable calibration echoes could be selected before use in the final analysis. This was necessary because sometimes normal echoes would be recorded during an attempted calibration or occasionally reading errors would make the phase value incorrect.

Meteors that only produced an echo from the remote transmitter were distinguished by the lack of recorded range values and were rejected because without the echo range no height or line density could be calculated.

Finally, the sorting program manipulated the range information so that the pairs of 6-bit characters became 12-bit range words. The program then wrote the record on to magnetic tape and proceeded to search for the next echo.

The main analysis program, called ANALYSE (Appendix 2), is written in the Algol language and the purpose of each procedure is outlined here. PROCEDURE PHASESORT Converts the two cosine and sine outputs for each pulse to two phase angles if the associated amplitude is sufficiently large. This procedure also converts the recorded time to local time if the time at which the internal clock was reset is read into the program.

PROCEDURE CALIBRATE calculates the value and uncertainty of the differential phases from each calibration echo. The

differential phase values are then updated if the uncertainty is not too large and if the values calculated do not differ from the previous values by an amount that is read into the program.

PROCEDURE ARRANGE sorts out the local amplitude and phases from those of the remote transmitter. If only local values are present this is indicated on the output record for that meteor.

PROCEDURE REGRESSION fits a regression line to the ln (amplitude) versus time curve for those points above a given threshold. This was modified to fit a weighted regression line as well for the third set of data.

PROCEDURE AMPLITUDE finds the maximum echo amplitude and then a point 25% of the echo duration away from the maximum to avoid plasma resonance effects. The end of the echo is found, but if its duration is greater than 0.3s it is terminated at that time to reduce the effect of second reflection point formation. If at least five pulses remain the regression line is fitted.

PROCEDURE RANGE finds the mean and standard deviation of the range values, if their associated pulse signal amplitude is sufficiently large. The range value is corrected by subtracting half of the pulse width and the receiver delay. The receiver delay had been found by measurements on aircraft echoes by Poulter (1978) and was checked with an oscilloscope by direct measurement of a calibration pulse put into the receiver and into the oscilloscope.

PROCEDURE DOPPLER was very similar to the subroutine used by Poulter to convert doppler information to wind velocities and standard deviations for each frequency offset.

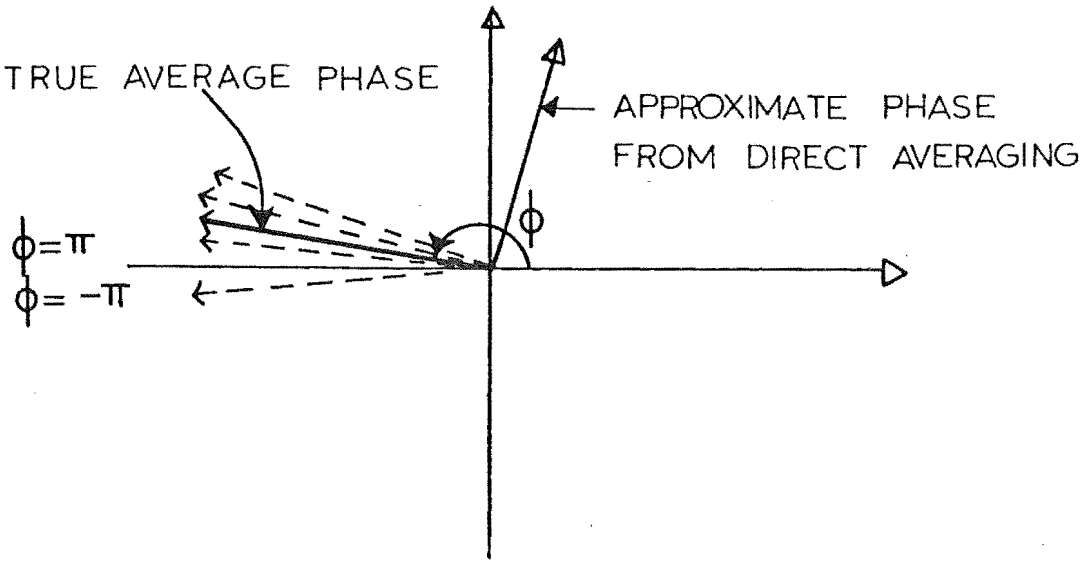

Figure 7.1: Gross errors from phase averaging

PROCEDURE PHASEHEIGHT calculates the echo height from the relative phases and range information (note that is not the "phase height" often used in ionospheric work, but is the meteor echo height inferred from measurements of phase differences at the receivers). The phases of pulses that occurred near the echo maximum were averaged (because of the effect of Fresnel diffraction discussed in section 3.6), but first a check was made to see if the first phase was in either of the third or fourth quadrants (Fig. 7.1). Between these quadrants the phase is discontinuous so that an average of phases on both sides of this point will give an incorrect result. If the first phase was in these quadrants, the negative phases were increased by 360^{o} and their average decreased by 360^{o} if necessary. Standard deviations were also calculated so that the height uncertainty could be found.

The phases were then corrected by subtracting the differential phase and the angle γ was found unambiguously. The angle β could only be found by considering the echo height so the phase angle was increased in steps of 360^{o} until the height was in the range 70 to 120 km. Heights outside this range were assigned the value nearest to 95 km. Ambiguities in height arising in this process were removed in later selection by considering range and azimuth values. Finally the angles γ and β were used to find the elevation and azimuth of the echo and the height uncertainty was found.

PROCEDURE LINEDENSITY estimated the line density of electrons in the train from the echo range, amplitude, elevation and azimuth. The antenna horizontal radiation patterns were known from measurements and the elevation pattern had been calculated by Poulter (1978) from the echo elevation distribution. A correction was made for the theoretical reduction in peak amplitude due to the train's initial radius, values from Baggaley's results (shown in Table 2.1) being used. This line density estimate, obtained by using a rearranged form of equation 6.1 for the backscatter case, assumes that q is directly proportional to the received amplitude which is only true for underdense meteors (see section 7.3).

The main program called each procedure in turn and some procedures twice for double echoes. The calculated values for each processed echo were then written on to magnetic tape before further selection.

The final stage of analysis was to select suitable echoes and process them in various ways. Three forms of the program were used: the first produced frequency distributions of the data (this form is shown in Appendix 3); the second found the coefficients necessary to calculate regression lines and the third produced data files which enabled echo properties to be plotted.

PROCEDURE OFFSPECANGLE calculated the magnetic off-specular angle for each selected echo. A modification to this procedure enabled the train orientation to be calculated if a double echo had occurred.

Several selection criteria were used for all echoes. Those with negative values of D, which could be inferred if there was pronounced echo fading (so that there was an overall increase in echo amplitude in the region where the regression line was fitted), were rejected. The correlation coefficient found in fitting a linear regression line to the echo decay curve was used to select decays having a good fit when required. Echoes whose peak amplitudes were near the maximum for the amplitude detector were rejected as the phase information from the A/D converter become meaningless for such amplitudes as did estimated line densities. Echoes with slow rise times were rejected as they had probably drifted into a specular position instead of being created in such a position (ideally echo amplitudes should increase quickly to a maximum as the train is formed - see Figs 3.9 and 3.10). This criterion was not so strict as to exclude low velocity meteors. Echoes with ranges that indicated that

the echo height could be ambiguous were rejected, the choice of minimum range depending on the interferometer spacing used. Echoes whose height uncertainty was greater than 5 km or whose range uncertainty was greater than 1 km were also rejected as were echoes for which fewer than three pulses had been used to determine the height. Echoes were only used if they were recorded within an hour of the previous differential phase calibration, except in the third run where calibrations were infrequent in the west direction. Persistent echoes were identified by their time of occurrence and the similarity of their range value to that of the previous echo. Finally, where only underdense echoes were wanted an upper limit of $q = 2 \times 10^{13}$ m^{-1} was used as a selection criterion.

7.3 GENERAL RESULTS

(1) Echo Height Measurement

The tests of the interferometer described in section 6.4 showed anomalous performance of the first - second antenna pair for negative azimuths. The spacing of 17.2 λ that was inferred from the tests, if correct, would cause an underestimation of echo heights of nearly 25 km for negative azimuths (to the east of the beam centre) if a 20λ spacing was used in analysis. Normally, a decreased spacing would cause heights to be overestimated, but if the decrease is large enough, the overestimated height will be above the meteor region and the analysis program would assign it to a lower height. To check this, the distributions of echo heights

and the mean heights for the positive and negative azimuths are presented in Figs. 7.2 to 7.5.

Figs 7.2 and 7.3 show data recorded with the same interferometer. The marked reduction in echo rate for the negative azimuths for the first set of data (Fig. 7.2) is surprising in view of the symmetry of the measured transmitting antenna radiation pattern and the symmetry of the second set of data. A possible cause of this asymmetry is interference from corona discharge from power lines 50 m away. This interference was initially a problem, but was not as severe in later runs because of prevailing weather conditions. This interference occurred in the negative azimuths, closest to the power lines, and would thus affect the phase measurement of the negative azimuths more than the positive ones. Noisier measurements are rejected by the selection criteria which could thus create the asymmetry. This was checked by finding the ratio of positive to negative azimuths with relaxed selection criteria giving 1.26 instead of 2.22 for more strict criteria which suggests corona discharge is the cause.

The mean height for negative azimuths in the second set of data is 4.2 km higher than that for positive azimuths which implies that the effective interferometer spacing is not reduced to 17.2 λ, but to 19.93 λ - a change of 0.80 m from the theoretical 20 λ. This suggests that either phase tests carried out at ground level are not reliable or the particular test was faulty. In such tests the direction in which the interferometer measures phase is perpendicular to that used in practice.

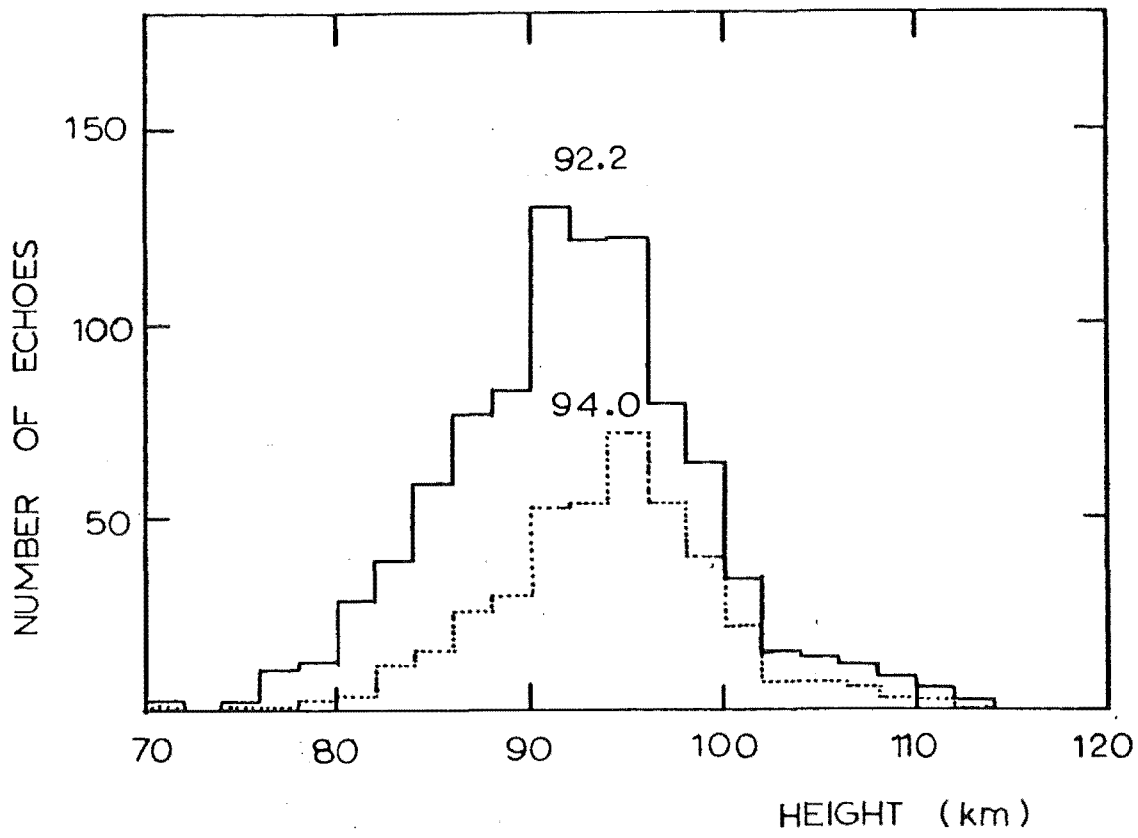

Figure 7.2: Height distributions for positive (——) and negative (•••) azimuth angles - first set of data.

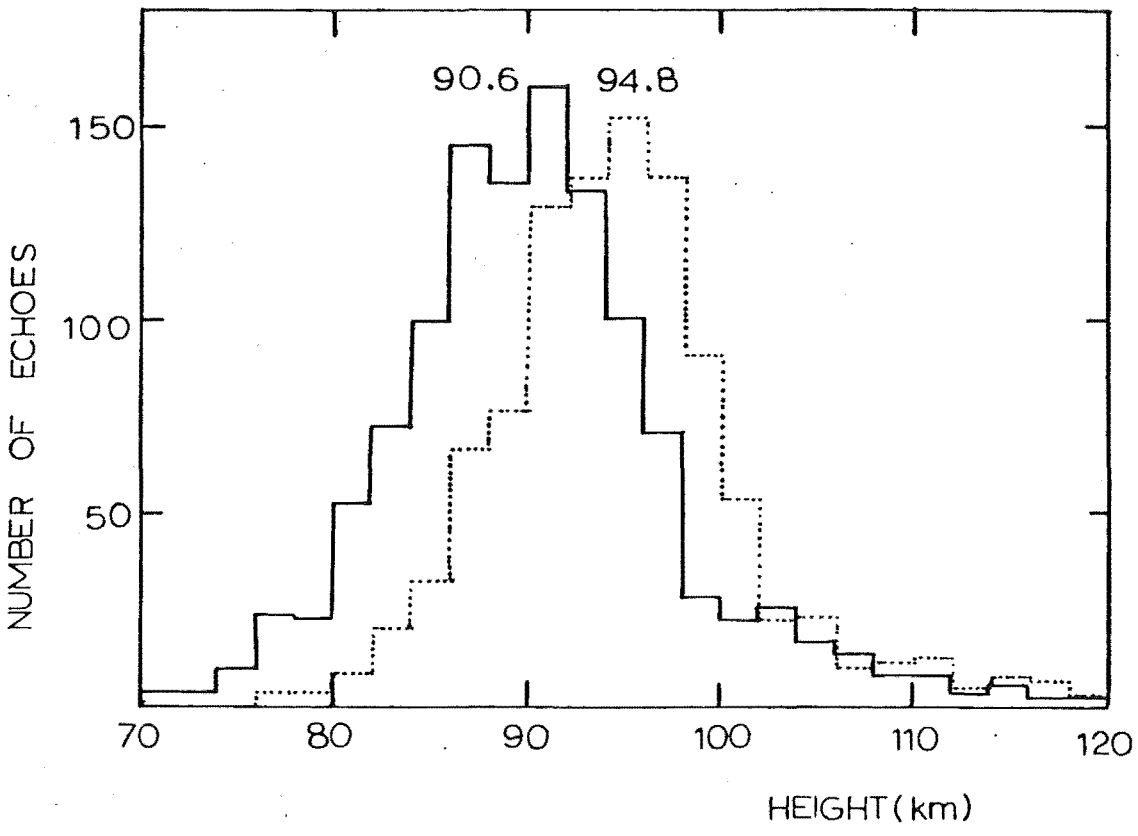

Figure 7.3: Height distributions for positive (——) and negative (•••) azimuths - second set of data.

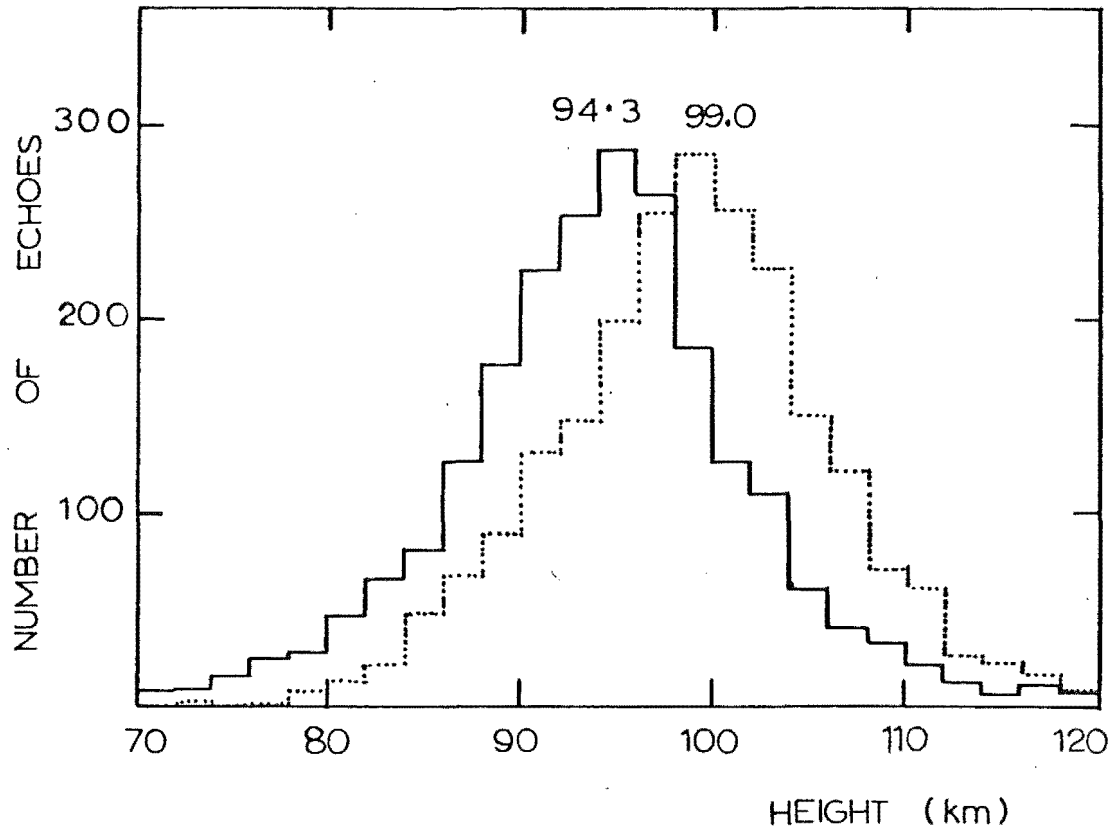

Figure 7.4: Height distributions for positive (——) and negative (•••) azimuths - third set of data (magnetic south).

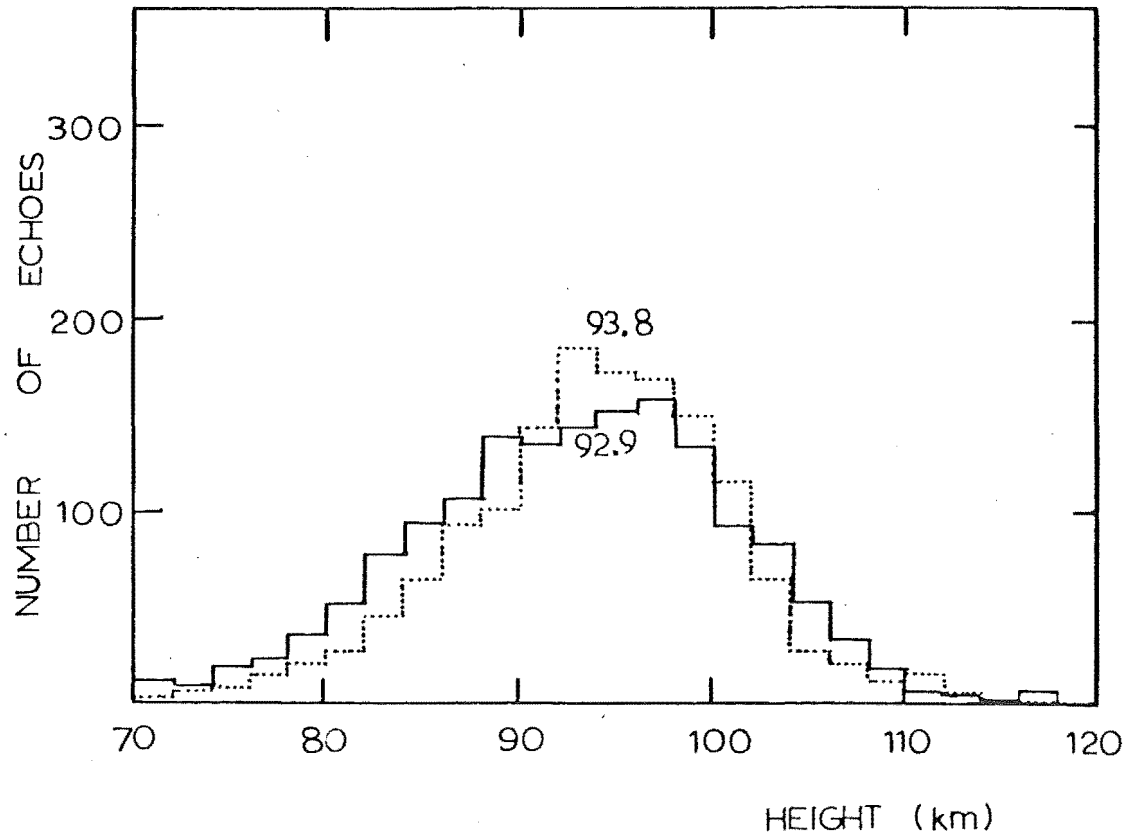

Figure 7.5: Height distributions for positive (——) and negative (•••) azimuths - fourth set of data (west).

Each set of southerly data shows a similar trend including the third set where a smaller interferometer spacing was used. However, the west data does not show the effect which indicates it is due to the south interferometer and not the data processing equipment.

It is possible that this is a physically real effect, perhaps caused by higher meteor velocities in a certain direction which would tend to produce different heights of ionization. For the first two sets of data the azimuth range of $\pm 8^{o}$ is very small to be able to resolve a physical effect. The fact that the larger range of $\pm 15^{o}$ for the third set of data gives rise to only a 0.5 km increase in the height difference suggests the effect is not real, especially as the west data shows no effect. Thus irregularities in ground conductivity, the presence of other conductors (e.g. power lines) or some effect in the antennas themselves are the likely cause.

The systematic height error of about 4 km is not critical for this work. For the two-station experiment height differences are important, but for the near-perpendicular trains observed the azimuths for each reflection point will be very similar. In terms of angle measurements (for off-specular angles) a change of 0.7^{o} could be expected across the azimuth range. The error will markedly increase the scatter observed in D versus height data however.

(2) Antenna Radiation Patterns

The way in which echoes are distributed in azimuth can be used to infer the combined transmitting and receiving azimuthal radiation pattern. If the sporadic meteor radiants are uniformly distributed over the observer's hemisphere and the exponent, s, of the meteor mass distribution is equal to 2(see sub-section 5), the combined antenna voltage pattern (effectively a power radiation pattern) is proportional to the echo rate at each particular azimuth (Kaiser, 1953).

Fig. 7.6 shows the inferred azimuth patterns for the first (⊙) and second (x) sets of data, together with the theoretical pattern. The agreement is good except for the offset of the pattern maximum from 0^{o}. This is most pronounced for the first set of data and corresponds to the asymmetry discussed in sub-section 1.

Fig. 7.7 shows the inferred patterns for the third (X, that is the third run in the south direction) and fourth (⊙, west direction) sets of data. Two theoretical patterns are shown because of different antenna spacings used in the transmitting arrays. Again the magnetic south data (third set) fit well which confirms that this interferometer works well in the azimuthal direction. However, the pattern in the west direction is broader than expected, behaviour that was also noted by Poulter (1978). He experienced trouble with feeding arrangements for the west transmitting array, but that was not the case for these results, although one driven element did develop a fault

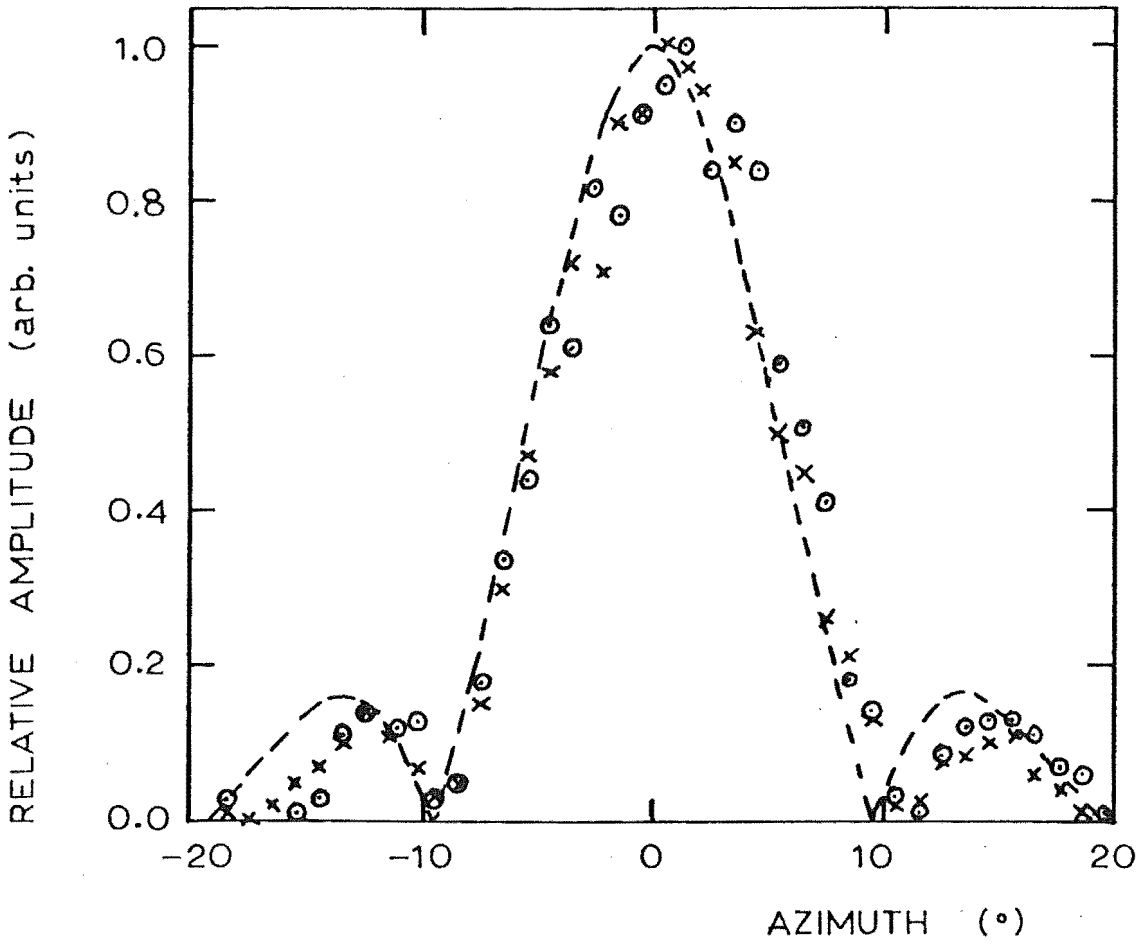

Figure 7.6: Inferred and theoretical (---) combined antenna azimuth patterns for the first (⊙) and second (X) sets of data.

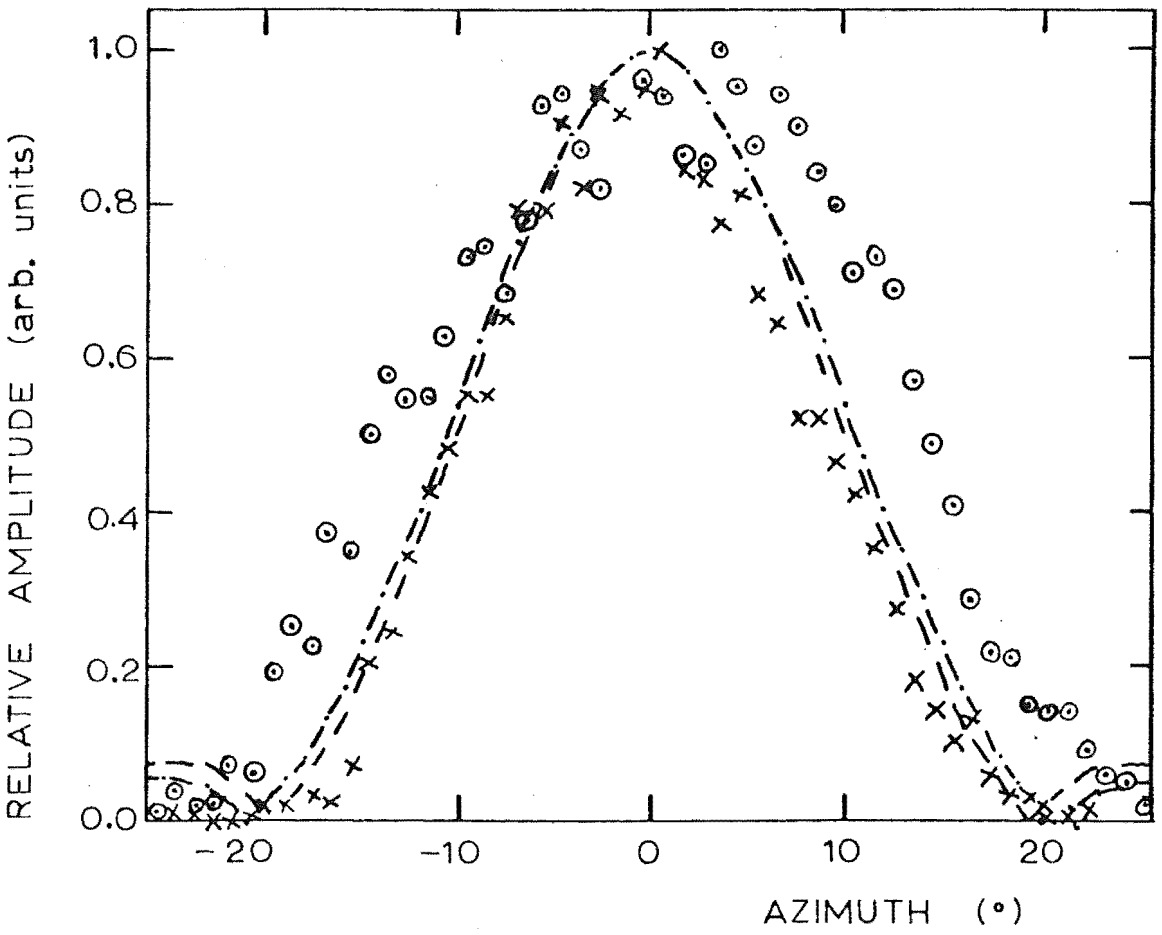

Figure 7.7: Inferred and theoretical combined antenna azimuth patterns for the third (X,---) and fourth (⊙, -·-·-) sets of data.

during the run. The difference could be caused by the west receiving antennas, but this was not apparent in a phase test performed by Poulter.

The combined elevation radiation patterns can also be inferred from the echo rate. This involves the same assumptions as for the azimuth pattern in addition to assuming that all meteors occur at the same height (the spread in the meteor height distribution is small in comparison with the overall height). Then with a flat earth geometry, the vertical radiation pattern, S(E), can be related to the echo rate, n(E), by

$$S(E) = \left(\frac{n(E)}{\cos^{2}(E) \sin^{\frac{1}{2}}(E)} \right)^{\frac{1}{2}} .$$

This expression is only valid for underdense meteors at elevations greater than about 10^{o}.

Fig. 7.8 shows the inferred elevation pattern for the first (⊙) and second (X) sets of data. For the antenna height of 6.8 m a maximum in the elevation pattern would be expected at 25^{o}. However, restrictions on the minimum range of echoes received rejects echoes from above 17^{o} so that the inferred pattern does not resemble the theoretical pattern.

Fig 7.9 shows the patterns for the third (X) and fourth (⊙) sets of data. The beam maxima are much nearer to the expected 25^{o} than for the previous data. The minimum range of 200 km will discriminate against echoes with elevations greater than 28^{o} which causes the sharp cutoff at the top of the pattern.

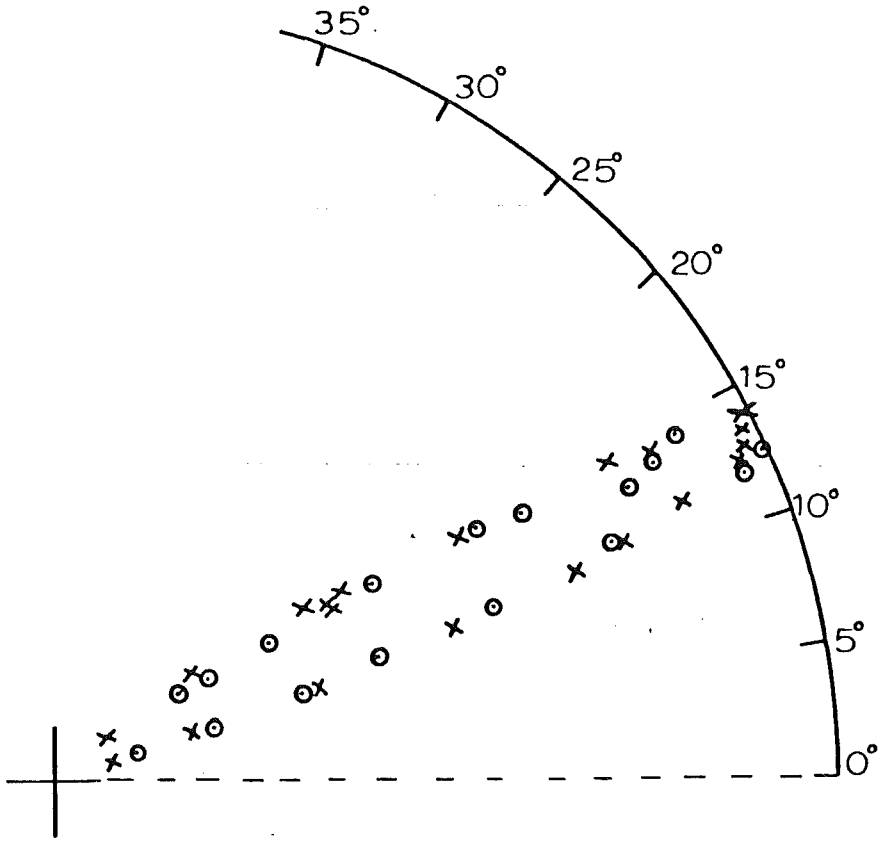

Figure 7.8: Inferred combined elevation patterns for the first (0) and second (X) sets of data .

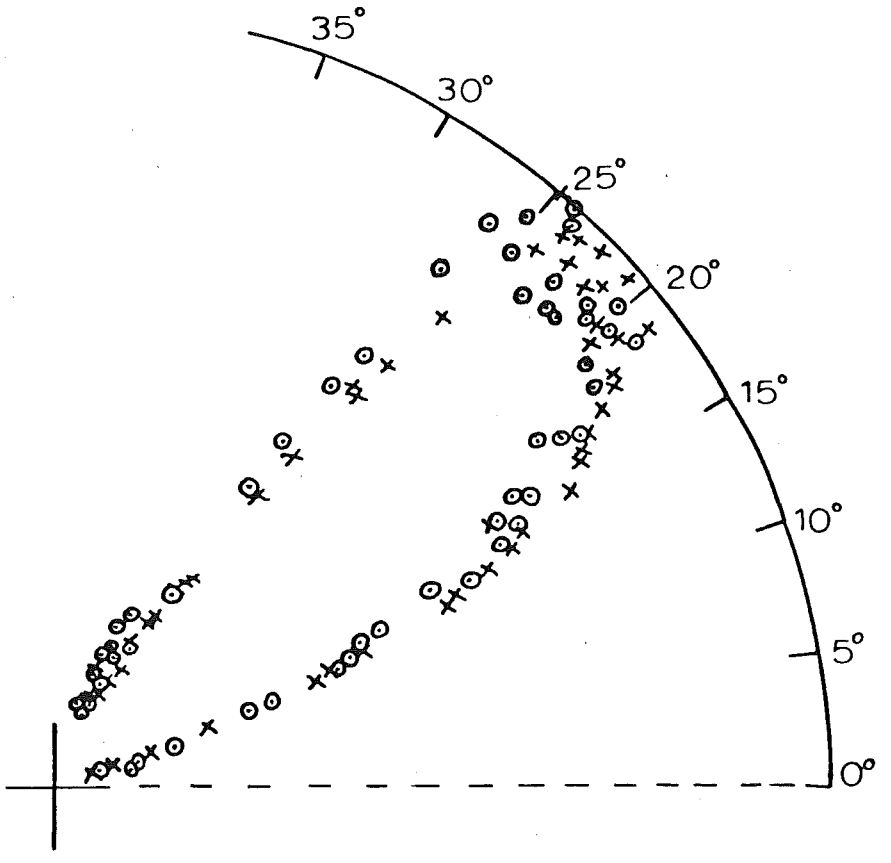

Figure 7.9: Inferred combined elevation patterns for the third (X) and fourth (0) sets of data.

(3) Range and Height Distributions

Fig. 7.10 shows the range distributions for the first and second sets of data. Ranges of less than 300 km are not included because the range gates were set at about this value to increase the proportion of specular echoes and to avoid height ambiguities. The antenna elevation patterns can be used to predict the range distribution, but this was not considered worthwhile in this case because of the effect of the range gate settings on the elevation pattern. The difference in slope for the two sets of data is attributed to the different range gate settings used in recording the data.

Fig. 7.11 shows the range distributions for the third and fourth sets of data. As identical range gate settings were used, the slight difference in slope for ranges past the peak of the distribution is probably due to slight differences in the elevation patterns of the south and west antennas. This agrees with Fig. 7.9 where more power appears to be radiated at higher elevations on the west antenna, thus giving smaller range values.

Fig. 7.12 shows the height distributions for the first and second sets of data (with the mean echo heights indicated) while Fig. 7.13 shows those for the third and fourth sets of data. The data of Poulter (1978), recorded in July, 1977, had a mean height of 95 km, but no corrections were made for tropospheric bending or the slope of the ground between the interferometer and echo transponder sites.

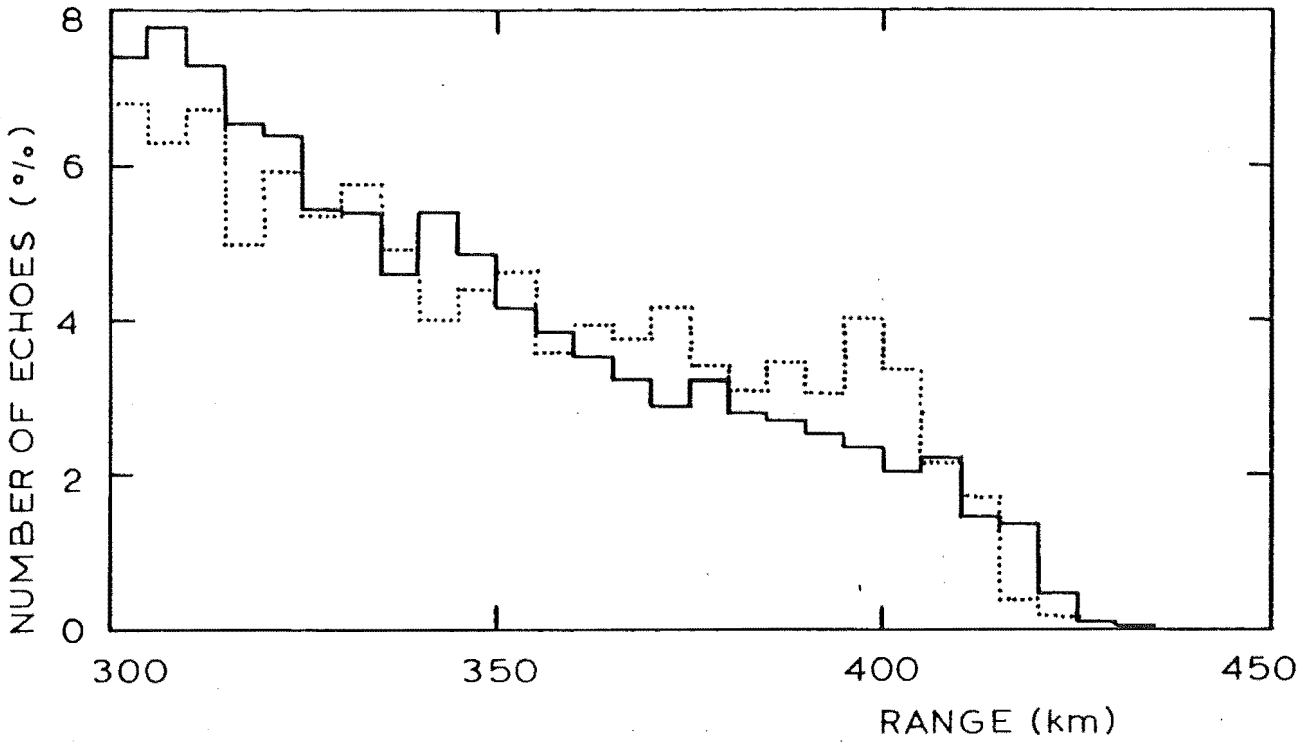

Figure 7.10: Echo range distributions for the first (•••) and second (——) sets of data.

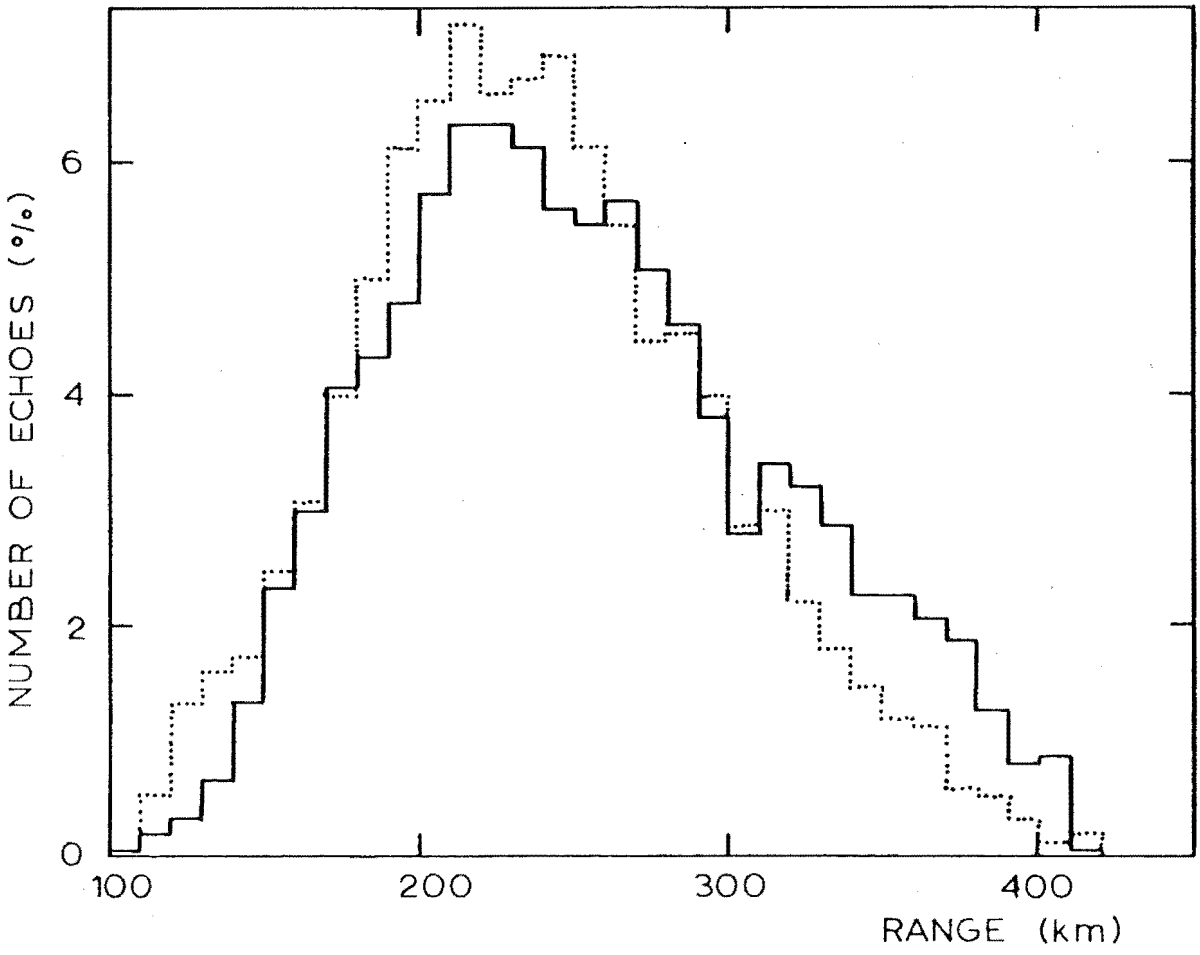

Figure 7.11: Echo range distributions for the third (——) and fourth (•••) sets of data.

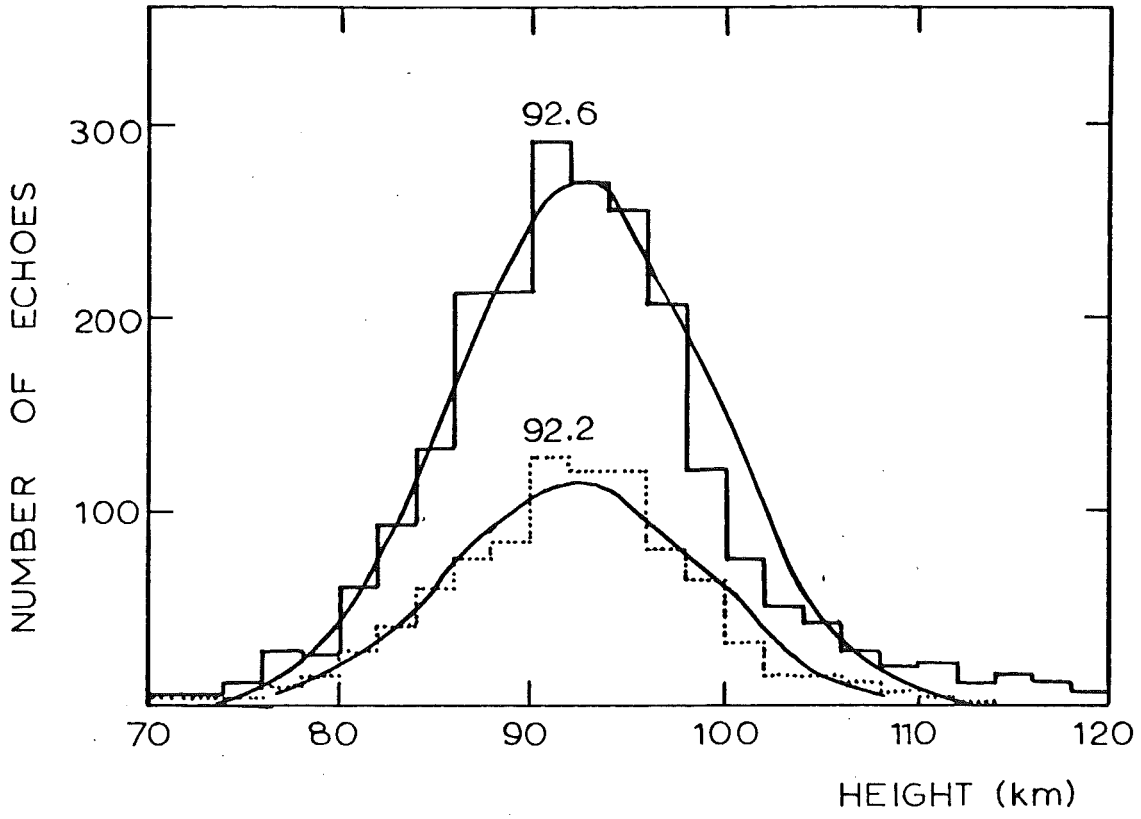

Figure 7.12: Echo height distributions for the first (•••) and second (——) sets of data.

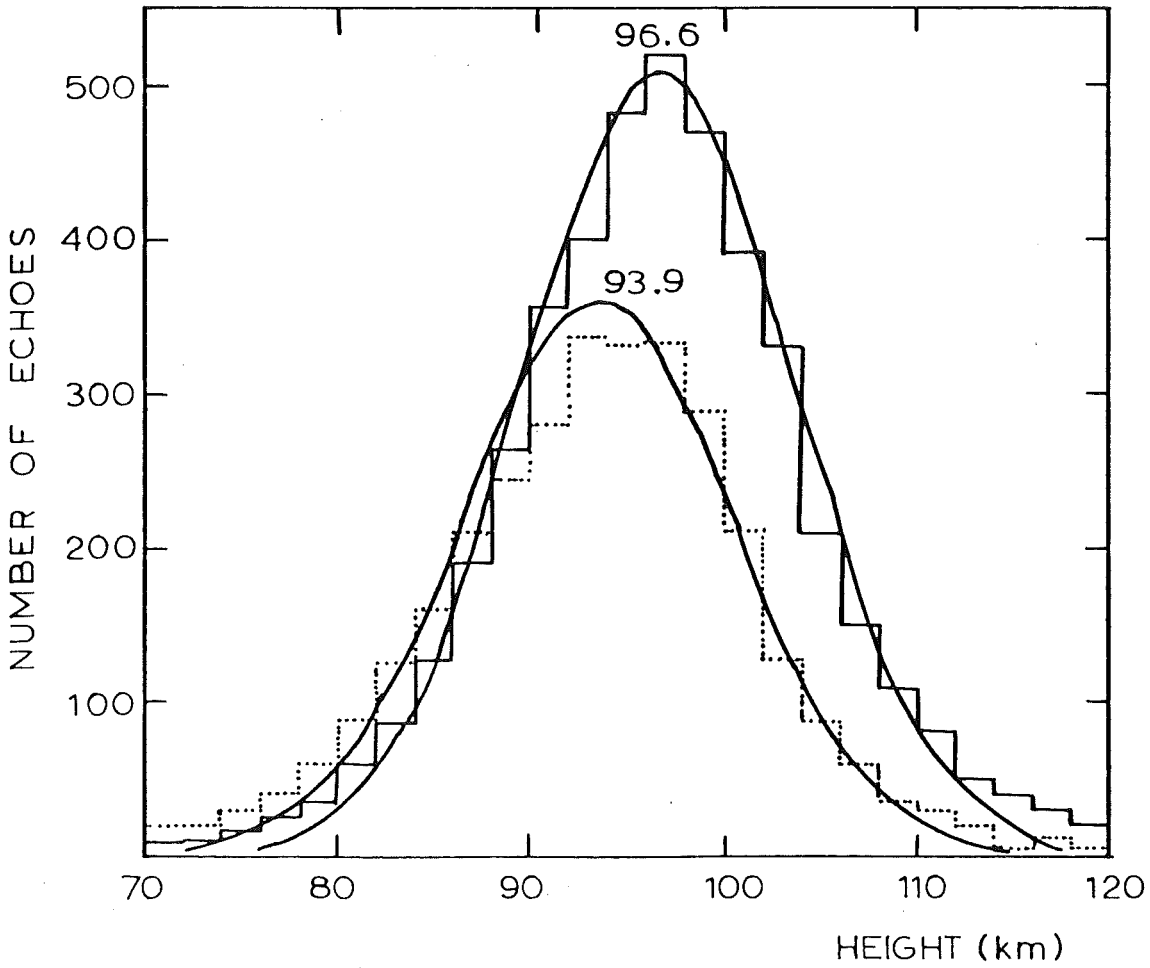

Figure 7.13: Echo height distributions for the third (——) and fourth (•••) sets of data.

These corrections would decrease the mean height by 0.9 km. Hess and Geller (1976) found the mean echo height to vary diurnally between 90 and 95 km.

Kaiser (1954b) found that the mean height of radio meteors depends on the mean meteor velocity, the atmospheric pressure and, to a smaller extent, on the antenna patterns and system sensitivity. The mean meteor velocity varies diurnally (as the position of the apex of the earth's way changes) and annually (as the elevation of the ecliptic changes). The diurnal change in mean height found by Poulter (1978) over a period of four hours (the approximate mean time difference between the data sets 1,2 and 3,4 in the present experiment) was 2 km and was such that the mean heights of the first and second sets of data should occur 2 km above that of the third and fourth. However, annual velocity variations are probably more important. Mean meteor velocities for each month may be estimated from the data of McKinley (1951) which were collected in the northern hemisphere so that an opposite variation occurs in the south. Over the time interval between the collection of the second and third sets of data, the mean meteor velocity could be expected to increase by about 7 km/s. This would increase the mean meteor height by about 4 km which would account for most of the difference in the data.

The only difference expected between the mean heights for the third and fourth sets of data is from the slightly different sensitivities. The more sensitive south antennas would "see" fainter meteors which classically ionize at

greater heights. However, some recent observations do not support this classical theory (Baggaley and Webb, 1980). A new mean height for the third set of data was found by selecting meteors with the largest line density so that the total number was the same as for the fourth set of data. This increased the mean height from 96.6 km to 98.6 km which is in the opposite direction to that expected classically.

As differences in system sensitivity do not account for the difference in mean heights it appears that the cause could be experimental. An uncertainty in the phase calibration for the west interferometer of 0.2 radians would account for the difference. The construction of a second echo transponder for this interferometer would thus seem advisable and would also allow regular differential phase calibrations while operating in this direction.

A Gaussian curve was fitted to each height distribution. A standard deviation of 6.5 km fitted the first two sets of data while 7 km was appropriate for the third and fourth sets. Kaiser (1954b) found that the width of the height distribution should depend on the atmospheric scale height and the mass distribution of the meteors. Assuming that s = 2 (see sub-section 5) and for a uniform meteor velocity, the standard deviation of the height distribution should almost be equal to the scale height. A larger spread in heights could imply systematic variations in the echo location system, but this is not apparent even for the west data where differential phase calibrations were infrequent. The larger spread in the March data (3 and

4) could reflect an increase in the scale height, but could also be caused by the longer periods over which the data were collected each day.

Some asymmetry is present in the second set of data. Kaiser (1954a) showed that this can be expected from the influence of the antenna patterns. Ionospheric refraction could cause meteor echo heights above about 100 km to be overestimated, a factor that would tend to reduce the asymmetry caused by the antenna patterns. This effect was examined by plotting height distributions for echoes that occurred during daylight hours (where ionospheric bending would be significant) and for those that occurred at night for the third set of data. Fig. 7.14 shows the night-time distribution with a Gaussian curve with a 7.5 km standard deviation fitted. Fig. 7.15 shows the day-time data where the standard deviation of the Gaussian is 6 km. No particular asymmetry is apparent in either set of data although the expected height error of 1.5 km would be difficult to resolve. The asymmetry in the second set of data is probably caused by the effective antenna elevation pattern produced by the range selection used.

The large spread in heights for the night data suggests that either a wider range of meteor velocities occurred or the scale height was greater. These data do include both times of peak meteor velocity (0600 hours local time) and minimum velocity twelve hours later. The day-time data were recorded mainly from 0700 hours to 1000 hours as sporadic-E reflections prevented operation during most of the day.

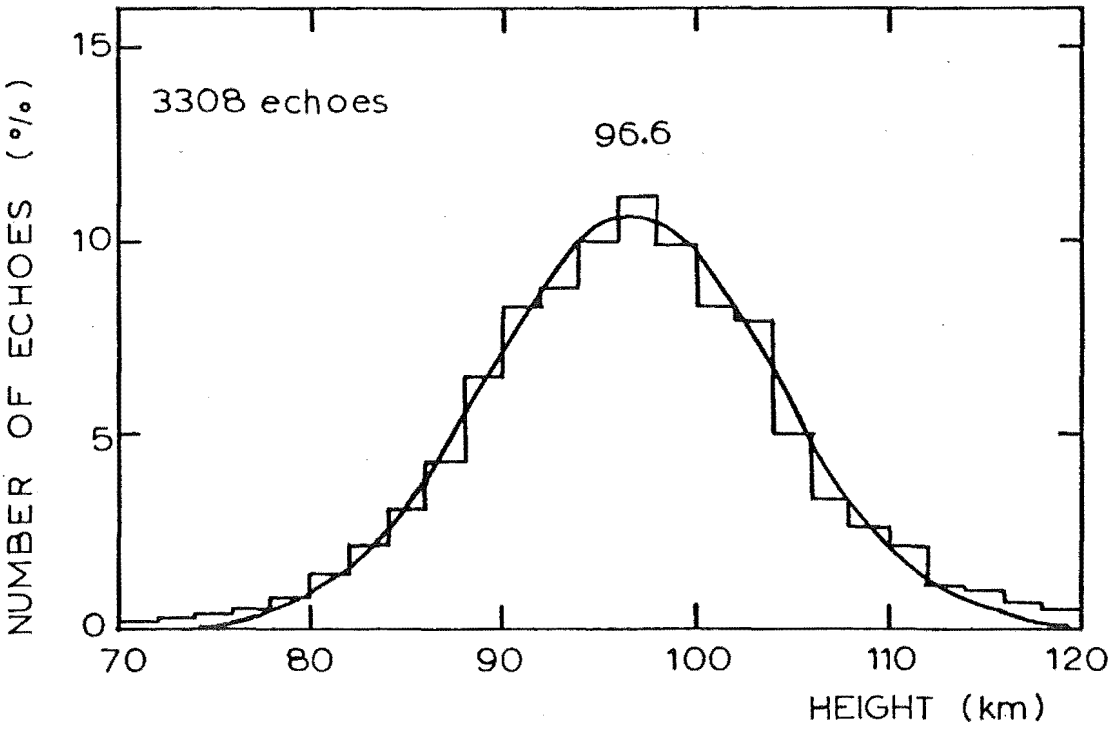

Figure 7.14: Echo height distribution for the part of the third set of data recorded at night.

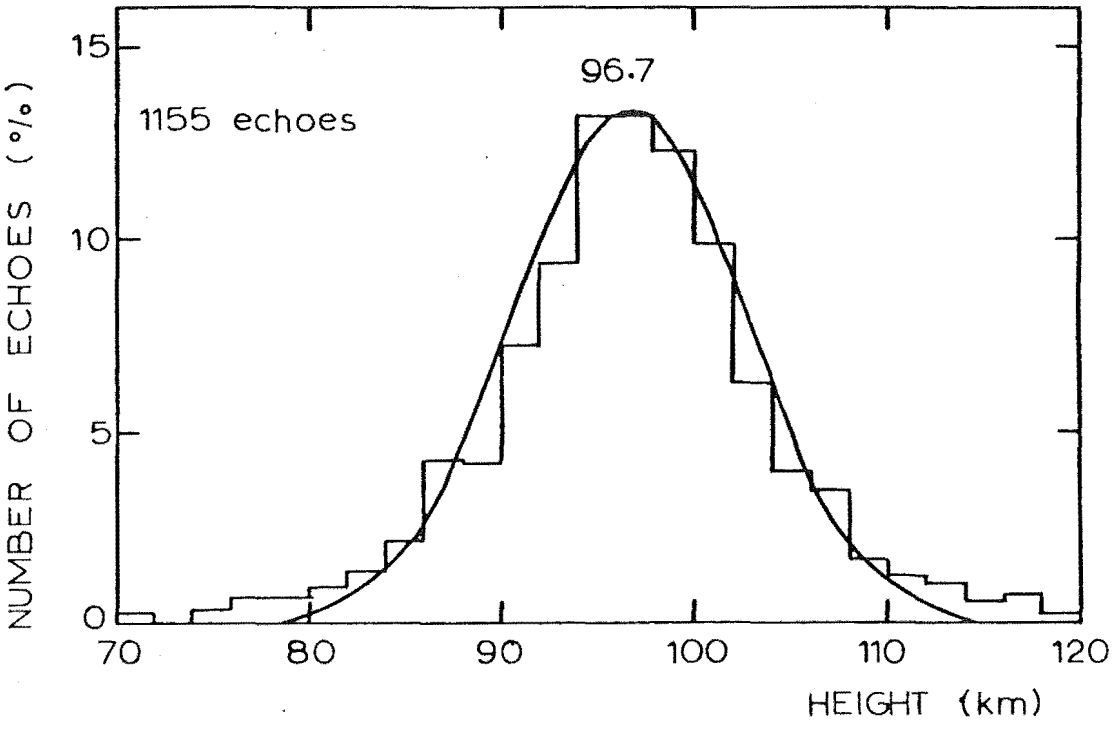

Figure 7.15: Echo height distribution for the part of the third set of data recorded during the day.

The mean meteor velocity would thus be more uniform in this case which would give a smaller height spread. There was little change in the mean meteor height for the two sets of data.

(4) Measurement Uncertainties

The uncertainties in the measurement of elevation, azimuth and echo height were calculated as a function of the signal-to-noise ratio on the peak echo amplitude and are shown in Figs 7.16 to 7.18. The uncertainty referred to is one standard error of the mean value and was found from the uncertainties in the measured phases and ranges. The use of a long interferometer spacing (the first two sets of data) appears to have had only a small effect on the elevation uncertainty (an improvement of 2.5 times was expected). This is possibly because about half as many individual phase measurements can be used to determine the echo height near the peak echo amplitude when a P.R.F. of 150 Hz is used, thus increasing the uncertainty by a factor of about $\sqrt{2}$. If this were the case, the azimuth uncertianty for the third set of data should be less than that for the second set (by $\sim \sqrt{2}$) which is not the case, so the long interferometer spacing may have introduced other uncertainties. For example, the Fresnel phase variation (discussed in section 3.6) would be increased because the distance between the specular reflection points for the first and second antennas would be longer. However, the difference in height uncertainties for the

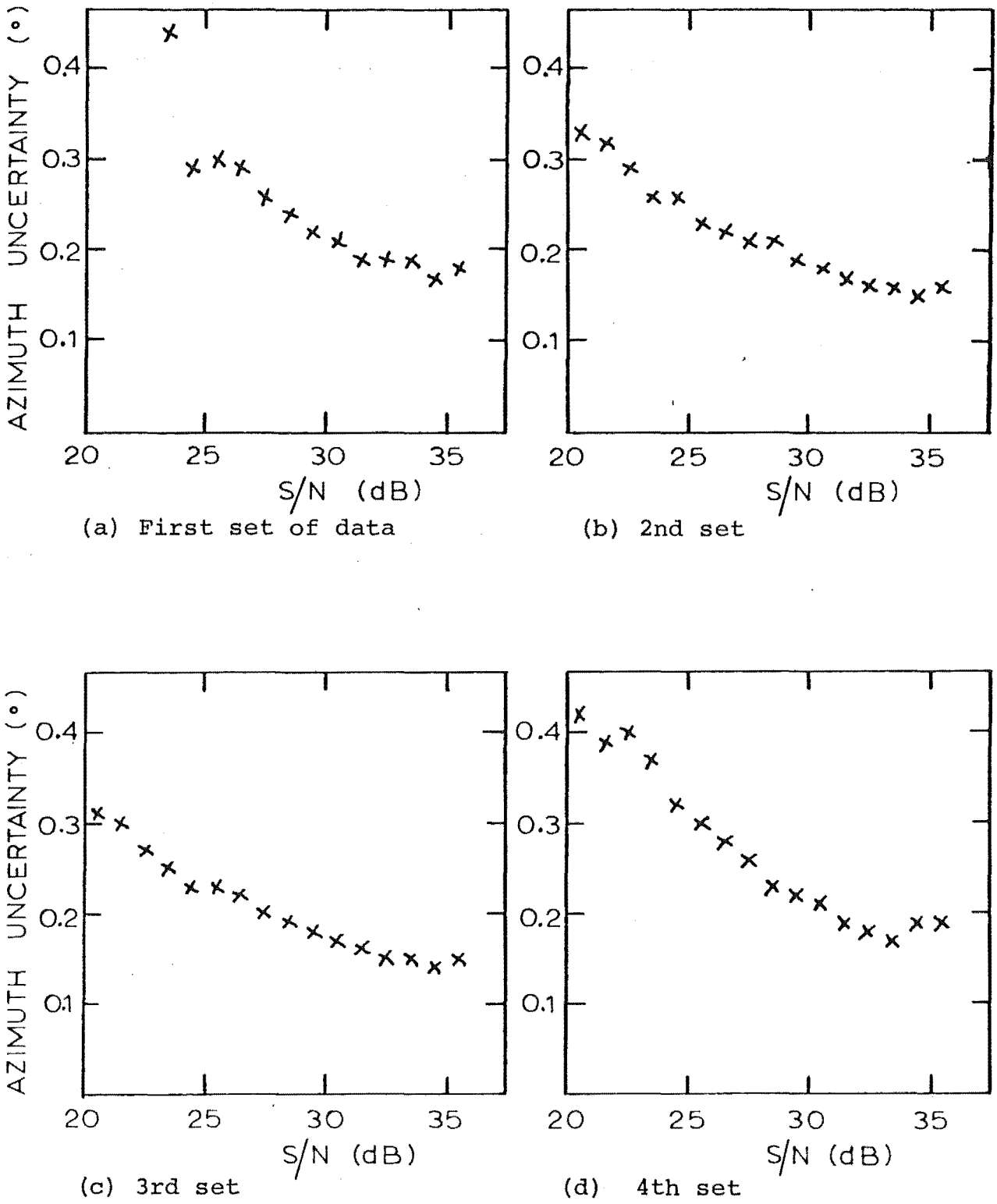

Figure 7.16: Estimated azimuth measurement uncertainty as a function of signal-to-noise ratio for the maximum echo amplitude.

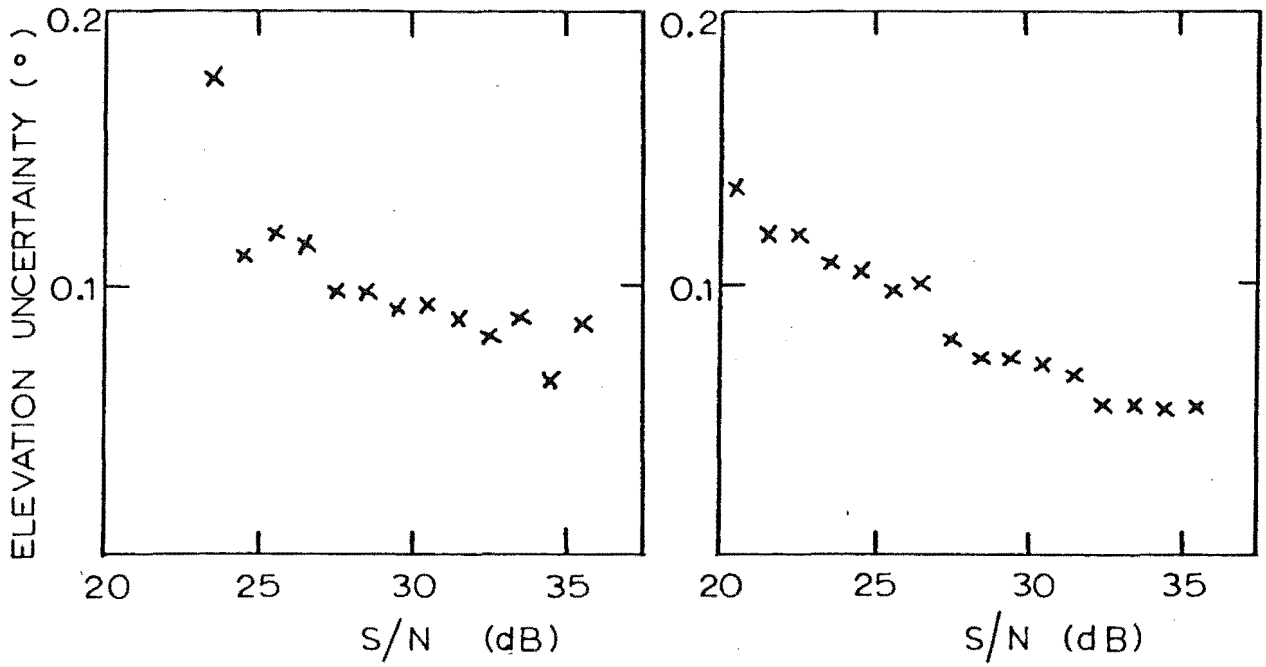

(a) First set of data

(b) 2nd set

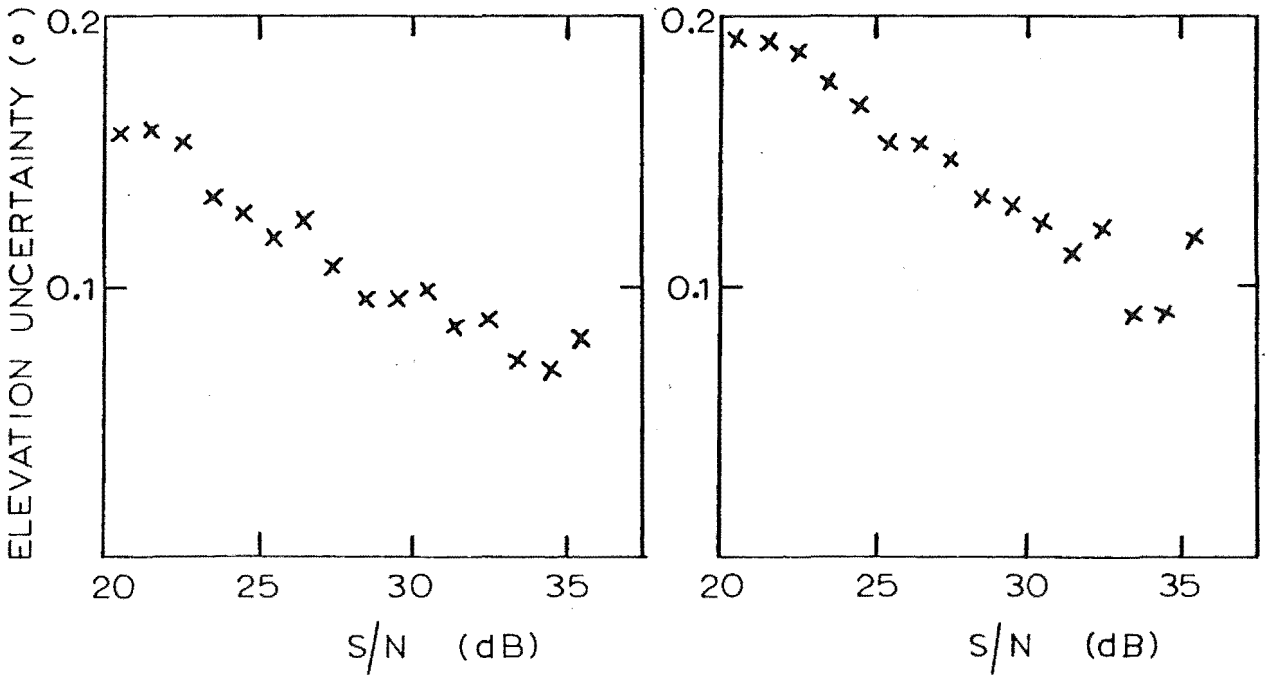

(c) 3rd set

(d) 4th set

Figure 7.17: Estimated elevation measurement uncertainty as a function of signal-to-noise ratio.

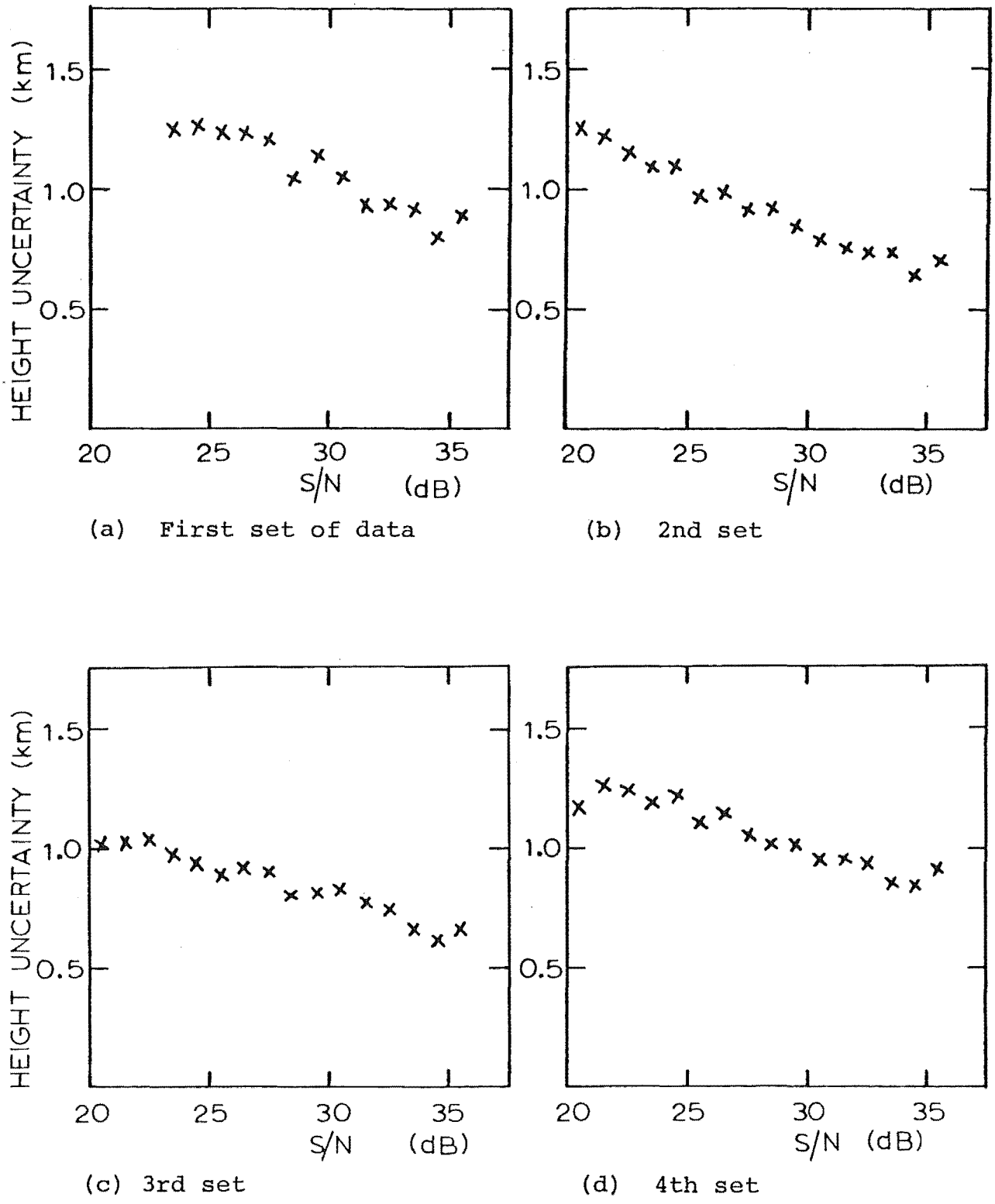

Figure 7.18: Estimated height measurement uncertainty as a function of signal-to-noise ratio.

third and fourth sets of data is largely accounted for by the interferometer spacing difference (d_{12} = 9λ for 3 and 7λ for 4).

A consideration of the height uncertainty introduced by the d_{12} spacing of the interferometer is worthwhile. This distance was determined with a metal tape measure to within an estimated uncertainty of 0.04% which would give a systematic height uncertainty of 0.31 km. However, this could be increased by variations in the pole alignment which was judged by eye and by differences in the position of the phase centre of each antenna. If a more precise absolute height determination was required the use of a survey chain for length measurement and a theodolite or spirit-level for pole alignment would seem worthwhile. The problem of the position of relative phase centres remains, but this can be minimised by the use of identical antennas and matching arrangements as were used in this work.

Although the height uncertainty shown in Fig. 7.18 is about 1 km, it must be remembered that most of the received power comes from the first Fresnel zone which, for an echo range of 300 km, is 2.6 km long and for most observed meteors will extend over a height of similar extent. Thus it is the uncertainty with which the height of this extended region is located that is given. Furthermore, this estimate does not take account of the systematic height uncertainty that was discussed in subsection 1.

The uncertainty for the ionization line density can be calculated from the uncertainties in elevation and azimuth. For the narrow transmitter beam used for the first two sets of data the greatest uncertainty is at the edges of the antenna pattern and is about 26%, while for the third and fourth sets it is about 11%. The azimuth antenna pattern is the critical factor so that wide beam antennas have a big advantage in accurate line density estimation. Representative uncertainties of 0.25^{o} for azimuth, 0.1^{o} for elevation and 1.2 km for height (to calculate r_o) were used in the calculation. As more echoes occur near the centre of the antenna pattern than near the edges, the uncertainty will usually be much less than that indicated. Even with a 26% uncertainty, the method gives a useful estimate of q so that underdense echoes can be selected. As for the echo heights, this uncertainty does not apply to the absolute value of q as this depends on the accuracy of antenna gains and transmitter power output. An absolute estimate of q can be derived from the cumulative line density distribution (discussed below) which can then be compared with that calculated from transmitter power, antenna gain and echo range.

(5) System Sensitivity

If it is assumed that the meteor mass-frequency distribution, ν_m, is given by

$$\nu_m \, dm = b \, m^{-s} \, dm$$

(Kaiser, 1953), the expected slope of a cumulative line density distribution can be shown to be

$$\frac{d \log[n(>q)]}{d \log[q]} = 1 - s \qquad 7.1$$

where m is the meteor mass, b is a constant, s is the meteor mass exponent and n(>q) is the number or frequency of meteors that have an electron line density greater than q.

The mass exponent for sporadic meteors is taken to be 2 in this work from the results of Hess and Geller (1976). An analysis of the results from a less sensitive system by Jones and Collins (1974) gave s = 2.17. The difference is probably not important in estimating system sensitivity.

As the underdense limit is approached, received echo amplitudes become less dependent on electron line density so that for overdense meteors $A \alpha q^{\frac{1}{4}}$. This means that the line densities estimated here will become unreliable as the underdense limit is approached. Unfortunately, the dynamic range of this system (from 20 dB above noise to 36 db above) limits measurements to a spread of line densities that does not embrace the transition region. It is thus more difficult to determine the system sensitivity accurately.

The cumulative frequency - line density distributions for each set of data are plotted in Figs. 7.19 and 7.20 together with lines with slope -1. The departure of the data from the line of slope -1 at small line densities is

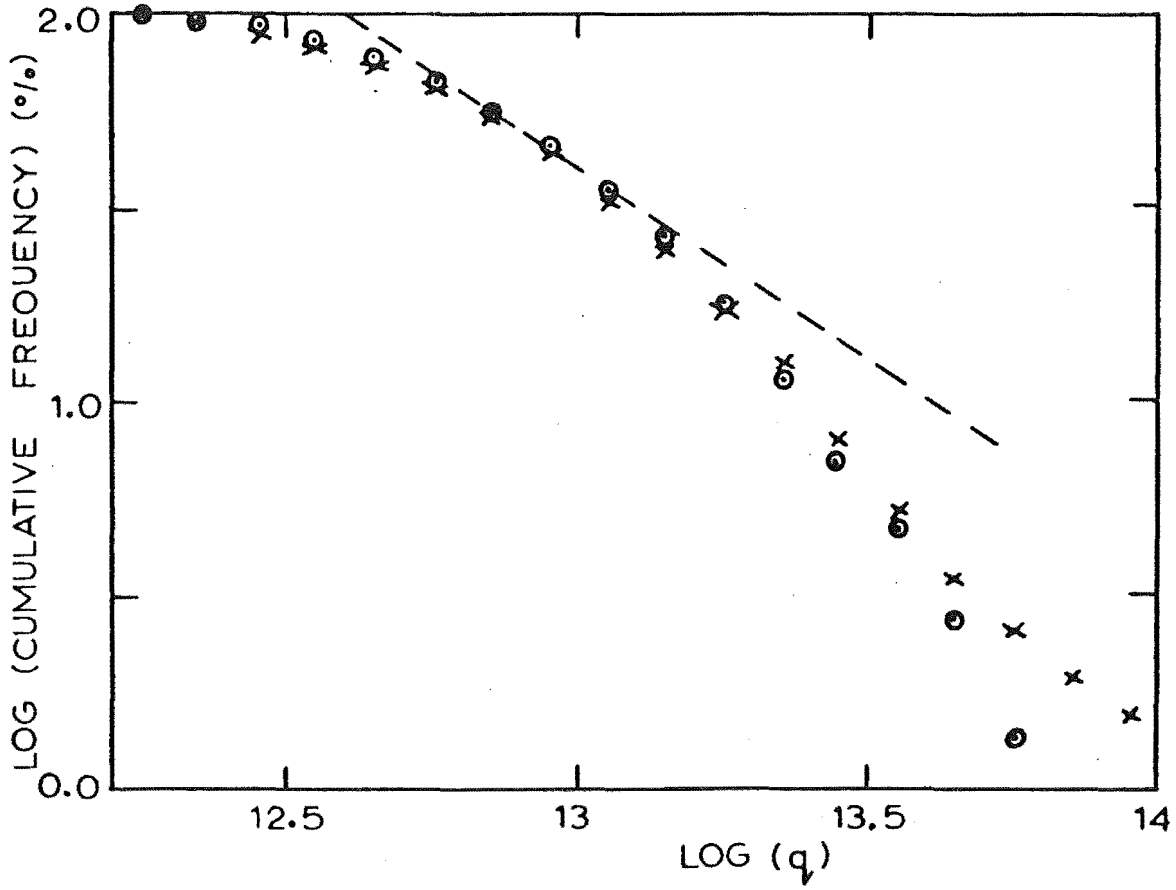

Figure 7.19: Cumulative frequency vs line density for the first (⊙) and second (X) sets of data.

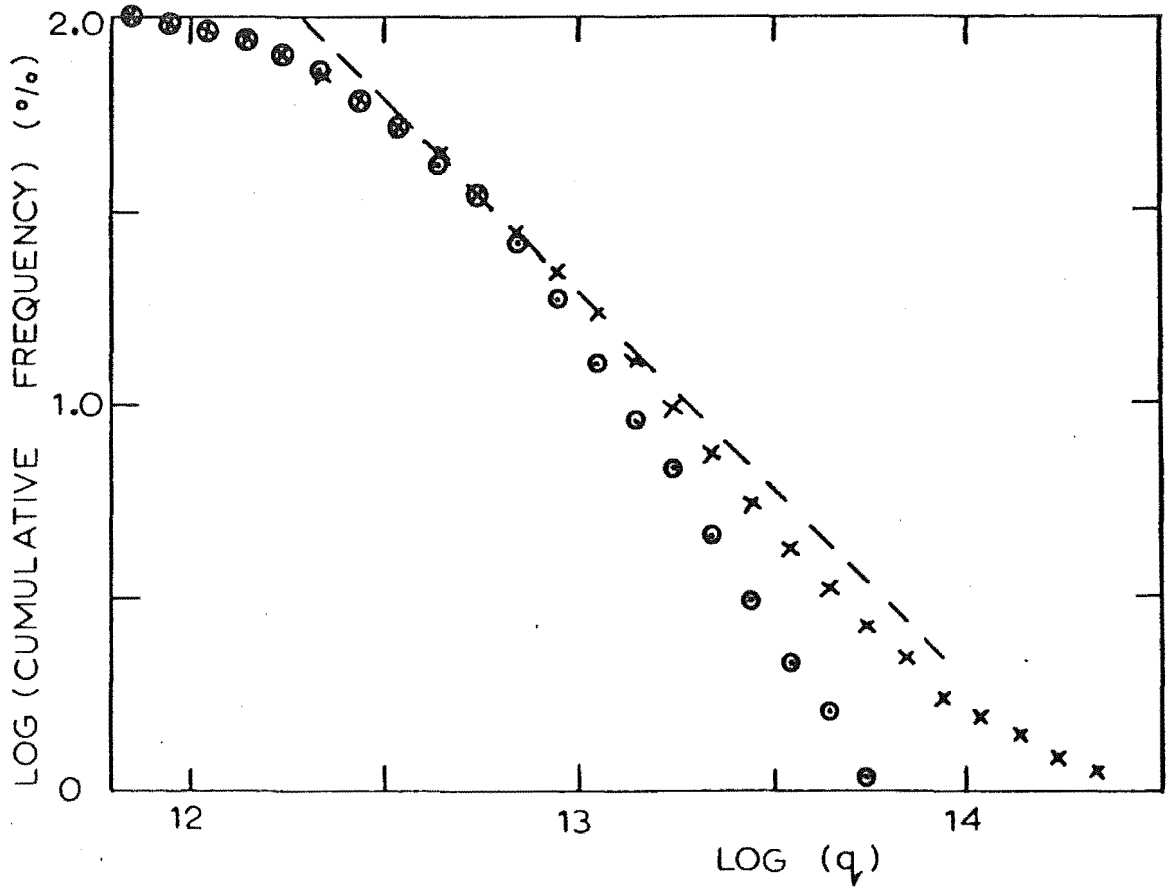

Figure 7.20: Cumulative frequency vs line density for the third (X) and fourth (⊙) sets of data.

caused by the discriminator trigger level i.e. faint echoes would need to occur in the middle of the radiation pattern to trigger the system so that many faint echoes will not be detected. The behaviour of the data at large line densities is influenced by receiver saturation and by the method of estimating q (it has been assumed that q is proportional to received amplitude).

One way in which to estimate the system sensitivity is to find at what value of q the curve is expected to depart from -1. This was determined from the full-wave scattering theory of Poulter (1978) to be $(8 \pm 2) \times 10^{12}$ m^{-1}. Generally, the data depart from this line at $q = 1.6 \times 10^{13}$ m^{-1} which is greater by a factor of two than expected suggesting that the system is more sensitive than estimated.

Another way of estimating q is by determining the apparent s value, s_a, from the results and then using reflection theory and the known s value to find q for the point where s_a was measured. This approach was described by Jones and Collins (1974), but an adaptation of their method using Poulter's reflection theory calculations is used here. s_a was calculated from a measurement on the most linear portion of the third set of data and was found to be 2.18 which corresponds to $q = (1.7 \pm 0.2) \times 10^{13}$ m^{-1}. The estimated line density for the centre of this linear part of the data is 1.6×10^{13} which agrees well. This latter method is probably more accurate than the former.

The third and fourth sets of data show that the system was more sensitive when used with two antennas in the transmitting array than with four. This is caused by the range selection imposed on the first two sets of data where the mean range is 345 km compared with 240 km for the later run. This also reduces the mean elevation angle so that most echoes occur away from the maximum antenna gain. These factors combine to reverse the effect of a transmitting array with more gain.

Fig. 7.20 shows that the west data is less sensitive than the south. In this analysis q is proportional to received amplitude so that fewer large amplitudes are being observed. The limiting sensitivity only appears to be the same because of assumptions made in the analysis. Ideally, the west data need to be translated to higher values of log q. The reduced sensitivity was caused by the lower transmitter power that had to be used because of matching problems and possibly the broader observed azimuth pattern which would reduce the gain, but not the echo rate.

(6) Resonance Effects

Resonance effects have been observed by several workers, for example Billam and Browne (1956) who used two antennas with perpendicular polarization so that the polarization ratio could be measured. In the present work no attempt is made to measure such resonances, but a precaution was taken to reduce their effect on D measurements. In this sub-section the effectiveness of this precaution, which

was to exclude the first 25% of the echo decay in fitting a decay curve, is examined briefly.

One section of data with 249 echoes that met the selection criteria for D measurements was reanalysed without a 25% rejection of the decay curve. This meant that more pulses were available for fitting decays so higher D values would result (since some short, rapid decays would then be included). This bias was avoided by selecting only those decays that could have been fitted if a 25% shift had been used. Mean values of log D were found for echoes below 90 km, between 90 and 100 km and above 100 km for both methods of analysis. The results are shown in Table 7.1.

Table 7.1: Alternative D measurements

Height range (km)	Mean log D (25% rej.) (m^2/s)	# of echoes	Mean log D(25% inc.) (m^2/s)	# of echoes
< 90	1.116	52	1.075	62
90 < h < 100	1.203	141	1.162	168
h > 100	1.310	56	1.299	72

If plasma resonance was important, higher D values would be inferred because of the rapid amplitude decrease at the beginning of the echo decay. In practice the opposite has occurred, but note that more echoes were selected when no precaution was taken against resonance effects. The use of the first 25% of the decay must result in higher correlation coefficients. This may have caused the change to lower D

values, so that the resonance effect was not observed. However, it appears that a rejection of 25% of the echo decay is not warranted.

(7) Phase Effects from Fresnel Diffraction

The variability of phases measured on individual pulses was noticed when an attempt was made to detect wind shears. This involved calculating the echo height for each received pulse and, by fitting a linear regression, finding the change in echo height and the apparent wind shear for that particular train. An analysis of 96 echoes gave a mean change in height of -2.9 km with a standard deviation of 5 km. The corresponding mean wind shear was -.77 m s^{-1} km^{-1} with a standard deviation of 107 ms^{-1} km^{-1}. While wind shears of up to 100 ms^{-1} km^{-1} may exist (Philips, 1969), a mean shear with a magnitude of 77 ms^{-1} km^{-1} is much greater than the expected mean magnitude of 20 ms^{-1} km^{-1} (see section 3.3). Wind shears of up to -300 ms^{-1} km^{-1} were inferred in the analysis which seem unrealistic.

The associated decrease in echo height of 2.9 km is consistent with the expected effect of Fresnel diffraction on interferometer phase measurements (see Figs 3.9 and 3.10). Since the P.R.F. used (up to 300 Hz) is usually insufficient to resolve Fresnel amplitude fluctuations, it is unlikely that the system can resolve the expected variations in the inferred echo height. Fig. 7.21 shows the amplitude and height from individual pulses on six selected echoes. The amplitude points have been joined to make the figures clearer.

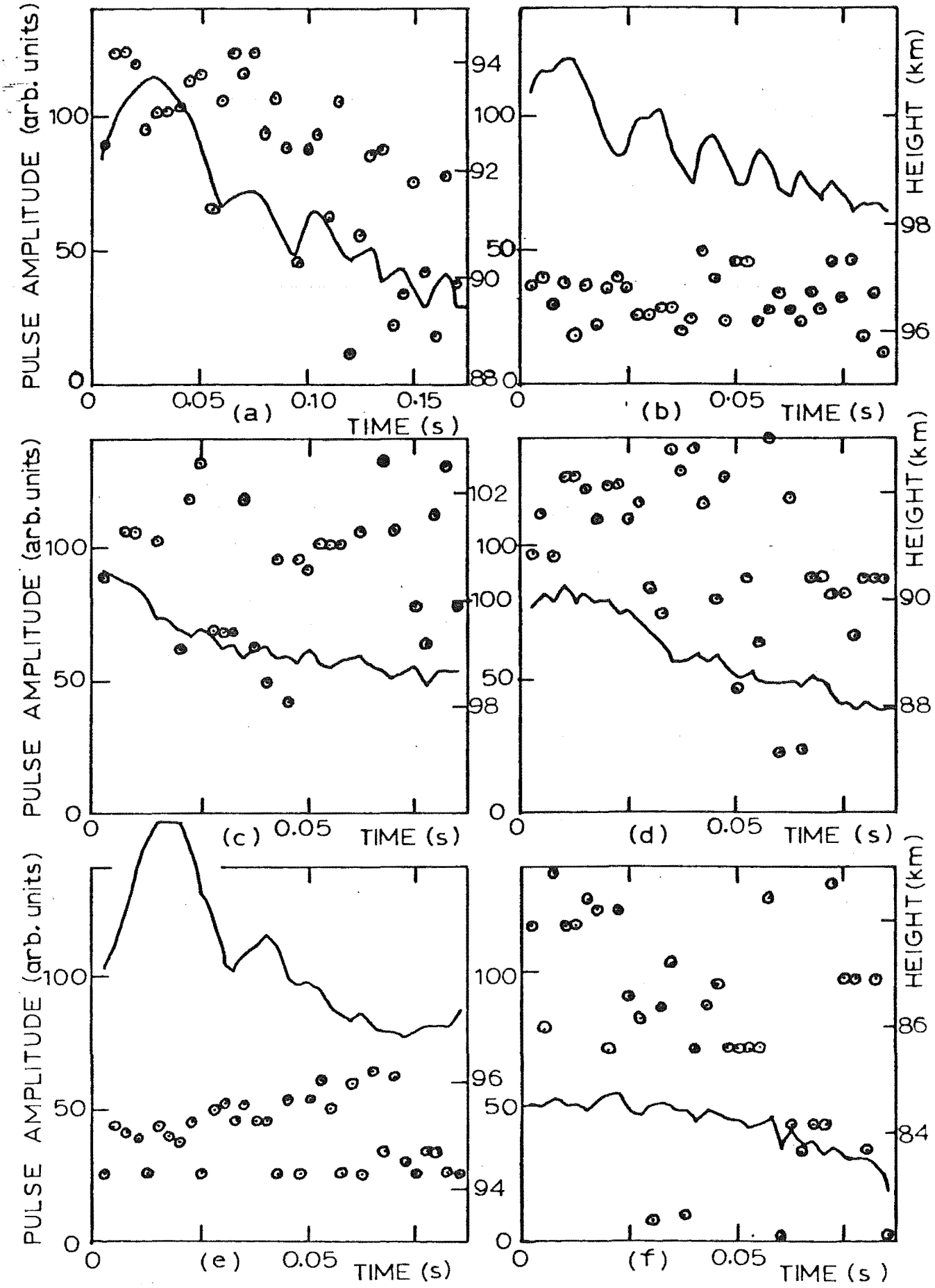

Figure 7.21: Six recorded echoes showing received amplitude (——) and inferred echo heights for each received pulse (0) .

The echo in Fig. 7.21(a) was recorded at 150 Hz while (b) to (f) were at a P.R.F. of 300 Hz.

Figs 7.21(a) and (b), although showing clear Fresnel amplitude fluctuations, do not show any particular pattern in the heights determined from each pulse. The size of the expected effect (~ 1 km) could be obscured by noise variations. In order to observe structure in the measured heights, a higher P.R.F. is desirable, combined with a longer effective interferometer spacing (i.e. d_{12} longer or larger elevation angles) and a higher signal-to-noise ratio.

Some echoes (e.g. (e)), show an increase in the scatter of measured heights late in the echo life. Again, this could be due to noise on the measured signals which has more effect as the echo amplitude decreases. A comparison of expected height uncertainty, calculated from the signal-to-noise ratio, with that found should show greater variability than expected. This cannot be done for these results because they have been analysed so that the Fresnel effect has been minimised. Such a study by Poulter (1978) on measured phases did show greater variability, but it was suggested that an underestimate of the noise level was responsible.

One positive result from these data is the decrease in inferred height during echo lifetimes on many echoes. Non-linearities in the phase detectors (i.e. if the measured phase depends on signal amplitude) could cause this effect as most measurements are made as the amplitude decreases. Three factors indicate that this is not a likely

cause. First, the phase detectors have been tested and shown to be linear (section 6.4). Secondly, the height decreases do not follow the Fresnel amplitude oscillations where these are resolved. Thirdly, where increases in echo amplitude occur (Fig. 7.21(e)) the measured height does not generally increase.

7.4 MAGNETIC EFFECTS

(1) Combined Forward-Scatter and Backscatter Results

Because of finite train lengths only meteors with certain orientations will give echoes from the two transmitters. Assuming an average train length of 6.7 km (Jones and Hawkes, 1975), the maximum angular separation of the reflection points, ε, at a range of 350 km is 0.64^{o} when allowance is made for the length of the first Fresnel zone. The total range of ε is then $\pm$ 0.64^{o} which gives a range of η (the angle between the train and a perpendicular train) of $\pm$ 3^{o}. Greater values of η could be observed as echo azimuth varies, but the range of 6^{o} will be constant for the train length assumed.

The fraction of meteors giving double echoes (i.e. a signal is received from both transmitters) can be estimated by assuming that the distribution of echoes about η follows a cosine function. This is the case for the zenith angle, χ, and is thus also true for η which is in a plane inclined at 16^{o} to the vertical. Integration of the cosine function shows that 5.2% of meteors that give a backscattered echo

could also give a forward-scatter signal. This percentage is reduced in this experiment because the remote transmitter has only one quarter of the power output of the local one. The underdense echo rate is independent of antenna gain (high antenna gains enable fainter meteors to be observed, but the observing region is decreased) so that the different antennas used have no effect and the echo rate is thus proportional to the square root of the transmitter power. The expected number of double echoes observed is thus 2.6% of the total number observed by backscatter.

Two transmitters were operating for much of the time in which the second set of data was recorded so that an estimated 3600 echoes met initial selection criteria. Thus 96 double echoes could be expected and 67 were in fact recorded. Of these, 44 had useful amplitude decays and occurred in suitable height ranges to enable them to be analysed further. Selection criteria relating to uncertainty in echo location were relaxed so that a useful number of echoes remained.

Fig. 7.22 shows the backscatter echo azimuth and backscatter echo height distributions for the 44 double echoes. The azimuth distribution is very different from that of the backscatter echoes alone (Fig. 7.6) and suggests that the remote transmitter beam was not pointing in the correct direction. The lack of echoes in the -8^{o} to -10^{o} azimuth range coincides with the local transmitter beam null where no local echoes could be observed and so the peak of the double echo azimuth distribution could have

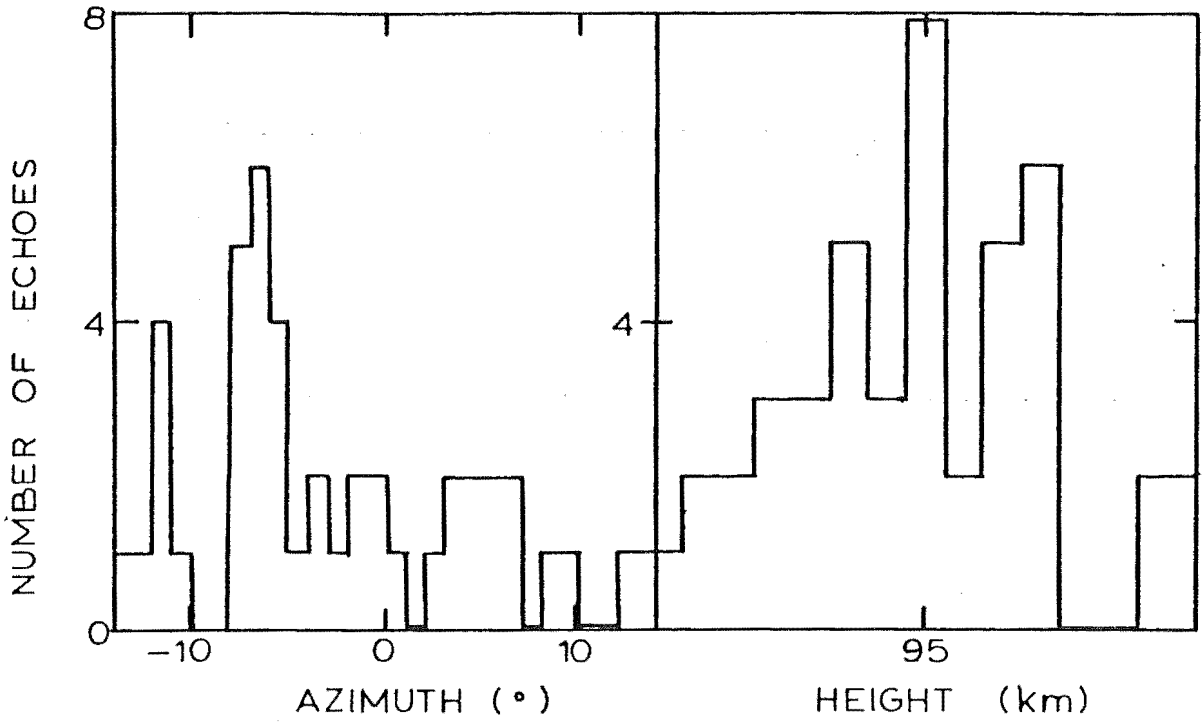

Figure 7.22: Azimuth and height distributions of double echoes.

occurred near this value. The rhombic antenna side lobe at an angle of 17° from the main lobe would appear to be at less than 17° from the main lobe when viewed from the backscatter direction because the forward-scatter range is longer. Thus, the group of echoes at +5° azimuth could be due to this side lobe.

The calculations of the forward-scatter reflection geometry were checked by measurements on a 1:500,000 scale New Zealand Lands and Survey Department map of the southern part of the South Island. This confirmed that the geometry calculations and the calculations for antenna alignment were correct within a 2° measurement uncertainty. Two possibilities remain for explaining a change in the beam direction. First,

a mistake could have been made in aligning the antenna, but this would seem unlikely in view of the two methods used (section 6.2). Secondly, the antenna, although correctly orientated, may have had its direction of propagation changed by some antenna fault such as a poor connection in one leg of the rhombic or in one feed line. This did not show in measurements of the antenna pattern at Rolleston (Fig. 6.5), but may have been created when the antenna was dismantled and reassembled.

The skewed azimuth distribution explains the 30% reduction in the expected number of double echoes. The problem is not as serious as it might seem because the local transmitter is more powerful and the receiving antennas have a broad radiation pattern. This means that meteors not occurring in the middle of the local transmitter beam will still give double echoes and only those echoes at azimuths of -9^{o} will be lost. Furthermore, echoes at azimuths of about -10^{o} are still useful in that a field-aligned orientation can still be obtained for $\eta \approx 3^{o}$ which corresponds to an angular separation of the reflection points of 0.5^{o} which is quite possible.

The distribution of backscatter echo heights for the double echoes shown in Fig. 7.22 appears to be erratic, but this is due to the small sample size. A Chi-square test showed that this distribution does not differ significantly from the parent distribution shown in Fig. 7.12.

Fig. 2.23 shows the frequency distribution of trains about the perpendicular direction, η. It was mentioned

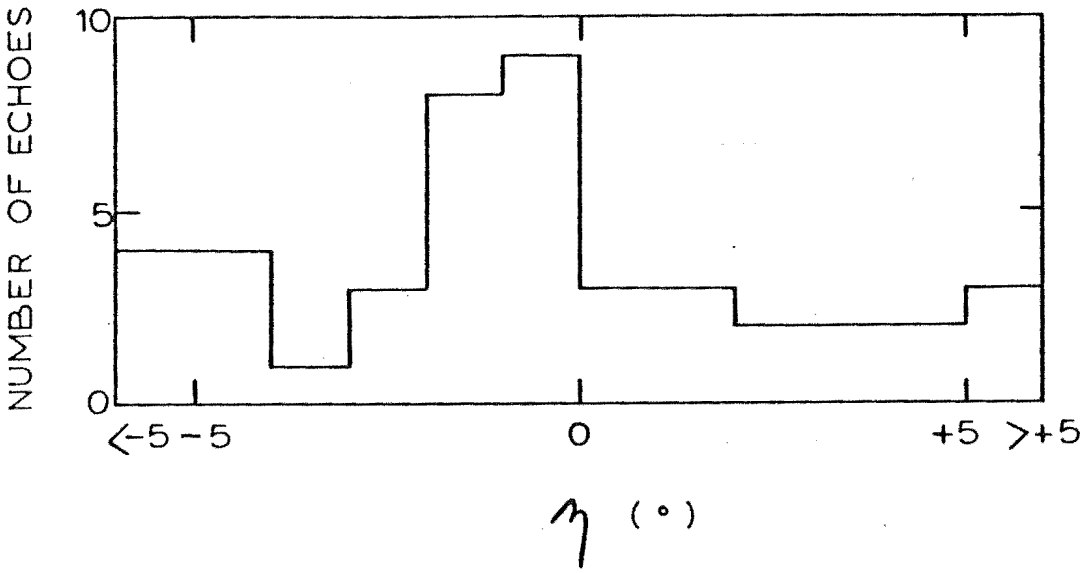

Figure 7.23: Distribution of double echoes about the perpendicular direction ($\eta = 0^{o}$).

above that this should be a cosine distribution which would be essentially uniform over the small range of angles measured. A range of $\pm\ 3^{o}$ in η was expected, but this is true only for a particular azimuth. The overall range for one azimuth is expected to be 6^{o}, but this could be, for example, from -5^{o} to $+1^{o}$. This effect will tend to change the uniform distribution of η to one that is peaked since extreme azimuth values are less likely to occur. With the observed azimuth distribution, the expected value of ε_{o} is zero (See Fig. 5.19. ε_{o} is the angular reflection point separation for a perpendicular train, $\eta = 0$), so that a mean value of η equal to zero would be expected. From Fig. 7.23

$$\eta = -\ 0.4^{o} \pm 0.6^{o}$$

where the uncertainty is the standard error of the mean

value. The high frequency of orientations between -2^{o} and 0^{o} is difficult to test for significance because of the small sample size. A chi-square test on the distribution of frequencies showed that no significant difference from a Poisson distribution existed. In view of the expected peak in the ditribution and the mean value near zero, the distribution of η is probably not significantly different from that expected.

In order to study magnetic effects on the diffusion of the double echoes they were separated into two groups according to their echo heights: those with both echo heights below 95 km were in one group and those with both heights above 98 km were in the other. All other echoes were rejected so that one group should be clearly magnetically affected while the other should not be.

With separated reflection points the problem arises of whether to correct each D value according to the distance from an arbitrary reference height. If D values are corrected, there should be some physical justification for the type of correction applied. One possibility is to use the theoretical variation of D with height based on laboratory values. This, however, assumes that no magnetic effect occurs. Fig. 7.24 shows the difference in values of log D from each reflection point for each double echo below 95 km as a function of the angular separation of the reflection points. In (a) each D value has been corrected to correspond to an echo height of 90 km by using the theoretical D vs height dependence discussed in section 2.3, while for (b) no

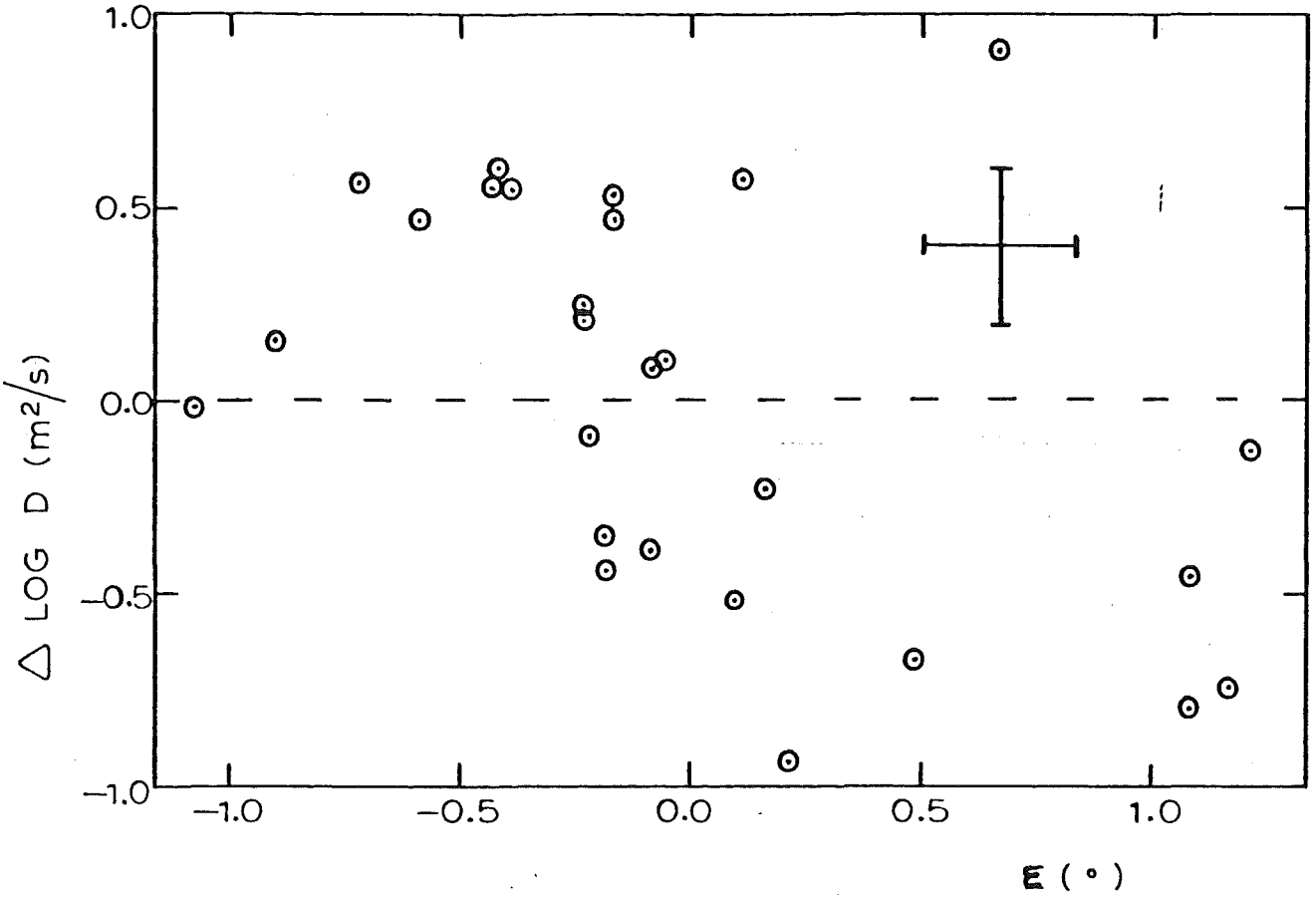

(a) Heights below 95 km with a height correction for D.

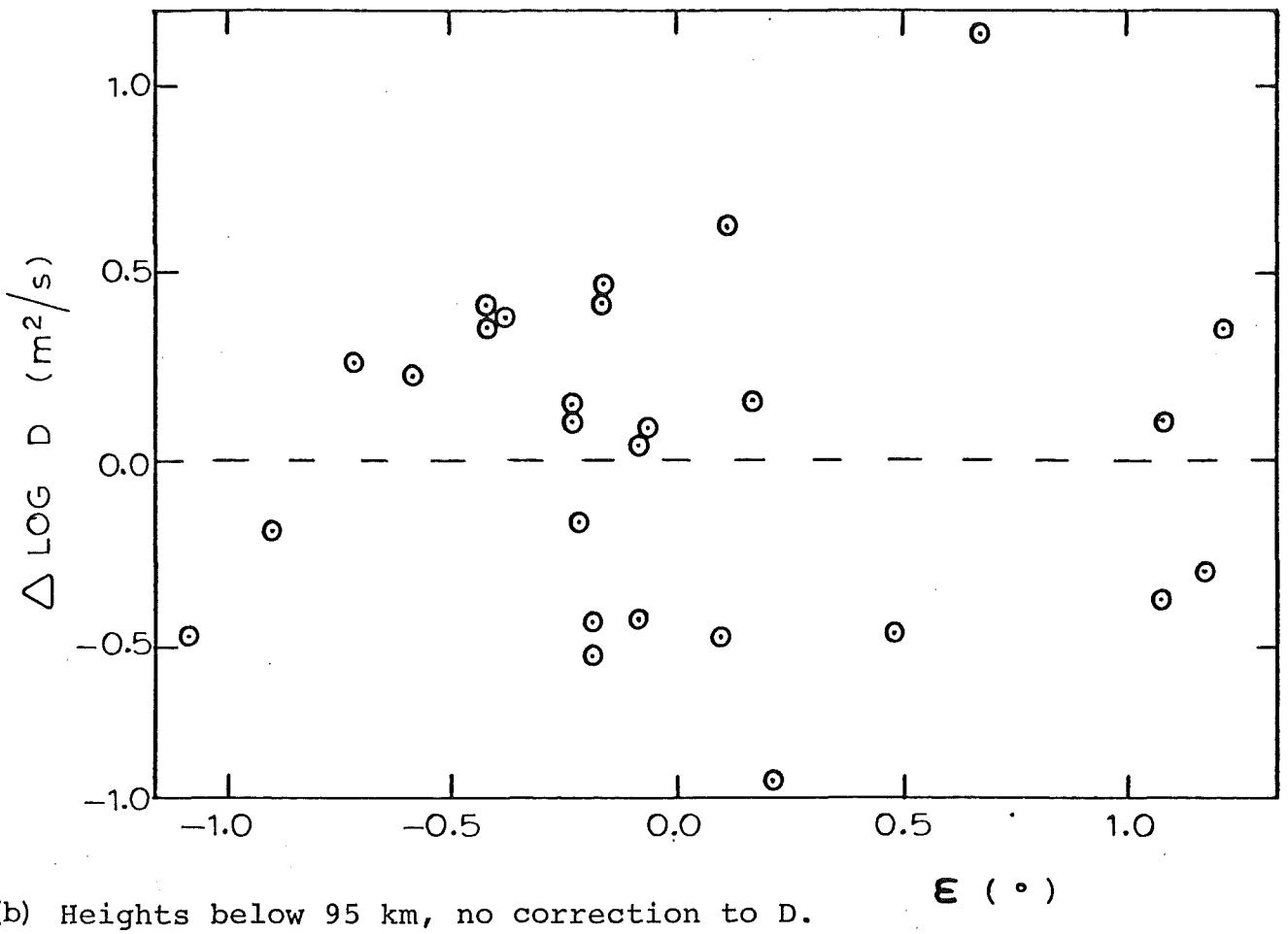

(b) Heights below 95 km, no correction to D.

Figure 7.24: Difference in measured diffusion coefficients on double echoes as a function of angular separation of reflection points.

corrections have been made. If the height dependence of D followed theoretical predictions, the points in (b) would fall on a line with a positive gradient while those in (a) would have zero gradient. The reverse of this is evident in that there is no trend in (b), but there is evidence of a negative slope in (a), which indicates that the correction is too large. This is not surprising in view of the uncertainty in measuring ε (one standard deviation is indicated in (a)) and the inherent scatter usually observed in D values. Fig. 7.25 is the same as Fig. 7.24, but the echo heights are above 98 km. Again the same trend of over correction is present. In view of these results, no height correction was applied in further analysis of the data.

A further trend that may be expected in Fig. 7.24(b) and Fig. 7.25(b) is an increase in the difference between diffusion coefficients as ε increases, caused by the echoes coming from different parts of the train where q is different. This trend is not obvious in these data, but could be obscured by the scatter in D.

A further problem that arises in the analysis of double echoes is the effect of ionospheric refraction. This affected the measured off-specular angles of the backscattered echoes (see the next sub-section) by an average of 1.3^{o}. This is consistent with theoretical calculations based on day-time values of electron density in the E-region (Fig. 7.13). A correction of 1.3^{o} was made to those echoes that occurred during daylight hours above 98 km. To simplify the analysis the correction was made by rotating the theoretical magnetic

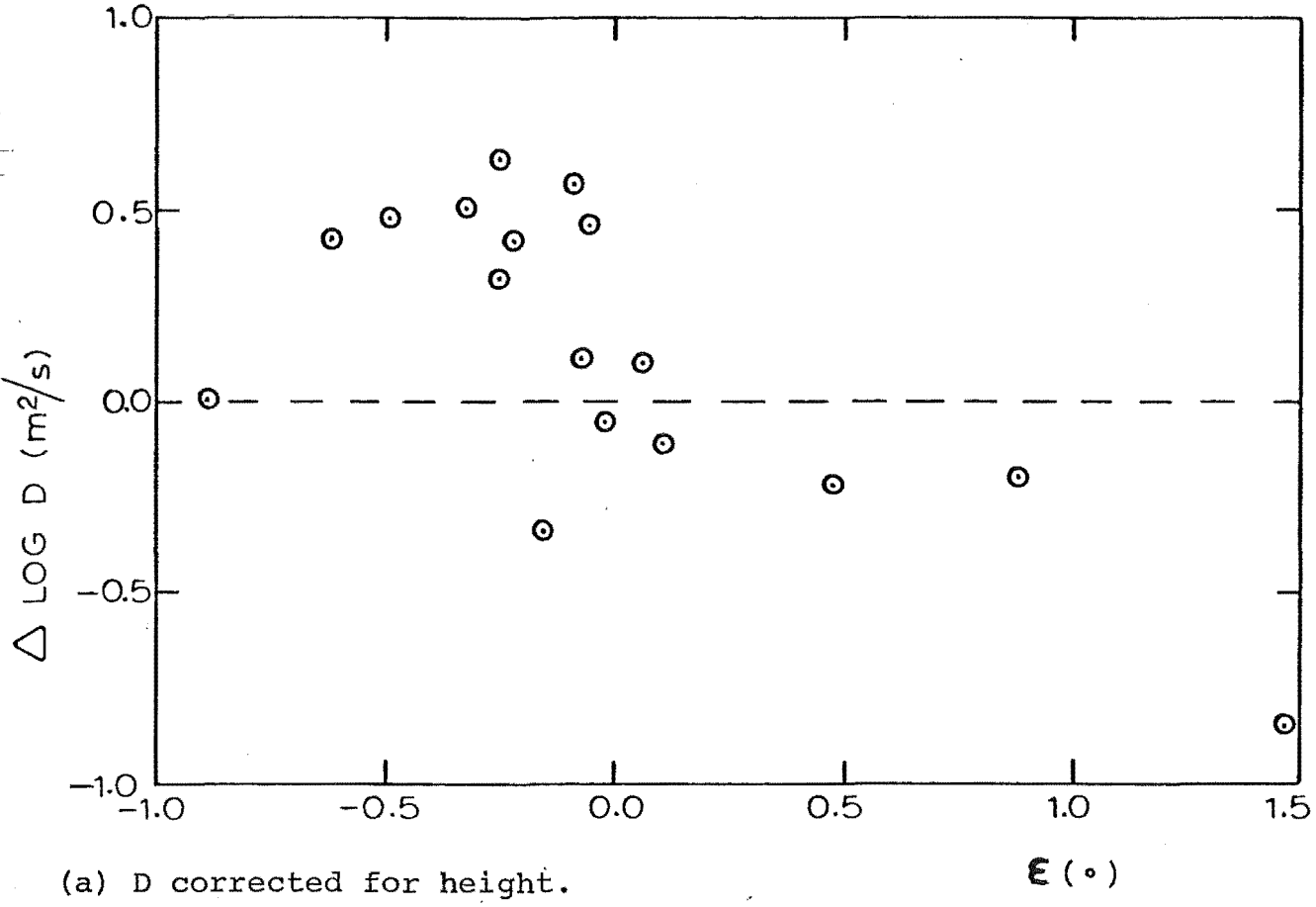

(a) D corrected for height.

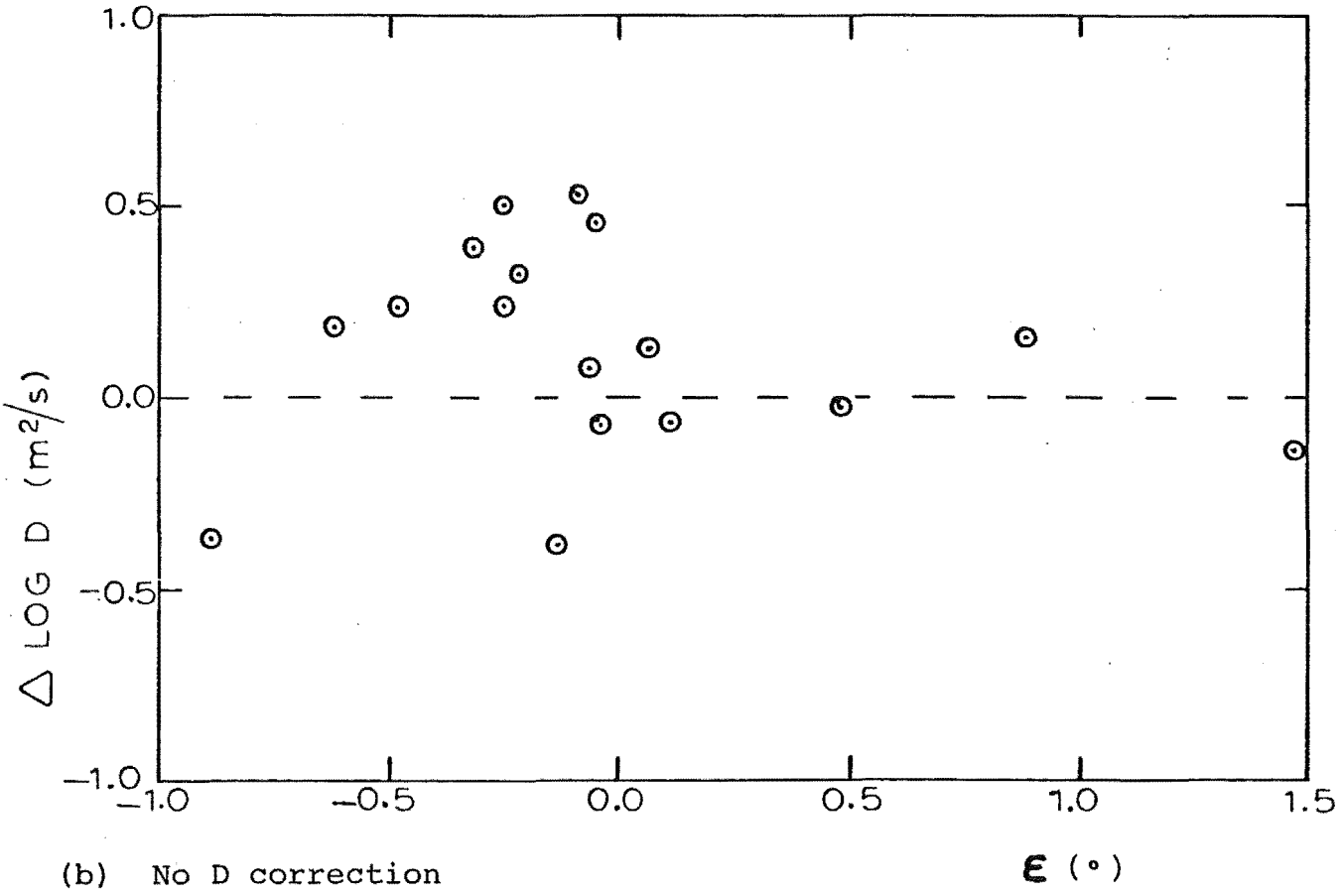

(b) No D correction

Figure 7.25: Difference in measured diffusion coefficients on double echoes as a function of angular separation of reflection points, echoes above 98 km.

field by 1.3^{o}, thus giving a true correction in the magnetic south direction, but with a slight error at azimuths of 10^{o}. No attempt was made to correct the values of ε which are affected because of the change to echo heights (Fig. 3.14). The ε values could be in error where the ambient electron density changes quickly with height, but an effective correction is difficult because of uncertainties in the actual height of the E-region.

Fig. 7.26 shows the double echo diffusion coefficients as a function of α for the backscatter and forward-scatter echoes for heights above 98 km (a) and below 95 km (b). The estimated standard deviation for the measurements is shown in (a). There are not enough echoes above 98 km at small angles ($\alpha < 1.4^{o}$) to determine if there is a magnetic effect about small α. The estimated uncertainty and overall range of α indicate that the transmitter separation was close to ideal. A slightly wider separation could be used, decreasing the uncertainty and range of α and also decreasing the fraction of double echoes observed. However, such a separation is not possible with New Zealand's geography. A 30% increase in the number of echoes would make little difference to the significance of these results so that the antenna alignment problem has not affected the outcome of this part of the experiment. A ten-fold increase in the number of double echoes would probably give significant results. This would mean recording about 40,000 echoes with the present system, but only 20,000 if the remote transmitter was upgraded to have a 40 kW peak power. Data

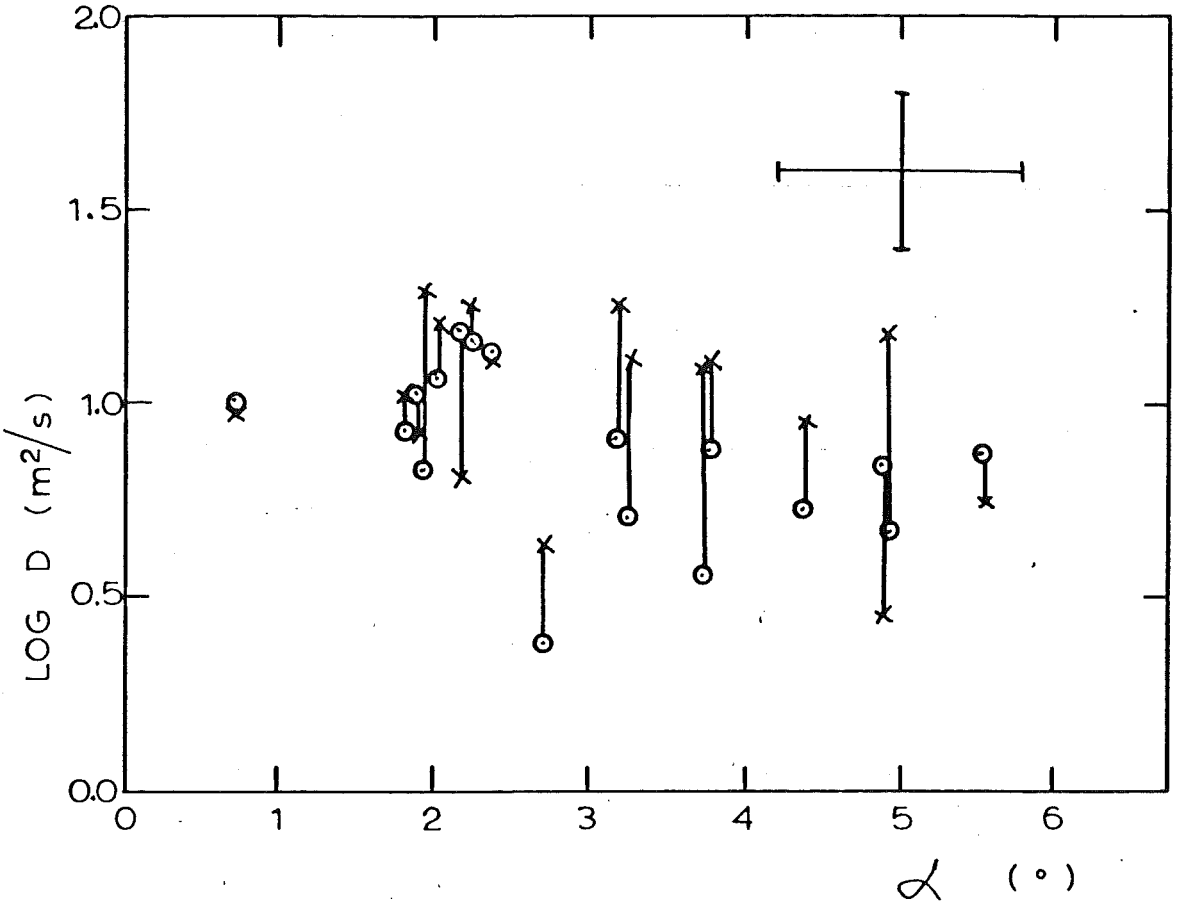

(a) Heights above 98 km.

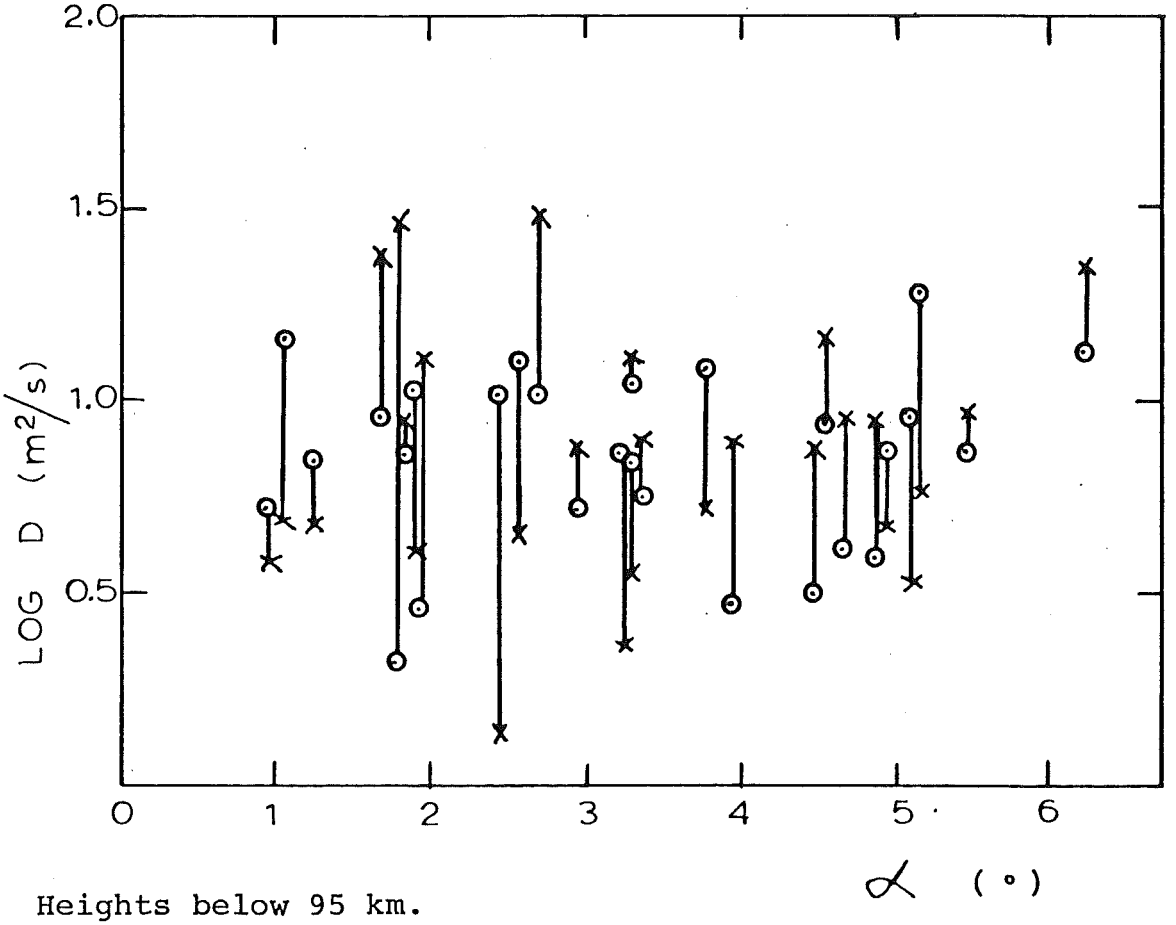

(b) Heights below 95 km.

Figure 7.26: Diffusion coefficients for backscatter (X) and forward-scatter (⊙) reflection points on double echoes.

collection, at the same rate as for the second set of data when two transmitters were kept operational, could be expected to take one year. This takes into account the number of days with suitable noise conditions (i.e. no sporadic-E or local power line corona discharge) and the time for which one or other of the transmitters is not operational. The amount of paper tape produced in recording this number of echoes is also a problem, although that used in recording about 10,000 echoes in the third run was manageable. Clearly, if the experiment were to be repeated, a 40 kW remote transmitter would be necessary and a magnetic tape recording system would be desirable.

Observations made during periods of field-aligned shower activity would increase the percentage of double echoes. A geographical location at which a very active shower reached a field-aligned orientation would thus have a big advantage. In this experiment the equipment was not able to record double echoes in a satisfactory manner at the time when there was possibly field-aligned shower activity (i.e. July 25 for Puppids).

Thus far, only the expected behaviour of the D values for small values of α has been mentioned. Different values of D could be expected from the backscatter and forward-scatter reflection points because of the elliptical train cross-section. Fig. 4.3 gives an example of this for a train that would have a zero off-specular angle. For a non-zero value of μ the situation is different as the train could be elongated in the backscatter direction or anywhere

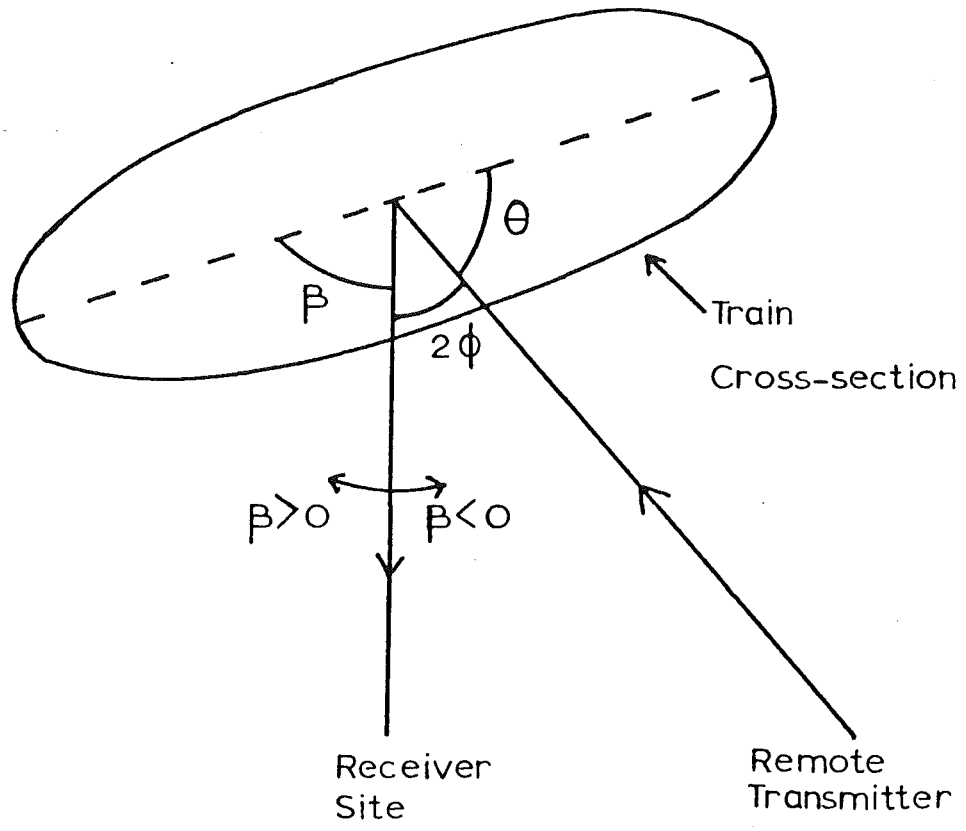

Figure 7.27: Forward-scatter geometry.

between these directions. Fig. 7.27 shows the angle β between the backscatter direction and the major axis of the train cross-section. In the backscatter case, β is related to μ and the angle between the train and the magnetic field, α, by

$$\cos \beta = \frac{\sin \mu}{\sin \alpha} \quad . \qquad 7.2$$

The sign of β is important when forward-scatter is considered and can be found by considering the sign of μ and η.

If both β and the forward-scatter angle, 2ϕ, are known, equation 3.5 can be used to predict the difference between diffusion coefficients measured by forward-scatter and

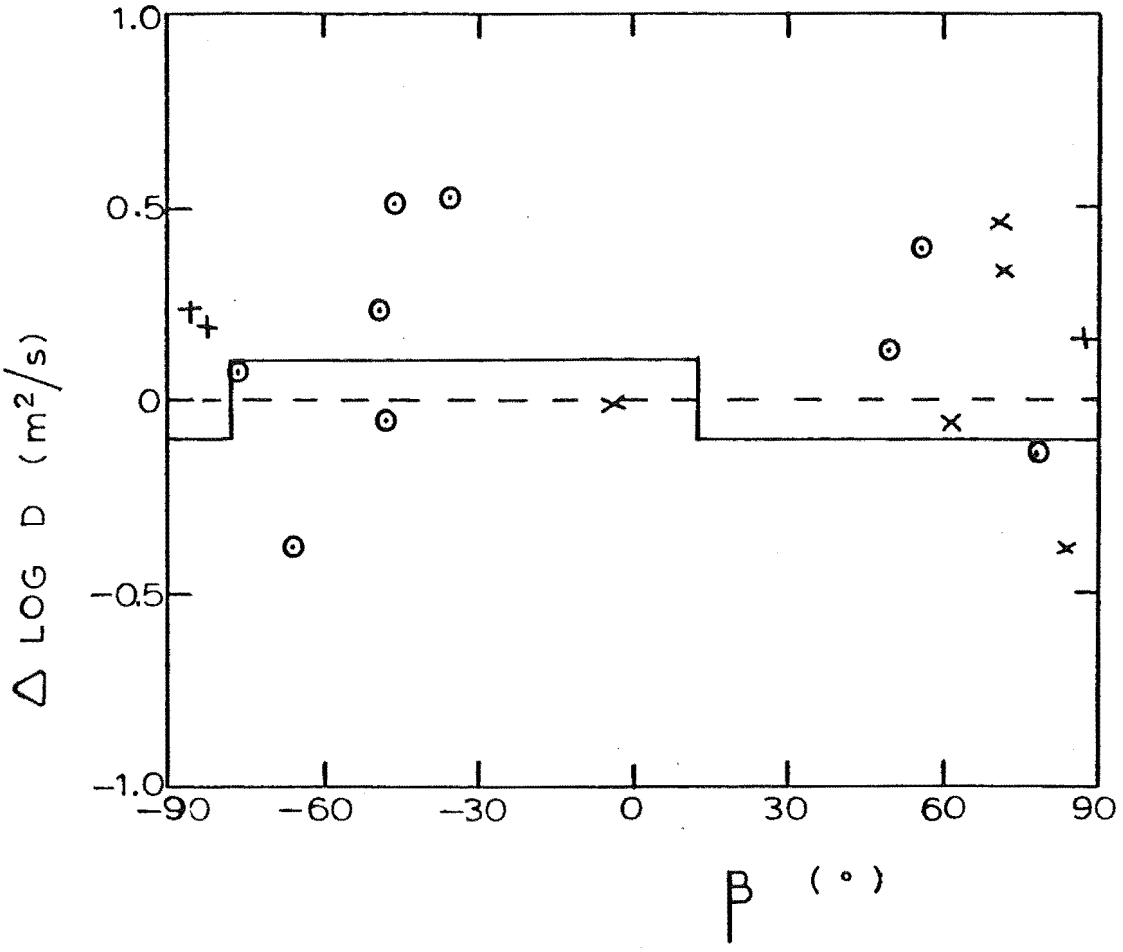

Figure 7.28: Difference in measured diffusion coefficients as a function of train orientation with respect to the receiver direction. ⊙: trains possibly affected by finite meteor velocity because of D value in receiver direction; X: trains affected because of D in direction of remote transmitter; +: trains not affected by the finite meteor velocity. Lines indicate where positive and negative values are expected to occur.

backscatter. For values of β from -78^{o} to -90^{o} and from $+90^{o}$ to $+12^{o}$ the forward-scatter decay should be more rapid, while for β between $+12^{o}$ and -78^{o} the backscatter decay should be more rapid. Fig. 7.28 shows the difference in log D values as a function of β for heights above 98 km. There is no obvious agreement with the predicted values of D which

may be caused by a combination of two factors. First, the inherent scatter in measured D values means that many observations are necessary to obtain a statistically significant result. Secondly, the finite velocity effect severely restricts the trains for which the expected diffusion coefficients could be observed especially if an electron ellipse is formed.

Consider the backscatter case. If the effective diffusion coefficient in the backscatter direction is greater than about 20 m^2/s (see section 3.5) the meteor echoes will be attenuated and will be harder to observe. Two angles determine the D value observed; α, which determines the degree of eccentricity of the electron ellipse and β, which describes the orientation of the ellipse with respect to the radar direction. For a purely elliptical train cross-section, these angles are related to the off-specular angle, μ (see the next subsection). For heights above 100 km, μ needs to be less than 1^o to avoid the effect of the finite meteor velocity in observing the electron ellipse. This reduces the number of useful points in Fig. 7.28 to eight. The lack of points between -30^o and $+30^o$ is caused by the geometry at small values of μ - the use of large values of μ would give a more uniform distribution, but then the finite velocity effect would be important.

When the forward-scatter case is considered, the number of points is further reduced because of the angle of the radar paths to the electron ellipse. D measurements from

trains with $\alpha > 5^{o}$ will be affected by the finite meteor velocity as will trains with $\alpha < 5^{o}$ for some values of β. Only three of the trains shown in Fig. 7.28 will be completely unaffected by the finite meteor velocity if an electron ellipse is being formed. For trains that are affected, the high initial diffusion will not be detected which will leave the contribution from the ion "ellipse" which is the same for forward-scatter and backscatter. (Remember that the electron and ion ellipses both contain ions and electrons, but the ions in the electron ellipse are mainly drawn from the background plasma as are the electrons contained in the ion ellipse).

The situation for anisotropic ambipolar diffusion (at higher electron line densities where the electron ellipse is much less dense than the ambipolar region) is less critical because the ellipse is less eccentric. However, Fig. 2.5 shows that for the heights and values of α considered, less than one third of the double echoes would diffuse in an ambipolar manner.

Thus the observation of magnetic effects on meteor diffusion by using forward-scatter is very difficult to interpret. Equipment able to handle large amounts of data may be able to verify effects about α_c, but the finite meteor velocity places severe restrictions on values of D that can be observed for the electron ellipse.

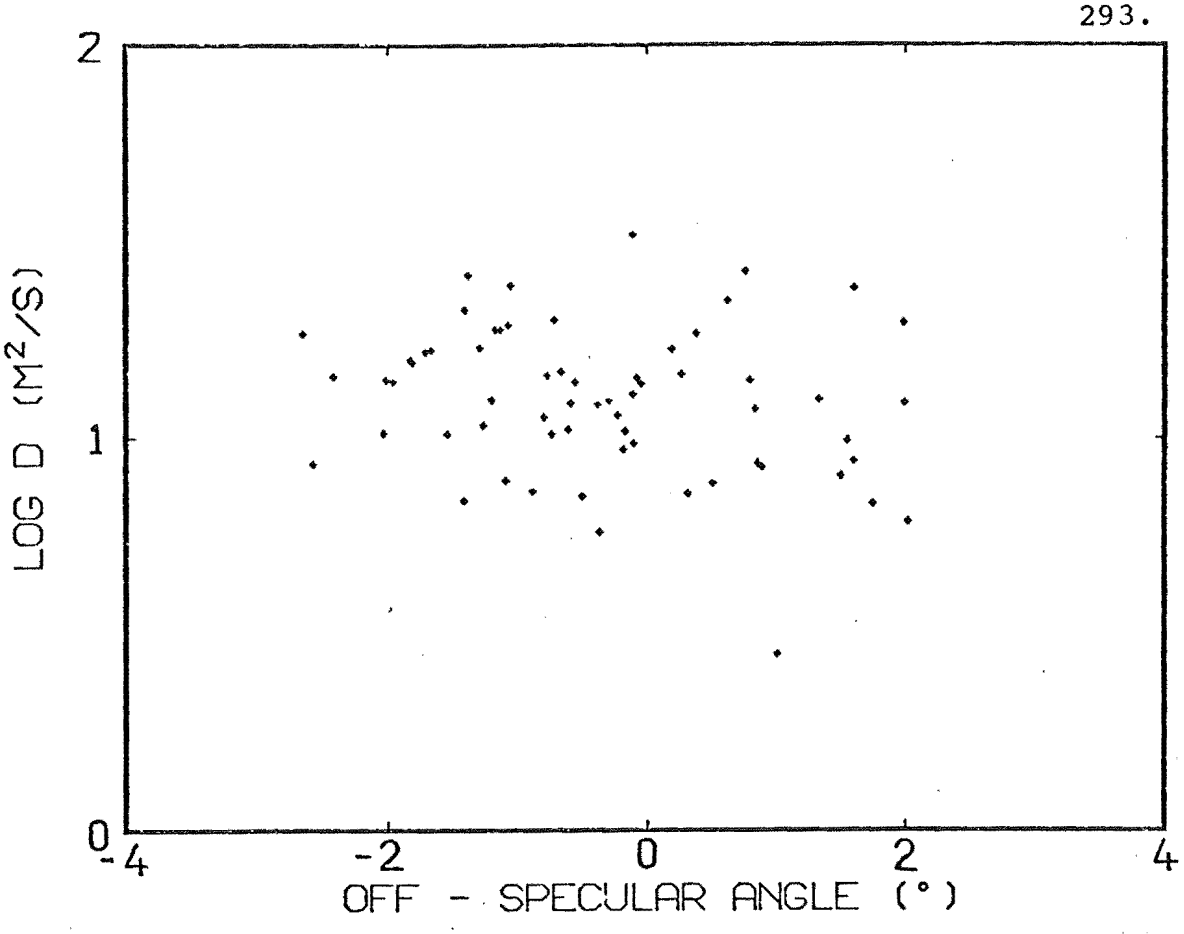

Figure 7.29: The first set of data, heights above 100 km.

(2) Backscatter Results

(a) The Data The only parameter related to the earth's magnetic field that can be found from backscatter measurements on meteor trains is the off-specular angle, μ, although assumptions about the meteor train zenith angle distribution may enable some more in inferences to be made. Because of this, the backscatter results are presented in this sub-section with log D as a function of μ ($\log_{10}D$ is written as log D here).

Fig. 7.29 shows the results for the first set of data for echo heights greater than 100 km. There is no obvious magnetic effect about $\mu=0$, but this is not surprising when the method of analysis is considered. All echoes for which

the double echo detector was triggered were rejected because the local and remote echoes could not be reliably distinguished. This process also rejected many echoes that were not true double echoes in that only one amplitude pulse may have been received from the remote transmitter while the local echo was being recorded. As magnetically affected echoes have longer durations than unaffected echoes, the double echo detector was far more likely to be triggered during such an echo and subsequent rejection of double echoes would discriminate strongly against long durations. Because of this selection effect these data are not used in the rest of this work.

Figs. 7.30 to 7.32 show the results for the second set of data for heights above 100 km, between 95 and 100 km and 90 and 95 km respectively. Above 100 km there is a clear tendency for low D values to occur about an off-specular angle of -1.3^{o}. This is consistent with the expected ionospheric bending calculated in section 3.6 and is discussed in sub-section (b). The agreement of the observed magnetic effect with that expected from theory is discussed in sub-section (c). Between 95 and 100 km there is also some effect in that D values decrease as the $\mu = -1^{o}$ condition is reached. The sudden cutoff at $\mu = -1.7^{o}$ is caused by the limits placed on the maximum observable elevation by the minimum echo range and maximum height. The lower limit of μ is increased as the height decreases so that between 90 and 95 km the $\mu=0$ condition is only just obtained. Ionospheric bending should be much less at these

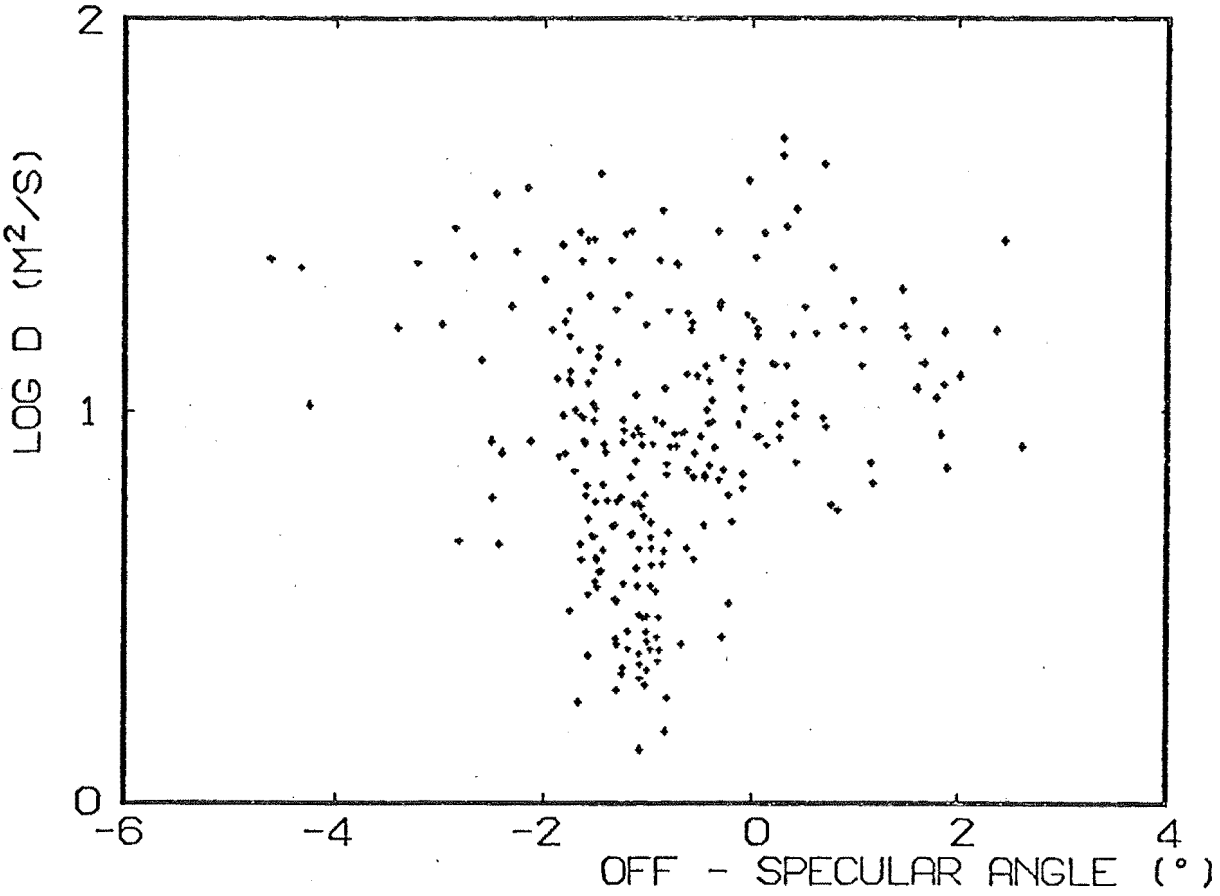

Figure 7.30: Second set of data, heights above 100 km.

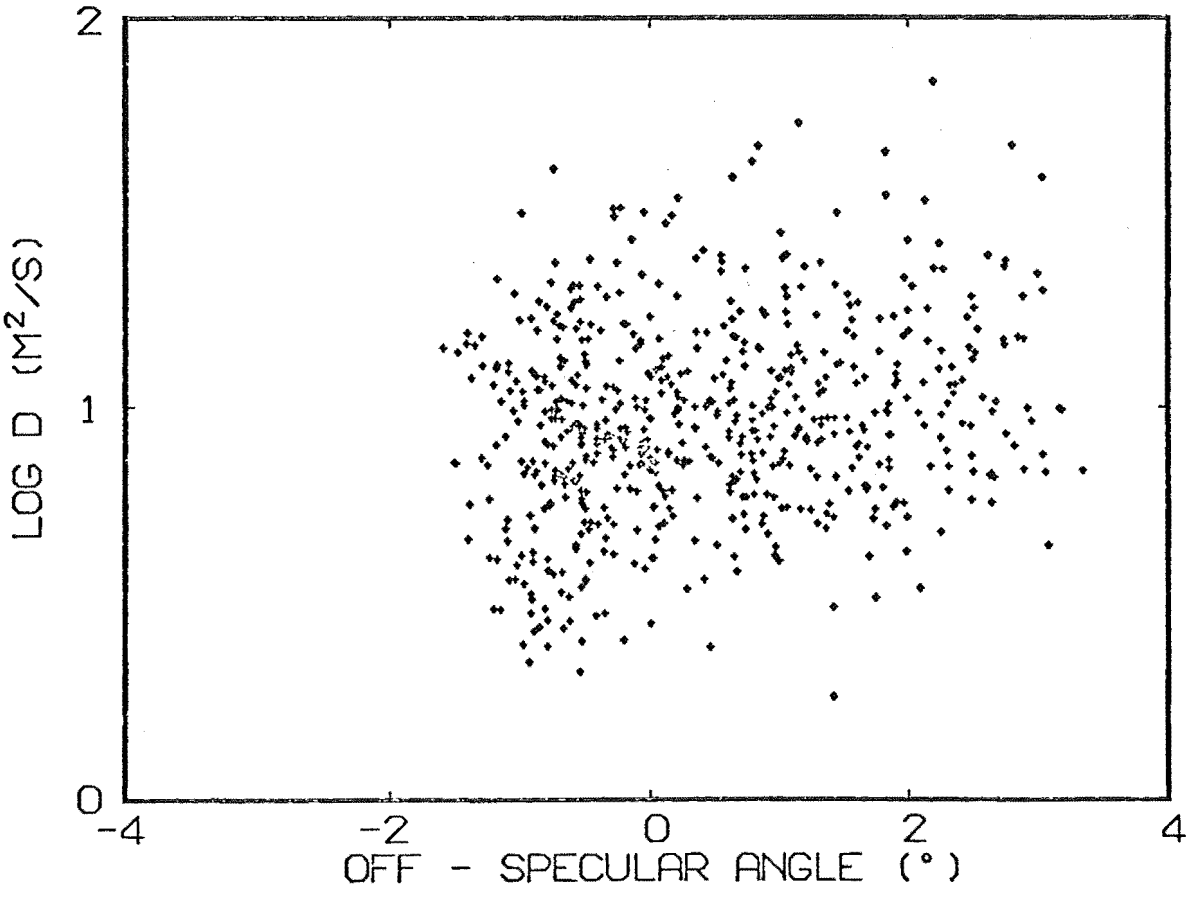

Figure 7.31: Second set of data, 95 km < h < 100 km.

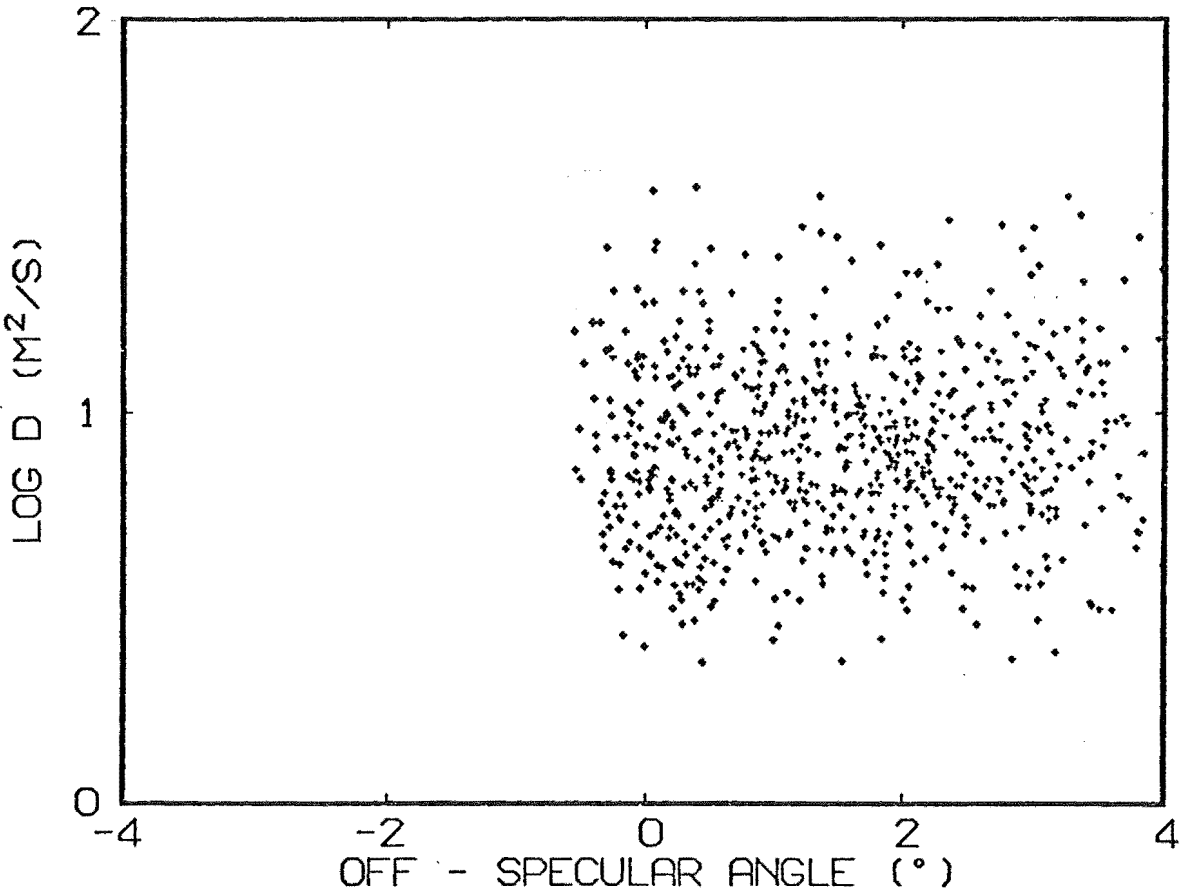

Figure 7.32: Second set of data, 90 km < h < 95 km.

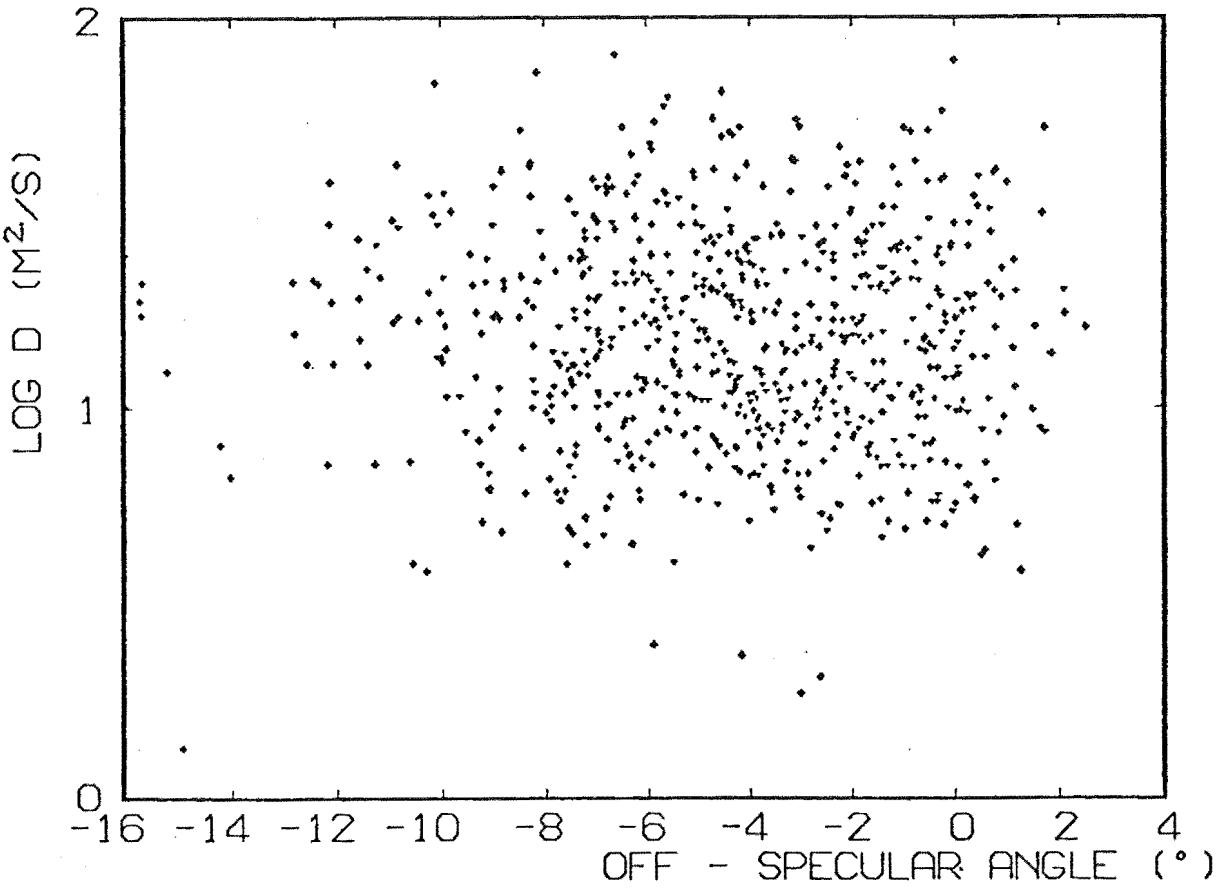

Figure 7.33: Third set of data, h > 100 km.

heights as they are below E-region ionization so that Fig. 7.32 perhaps indicates the lack of any magnetic effect below 95 km although a wider range of μ would have been desirable.

Figs 7.33 to 7.35 show the results for the third set of data for three height ranges. The wider spread of μ was obtained by using shorter echo ranges which was possible because of the decreased antenna interferometer spacing. There is no obvious magnetic effect in any height range and it is important to examine why in order to confirm that the second set of data is not a spurious result of some kind. The analysis program used for the third set of data was different from that used previously as it was made more efficient because no remote transmitter pulses had to be analysed. This program was checked by reanalysing a part of the third set of data with the program that had been used on the part of the second set of data recorded at 300 Hz and which did have magnetically affected echoes. The results were identical which confirms that the absence of a magnetic effect is not due to an analysis error or to the use of the higher P.R.F. of 300 Hz.

The only other apparent differences in the recording of the two sets of data are the transmitting antenna gain and the season and time of day in which most echoes were recorded. It was mentioned in section 7.3 that the system sensitivity with the smaller transmitting array used to record the third set of data was little different from the previous system because shorter ranges and elevations in

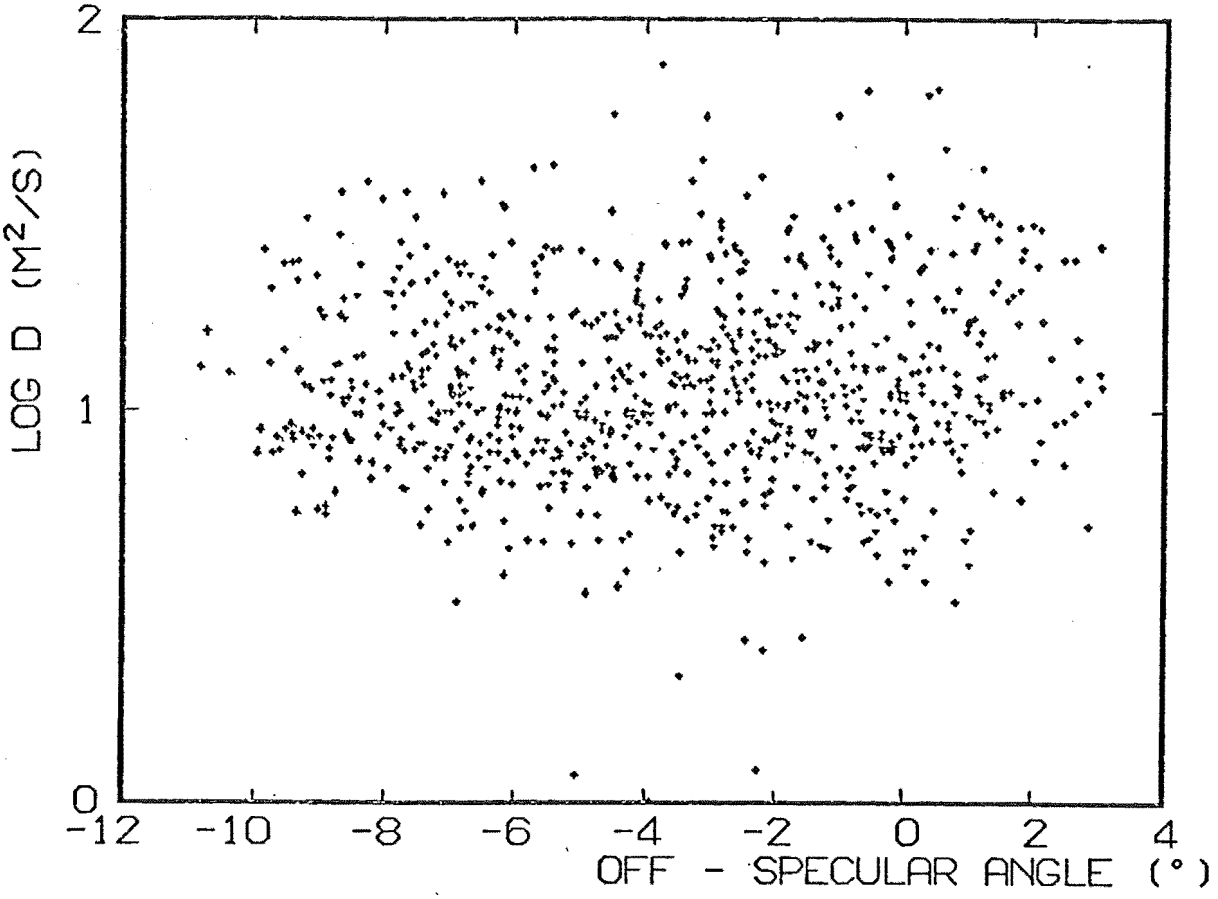

Figure 7.34: Third set of data, 95 km < h < 100 km.

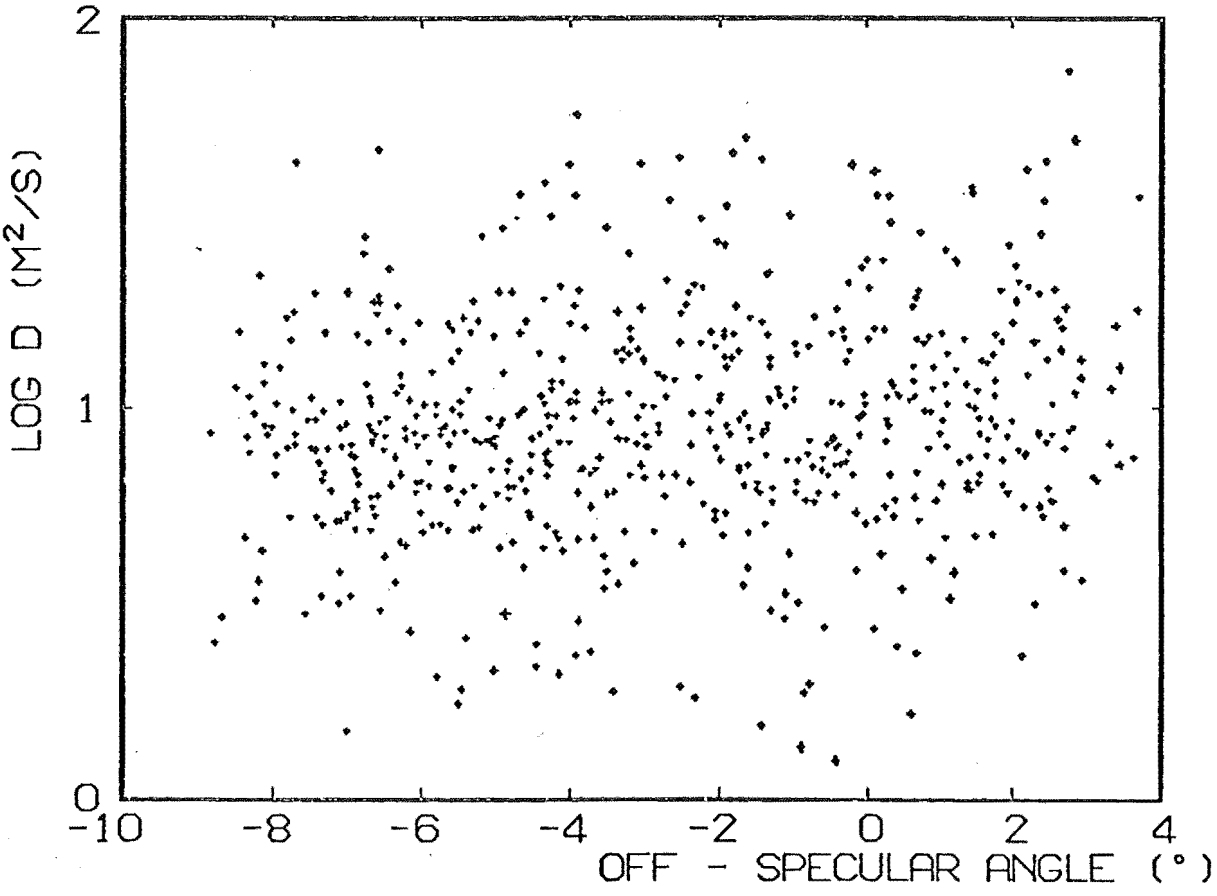

Figure 7.35: Third set of data, 90 km < h < 95 km.

the maximum of the antenna patterns were used. However, in the case of specular echoes ($\mu = 0^{o}$), which occur at low elevations and long ranges, the above argument does not apply and there is a difference by a factor of two between the transmitted powers. The minimum detectable line density is thus a factor of $\sqrt{2}$ higher for the third set of data.

The mean value of log q for the magnetically affected echoes ($D < 4.5$ m^2/s and $-1.5^{o} < \mu < -0.8^{o}$) was found to be 12.55 ± 0.03 (q in electrons/m) where the uncertainty is one standard error of the mean value. That for the parent population was found to be 12.84 which is significantly higher. It thus appears that the smaller meteors detected are most likely to be magnetically affected which would make their detection by the less sensitive system less likely.

Fig 7.36 shows the distribution in recorded time of the echoes in the second set of data and of the magnetically affected echoes. Times (L.M.T.) have been corrected for the changing time of sunrise. The points and dotted line indicate the electron density at the peak of the E-region inferred from ionosonde data from Godley Head, near Christchurch (N.Z. D.S.I.R., 1979). This station is about 350 km north of the region where specular echoes occur. Magnetically affected echoes were recorded only after the peak electron density had reached about 8.9×10^{10} m^{-3} (the relationship of this density to depletion region depth is considered in sub-section (c)). This value is probably quite uncertain because only 64 echoes behaved as though magnetically affected

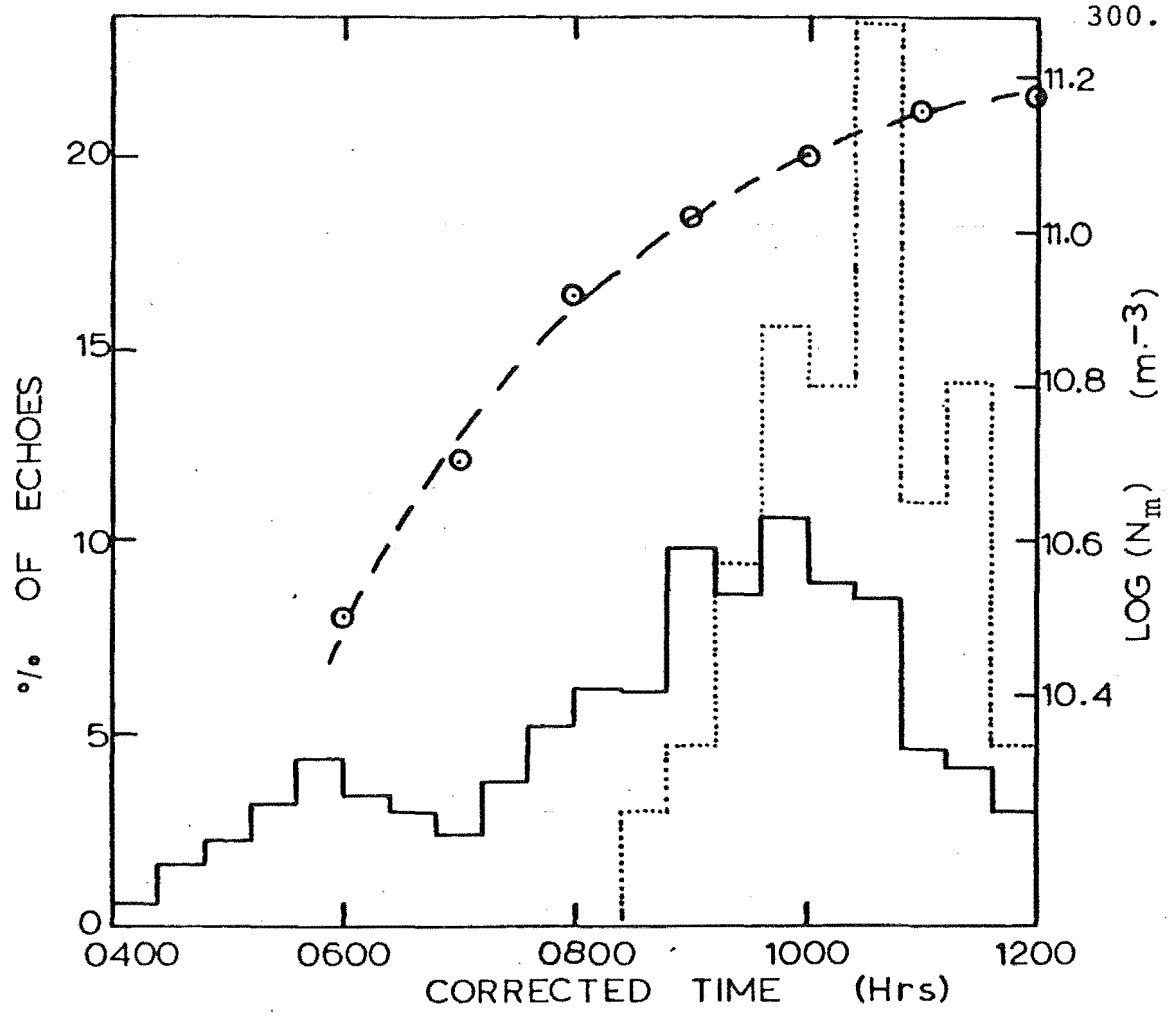

Figure 7.36: Time distribution of all echoes (——) and magnetically affected echoes (•••) for the second set of data with E-region electron density (--⊙--).

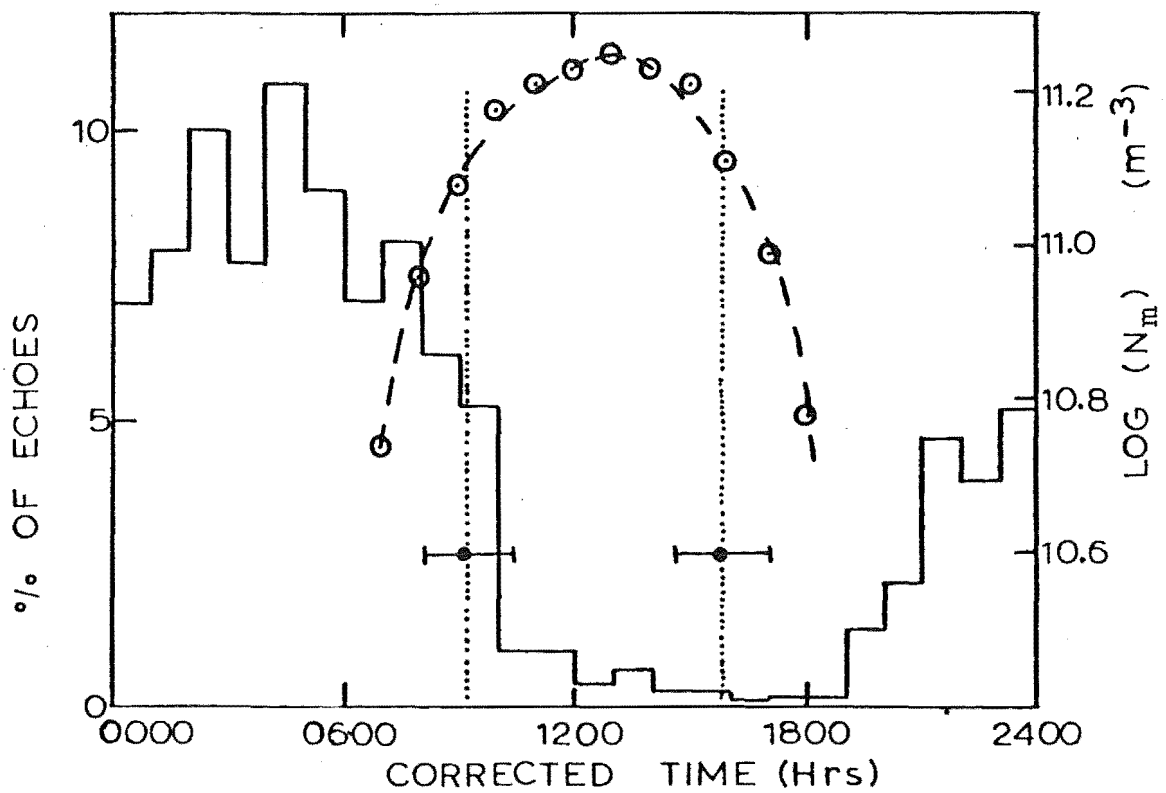

Figure 3.37: Time distribution for the third set of data with the peak E-region density. Dotted lines indicate the period when magnetically affected echoes are likely to be observed.

and only two of these define the electron density which could thus depend on the occurrence of a suitable meteor in a favourable location. A rough estimate would indicate an ambient density of $(8.9 \pm 1.0) \times 10^{10}$ m^{-3}.

A correction to the value of N_m for the third set of data can be made if it is assumed that the observed magnetic effect is caused by reflections from an electron ellipse of ionization. Equation 2.20 describes the relative depth of depletion regions and thus the conditions under which an electron ellipse can form. This condition depends on q and the ambient electron density, N_a, and since these quantities are proportional, if the minimum detectable line density is larger for a particular set of data, a larger value of N_a is needed before an electron ellipse can contain a significant proportion of the meteor ionization and thus be observed. Fig. 7.37 shows the echo time distribution for the third set of data with the calculated electron density (for the peak of the E-region). The dotted lines indicate the times for which magnetically affected echoes could occur, taking into account the reduced sensitivity. The estimated uncertainty is shown which includes the uncertainty in measuring N_m, but does not take account of any day-to-day variability. By using the proportion of magnetic to normal echoes in the second set of data and a more finely divided time distribution, the expected number of magnetically affected echoes observed in the third set of data was calculated to lie between one and eight. This explains the lack of a clear effect in Fig. 7.33 where only two echoes could be magnetically affected, although they are over 2^{o} from the specular condition.

Figs. 7.38 to 7.40 show the results for the fourth set of data. It was hoped that such results would confirm the absence of magnetic effects at large off-specular angles. In view of the lack of any magnetic effect in the third set of data, the fourth set could not be expected to show any magnetic effect either, which is the case.

(b) Ionospheric Refraction In section 3.6 the effect of ionospheric refraction on off-specular angle measurements was determined as a function of the electron density at the peak of the E-region. The results (Fig. 3.13), when compared with the values of N_m occurring during the recording of magnetically affected echoes (Fig. 7.36), show that a bending of between 1.0 and 1.8^o could be expected above 105 km while it would be, on average, 0.3^o less between 100 and 105 km. This is based on the height of the maximum of the E-region being between 108 and 110 km (e.g. Bremer and Singer, 1977). Heights estimated from ionosonde values are a little higher (typically ~ 115 km) which would reduce the expected bending between 100 and 110 km and would imply none below 100 km. However, the shift of values in Fig. 7.31 would suggest a bending of about 0.8^o below 100 km, which agrees more closely with an E-region maximum at 110 km. Such a shift could be caused by a systematic uncertainty in the elevation angle measurement or incorrect magnetic field values. The field values should be accurate to at least 0.1^o and a 0.8^o elevation error would cause a 5 km height error which is not likely in view of the height distribution obtained (Fig.

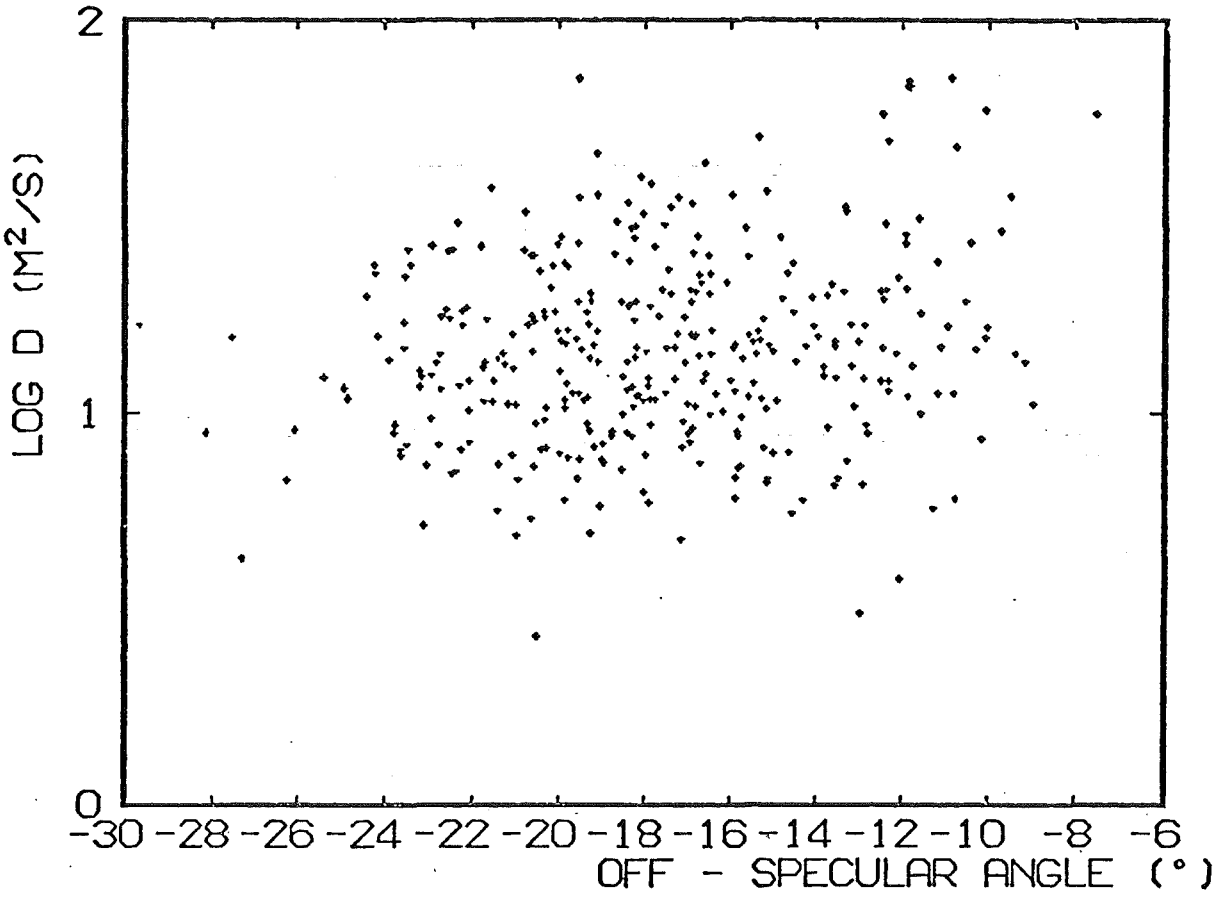

Figure 7.38: Fourth set of data, h > 100 km.

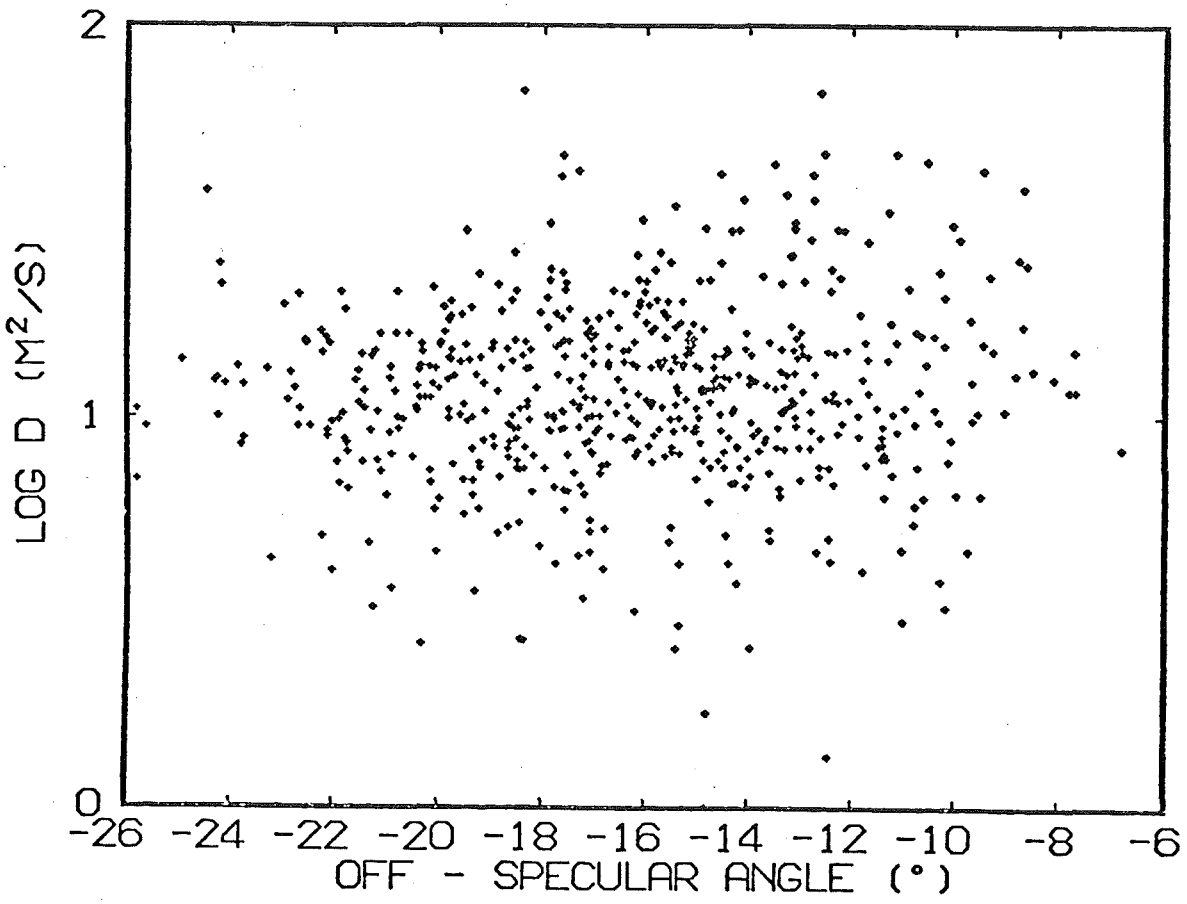

Figure 7.39: Fourth set of data, 95 km < h < 100 km

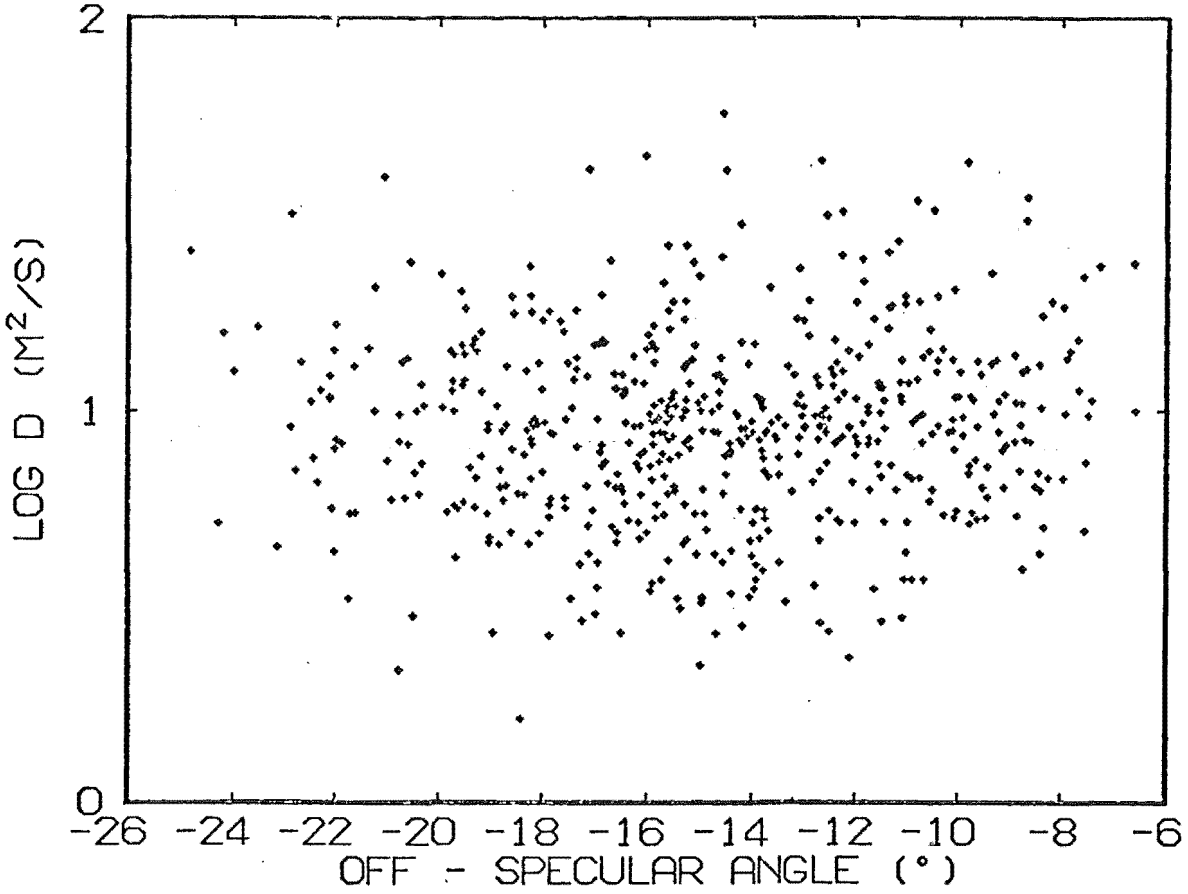

Figure 7.40: Fourth set of data, 90 < h < 95 km.

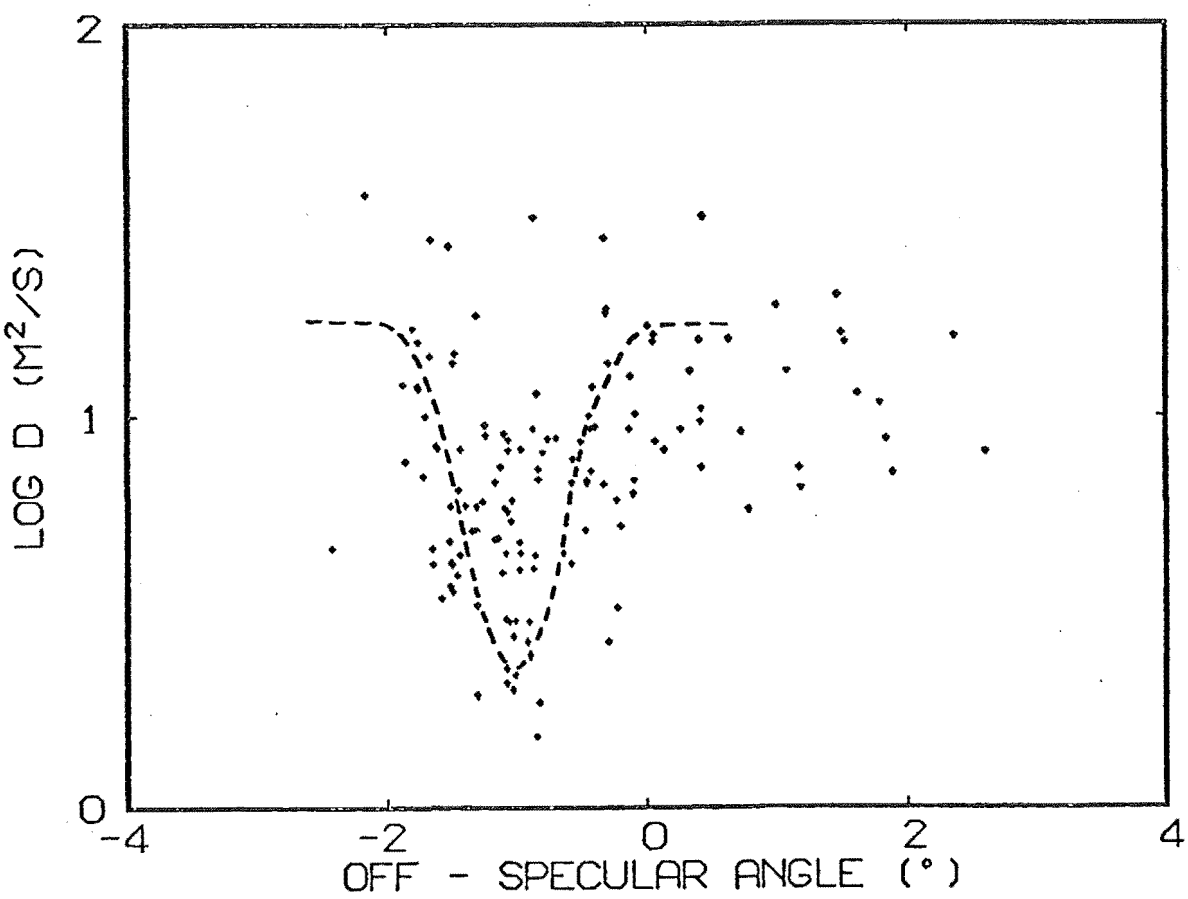

Figure 7.41: Second set of data, 100 < h < 105 km, times after 0800 hrs.

7.12) which is the same as that measured in many similar experiments.

Figs. 7.41 and 7.42 show the data split into the height ranges 100 to 105 km and above 105 km respectively. The mean value of μ for echoes with $D < 4.5$ m^2/s for heights above 105 km is -1.22 ± 0.07^{o}, for heights between 100 and 105 km is -1.15 ± 0.05^{o} and for heights below 100 km is -0.93 ± 0.03^{o}. Although the difference in μ for the first height ranges is not significant, that below 100 km is markedly less, which is consistent with the presence of ionospheric refraction.

The uncertainty in μ has not been shown in these diagrams because that due to variable ionospheric refraction is much larger. The measurement uncertainty would be similar to the elevation uncertainty (Fig. 7.17(b)) which is between 0.05 and 0.15^{o}.

It is worth noting that ionospheric refraction of reflected radio waves from meteor trains (or any field-aligned ionization) could be used to measure electron density. A system set up to do this could be calibrated at night when electron density was low (although high sensitivity would be needed) so that problems of systematic uncertainties in absolute angle measurement and in field line orientation would be eliminated. Height measurement would still be needed so that an ionization profile could be obtained in the 95 - 110 km region. The uncertainties in D measurements would mean that many echoes would need to be recorded so again high sensitivity is desirable and measurements may

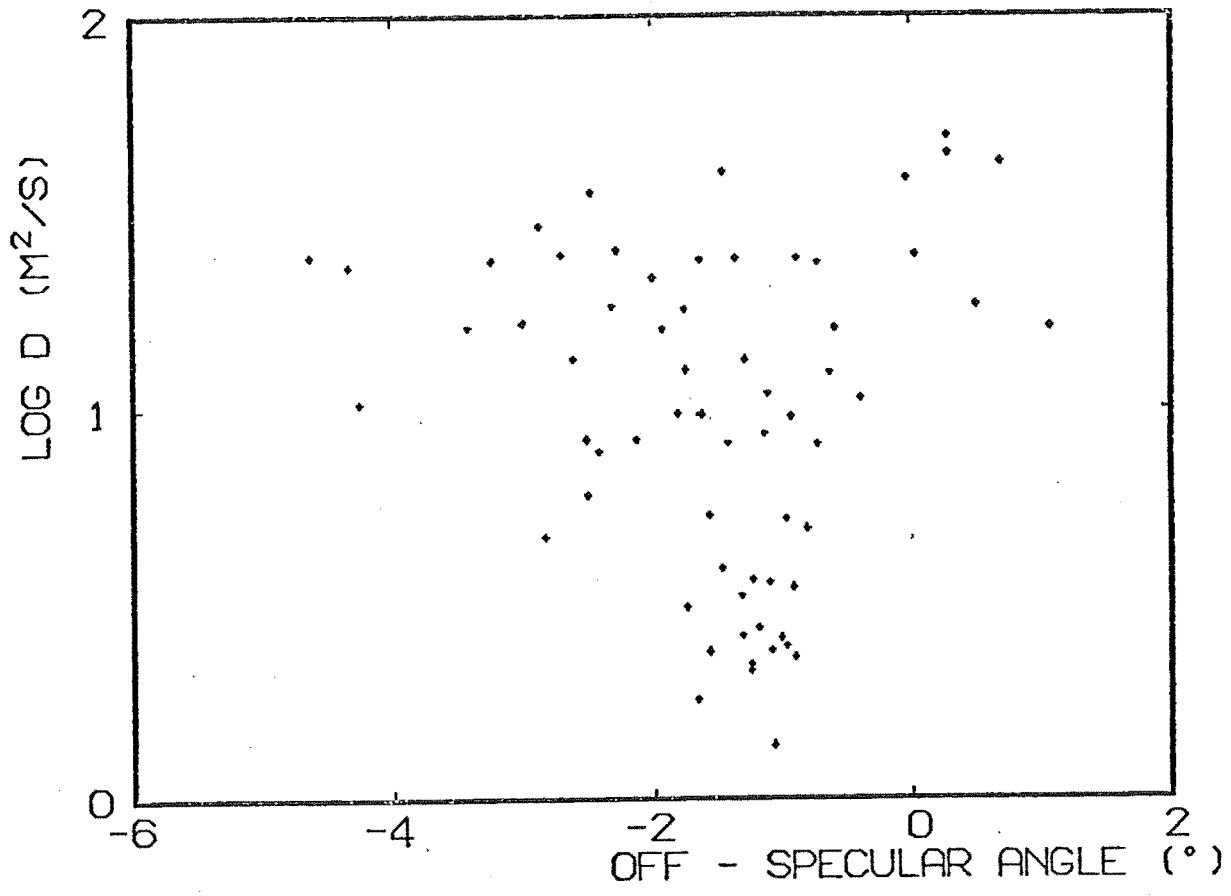

Figure 7.42: Second set of data, h > 105 km.

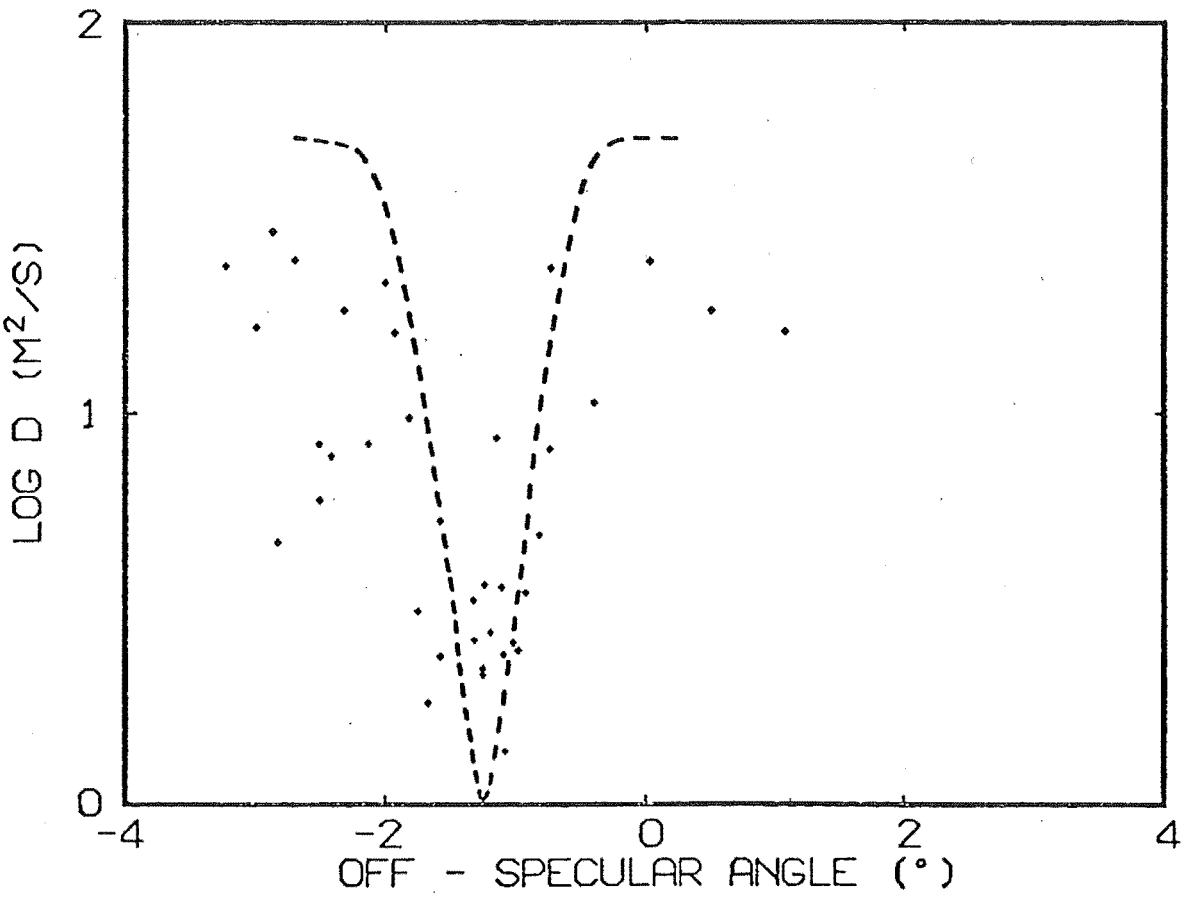

Figure 7.43: Second set of data, h > 105 km, after 0800 hrs.

not be accurate when the electron density was changing rapidly. However, ambient ionization densities in the 95 to 110 km height interval can be measured quite well with ionosondes (it is above the maximum of the E-region that difficulties arise) which are less complex and thus more suited to performing these measurements than a meteor radar.

In the following discussion $\mu = 0^{o}$ is regarded as the specular condition since ionospheric refraction explains the observed offset in μ values.

(c) Comparison with Theory The magnetic effect that has been observed is the occurrence of low measured D values over a narrow range of off-specular angles. It has been shown that echo decays affected in this way are associated with smaller electron line densities than average and only occur when the ambient number density is sufficiently high. This would seem to indicate that the effect is caused by reflections from trains that have developed electron and ion ellipses by forming depletion regions in the background plasma. The electron ellipse has an effective diffusion coefficient along its major axis of (section 2.6)

$$\hat{D}_{-} = D_{T-} \cos^2\alpha + D_{-} \sin^2\alpha$$

while the minor axis diffuses at a rate governed by D_{T-}. The observed D value will be (section 3.2)

$$D_{eff} = D_{\perp} \sin^2\beta + D_{\parallel} \cos^2\beta$$

so that by using equation 7.2 the result found by Kaiser (1968) is obtained

$$D_{eff} = D_{T-} \cos^2\mu + D_- \sin^2\mu \ . \qquad 7.3$$

This has ignored the effect of the central core of ionization contained in the ion ellipse. For values of $\mu \gtrsim 1^o$ D_{eff} becomes very large and cannot be observed because of the finite velocity effect and the method of analysis which needs at least five pulses to fit an echo decay. In this case the second term in equation 3.5 dominates and a diffusion coefficient of D_+ should be measured. For $\mu << 1^o$, $D_{eff} \approx D_{T-}$ which is less than D_+ above 95 km. In this case the method of analysis should mean that just D_{T-} will be observed as the signal from the ion ellipse will decay in the initial 25% of the echo that is rejected during the analysis. A change in the decay rate could then be expected for such echoes.

In Figs 7.41 and 7.43 the dotted lines show the expected diffusion coefficients that should be measured from trains forming electron and ion ellipses at heights of 102 and 108 km respectively. Echoes recorded after 0800 hours (corrected L.M.T.) have been used in order to decrease the scatter in μ caused by ionospheric refraction. The effect of this can be seen by comparing Figs 7.42 and 7.43 where a dip has become apparent. The change in N_a even after 0800 hours will still cause some scatter in μ, but more severe time restrictions will result in too few echoes to show the effect clearly.

Fig. 7.41 shows that the theory and results are consistent when the scatter in μ and expected scatter in log D are considered. In the case of Fig. 7.43 it appears that the choice of 108 km for the theoretical diffusion curve was too high as all points lie between the extreme theoretical values. However, the finite velocity effect could cause the measured D values to be too low (high D values will not be observed).

In theory it would be possible to measure the value of α_c by using the backscatter results. α is related to μ and the angle from a perpendicular train, η, by

$$\cos \alpha = \cos \eta \cos \mu \quad . \qquad 7.4$$

If the zenith angle distribution follows a cosine law, η will do likewise and this characteristic can be used to predict the percentage of trains with $\alpha < \alpha_c$ for a given μ. For example, if $\alpha_c = 5^o$ then 8% of echoes at $\mu = 2^o$ would show inhibited diffusion. At $\mu = 4^o$, 5% of decays should be inhibited, while for $\mu > 5^o$ no inhibited diffusion would be observed. For the expected value of $\alpha_c = 1.4^o$, the percentage of inhibited decays expected at $\mu = 0.5^o$, 0.75^o and 1^o are 2.3%, 2.1% and 1.7% respectively. For $\mu > 1.4^o$, no inhibited diffusion should be observed. In practice it is not possible to get a good estimate of α_c because of the scatter in μ caused by variations in ambient electron density. Furthermore, a larger number of echoes are really needed when probabilities ~ 0.02 are being

considered. However, the sharpness of the dip (clearest in Fig. 7.30) would suggest that α_c was less than 5^o, but a better limit for α_c or even verification that inhibited diffusion does occur for $\alpha < \alpha_c$ cannot be found from these results.

The individual pulse amplitudes from eight decay echoes were examined to see if there was a change in the decay slope during the echo life. This behaviour is expected because the signal reflected from the ion ellipse will decay in the early part of the echo (in about 0.07s at 100 km). No change in the slope was apparent on a logarithmic plot, but the oscillations from Fresnel diffraction occurring in the early parts of the decay where the change is expected may have obscured the effect. The initial radius of the ion ellipse could also make the signal from the electron ellipse dominant even at the beginning of the decay.

The ionization density at the peak of the E-region was estimated to be $(8.9 \pm 1) \times 10^{10}$ m^{-3} when inhibited diffusion was first observed. The mean height of the magnetically affected echoes was 102.7 km, so an electron density for a point 7.3 km below the E-region maximum is appropriate. Assuming a Chapman layer for the electron density distribution gives

$$N_a = 0.75\ N_m = (6.7 \pm 1.0) \times 10^{10}\ m^{-3}$$

to be considered with a mean electron line density of magnetically affected echoes of 3.5×10^{12} m^{-1}. These

values, together with the value of D_{T+} and expected value of $\hat{D}_-$ appropriate to 103 km can be used to find $H_d.t$ - the product of relative depletion region depth, H_d, and echo lifetime

$$H_d.t = 3.7 \times 10^{-3} \text{ s.}$$

Since anisotropic ambipolar diffusion does not occur until $H_d > 1$, the electron and ion ellipses can form after about 4 ms so that inhibited diffusion should be seen about $\mu = 0^o$. The wide range of possible values of α and variation on echo heights make this a very rough calculation, but it does show that the interpretation of the results in terms of the formation of electron and ion ellipses is probably correct.

Thus far, only the behaviour of trains forming electron and ion ellipses has been considered. No magnetic effect was observed in the third set of data about $\mu = 0^o$. The absence of an effect such as was seen in the second set of data implies that a model with ambipolar diffusion producing a train with an elliptical cross-section is appropriate. The expansion of the ellipse is described by the diffusion coefficients $2D_+$ and $2D_{T-}$ so the ellipse dimensions do not depend on α providing $\alpha > \alpha_c$. Thus the D values observed with backscatter will only depend on μ and the zenith angle distribution.

By using equations 7.2 and 7.4 it is possible to find the expected values of the angle between the ellipse major

axis and the backscatter direction, β, for a cosine zenith angle distribution. For $\mu = 0^{o}$, β is always 90^{o} so that $2D_{T-}$ should be measured; for $\mu = 0.5^{o}$, only 1% of echoes should have $\beta < 63^{o}$; for $\mu = 1^{o}$, 1% have $\beta < 45^{o}$ and when $\mu = 2^{o}$, 1% have $\beta < 27^{o}$. Thus there should be a definite decrease in the measured D values about $\mu = 0^{o}$ although the minimum observable D of $2D_{T-}$ could occur for all μ values less than 90^{o}. This effect thus differs from that caused by the electron ellipse where low D values occurred only about $\mu = 0^{o}$ and is consequently more difficult to observe because scatter in μ can conceal the dip.

In Figs. 7.44 and 7.45 the larger echoes (5×10^{12} $m^{-1} < q < 2 \times 10^{13}$ m^{-1}) were selected and times were restricted to between midnight and 0400 hours so that N_a should be fairly constant. In neither case is any dip about $\mu = 0^{o}$ (ionospheric refraction should be negligible) observable, although in Fig. 7.45 the points are very sparse.

Possible reasons for the lack of an effect are scatter in μ (although dips were distinguishable in Figs. 7.41 and 7.43); the large inherent scatter in D measurements or the train not having an elliptical cross-section at all. The fact that previous workers have observed magnetic effects in overdense meteor studies (Watkins et al, 1971) make the last reason unlikely.

The interpretation of the results of overdense studies in terms of aspect sensitivity of elongated ionization is an over-simplification. The effect depends on the geometry; namely the relationship between β,μ and η, and is thus not

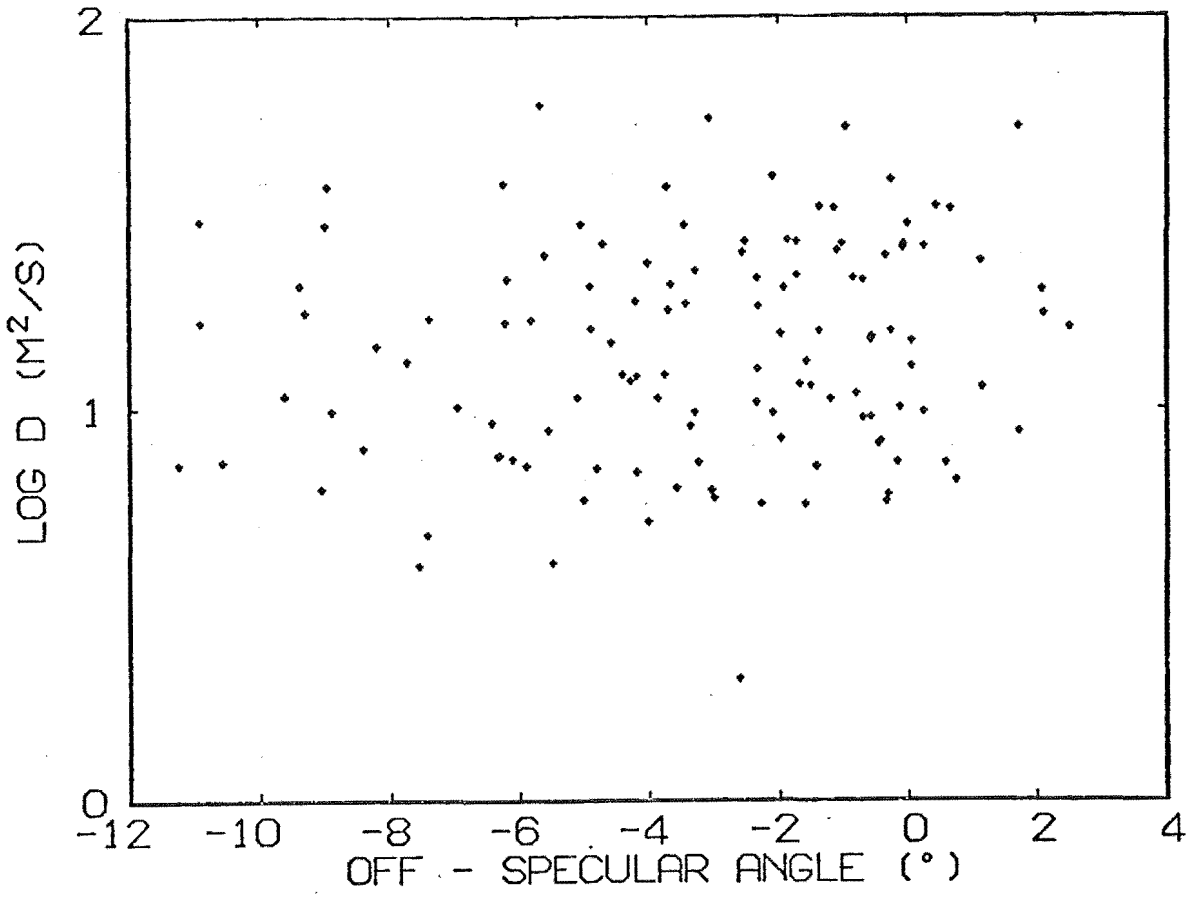

Figure 7.44: Third set of data, 100 < h < 105 km, $5 \times 10^{12} < q < 2 \times 10^{13}$ m^{-1}.

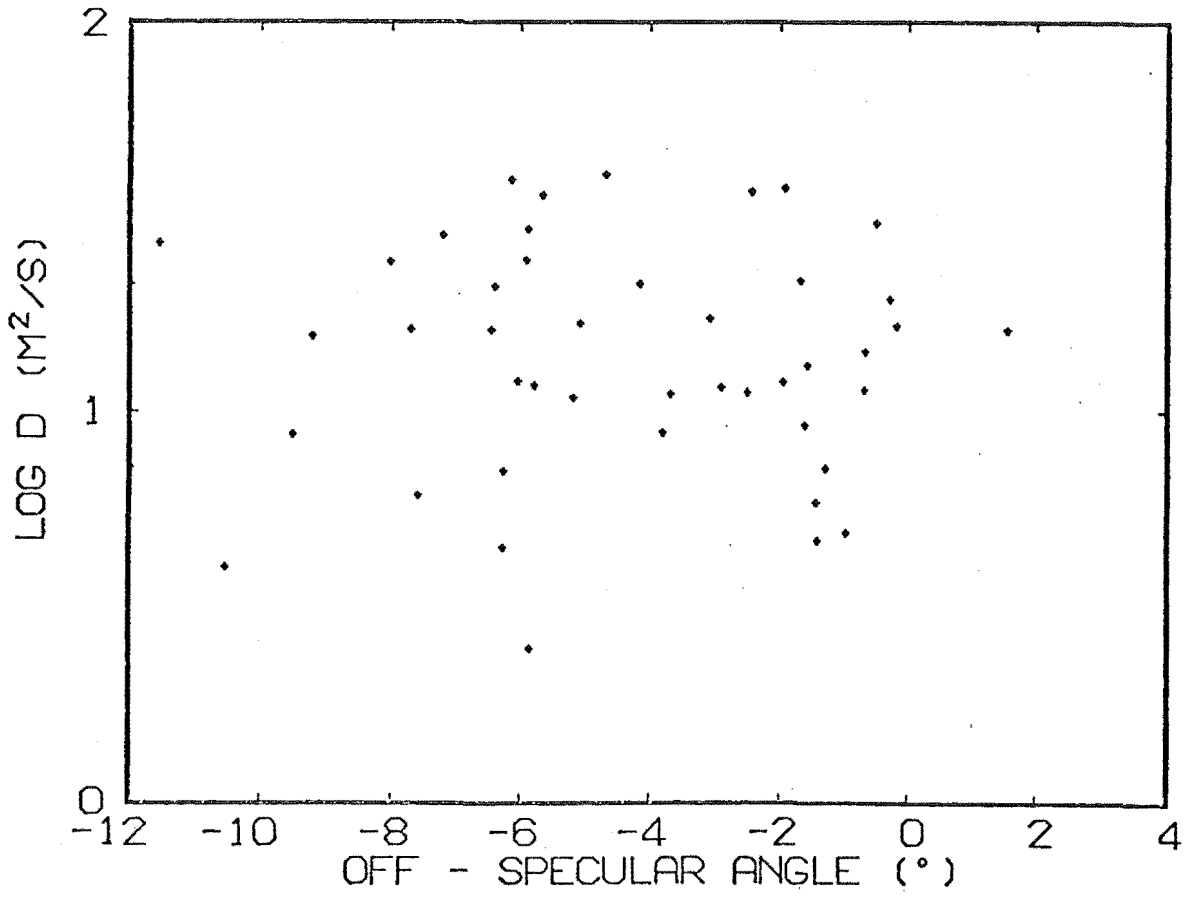

Figure 7.45: Third set of data, 105 < h < 120 km and $5 \times 10^{12} < q < 2 \times 10^{13}$ m^{-1}.

wavelength dependent (unless measurements are affected by the finite meteor velocity). For $\mu < 1^{o}$, β changes rapidly from 0^{o} when $\eta = 0^{o}$ to $\sim 90^{o}$ when η is a little greater than 0^{o}. As μ increases the rate of change is slower and diffusion at the rate $2D_{+}$ could be observed.

It is important to remember that the diffusion of all meteor trains above 95 km is expected to be affected by the earth's magnetic field. The diffusion will then be ambipolar, but anisotropic, for larger trains while electron and ion ellipses will be important when the relative depletion region depth is less than 1. In each case the observed value of D will be different for general train orientations ($\mu > 1^{o}$). First, in trains where the electron ellipse is important a coefficient of D_{+} should be observed for $\mu > 1^{o}$ because most of the signal will come from the central core of ionization. Measurements of the ambipolar ellipse will be more variable with values in the range $2D_{T-}$ to $2D_{+}$ being possible, although the finite velocity effect must be considered. A knowledge of likely μ values for a particular radar location is desirable so that effects about $\mu = 0^{o}$ can be avoided (or studied). Furthermore, the range of μ values encountered could be used to determine the likely spread in D values measured from elliptical trains if assumptions are made about the zenith angle distribution.

In view of these effects it is not surprising to find that D values measured above 95 km are consistently less than $2D_{+}$. Furthermore, variations in train orientation will increase the scatter observed in D and diurnal variations

in electron density could cause similar variations in D.

In section 2.6 the possibility that the drift of some meteor ionization could be affected by the earth's magnetic field was mentioned. This could reduce the neutral wind velocities inferred from such trains. This was checked by measuring train drifts with the doppler wind system built into the receiving equipment (section 6.4). The mean absolute inferred wind velocities were compared for magnetically affected and unaffected trains. The criteria for selecting affected echoes were that $D < 4.5\ m^2/s$ and $-1.5^o < \mu < -0.8^o$. The results were 16.1 and 15.0 m/s respectively and were found not to be significantly different. R.m.s. values were not used because it is the wind magnitude that is important and the greater spread in wind velocities in non-magnetic echoes will give a significantly higher r.m.s. velocity. This greater spread is probably due to echoes being selected from a much larger volume of the atmosphere. These results do not rule out the possibility that field-aligned trains will be fixed to the field lines, but it appears that field-aligned fins of ionization are not.

7.5 VARIATION OF D WITH HEIGHT

(1) Introduction

Figs. 7.46 to 7.49 show the variation of log D with height for each set of data. Correlation coefficients (in the fitting of a straight line to the natural logarithm of the echo amplitude decay) greater than 0.95 were used,

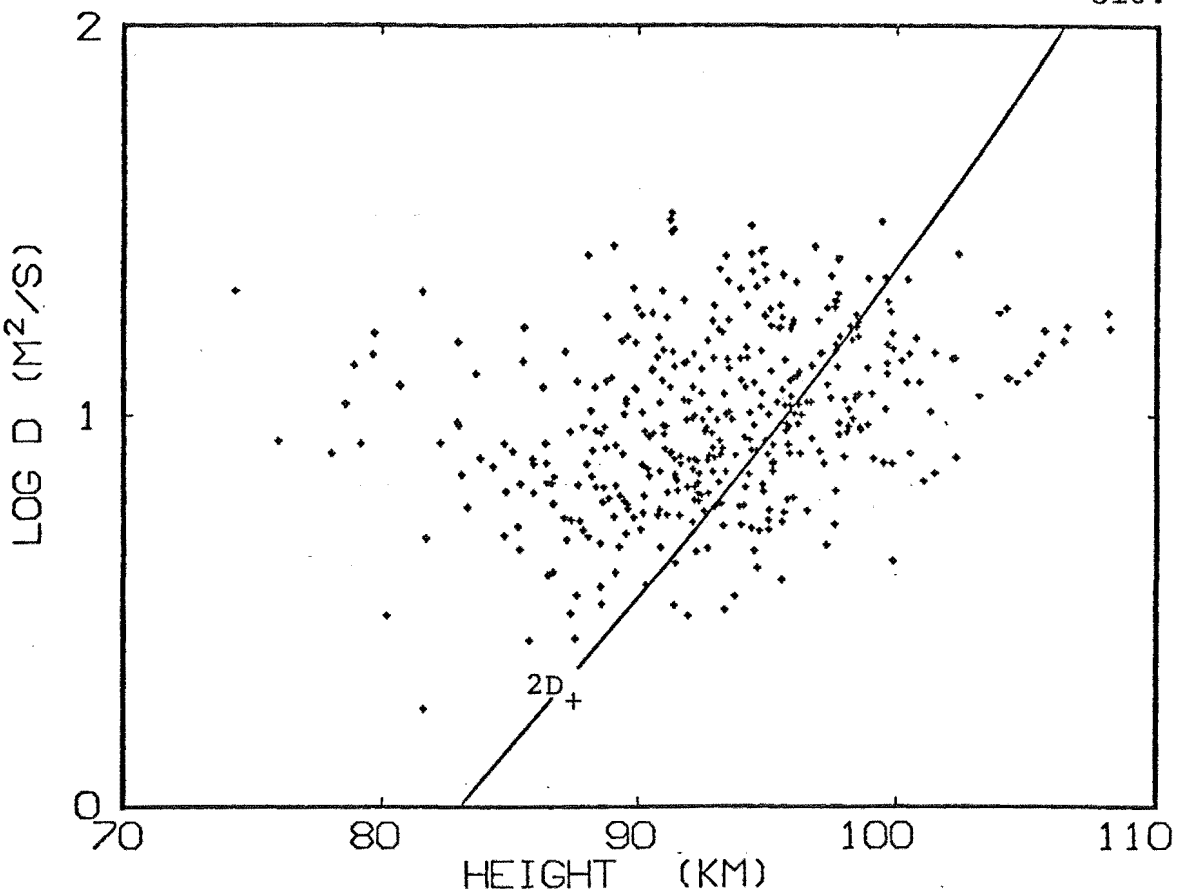

Figure 7.46: First set of data, correlations (r) > 0.95.

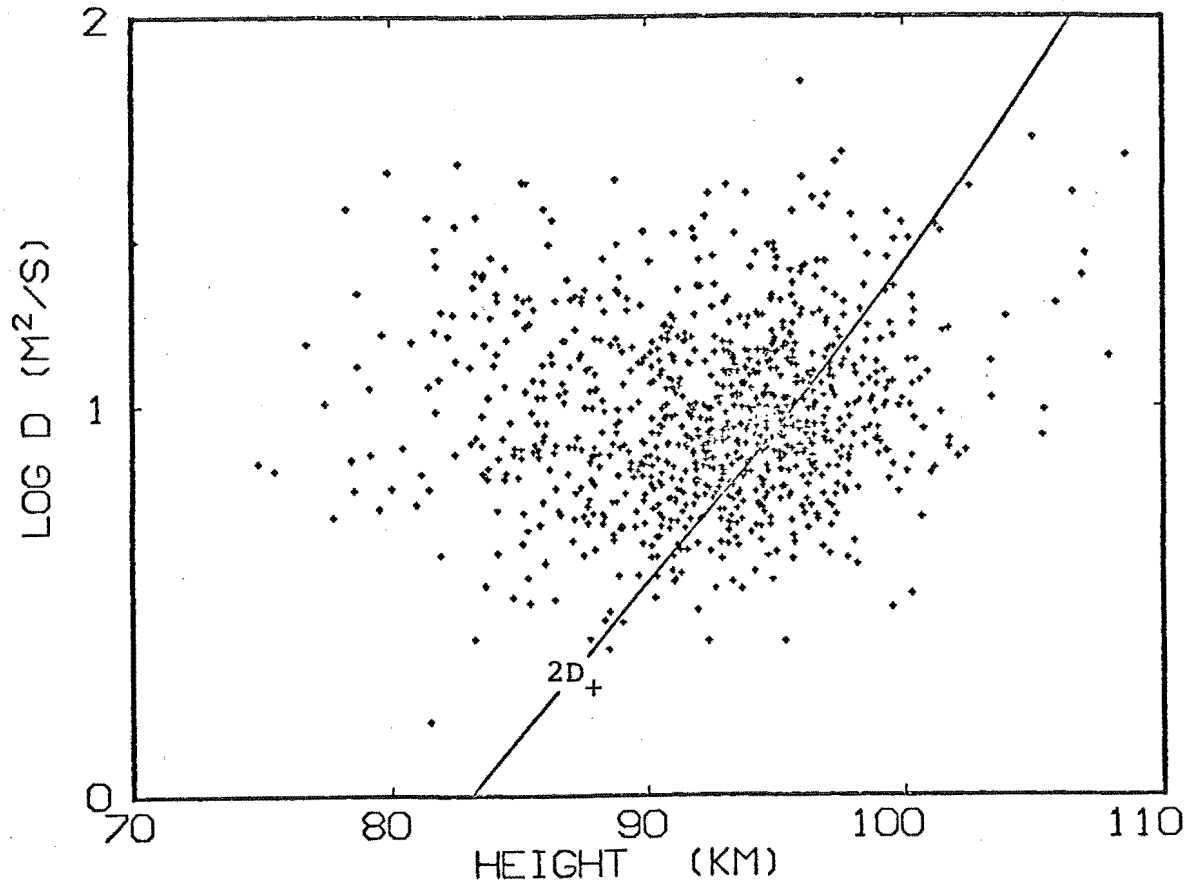

Figure 7.47: Second set of data with magnetically affected echoes removed.

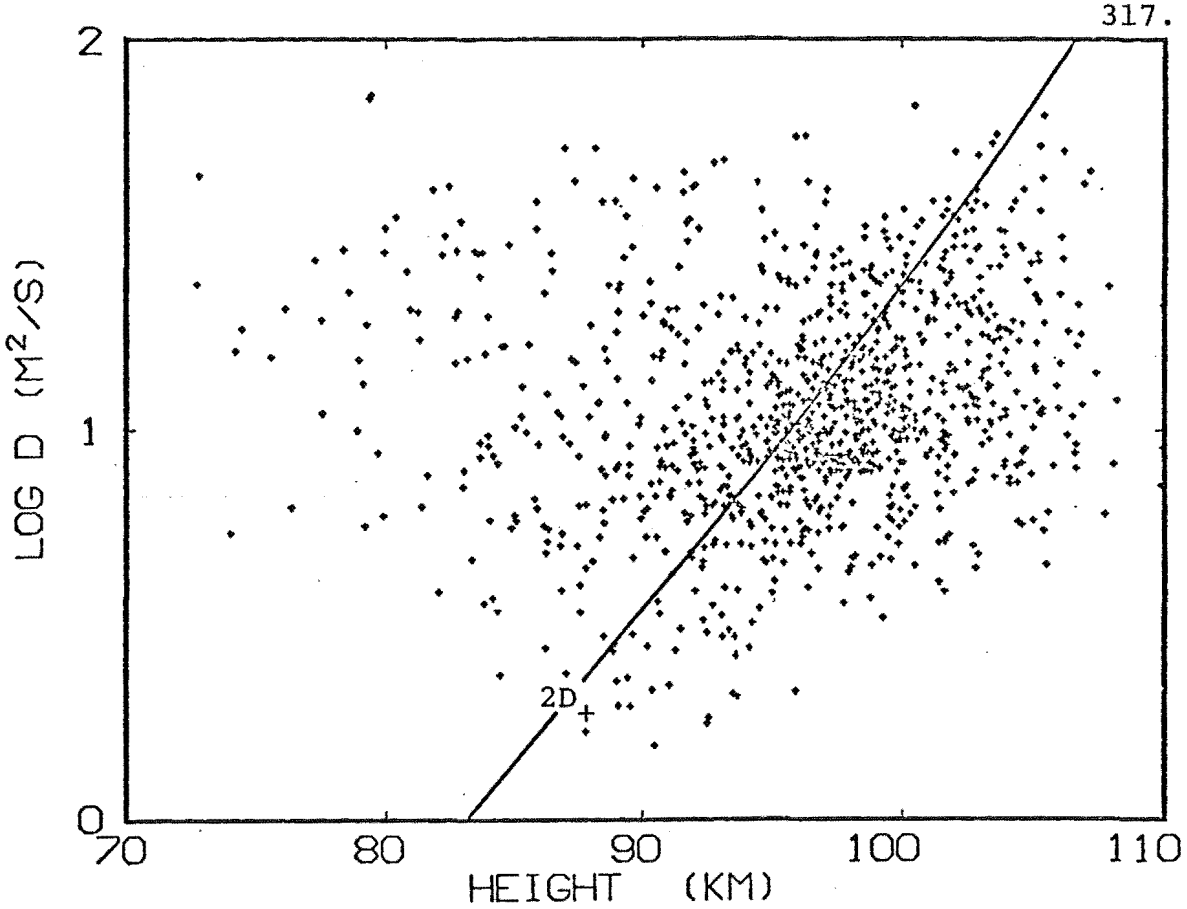

Figure 7.48: Third set of data.

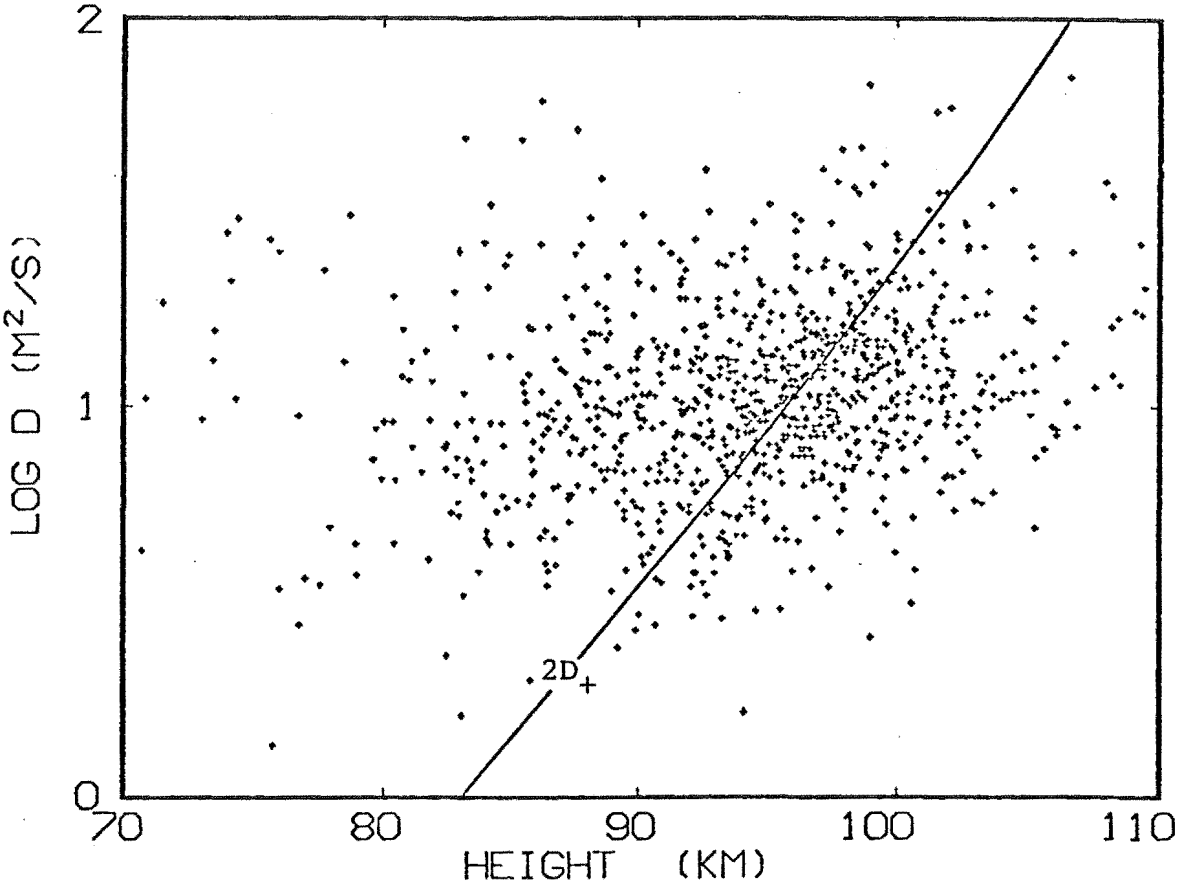

Figure 7.49: Fourth set of data.

mainly to reduce the total number of echoes to a manageable number for the plots. The use of correlation coefficients to select decays is discussed in the next sub-section. Also shown is the theoretical ambipolar diffusion coefficient ($2D_+$) which was calculated in Chapter 2 (Table 2.5).

The last three figures have some higher D values than the first because of the use of the higher 300 Hz P.R.F. (this was used in a part of the second set of data). Each set of data shows a similar pattern: below about about 95 km D values are significantly higher than expected, possibly due to chemical effects; around 95 km theory and experiment agree, but there is a large scatter in log D; above 100 km the D values are significantly lower than $2D_+$ which is consistent with the expected magnetic effect and the height ceilings imposed by the analysis and finite meteor velocity.

(2) Method of Analysis

The use of linear regression and weighted linear regression to fit straight lines to the natural logarithm of the echo amplitude decay and hence infer a diffusion coefficient was mentioned in section 3.5. The weighted linear regression was only used for the third and fourth sets of data, together with an unweighted regression so that the measured D values can be compared. Table 7.2 is a comparison of the two regression methods for these data in the height range 90 to 95 km. In both cases the spread in log D is less for the unweighted regression which is an opposite result to that

Table 7.2: Comparison of regression methods.

Data set	Mean height (km)	σ_h	Unweighted regrn.		Weighted regrn.	
			$\overline{\log D}$	σ	$\overline{\log D}$	σ
3	92.67	1.40	0.959	0.283	0.993	0.301
4	92.70	1.41	0.954	0.241	0.982	0.251

expected. Furthermore, the mean value of log D is consistently higher for the weighted regression. This is not surprising since the weighted regression takes more account of high amplitudes and will therefore tend to fit the regression line to an earlier part of the echo decay, which is more likely to be more rapid because of chemical reactions, plasma resonance and magnetic effects. The fact that higher average D values are measured may also mean that the scatter in log D is larger. The weighted regression was used in the later analysis because it should theoretically give better inferred D values.

Another feature of the results in Table 7.2 is the significantly larger spread in log D for the third set of data even though the spread of heights in the range 90 to 95 km is very similar. Remembering that these sets of data were recorded in alternate hourly intervals, the cause is unlikely to be physical. A likely explanation is the problem with the south-facing interferometer that had a systematic height uncertainty dependent on echo azimuth. Thus the real scatter in the heights is larger than that indicated in the analysis which causes a larger variation in the measured D values.

The correlation coefficient found when fitting the echo decay was used to select exponential decays. Suitable correlation values were found by plotting some decays and echoes having r > 0.85 were used in later analysis. This is not an entirely satisfactory way of selecting the best echoes because it cannot distinguish between a poor fit due to Fresnel amplitude fluctuations or sky noise and one due to a non-exponential decay. Selection by eye would have some advantages, but could introduce bias and is not practical for thousands of echoes. To test the effect of different correlations three ranges of r were tried on echoes in the 90 to 95 km height span and the results are given in Table 7.3.

Table 7.3: Test of correlation coefficients.

r	$\overline{\log(D,\ m^2/s)}$	σ
> 0.5	0.875	0.302
> 0.85	0.913	0.277
> 0.95	0.951	0.308

A strict comparison is difficult because, although the same number of echoes were used in each case, the time intervals in which they were recorded is different which may explain the large scatter for r > 0.95. The choice of r also appears to introduce some bias into the mean log D value.

When fitting lines to the log D versus height data, account must be taken of the uncertainties in both heights

and diffusion coefficients in order to get a representative fit. By ignoring one set of uncertainties (thus obtaining a regression line for one variable on the other) or the other set, two lines will be obtained, but the correct result will lie between these lines. When the correlation coefficient between log D and height is high these two lines will be close together, but for the low correlations in these data the gradients will be quite different. A simple method of finding the central regression line is given by Ross (1980) where the slope is

$$m = \frac{(\beta^2\sigma_y^2 - \sigma_x^2) + [(\beta^2\sigma_y^2 - \sigma_x^2)^2 + 4\beta^2(\sigma_{xy}^2)^2]^{\frac{1}{2}}}{2\beta^2\sigma_{xy}^2} \qquad 7.5$$

where σ_y^2, σ_x^2 are the variances of the y and x variables ($x \equiv$ height, $y \equiv \log D$),

$$\sigma_{xy}^2 = \frac{\sum xy}{n} - \frac{\sum x \sum y}{n^2}$$

where n is the number of points and

$$\beta = \frac{\Delta x}{\Delta y}$$

is the ratio of the uncertainties in the x and y variables. Equation 7.5 is a least squares fit, but the distances of the points from the final regression line (at an angle determined by Δx and Δy) are being minimised and not the distances in the x or y direction.

The final result for m or the inferred value of D for a particular height thus depends on the estimation of uncertainties in height and log D. The appropriate height uncertainty has been estimated in the analysis and is the standard error of the mean height for each meteor, average values being given in Fig. 7.18. While a value of Δh = 1km is suitable for the fourth set of data, some account must be taken of the systematic uncertainty in height measurement in the magnetic south direction. As the difference in mean height between positive and negative azimuths is about 4 km an additional uncertainty of about $\pm$ 2 km (corresponding to one standard deviation) is probably appropriate. A final height uncertainty of 2.5 km was used.

The uncertainty in log D is more difficult to evaluate as there is an inherent spread, probably due to wind effects (section 3.3). However, by assuming that in the height range 90 to 95 km the echo decay is caused only by diffusion, the uncertainty in log D can be estimated by using the theoretical log D versus height variation and the known height uncertainty and spread in heights. For the third and fourth sets of data, Δ(log D) is 0.21 and 0.22 respectively, which confirms that the smaller scatter in the fourth set of data is due to the more reliable interferometer. The size of the inherent spread is consistent with other work (section 4.3) and with that expected from wind effects (Fig. 3.3, Δ(log D) = 0.21 $\equiv$ $\Delta D/D$ = 0.5). The results for the first and second sets of data are 0.05 and 0.06 respectively and this reduced scatter is noticeable in Figs.

7.46 and 7.47. If the expected uncertainty in D measurement is subtracted, the inherent scatter is about 0.04 in log D. This is smaller than that generally observed, the difference being too great to be explained by the height uncertainty being overestimated. These data were recorded over shorter time intervals than sets 3 and 4 which would mean less atmospheric variability as would the smaller volume of atmosphere covered because of the range selection imposed. The P.R.F. of 150 Hz also limits the scatter at high D values, but an increase in the scatter in both directions is apparent in later runs.

Having found the inherent scatter in log D appropriate to each set of data, the scatter for other height intervals could be estimated by looking at the relative change expected due to wind effects (Fig. 3.3). As the relative contribution is not well known, the approximation is crude. Little change in inherent scatter could be expected above 95 km (apart from that due to D measurement), but there could be an increase below 90 km by a factor of two. The method used to estimate the scatter in the 90 to 95 km height range is not appropriate for other heights because ambipolar diffusion does not appear to be the major cause of echo decays.

An attempt to fit a regression line to the third set of data gave the opposite slope to that expected if ambipolar diffusion was dominant. This suggested that the effect causing high measured D values at lower altitudes is still important above 90 km. Thus for this system sensitivity and radar wavelength there is no height range where ambipolar

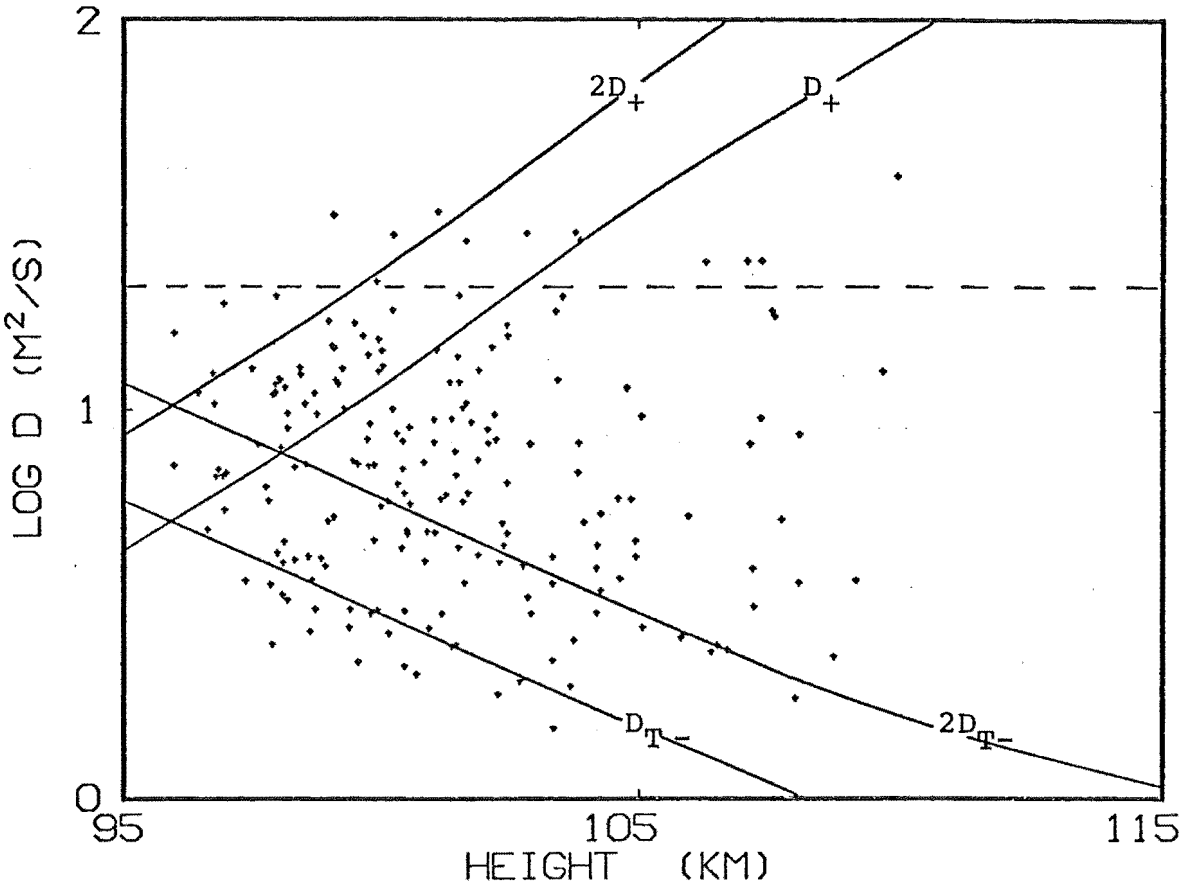

Figure 7.50: Second set of data, $-1.8^{o} < \mu < 0.8^{o}$, $r > 0.85$.

diffusion is dominant and where scale heights can be measured.

(3) Magnetic Effects

Fig. 7.50 shows the echoes from the range of off-specular angles that showed a magnetic effect in the second set of data. No attempt has been made to fit a regression line to these data because there will tend to be two types of decay present. First, the inhibited decays caused by the low transverse diffusion in the electron ellipse and secondly the decays for larger μ values that appear in the magnetic range of μ because of ionospheric refraction. Decays in the transition region will also be present.

The low values of D follow the expected D_{T-} line and, as expected, a range of higher values occurs. The dashed line shows where the finite meteor velocity will begin to discriminate against higher D values and this discrimination will become severe above 105 km.

Figs. 7.51 and 7.52 show the second set of data with the magnetically affected echoes removed; this procedure should leave only echoes whose decays are caused either by diffusion of the central column (D_+) or by diffusion of an ambipolar ellipse ($2D_+$ to $2D_{T-}$). As echoes in which the electron ellipse was important appeared only after 0800 hours (corrected L.M.T.), the data are split into two groups before and after this time. The linear regression analysis is not useful here because a wide range of D values can occur, thus making estimates of β unreliable. A comparison of the mean values of log D for echoes above 100 km shows that the night-time value is significantly higher at a 5% level and more significantly different if a correction is made for the different mean heights. This could be caused by the ambipolar type of diffusion expected when the ambient electron density is low. Atmospheric temperatures and densities deduced from inferred diffusion coefficients and scale heights will not be correct if changes in the type of diffusion such as those suggested are occurring.

In general terms, $2D_+$ appears to suit the D values measured at about 94 km while D_+ is more characteristic just below 100 km. Above this height the finite meteor velocity will begin to be important. Consequently, there is

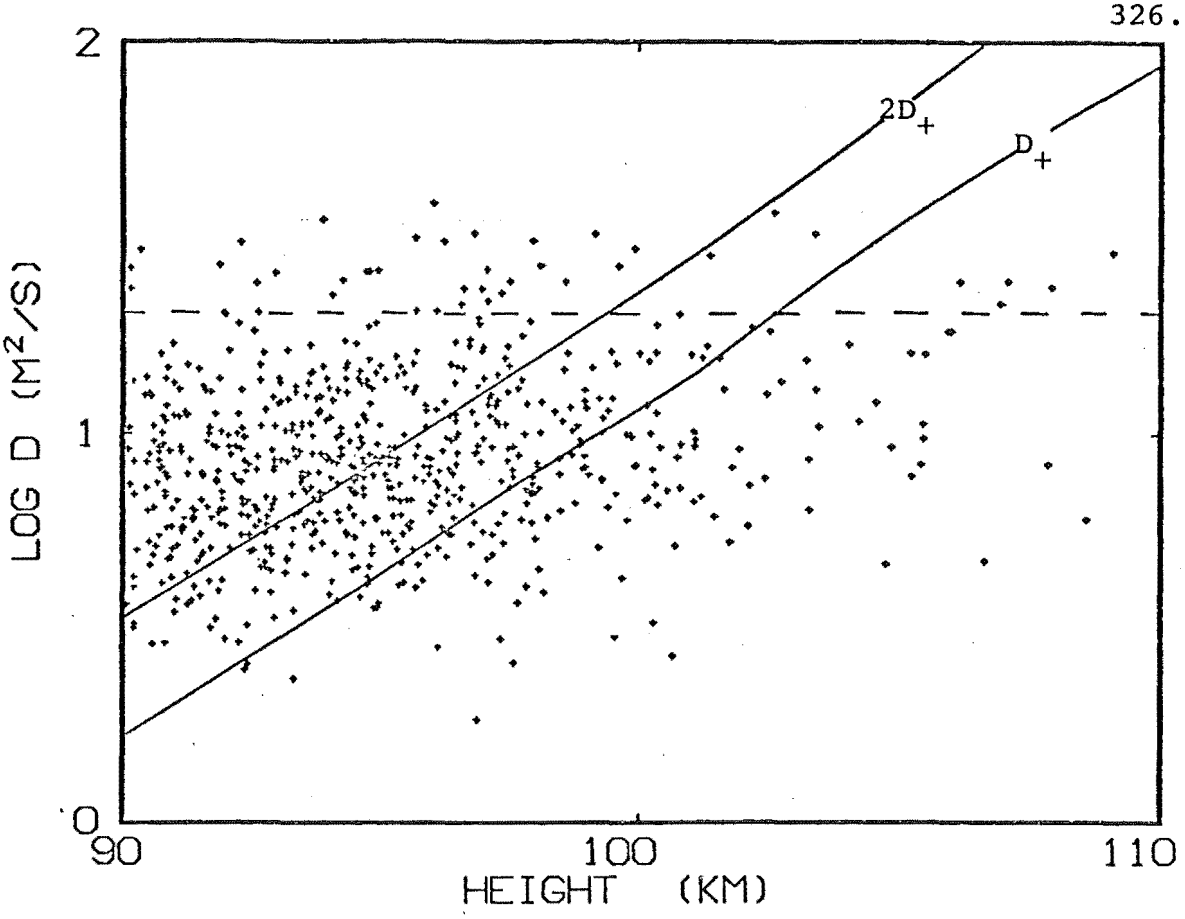

Figure 7.51: Second set of data, magnetically affected echoes excluded, times after 0800 hours, r > 0.85.

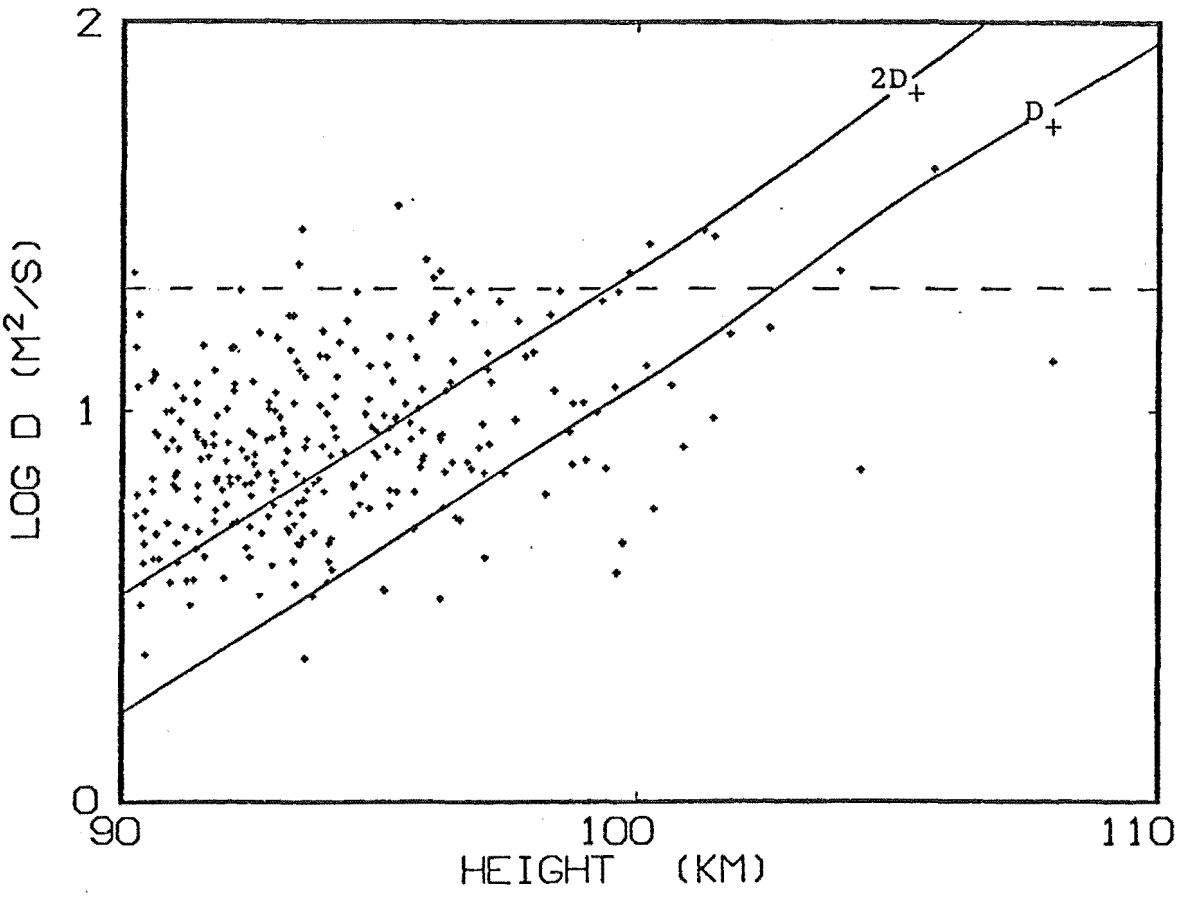

Figure 7.52: Second set of data, magnetically affected echoes excluded, times before 0800 hrs, r > 0.85.

no height range that is large in comparison with the height uncertainty over which the variation of D with height can be studied. The use of longer wavelengths and smaller height uncertainty could enable D at heights above 95 km to be studied. Furthermore, the range of D expected from anisotropic ambipolar diffusion should cause a noticeable increase in the scatter in log D.

Fig. 7.53 shows the third set of data above 90 km which differs from the second set in that the diffusion ceiling is higher and there is more scatter. However, the basic trends are the same and again a linear regression is of no use because there are more processes than ambipolar diffusion affecting echo decays.

Brown (1976), in a backscatter experiment at 1.98 MHz. found that meteor diffusion coefficients above 105 km were a factor of two smaller than expected. However, his results are in good agreement with values for D_+ which would be measured if electron and ion ellipses were formed. At 1.98 MHz, the ambient electron density must be less than 4.9×10^{10} m^{-3} for echoes to be observed which suggests a system sensitivity twice as great as that used in this work. A 26 kW transmitter was used by Brown with an antenna beamwidth of $\pm 5^{o}$ in one direction, so that this increase in sensitivity may have been obtained. The departure from D_+ to more than $2D_+$ observed below 105 km may be caused by chemical effects which are more prominent at this frequency because of slow decay times.

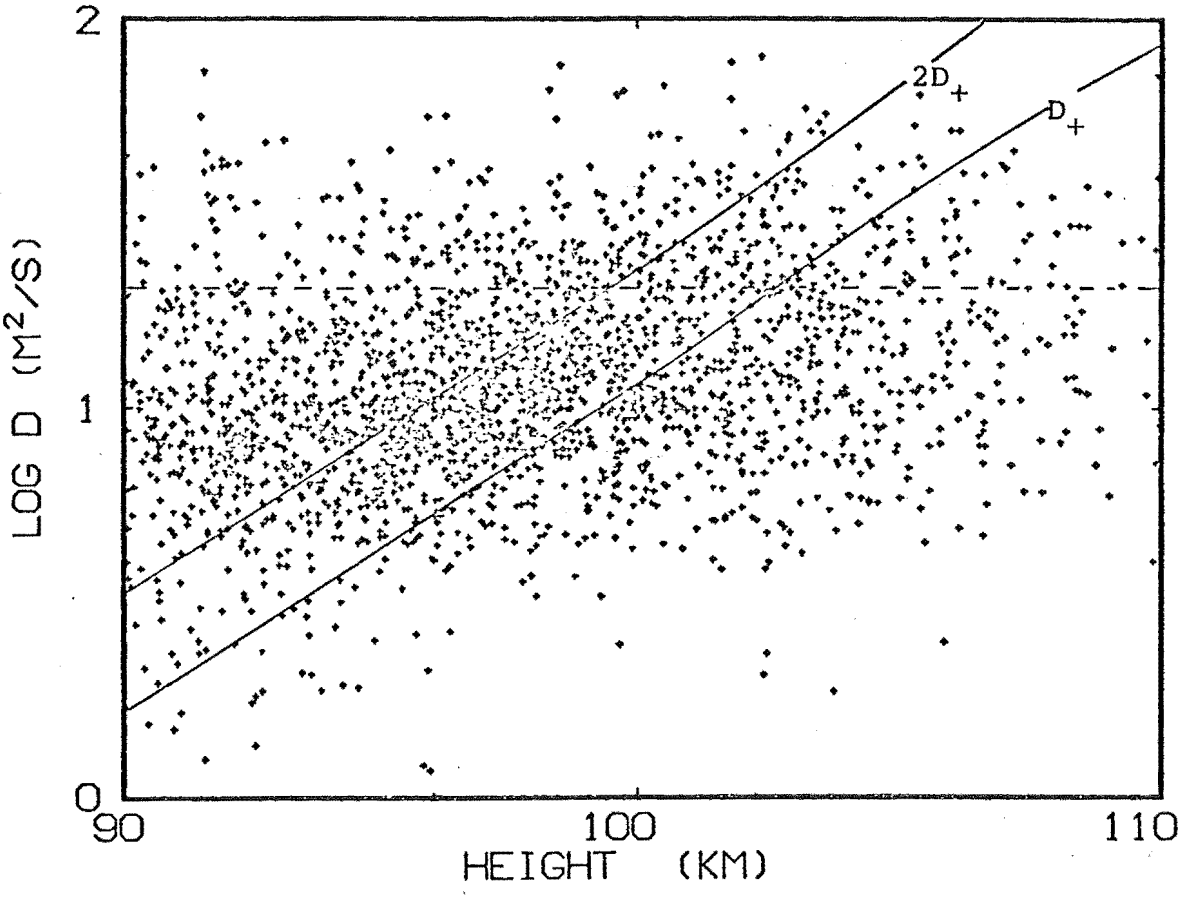

Figure 7.53: Third set of data, r > 0.85.

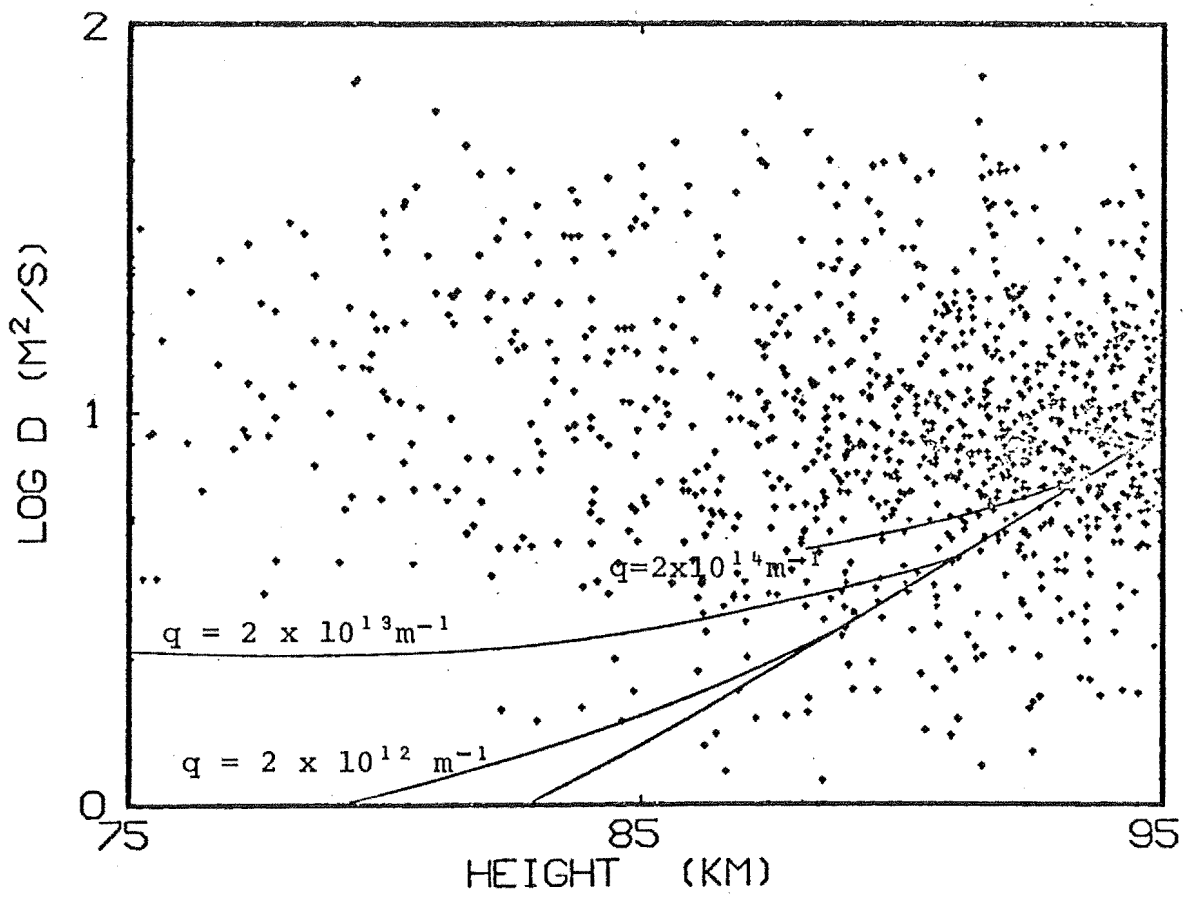

Figure 7.54: Third set of data showing expected D values due to chemical effects for three electron line densities.

(4) Chemical Effects

Measured D values in Figs. 7.46 to 7.49 below 90 km are consistently higher than those expected from ambipolar diffusion alone. The effect is more pronounced than that in Verniani's (1973) data presented in Fig. 4.2, but this is not surprising in view of the greater wavelength and lower sensitivity of the system used in this work. Fig. 7.54 shows the third set of data below 95 km with expected D values calculated from Fig. 2.6. This was done by calculating the decrease in echo amplitude due to diffusion and chemical ionization loss and then finding the D value in the same way as the analysis program. These calculations do not explain the behaviour of the data which have higher D values than those expected although this could be due, in part, to the way in which the theoretical calculations were done. In finding the decrease in received amplitude due to diffusion, a Gaussian distribution of ionization in the train cross-section was assumed (section 3.2). Such a distribution could be incorrect as chemical reactions will deplete the ionization in the most dense parts of the train cross-section more quickly than at the edges and will thus change the decay characteristics.

A further problem arises in denser trains ($q \sim 2 \times 10^{14}$ m^{-1}) as the reactions are completed in a time comparable with that for train formation at heights less than 85 km. This is effectively a finite velocity effect that may obscure chemical effects in larger meteors. The ionization line density would also be misinterpreted in such meteors.

For this reason the calculations for $q = 2 \times 10^{14}$ m^{-1} in Fig. 7.54 have not been extended below 87 km.

Mean values of log D in the height ranges 70 to 85 km and 90 to 95 km were not significantly different and neither were mean log D values over three ranges of electron line density in each of the height ranges. Thus, although chemical effects are likely to cause higher measured D values below 90 km, the theoretical calculations presented here do not agree with the effects observed in these data.

CHAPTER 8

CONCLUSIONS

8.1 EFFECT OF THE EARTH's MAGNETIC FIELD

(1) Previous Work

Theoretical models predict that field-aligned meteor trains occurring above 95 km will be affected by the earth's magnetic field so that their diffusion is inhibited. The type of diffusion in trains that are at an angle greater than 1.4^{o} to the field direction depends on the line density of electrons in the trains and on the volume density of electrons in the surrounding atmosphere. The ionization from faint meteor trains formed in a sufficiently dense ambient plasma will diffuse by forming electron and ion ellipses, both of which contain a neutral plasma. The electron ellipse is strongly elongated in the field direction while the ion ellipse is almost circular at meteor heights. Quasi-neutrality is maintained in these regions by flows of electrons along field lines and ions across field lines; a process that forms depletion regions in the background plasma.

The amount of ionization that can be contained in the ellipses is limited by the depletion region depth and thus the ambient ionization density. When trains contain more ionization than can diffuse into these ellipses the remaining ionization diffuses in an ambipolar, but anisotropic manner. The ellipse dimensions are governed by diffusion at the

rate $2D_+$ in the plane formed by the field direction and the meteor train and at the rate $2D_{T-}$ perpendicular to this plane.

Previous successful experimental observation of these effects has been limited to overdense meteors, studied by backscatter radar operated at frequencies of about 500 MHz. Increased rates and durations of meteor echoes were observed within about 1^o of the magnetic specular condition for the radar beam. Such increases are explained if the meteor zenith angle distribution and the reflection geometry discussed in this work are considered. The slow rise times measured for these meteors is consistent with an increase in the reflecting area of the train as it becomes elongated in the field direction. No particular magnetic effect was measured when observations were made of meteor showers at times when they were expected to produce field-aligned trains. This is also consistent with theory as a backscatter radar should measure a diffusion coefficient of $2D_{T-}$ for all meteors diffusing in an ambipolar manner above 95 km when the specular condition is met.

(2) Forward-Scatter Experiment

The forward-scatter experiment performed here has shown that this system can be used successfully to determine meteor train orientations. A theoretical model has been developed here to describe forward-scatter reflections from meteor trains with elliptical cross-sections. It has been shown that at lease 40,000 echoes would need to

be recorded with the present system to resolve any magnetic effect for field-aligned trains. However, this could be reduced to 20,000 echoes if two 40 kW transmitters were used and may be further reduced if strong field-aligned shower activity was utilised.

A forward-scatter experiment is also suited to observing the elliptical train cross-sections expected from ambipolar diffusion above 95 km. However, the data presented in Chapter 7 were mainly recorded when electron and ion ellipses were to be expected. This mode of diffusion is much more difficult to observe by forward-scatter as the high D values anticipated cannot be successfully measured because of the finite meteor velocity and limits imposed by the method of analysis.

(3) Backscatter Observations

The backscatter observations have shown that the diffusion measured from underdense meteor trains is inhibited for radar off-specular angles of less than about 1^{o}. This is consistent with reflections from an ellipse of ionization whose degree of elongation depends on the train orientation with respect to the field direction. This suggests that the electron ellipse is the origin of the effect. For off-specular angles greater than about 1^{o}, the high D values expected from the diffusion of the electron ellipse would not be observed; reflections from the central core of ionization (the ion ellipse) would dominate the received signal and a diffusion coefficient of D_{+} should be measured.

The lack of a similar magnetic effect in a separate set of echo data is explained by the fact that the system used in its collection was less sensitive than that used previously and the fact that the ambient ionization density was lower. In this case anisotropic, ambipolar diffusion is more likely, but the magnetic effect expected with this mode of diffusion was not observed, although it would, because of its nature, be harder to detect. Such diffusion is better observed with a forward-scatter experiment.

A shift in the measured off-specular angles of up to 1.5^{o} was observed. This has been shown to be consistent with the ionospheric refraction expected from ambient ionization in the upper meteor region. The refraction effect introduces uncertainties into the off-specular angle measurements which are greater than the measurement uncertainties.

Meteor train drifts measured by the doppler facility built in to this experiment have been compared for magnetically affected and unaffected echoes. No significant difference between the mean absolute velocities was found although there was a larger spread in drifts measured from unaffected trains. This behaviour was probably due to the larger atmospheric volume in which these magnetically unaffected trains were observed.

(4) Variation of D with Height

The height variation of the lower limit of the diffusion coefficients measured from magnetically affected echoes agreed with that of D_{T-}. The higher D values also measured

were expected as they arise when the trains are not quite specular ($0^{o} < \mu < 1^{o}$, say). It has been mentioned here that the results of Brown (1976), which follow the D_{+} height dependence, are to be expected if the system used was sensitive enough to observe trains in which electron and ion ellipses of ionization are important.

For general magnetic off-specular angles ($\mu > 1^{o}$), the diffusion coefficients measured should depend on the system sensitivity and ambient ionization density. If electron and ion ellipses are important, D_{+} should govern the apparent diffusion. If anisotropic ambipolar diffusion is prevalent, coefficients in the range $2D_{T-}$ to $2D_{+}$ would control the diffusion, depending on the orientation of the train cross-section with respect to the transmitter beam. This would increase the variability of D values measured at particular heights above 95 km.

8.2 OTHER EFFECTS

(1) Thermalization

Thermalization times for the neutral atoms, positive ions and electrons in meteor trains have been calculated. In underdense meteors the neutral atoms and positive ions should cool in times that are short in comparison with echo decay times. However, the electron thermalization time is comparable with echo lifetimes for heights above 100 km. Several effects, such as plasma resonance and magnetic diffusion, could cause a change in the decay rate during

an echo so that evidence of these changes is not proof of thermalization effects.

(2) Fresnel Diffraction and Phase Measurements

It has been shown that phase variations caused by Fresnel diffraction as meteor trains are formed may affect echo height measurements if separate reflection points on the train are used, as is the case for an interferometer. Ways to minimise these variations by using only individual pulse measurements in the region of the maximum amplitude of the echo have been discussed.

An attempt to observe this effect was partially successful in that decreases in measured height during echo decays occurred in many cases. To resolve the predicted height fluctuations early in the echo life the system to be used needs a wider effective interferometer spacing than that used in this work. This could be achieved with a large physical spacing ($\sim 10\lambda$) and selection of echoes at high elevations. If height ambiguities are to be avoided (although an absolute height measurement is probably not necessary) a vernier-type interferometer with more than three antennas would be necessary. The system should also have a higher P.R.F. than the 300 Hz used here ($\sim$ 600 Hz which would make P.R.F. coding necessary to avoid range ambiguities) and only echoes with a high signal-to-noise ratio should be used. Further improvements in resolution could be obtained by observing low velocity meteors which are more likely to be recorded during the minimum of the diurnal rate variation.

(3) Scatter in Diffusion Coefficient Measurements

It has previously been shown that wind shears and other irregularities in atmospheric motions, when considered in relation to an irregular ionization profile, can cause a scatter in D measured at a particular height. The contributions of each wind effect have been summarised in this work and the additional effect of the measurement uncertainty has been investigated. This work shows that these effects appear to explain the scatter in D observed by other workers and measured in this study.

A systematic height uncertainty that is dependent on echo azimuth was found in the present work. This uncertainty reduces somewhat the value of the present D versus height data, but has not significantly affected the results of the magnetic study.

(4) Chemical Effects

The effect of ionization loss has been calculated using a chemical model for the data of Verniani (1973) and the results are shown to be consistent with the observed departure from expected ambipolar diffusion coefficients below 90 km. This effect is expected to be more prominent in the present work because of the lower system sensitivity and greater radar wavelength used. Higher D values than those expected from ambipolar diffusion occur in these results below about 95 km, but theoretical estimates of the effect of ionization loss do not agree with the observations. This may be due to assumptions made in the theoretical calculations.

ACKNOWLEDGEMENTS

I would like to thank the following people for assistance during the course of this work:

Dr W.J. Baggaley, my supervisor, for his help and enthusiasm at all stages of this work;

Dr R.G.T. Bennett for helpful advice and suggestions on a variety of problems, help in maintaining equipment, and for supervision at one stage;

Dr E.M. Poulter for stimulating discussions and guidance in the early parts of this work;

The technical staff of the department of Physics for help with construction of equipment and especially Ian Foster for his patience, helpful advice and assistance with the electronics;

The New Zealand Lands and Survey Department and especially their farm manager Mr Wesley Smith of Hari Hari, Westland for the use of land as a remote transmitter site; and

Professor A.G. McLellan for financial support in the form of a Teaching Fellowship.

REFERENCES

ALPHER, R.A. and WHITE, D.R. (1959) Optical refractivity of high-temperature gases. Phys. Fluids, 2: 153-161.

A.R.R.L. (1970) American Radio Relay League antenna handbook 13th ed., Connecticut, A.R.R.L. Inc, 336p.

BAGGALEY, W.J. (1966) Dual-wavelength studies of meteoric ionization. Sheffield, University of Sheffield. 234p. (Thesis: Ph.D.: Physics).

BAGGALEY, W.J. (1970) The determination of the initial radii of meteor trains. Mon. Not. R. Astron. Soc., 147:231-243.

BAGGALEY, W.J. (1979a) The influence of recombination on under-dense radio-meteor data. Planet. Space Sci., 27:905-907.

BAGGALEY, W.J. (1979b) Atmospheric scale heights and radio-meteor data. Planet. Space Sci., 27:1131-1133.

BAGGALEY, W.J. (1979c) Multi frequency studies of radio-meteor train diffusion. Bull. Astron. Inst. Czech. In Press.

BAGGALEY, W.J. and CUMMACK, C.H. (1974) Meteor train ion chemistry. J. Atmos. & Terr. Phys. 36: 1759-1773.

BAGGALEY, W.J. and WEBB T.H. (1980) Measurements of the ionization heights of sporadic meteors. Mon. Not. R. Astron. Soc., In Press.

BANKS, P (1966a) Collision frequencies and energy transfer. Electrons. Planet. Space Sci., 14:1085-1103.

BANKS, P. (1966b) Collision frequencies and energy transfer. Ions. Planet. Space Sci., 1105-1122.

BENNETT, R.G.T. (1958) The diffraction of radio waves from meteor trails. Christchurch, University of Canterbury. 72p. (Thesis: Ph.D.: Physics).

BILLAM, E.R. and BROWNE, I.C. (1956) Characteristics of radio echoes from meteor trails. IV: Polarization effects. Proc. Phys. Soc. B, 69: 98-113.

BLANK, C.A. et al (1974) A pocket manual of the physical and chemical characteristics of the earth's atmosphere. Washington, Defense Nuclear Agency, Report Number DNA 3467H 282p.

BREMER, J. and SINGER, W (1977) Diurnal, seasonal and solar-cycle variations of electron densities in the ionospheric D- and E-regions. J. Atmos. & Terr. Phys., 39:25-34.

BROWN, N. (1976) Radio echoes from meteor trains at a radio frequency of 1.98 MHz. J. Atmos. & Terr. Phys., 38: 83-87.

BROWN, N. and ELFORD, W.G. (1971) Radio echoes from randomly ionized meteor trails. J. Atmos. & Terr. Phys., 33: 1659-1666.

BROWN, T.L. (1973) The chemistry of metallic elements in the ionosphere and mesosphere. Chem. Rev., 73:645-667.

BRUCE, E., BECK, A.C. and LOWRY, L.R. (1935) Horizontal rhombic antennas. Proc. I.R.E., 23:24-46.

BUTKO, A.S. et al (1975) Some results on the daytime measurement of temperature and wind in the mesosphere and lower thermosphere. Space Res., 15: 199-201.

BUTKO, A.S. et al (1976) On the character of short-term variations of temperature and wind in the upper atmosphere during June 1973. Space Res., 16:327-331.

CHASOVITIN, Yu. K. et al (1976) Concentration and collision frequency of electrons from 80 to 250 km. Space Res., 16:365-370.

CIRA (1972) Cospar international reference atmosphere. International Council of Scientific Unions, Committee on Space Research. Committee for International Reference Atmosphere. Berlin, Akademie-Verlay. 450p.

CLOSS, R.L. et al (1953) An experimental study of radio reflections from meteor trails. Philos. Mag., 44:313-324.

DALGARNO, A. (1961) Charged particles in the upper atmosphere. Ann. Gerphys., 17:16-49.

DALGARNO, A. (1969) Inelastic collisions at low energies. Can. J. Phys., 47:1723-1731.

DALGARNO, A., McDOWELL, M.R.C. and WILLIAMS, A. (1958) The mobilities of ions in parent gases. Philos. Trans. A, 250:426-439.

DALGARNO, A. et al (1967) The diurnal variation of ionospheric temperatures. Planet. Space Sci., 15:331-345.

DALGARNO, A. et al (1968) The effect of oxygen cooling on ionospheric electron temperatures. Planet. Space Sci., 16:1371-1380.

DEEGAN, N.F. et al (1970) Study of meteor wind measurement techniques. Final rept. Contract AF 19(628)-3248. 128p.

DELOV, I.A. (1975) Nonisothermicity of meteor trails. Sol. Syst. Res., 9:191-194.
DELOV, I.A. (1976)

ELLYETT, C. et al (1961) the identification of meteor showers with application to southern hemisphere results. Mon. Not. R. Astron. Soc., 123:37-50.

FINGER, F.G. and GELMAN, M.E. (1975) Some results of the WMO (CIMO) rocketsonde intercomparisons - phase II. Space Res., 15:143-149.

FORTI, G. (1968) On the relation between diffusion coefficients and height from radar meteor echoes. J. Atmos. & Terr. Phys., 40:89-93.

GILES, M.J. (1973) Ambipolar diffusion as a singular perturbation problem. J. Plasma Phys., 10:317-336.

GRADSHTEIN, I.S. and RYZHIK, I.M. (1965) Table of integrals, series and products. 4th ed., N.Y., Academic Press, 1086p.

GREENHOW, J.S. (1952) Characteristics of radio echoes from meteor trails: III The behaviour of the electron trails after formation. Proc. Phys. Soc. B, 65:169-181.

GREENHOW, J.S. and HALL, J.E. (1960) The importance of initial trail radius on the apparent height and number distributions of meteor echoes. Mon. Not. R. Astron. Soc., 121:183-196.

GREENHOW, J.S. and HALL, J.E. (1961) The height variation of the ambipolar diffusion coefficient for meteor trails. Planet. Space. Sci., 5:109-114.

GREENHOW, J.S. and NEUFELD, E.L. (1955) The diffusion of ionized meteor trails in the upper atmosphere. J. Atmos. & Terr. Phys. 6:133-140.

GREENHOW, J.S. and NEUFELD, E.L. (1959) Measurements of turbulence in the 80 to 100 km region from the radio echo observations of meteors. J. Geophys. Res., 64:2050-2053.

GREENHOW, J.S. and WATKINS, C.D. (1964) The characteristics of meteor trails observed at a frequency of 300 Mc/s. J. Atmos. & Terr. Phys., 26:539-558.

HAWKES, R.L. and JONES, J. (1975) A quantitative model for the ablation of dustball meteors. Mon. Not. R. Astron. Soc., 173:339-356.

HAWKES, R.L. and JONES, J. (1978) The effect of rotation on the initial radius of meteor trains. Mon. Not. R. Astron. Soc. 185:727-734.

HENDERSON, W.R. (1974) Atomic oxygen profile measurements. J. Geophys. Res. 79:3819-3826.

HENRY, R.J.W. and McELROY, M.B. (1968) The atmospheres of Venus and Mars. (Edited by J.C. Brandt and M.B. McElroy). N.Y., Gordon and Breach, p251.

HERLOFSON, N. (1951) Plasma resonance in ionospheric irregularities. Arkiv For Fysik, 3: 247-297.

HERITAGE, J.L., FAY, W.J. and BOWEN, E.D. (1962) Evidence that meteor trails produce a field-aligned scatter signal at VHF. J. Geophys. Res. 67:953-964.

HESS, G.C. and GELLER, M.A. (1976) The Urbana meteor-radar system: design, development and first observations. Aeronomy rept. no. 74, Univ. Illinois, Urbana Ill., U.S.A.

HIRSCHFELDER, J.O., CURTISS, C.F. and BIRD, R.B. (1954) Molecular theory of gases and liquids. Corrected printing with notes added, N.Y., John Wiley & Sons Inc., 1249p.

JONES, J. (1969a) The reflection of radio waves from irregularly ionized meteor trains. Planet. Space Sci., 17:1519-1526.

JONES, J. (1969b) Measurement of radio-meteor ionization profiles. Can. J. Phys., 47:1467-1473.

JONES, J. (1970) On the variation of the ambipolar diffusion coefficient with height. Planet. Space Sci., 18:1836-1842.

JONES, J. (1972) On the effect of small-scale wind shears on radio meteor echoes. Planet. Space Sci., 20:301-312.

JONES, J. (1975) On the decay of underdense radio meteor echoes. Mon. Not. R. Astron. Soc., 173:637-647.

JONES, J. AND COLLINS, J.G. (1974) The mass distribution of radio meteors and the full-wave scattering theory. Mon. Not. R. Astron. Soc., 166:529-542.

JONES, J. and HAWKES, R.L. (1975) Television observations of faint meteors - II light curves. Mon. Not. R. Astron. Soc. 171:159-169.

JONES, J. and READ, B.A. (1972) The effect of wind shear gradients on underdense radio meteor decay times. Can. J. Phys., 50:1277-1281.

KAISER, T.R. (1953) Radio echo studies of meteor ionization. Philos. Mag. Suppl., 2:495-544.

KAISER, T.R. (1954a) Theory of the meteor height distribution obtained from radio-echo observations - I. Shower meteors. Mon. Not. R. Astron. Soc., 114:39-51.

KAISER, T.R. (1954b) Theory of the meteor height distribution obtained from radio-echo observations - II. Sporadic meteors. Mon. Not. R. Astron. Soc., 114:52-62.

KAISER, T.R. (1968) Diffusion of meteor trains in the geomagnetic field. In Kresak and Millman, Physics and dynamics of meteors. IAU Symposium 33.

KAISER, T.R., PICKERING, W.M. and WATKINS, C.D. (1969) Ambipolar diffusion and motion of ion clouds in the earth's magnetic field. Planet. Space Sci., 17:519-552.

KANE, J.A. (1961) Electron density profiles in the ionosphere and exosphere. Nato Conference Series, 2:67-79.

KASHCHEYEV, B.L. and LEBEDINETS, V.N. (1963) The initial radius of ionized meteor trails. Contrib. Astrophys., 7:19-22.

KELSO, J.M. (1964) Radio ray propagation in the ionosphere. 1st ed., N.Y., McGraw-Hill, 408p.

KRAUS, J.D. (1950) Antennas. 1st ed., N.Y., McGraw-Hill, 553p.

LANE, N.F. and DALGARNO, A. (1969) Electron cooling by vibrational excitation of O_2. J. Geophys. Res., 74:3011-3012.

LEBEDINETS, V.N. and PORTNYAGIN, Yu. I. (1966) Initial radius of an ionized meteor trail. Geomag. & Aeron., 6:544-547.

LOVELL, A.C.B. (1954) Meteor astronomy. 1st ed, Oxford, Clarendon Press, 463p.

MANNING, L.A. (1958) The initial radius of meteoric ionization trails. J. Geophys. Res., 63:181-196.

MANNING, L.A. (1959) Air motions and the fading, diversity and aspect sensitivity of meteoric echoes. J. Geophys. Res., 64:1415-1425.

MAYR, H.G. and HARRIS, I. (1977) Diurnal variations in the thermosphere 2. Temperature, composition and winds. J. Geophys. Res. 82:2628-2640.

McINTOSH, B.A. (1969) The effect of wind shear on the decay constant of meteor echoes. Can. J. Phys., 47:1337-1341.

McKINLEY, D.W.R. (1951) Meteor velocities determined by radio observations. Astrophys. J., 113:225-267.

McKINLEY, D.W.R. (1961) Meteor science and engineering. N.Y., McGraw-Hill, 309p.

MEULLER, H.G. (1968) Wind shears in the meteor zone. Planet. Space Sci., 16:61-90.

MEYER, S.L. (1975) Data analysis for scientists and engineers. N.Y., John Wiley & Sons Inc. 513p.

MILLMAN, G.H. (1958) Atmospheric effects on VHF and UHF propagation. Proc. I.R.E., 46:1492-1501.

MILLMAN, G.H. (1959) The geometry of the earth's magnetic field at ionospheric heights. J. Geophys. Res., 64:717-726.

MURGATROYD, R.J. (1970) The physics and dynamics of the stratosphere and mesosphere. Rep. Prog. Phys., 33:817-880.

MURRAY, E.L. (1959) Ambipolar diffusion of a meteor trail and its relation with height. Planet. Space Sci., 1:125-129.

NOVOTNY, V. (1978) The height dependence of the error in ambipolar diffusion coefficient measurement. Bull. Astron. Inst. Czech., 29:155-158.

N.Z. D.S.I.R. (1979) Ionospheric data. Geophysics Div.

PHILIPS, E. (1969) Wind structure from the amplitude fluctuations in persistent radio meteor echoes. Planet. Space Sci., 17:553-559.

PICKERING, W.M. (1973) A computational study of the diffusion of meteor trains using a self consistent model for the space-charge electric field. Planet. Space Sci., 21:1671-1680.

PICKERING, W.M. and WINDLE, D.W. (1974) A non-linear study of the possible effects of electron-ion collisions on the diffusion of a cylindrical column of ionisation in the earth's ionosphere. Planet. Space Sci. 22:833-839.

PORTNYAGIN, Yu. I. (1966) Effective diffusion cross section of meteoric atoms in the atmosphere. Geomag. & Aeron., 6:540-543.

PORTNYAGIN, Yu. I. (1971) Effect of the multicomponent composition of meteoroids on the characteristics of radio reflections from meteor trails. Geomag. & Aeron., 11:532-534.

PORTNYAGIN, Yu. I. (1972) Determination of upper atmosphere parameters from measurements of the ambipolar diffusion coefficient by radar observations of meteor trails. Geomag. & Aeron., 12:411-414.

POULTER, E.M. (1978) Radio-meteor investigations of atmospheric motion. Christchurch, University of Canterbury. 367p. (Thesis: Ph.D.: Physics)

POULTER, E.M. and BAGGALEY, W.J. (1978) The applications of radio-wave scattering theory to radio-meteor observations. Planet. Space Sci., 26:969-977.

REILLY, W.I. and BURROWS, A.L. (1973) The geomagnetic field in New Zealand at epoch 1970.5. N.Z. D.S.I.R. research bulletin 211, Wellington, 43p.

RICE, D.W. and FORSYTH, P.A. (1963) Variations in meteoric radio signal decay rates. Can. J. Phys., 41: 679-690.

RICE, D.W. and FORSYTH, P.A. (1964) The distribution of ionization along underdense meteor trails. Can. J. Phys., 42:2035-2047.

ROSS, A.W. (1980) Regression line analysis. Am. J. Phys. In Press.

ROZHANSKII, V.A. and TSENDIN, L.D. (1977a) Spreading of a pronounced inhomogeneity in the presence of an unbounded weakly ionized background plasma in a magnetic field. Sov. J. Plasma Phys., 3:217-220.

ROZHANSKII, V.A. and TSENDIN, L.D. (1977b) Diffusion of a weakly ionized plasma filament forming an angle with the magnetic field. Geomag. & Aeron., 17:673-676.

SALAH, J.E. and EVANS, J.V. (1973) Measurements of thermospheric temperatures by incoherent scatter radar. Space Res., 13:267-286.

SIDA, D.W. (1969) The production of ions and electrons by meteoric processes. Mon. Not. R. Astron. Soc., 143:37-47.

STUBBE, P. and VARNUM, W.S. (1972) Electron energy transfer rates in the ionosphere. Planet. Space Sci., 20:1121-1126.

UNWIN, R.S. (1966) The importance of refraction in the troposphere and ionosphere in determining the aspect sensitivity and height of the radio aurora. J. Geophys. Res., 71:3677-3686.

U.S. Standard Atmosphere Supplements (1966). Washington, D.C., U.S. Government Printing Office. 289p.

VERNIANI, F. (1969) Structure and fragmentation of meteoroids. Space Sci. Rev., 10:230-261.

VERNIANI, F. (1973) An analysis of the physical parameters of 5759 faint radio meteors. J. Geophys. Res., 78:8429-8462.

VOLLAND, H. and MAYR, H.G. (1970) A theory of the diurnal variations of the thermosphere. Ann. Geophys., 26:907-919.

WATKINS, C.D. (1965) Influence of the geomagnetic field on meteor trains. Nature, 206:1027-1029.

WATKINS, C.D. (1968) Height dependence of the effect of the geomagnetic field on meteor trains. J. Atmos. & Terr. Phys., 30:1827-1832.

WATKINS, C.D. (1970) Radar measurements of the magnetic dip in the E-region. J. Atmos. & Terr. Phys., 32:247-250.

WATKINS, C.D., EAMES, R. and NICHOLSON, T.F. (1971) Further studies of the effect of the earth's magnetic field on meteor trains. J. Atmos. & Terr. Phys., 33:1907-1921.

WATSON, G.N. (1966) A treatise on the theory of Bessel Functions. 2nd ed., Cambridge, University Press, 804p.

WEISS, A.A. (1955) Diffusion coefficients from the rate of decay of meteor trails. Aust. J. Phys., 8:279-288.

WHITEHEAD, J.D. (1973) The seasonal variation of the height and thickness of the E-region. J. Atmos. & Terr. Phys. 35:183-185.

WILKINSON, P.J. (1973) Upper atmospheric studies using radio meteors. Christchurch, University of Canterbury, 1973. 200p. (Thesis: Ph.D.:Physics)

```
TTTTT  AAA  PPPP  EEEE   SSS   OOO  RRRR  TTTTT EEEE  RRRR
  T   A   A P   P E     S   S O   O R   R   T   E     R   R
  T   A   A P   P E     S     O   O R   R   T   E     R   R
  T   AAAAA PPPP  EEE    SSS  O   O RRRR    T   EEE   RRRR
  T   A   A P     E         S O   O R R     T   E     R R
  T   A   A P     E     S   S O   O R  R    T   E     R  R
  T   A   A P     EEEEE  SSS   OOO  R   R   T   EEEEE R   R

286 RECORDS, CREATED 30/01/80

     100 BEGIN
     200    % THIS PROGRAMME READS PAPERTAPE,SORTS DATA AND OUTPUTS TO
     300    % MAG. TAPE AND THE LINE PRINTER.
     400
     500    % THREE FILES ARE NEEDED.
     600    FILE LP(KIND=PRINTER,MAXRECSIZE=22);
     700    FILE CARD(KIND=READER);
     800    FILE MAGTAPE(UNITS=CHARACTERS,MAXRECSIZE=2730,BLOCKSIZE=2730,
     900    AREASIZE=50,AREAS=12,KIND=DISK,PROTECTION=SAVE);
    1000    FILE PAPERDATA(FILETYPE=7);
    1100    LABEL EOFILE,READTAPE,FINISH,EOF,NEWSTART,WESTCOASTONLY,RRESTART;
    1200    REAL ARRAY INPUTDATA[1:540],WORKDATA[1:1080],A[1:460],TIME[1:12];
    1300    REAL PIE,CALTHRESH;
    1400    BOOLEAN FILEND,ALERT,COS12POS,COS13POS,NOT3PHASES;
    1500    INTEGER I,K,CALIB,KOUNT,J,NWORDS,DOUBLECHO,ECHOCOUNTER,STARTHRS,
    1600    STARTMINS;
    1700    POINTER PTRINPT,PTRWK,PTRWKUPDATE,PTRWKSCAN,PTRA,PTRWK2,
    1800    PTRWKSCAN1,PTRWKSCAN2;

    1900    PROCEDURE PHASESORT;
    2000    %THIS PROCEDURE REMOVES PHASES ASSOCIATED WITH
    2100    %SMALL AMPLITUDES AND FINDS THE ARCTAN2 THEN
    2200    %REPLACES THEM IN ARRAY A. THE NUMBER OF GOOD
    2300    %PHASES IS STORED IN A[456].
    2400    BEGIN
    2500       REAL THRESH; INTEGER I,J;
    2600       J:=0;
    2700       % CONVERT TO LOCAL TIME
    2800       A[2]:=A[2]+STARTMINS;
    2900       IF A[2] GEQ 60 THEN
    3000       BEGIN
    3100          A[2]:=A[2]-60;
    3200          A[3]:=A[3]+1;
    3300       END;
    3400       A[3]:=A[3]+STARTHRS;
    3500       IF A[3] GEQ 24 THEN
    3600       BEGIN
    3700          A[3]:=A[3]-24;
    3800          A[4]:=A[4]+1;
    3900       END;
    4000       THRESH:=CALTHRESH;
    4100       FOR I:=5 STEP 1 UNTIL 244 DO
    4200       BEGIN
    4300          A[I]:=A[I]-129;
    4400          IF A[I] EQL 0 THEN A[I]:=1.0@-6;
    4500       END;
    4600       FOR I:=1 STEP 1 UNTIL 60 DO
    4700       BEGIN
    4800          IF A[I+244] GTR THRESH AND A[I+244] LSS 230 THEN
    4900          BEGIN
    5000             IF A[I+4] GEQ 0 THEN
    5100             COS12POS:=TRUE ELSE COS12POS:=FALSE;
    5200             IF A[I+124] GEQ 0 THEN
    5300             COS13POS:=TRUE ELSE COS13POS:=FALSE;
    5400             I:=61;
    5500          END;
    5600       END;
    5700       FOR I:=1 STEP 1 UNTIL 60 DO
    5800       BEGIN
    5900          IF A[I+244] GTR THRESH AND A[I+244] LSS 230 THEN
    6000          BEGIN
    6100             A[I+4]:=ARCTAN2(A[I+64],A[I+4]);
    6200             A[I+124]:=ARCTAN2(A[I+184],A[I+124]);
    6300             J:=J+1;
    6400          END
    6500          ELSE BEGIN
    6600             A[I+4]:=A[I+124]:=0;
    6700          END;
    6800       END;
    6900       IF J LSS 3 THEN NOT3PHASES:=TRUE ELSE NOT3PHASES:=FALSE;
    7000       A[456]:=J;
    7100    END OF PHASESORT;
    7200
```

```
7300

7400    PROCEDURE CALIBRATE;
7500    %THIS PROCEDURE UPDATES DIFFERENTIAL PHASES IF THE
7600    %CALIBRATION ECHO WAS OK.
7700    BEGIN
7800       REAL SUM12,SUM13,CAL12,CAL13,SUM212,SUM213,STNDEV12,STNDEV13,
7900       CALSIG12,CALSIG13;
8000       INTEGER I,J;
8100       J:=A[456];
8200       SUM12:=SUM13:=0;
8300       SUM212:=SUM213:=0;
8400       IF COS12POS THEN
8500       BEGIN
8600          FOR I:=1 STEP 1 UNTIL 60 DO
8700          BEGIN
8800             SUM12:=SUM12+A[I+4];
8900             SUM212:=SUM212+A[I+4]**2;
9000          END;
9100          CAL12:=SUM12/J;
9200       END ELSE
9300       BEGIN
9400          FOR I:=1 STEP 1 UNTIL 60 DO
9500          BEGIN
9600             IF A[I+4] LSS 0 THEN A[I+4]:=A[I+4]+2*PIE;
9700             SUM12:=SUM12+A[I+4];
9800             SUM212:=SUM212+A[I+4]**2;
9900          END;
10000         CAL12:=SUM12/J;
10100      END;
10200      IF COS13POS THEN
10300      BEGIN
10400         FOR I:=1 STEP 1 UNTIL 60 DO
10500         BEGIN
10600            SUM13:=SUM13+A[I+124];
10700            SUM213:=SUM213+A[I+124]**2;
10800         END;
10900         CAL13:=SUM13/J;
11000      END ELSE
11100      BEGIN
11200         FOR I:=1 STEP 1 UNTIL 60 DO
11300         BEGIN
11400            IF A[I+124] LSS 0 THEN A[I+124]:=A[I+124]+2*PIE;
11500            SUM13:=SUM13+A[I+124];
11600            SUM213:=SUM213+A[I+124]**2;
11700         END;
11800         CAL13:=SUM13/J;
11900      END;
12000      STNDEV12:=((SUM212-SUM12*SUM12/J)/(J-1));
12100      IF STNDEV12 LSS 0 THEN STNDEV12:=10000;
12200      STNDEV12:=SQRT(STNDEV12);
12300      STNDEV13:=((SUM213-SUM13*SUM13/J)/(J-1));
12400      IF STNDEV13 LSS 0 THEN STNDEV13:=10000;
12500      STNDEV13:=SQRT(STNDEV13);
12600      IF CAL12 LSS 0 THEN CAL12:=CAL12+2*PIE;
12700      IF CAL13 LSS 0 THEN CAL13:=CAL13+2*PIE;
12800      % ACCOUNT FOR PEST OFF-CENTRE
12900      CAL12:=CAL12+0.037;CAL13:=CAL13-0.205;
13000      CALSIG12:=STNDEV12;CALSIG13:=STNDEV13;
13100      WRITE(LP,<11F7.3>,A[1],A[2],A[3],A[4],A[453],
13200      A[454],CAL12,CALSIG12,CAL13,CALSIG13,J);
13300   END OF CALIBRATE;
13400
13500
13600   % THIS PROCEDURE READS THE PAPERTAPE FILE RECORD AT A TIME.

13700   PROCEDURE PAPEREAD(INPUTDATA,FILEND);
13800   BOOLEAN FILEND;
13900   REAL ARRAY INPUTDATA [1];
14000   BEGIN
14100      LABEL PROCEND,EOF;
14200      INTEGER J;
14300      FOR J:=1 STEP 1 UNTIL 540 DO INPUTDATA[J]:=0;
14400      READ (PAPERDATA,<540A1>,FOR J:=1 STEP 1 UNTIL 540 DO INPUTDATA
14500      [J])[EOF];
14600      GO TO PROCEND ;
14700      EOF:FILEND:=TRUE;
14800      PROCEND: END OF PROCDURE PAPEREAD;
```

```
14900    % INITIALISATION
15000    FILEND:=FALSE;PIE:=4*ARCTAN(1);
15100    PTRINPT:=POINTER(INPUTDATA);
15200    PTRWK:=POINTER(WORKDATA);
15300    PTRWKSCAN:=POINTER(WORKDATA);
15400    PTRWKUPDATE:=POINTER(WORKDATA);
15500    PTRWKSCAN1:=PTRWKSCAN2:=POINTER(WORKDATA);
15600    ECHOCOUNTER:=1;
15700    READ(CARD,/,CALTHRESH,STARTHRS,STARTMINS);
15800    WRITE(LP,/,CALTHRESH,STARTHRS,STARTMINS);
15900    % READ IN PAPERTAPE AFTER CHECKING FOR EOF
16000    ALERT:=FALSE;
16100    READTAPE:IF NOT FILEND THEN
16200    PAPEREAD(INPUTDATA,FILEND) ELSE
16300    BEGIN
16400       WRITE (LP,<"END OF TAPE">);
16500       GO TO FINISH;
16600    END;
16700    % MOVE DATA ALONGSIDE ANYTHING LEFT FROM PREVIOUS READ IN WORKDATA
16800    REPLACE PTRWKUPDATE:PTRWKUPDATE BY PTRINPT FOR 540 WORDS;
16900    % FIND FIRST NON ZERO CHARACTER AND MOVE IT TO THE ARRAY START.
17000    % IF THE ARRAY IS ALL BLANK THEN READ SOME MORE.
17100    NEWSTART: SCAN PTRWKSCAN:PTRWK FOR KOUNT:6474 WHILE = 0;
17200    IF KOUNT EQL 0     THEN
17300    BEGIN
17400       PTRWKUPDATE:=POINTER(WORKDATA);
17500       GO TO READTAPE;
17600    END;
17700    NWORDS:=(6474-KOUNT) DIV 6;
17800    IF NWORDS EQL 0 AND ALERT THEN
17900    BEGIN
18000       LABEL RESCAN;
18100       ALERT:=FALSE;
18200       PTRWKSCAN1:=PTRWKSCAN;
18300       RESCAN:SCAN PTRWKSCAN1:PTRWKSCAN1 UNTIL EQL 0;
18400       PTRWKSCAN2:=PTRWKSCAN1;
18500       IF DELTA(PTRWK,PTRWKSCAN2) GEQ 6372 THEN BEGIN
18600          PTRWKUPDATE:=POINTER(WORKDATA);GO TO READTAPE;END;
18700       SCAN PTRWKSCAN2:PTRWKSCAN2 FOR 17*6 WHILE = 0;
18800       IF DELTA(PTRWKSCAN1,PTRWKSCAN2) GEQ 16*6 THEN
18900       BEGIN
19000          NWORDS:=DELTA(PTRWKSCAN,PTRWKSCAN2) DIV 6;
19100          GO TO RRESTART
19200       END
19300       ELSE BEGIN
19400          PTRWKSCAN1:=PTRWKSCAN1+6;
19500          GO TO RESCAN;
19600       END;
19700    END;
19800    IF NWORDS EQL 0 THEN ALERT:=TRUE ELSE ALERT:=FALSE;
19900    RRESTART:A[453]:=NWORDS;
20000    A[454]:=ECHOCOUNTER;
20100    IF NWORDS NEQ 8 THEN WRITE (LP,*/,NWORDS,ECHOCOUNTER,A[1],A[2]
20200    ,A[3],A[4]);
20300    % WATCH FOR NO TIME PUNCHED
20400    IF NWORDS EQL 4 THEN
20500    WRITE (LP,<"NO TIME PUNCHED?",F 5.0>,ECHOCOUNTER-1);
20600    % SHIFT PTRWKSCAN TO START OF NON ZERO WORD.
20700    PTRWKSCAN:=PTRWK+(6*NWORDS);
20800    REPLACE PTRWK BY PTRWKSCAN FOR (1079-NWORDS) WORDS;
20900    % READJUST PTRWKUPDATE BECAUSE OF SHIFT.
21000    PTRWKUPDATE:=PTRWKUPDATE-(6*NWORDS);
21100    % CHECK FOR FULL RECORD.
21200    IF DELTA(PTRWK,PTRWKUPDATE) LSS 2864 THEN GO READTAPE;
21300    % WE HAVE NOW GOT A COMPLETE RECORD IN THE START OF WORKDATA
21400    % AND CAN ANALYSE IT .
21500    % CHECK FOR WEST COAST ONLYS
21600    IF WORKDATA[405] EQL 0 AND WORKDATA[406] EQL 0 THEN
21700    GO TO WESTCOASTONLY;
21800    ECHOCOUNTER:=ECHOCOUNTER+1;
21900    % DECODE THE TIME.
22000    TIME[1]:=(WORKDATA[1].[4:4]);
22100    TIME[2]:=(WORKDATA[1].[6:2]);
22200    TIME[3]:=(WORKDATA[1].[7:1]);
22300    TIME[4]:=(WORKDATA[2].[3:4]);
22400    TIME[5]:=(WORKDATA[2].[5:2]);
22500    TIME[6]:=(WORKDATA[2].[6:1]);
22600    TIME[7]:=0&WORKDATA[2][0:7:1]&WORKDATA[3][2:1:2];
22700    TIME[8]:=(WORKDATA[3].[2:1]);
22800    TIME[9]:=(WORKDATA[3].[3:1]);
22900    TIME[10]:=(WORKDATA[3].[7:4]);
23000    TIME[11]:=(WORKDATA[4].[3:4]);
23100    TIME[12]:=(WORKDATA[4].[7:4]);
```

```
23200     % A[1] SECS,A[2] MINS,A[3] HOURS,A[4] DAYS.
23300     A[1]:=TIME[1]+10*TIME[2]+30*TIME[3];
23400     A[2]:=TIME[4]+10*TIME[5]+30*TIME[6];
23500     A[3]:=TIME[7]+6*TIME[8]+12*TIME[9];
23600     A[4]:=TIME[10]+10*TIME[11]+100*TIME[12];
23700     % DECODE THE RANGE.
23800     I:=405;
23900     FOR J:=405 STEP 2 UNTIL 436 DO
24000     BEGIN
24100        A[I]:=0&WORKDATA[J][5:5:6]&WORKDATA[J+1][11:5:6];
24200        I:=I+1;
24300     END;
24400     % COMPLETE A[I] TIDILY FOR OUTPUT.
24500     FOR I:=1 STEP 1 UNTIL 60 DO
24600     BEGIN
24700        A[I+4]:=WORKDATA[5*I];
24800        A[I+64]:=WORKDATA[5*I+1];
24900        A[I+124]:=WORKDATA[5*I+2];
25000        A[I+184]:=WORKDATA[5*I+3];
25100        A[I+244]:=WORKDATA[5*I+4];
25200     END;
25300     % PUT AMPLITUDES AND DOPPLERS IN A_RANGES ALREADY THERE.
25400     PTRA:=POINTER(A)+1824;
25500     PTRWK2:=PTRWK+1824;
25600     REPLACE PTRA BY PTRWK2 FOR 100 WORDS;
25700     PTRA:=POINTER(A)+2520;
25800     PTRWK2:=PTRWK+2616;
25900     REPLACE PTRA BY PTRWK2 FOR 32 WORDS;
26000     % NOW OUTPUT TO THE LINE PRINTER AND MAG. TAPE.
26100     DOUBLECHO:=(WORKDATA[420].[6:1]);
26200     IF DOUBLECHO EQL 1 THEN A[455]:=2 ELSE A[455]:=1;
26300     % CHECK FOR A CALIBRATION AND INDICATE
26400     CALIB:=(WORKDATA[1].[0:1]);
26500     IF CALIB EQL 0 THEN A[455]:=0;
26600     PTRA:=POINTER(A);
26700     WRITE (MAGTAPE,2730,PTRA);
26800     IF A[455] EQL 0 THEN PHASESORT;
26900     IF A[455] EQL 0 THEN IF NOT3PHASES THEN
27000     WRITE(LP,<"NOT THREE PHASES ON CALIBRATION",F5.0>,A[454])
27100     ELSE BEGIN
27200        CALIBRATE;
27300     END;
27400     % CLEAR PROCESSED RECORD FROM FRONT OF WORKDATA AND UPDATE
27500     % PTRWKUPDATE SO THAT IT LOCATES LAST READ CHARACTER.
27600     WESTCOASTONLY:PTRWK2:=PTRWK+2856;
27700     REPLACE PTRWK BY PTRWK2 FOR 603 WORDS;
27800     PTRWKUPDATE:=PTRWKUPDATE-2856;
27900     % CLEAR LEFTOVER PART OF WORKDATA.
28000     PTRWK2:=PTRWKUPDATE+6;
28100     I:=DELTA(PTRWK,PTRWKUPDATE);
28200     REPLACE PTRWK2 BY 0 FOR (1079-I/6) WORDS;
28300     % CHECK FOR ANOTHER FULL RECORD.
28400     IF I LSS 3000 THEN GO READTAPE ELSE GO NEWSTART;
28500     FINISH:LOCK (MAGTAPE,CRUNCH);
28600  END OF PROGRAM.
```

```
 AAA  N   N  AAA  L     Y   Y  SSS  EEEE
A   A N   N A   A L      Y Y  S   S E
A   A NN  N A   A L       Y   S     E
AAAAA N N N AAAAA L       Y    SSS  EEE
A   A N  NN A   A L       Y       S E
A   A N   N A   A L       Y   S   S E
A   A N   N A   A LLLLL   Y    SSS  EEEEE


1000 RECORDS, CREATED 30/01/80

     100 BEGIN
     200    % THE MAIN PROGRAM
     300    FILE LP(KIND=PRINTER,MAXRECSIZE=22);
     400    FILE CARD(KIND=READER);
     500    FILE MAGTAPE(FILETYPE=7);
     600    FILE OUTPUT(UNITS=CHARACTERS,MAXRECSIZE=318,BLOCKSIZE=636,
     700    AREASIZE=50,AREAS=12,KIND=DISK,PROTECTION=SAVE);
     800    LABEL READECHO,EOF,FINISH,SKIP;
     900    REAL ARRAY A[1:460],NEWA[1:600],CL[1:8],CR[1:8],
    1000    OPUT[0:52],DL[0:8],DR[0:8];
    1100    REAL CALTHRESH,GOODCALTHRESH,DIFF12,DIFF13,RE,
    1200    REGRESSTDDEVN,RXDELAY,VELOCITY1,VELOCITY2,MEANRANGE,RANGESIG,
    1300    DOPP1SIG,DOPP2SIG,PIE,RANGECHECK,RANGENUM,CALSIG12,CALSIG13;
    1400    INTEGER ARRAY CARDECHOES[0:600];
    1500    INTEGER I,CALTIME,DUDRANGE,RTHRESH,PHASETHRESH,
    1600    ECHOTIME,TIMECHECK,RANGETHRESH,AMPLTHRESH,STARTHRS,STARTMINS,
    1700    STARTDAYS;
    1800    BOOLEAN FILEND,DDOUBLE,LOCAL,COS12POS,COS13POS,NOT3PHASES;
    1900    POINTER PTRA,PTROUT;
    2000
    2100

    2200    PROCEDURE PHASESORT;
    2300    %THIS PROCEDURE REMOVES PHASES ASSOCIATED WITH
    2400    %SMALL AMPLITUDES AND FINDS THE ARCTAN2 THEN
    2500    %REPLACES THEM IN ARRAY A. THE NUMBER OF GOOD
    2600    %PHASES IS STORED IN A[456].
    2700    BEGIN
    2800       REAL THRESH; INTEGER I,J;
    2900       J:=0;
    3000       % CONVERT TO LOCAL TIME
    3100       A[2]:=A[2]+STARTMINS;
    3200       IF A[2] GEQ 60 THEN
    3300       BEGIN
    3400          A[2]:=A[2]-60;
    3500          A[3]:=A[3]+1;
    3600       END;
    3700       A[3]:=A[3]+STARTHRS;
    3800       IF A[3] GEQ 24 THEN
    3900       BEGIN
    4000          A[3]:=A[3]-24;
    4100          A[4]:=A[4]+1;
    4200       END;
    4300       A[4]:=*+STARTDAYS;
    4400       IF A[455] EQL 0 THEN
    4500       BEGIN
    4600          THRESH:=CALTHRESH;
    4700       END
    4800       ELSE BEGIN
    4900          THRESH:=PHASETHRESH;
    5000       END;
    5100       FOR I:=5 STEP 1 UNTIL 244 DO
    5200       BEGIN
    5300          A[I]:=A[I]-129;
    5400          IF A[I] EQL 0 THEN A[I]:=1.0@-6;
    5500       END;
    5600       FOR I:=1 STEP 1 UNTIL 60 DO
    5700       BEGIN
    5800          IF A[I+244] GTR THRESH AND A[I+244] LSS 230 THEN
    5900          BEGIN
    6000             IF A[I+4] GEQ 0 THEN
    6100             COS12POS:=TRUE ELSE COS12POS:=FALSE;
    6200             IF A[I+124] GEQ 0 THEN
    6300             COS13POS:=TRUE ELSE COS13POS:=FALSE;
    6400             I:=61;
    6500          END;
    6600       END;
    6700       FOR I:=1 STEP 1 UNTIL 60 DO
    6800       BEGIN
    6900          IF A[I+244] GTR THRESH AND A[I+244] LSS 230 THEN
    7000          BEGIN
```

```
7100            A[I+4]:=ARCTAN2(A[I+64],A[I+4]);
7200            A[I+124]:=ARCTAN2(A[I+184],A[I+124]);
7300            J:=J+1;
7400         END
7500         ELSE BEGIN
7600            A[I+4]:=A[I+124]:=0;
7700         END;
7800      END;
7900      IF J LSS 3 THEN NOT3PHASES:=TRUE ELSE NOT3PHASES:=FALSE;
8000      A[456]:=J;
8100   END OF PHASESORT;
8200
8300

8400   PROCEDURE CALIBRATE;
8500   %THIS PROCEDURE UPDATES DIFFERENTIAL PHASES IF THE
8600   %CALIBRATION ECHO WAS OK.
8700   BEGIN
8800      REAL SUM12,SUM13,CAL12,CAL13,SUM212,SUM213,STNDEV12,STNDEV13;
8900      INTEGER I,J;
9000      J:=A[456];
9100      SUM12:=SUM13:=0;
9200      SUM212:=SUM213:=0;
9300      IF COS12POS THEN
9400      BEGIN
9500         FOR I:=1 STEP 1 UNTIL 60 DO
9600         BEGIN
9700            SUM12:=SUM12+A[I+4];
9800            SUM212:=SUM212+A[I+4]**2;
9900         END;
10000        CAL12:=SUM12/J;
10100     END ELSE
10200     BEGIN
10300        FOR I:=1 STEP 1 UNTIL 60 DO
10400        BEGIN
10500           IF A[I+4] LSS 0 THEN A[I+4]:=A[I+4]+2*PIE;
10600           SUM12:=SUM12+A[I+4];
10700           SUM212:=SUM212+A[I+4]**2;
10800        END;
10900        CAL12:=SUM12/J;
11000     END;
11100     IF COS13POS THEN
11200     BEGIN
11300        FOR I:=1 STEP 1 UNTIL 60 DO
11400        BEGIN
11500           SUM13:=SUM13+A[I+124];
11600           SUM213:=SUM213+A[I+124]**2;
11700        END;
11800        CAL13:=SUM13/J;
11900     END ELSE
12000     BEGIN
12100        FOR I:=1 STEP 1 UNTIL 60 DO
12200        BEGIN
12300           IF A[I+124] LSS 0 THEN A[I+124]:=A[I+124]+2*PIE;
12400           SUM13:=SUM13+A[I+124];
12500           SUM213:=SUM213+A[I+124]**2;
12600        END;
12700        CAL13:=SUM13/J;
12800     END;
12900     STNDEV12:=((SUM212-SUM12*SUM12/J)/(J-1));
13000     IF STNDEV12 LSS 0 THEN STNDEV12:=10000;
13100     STNDEV12:=SQRT(STNDEV12);
13200     STNDEV13:=((SUM213-SUM13*SUM13/J)/(J-1));
13300     IF STNDEV13 LSS 0 THEN STNDEV13:=10000;
13400     STNDEV13:=SQRT(STNDEV13);
13500     IF CAL12 LSS 0 THEN CAL12:=CAL12+2*PIE;
13600     IF CAL13 LSS 0 THEN CAL13:=CAL13+2*PIE;
13700     % ACCOUNT FOR PEST OFF-CENTRE
13800     CAL12:=CAL12+0.037;CAL13:=CAL13-0.205;
13900     %AVERAGE PHASES AND COMPARE WITH PRESENT DIFF
14000     %PHASES EXCEPT NEAR BEGINNING OF RUN. IF OK.
14100     %UPDATE DIFF PHASES ELSE WRITE AND KEEP OLD ONES;
14200     IF A[454] GTR 0 THEN
14300     BEGIN
14400        IF (ABS(CAL12-DIFF12) LSS GOODCALTHRESH
14500        OR ABS(CAL12+2*PIE-DIFF12) LSS GOODCALTHRESH
14600        OR ABS(CAL12-2*PIE-DIFF12) LSS GOODCALTHRESH )
14700        AND STNDEV12 LSS 0.1 THEN
14800        BEGIN
14900           IF (ABS(CAL13-DIFF13) LSS GOODCALTHRESH
15000           OR ABS(CAL13+2*PIE-DIFF13) LSS GOODCALTHRESH
15100           OR ABS(CAL13-2*PIE-DIFF13) LSS GOODCALTHRESH )
15200           AND STNDEV13 LSS 0.1 THEN
15300           BEGIN
15400              DIFF12:=CAL12;DIFF13:=CAL13;
```

```
15500                CALSIG12:=STNDEV12;CALSIG13:=STNDEV13;
15600                CALTIME:=A[1]+60*A[2]+3600*A[3]+24*3600*A[4];
15700                WRITE (LP,<"GOOD CAL 13",X2,11F7.3>,A[1],A[2],A[3],
15800                A[4],A[453],A[454],CAL12,CALSIG12,CAL13,CALSIG13,J);
15900                GO TO READECHO;
16000             END
16100             ELSE BEGIN
16200                WRITE (LP,<"BAD CAL 13",X2,9F7.3>,A[1],A[2],A[3],A[4],
16300                A[453],A[454],CAL12,CAL13,J);
16400                GO TO READECHO;
16500             END;
16600          END
16700          ELSE BEGIN
16800             WRITE (LP,<"BAD CAL 12",X2,9F7.3>,A[1],A[2],A[3],
16900             A[4],A[453],A[454],CAL12,CAL13,J);
17000             GO TO READECHO;
17100          END;
17200       END
17300       ELSE BEGIN
17400          DIFF12:=CAL12;DIFF13:=CAL13;
17500          CALSIG12:=STNDEV12;CALSIG13:=STNDEV13;
17600          CALTIME:=A[1]+60*A[2]+3600*A[3]+24*3600*A[4];
17700          WRITE (LP,<"GOOD CAL 12",X2,11F7.3>,A[1],A[2],A[3],
17800          A[4],A[453],A[454],CAL12,CALSIG12,CAL13,CALSIG13,J);
17900          GO TO READECHO;
18000       END;
18100    END OF CALIBRATE;
18200
18300

18400    PROCEDURE ARRANGE;
18500    % ARRANGE READS B FROM THE CARD FILE IF NECESSARY,
18600    % AND SORTS AMPLITUDES AND PHASES INTO LOCAL AND WEST
18700    % COAST POSITIONS.EACH AMPLITUDE DURATION IS ALSO
18800    % FOUND.FINALLY,THE RANGES ARE REMOVED IF THEY
18900    %DO NOT MEET THRESHOLD REQUIREMENTS.
19000    BEGIN
19100       INTEGER ARRAY B[1:240];
19200       POINTER PNEW,PB;
19300       INTEGER I,BCOUNT,I2;
19400       LABEL SINGLE,CARDREAD,RANGEARRANGE,LONGDURN1,LONGDURN2,WCDURN;
19500       INTEGER MAXPLOCAL,MAXALOCAL,MAXPWC,MAXAWC,DUML,DUMWC;
19600       LOCAL:=FALSE;
19700       PNEW:=POINTER(NEWA);PB:=POINTER(B);
19800       REPLACE PNEW BY 0 FOR 600 WORDS;
19900       REPLACE PB BY 0 FOR 180 WORDS;
20000       SINGLE:IF DDOUBLE THEN
20100       BEGIN
20200          FOR I:=1 STEP 1 UNTIL CARDECHOES[0] DO
20300          IF A[454] EQL CARDECHOES[I] THEN GO TO CARDREAD;
20400          % AUTOMATIC DOUBLE-ECHO SORTER.
20500          NEWA[580]:=2;
20600          FOR I:=1 STEP 1 UNTIL 30 DO
20700          BEGIN
20800             NEWA[I]:=A[2*I+3];
20900             NEWA[I+60]:=A[2*I+123];
21000             NEWA[I+280]:=A[2*I+4];
21100             NEWA[I+340]:=A[2*I+124];
21200          END;
21300          MAXALOCAL:=MAXAWC:=0;
21400          FOR I:=1 STEP 1 UNTIL 80 DO
21500          BEGIN
21600             NEWA[I+120]:=DUML:=A[2*I+243];
21700             NEWA[I+400]:=DUMWC:=A[2*I+244];
21800             IF DUML GEQ MAXALOCAL AND I LEQ 45 THEN
21900             BEGIN
22000                MAXALOCAL:=DUML;
22100                MAXPLOCAL:=I;
22200             END;
22300             IF DUMWC GEQ MAXAWC AND I LEQ 45 THEN
22400             BEGIN
22500                MAXAWC:=DUMWC;
22600                MAXPWC:=I;
22700             END;
22800          END;
22900          % START AT MAXPLOCAL TO ALLOW FOR 2ND ECHO TO RISE
23000          FOR I:=MAXPLOCAL STEP 1 UNTIL 80 DO
23100          BEGIN
23200             IF NEWA[I+120] LEQ AMPLTHRESH THEN
23300             BEGIN
23400                IF NEWA[I+1+120] LEQ AMPLTHRESH THEN
23500                BEGIN
23600                   IF NEWA[I+2+120] LEQ AMPLTHRESH THEN
23700                   BEGIN
23800                      LONGDURN1:NEWA[578]:=I-1;
```

```
23900                   IF I LEQ 1 THEN
24000                   BEGIN
24100                      WRITE(LP,<"NO AMPLITUDES",F5.0>,A[454]);
24200                      GO TO READECHO;
24300                   END;
24400                   GO TO WCDURN;
24500                END;
24600             END;
24700          END;
24800       END;
24900       I:=81;
25000       GO TO LONGDURN1;
25100       WCDURN:FOR I:=MAXPWC STEP 1 UNTIL 80 DO
25200       BEGIN
25300          IF NEWA[I+400] LEQ AMPLTHRESH THEN
25400          BEGIN
25500             IF NEWA[I+1+400] LEQ AMPLTHRESH THEN
25600             BEGIN
25700                IF NEWA[I+2+400] LEQ AMPLTHRESH THEN
25800                BEGIN
25900                   LONGDURN2:  NEWA[579]:=I-1;
26000                   IF I LEQ 1 THEN
26100                   BEGIN
26200                      WRITE(LP,<"NO AMPLITUDES",F5.0>,A[454]);
26300                      GO TO READECHO;
26400                   END;
26500                   GO TO RANGEARRANGE;
26600                END;
26700             END;
26800          END;
26900       END;
27000       I:=81;
27100       GO TO LONGDURN2;
27200       CARDREAD:READ (CARD,/,FOR I:=1 STEP 1 UNTIL 240 DO B[I]);
27300       WRITE(LP,/,FOR I2:=1 STEP 1 UNTIL I-1 DO B[I2]);
27400       IF B[1] EQL A[454] THEN
27500       BEGIN
27600          IF NOT3PHASES THEN
27700          BEGIN
27800             WRITE(LP,<"NOT THREE PHASES ON DOUBLE",F5.0>,A[454]);
27900             GO TO READECHO;
28000          END;
28100          IF B[2] EQL 0 THEN GO TO READECHO;
28200          IF B[2] EQL 1 THEN
28300          BEGIN
28400             DDOUBLE:=FALSE;
28500             GO TO SINGLE;
28600          END
28700          ELSE BEGIN
28800             INTEGER J;J:=1;
28900             NEWA[580]:=2;
29000             I:=3;
29100             WHILE B[I] NEQ 222 DO
29200             BEGIN
29300                A[B[I]+4]:=A[B[I]+124]:=0;
29400                I:=I+1;
29500             END;
29600             I:=I+1;
29700             WHILE B[I] NEQ 333 DO
29800             BEGIN
29900                IF B[I] LEQ 60 THEN
30000                BEGIN
30100                   NEWA[J]:=A[B[I]+4];
30200                   NEWA[J+60]:=A[B[I]+124];
30300                END;
30400                NEWA[J+120]:=A[B[I]+244];
30500                J:=J+1;I:=I+1;
30600             END;
30700             NEWA[578]:=J-1;
30800             I:=I+1;J:=1;
30900             WHILE B[I] NEQ 444 DO
31000             BEGIN
31100                IF B[I] LEQ 60 THEN
31200                BEGIN
31300                   NEWA[J+280]:=A[B[I]+4];
31400                   NEWA[J+340]:=A[B[I]+124];
31500                END;
31600                NEWA[J+400]:=A[B[I]+244];
31700                J:=J+1;I:=I+1;
31800             END;
31900             BCOUNT:=I+1;
32000             NEWA[579]:=J-1;
32100             FOR I:=BCOUNT STEP 1 UNTIL BCOUNT+15 DO
32200             BEGIN
```

```
32300                IF B[I] NEQ 0 THEN A[B[I]+404]:=0;
32400             END;
32500          END;
32600       END
32700       ELSE BEGIN
32800          WRITE (LP,<"CARDS NOT ALIGNED">);
32900          GO TO FINISH;
33000       END;
33100    END
33200    ELSE BEGIN
33300       INTEGER J;LABEL SORTOUT,LONGDURATION;
33400       %HAVING SORTED PHASES AND AMPLITUDES FOR DOUBLE ECHOES
33500       % FRCM CARD INPUT WE NOW DO THE SAME FOR SINGLE
33600       % ECHOES.IF RANGE IS ZERO THEY ARE WEST COAST.
33700       IF NOT3PHASES THEN
33800       BEGIN
33900          WRITE(LP,<"NOT THREE PHASES ON SINGLE",F5.0>,A[454]);
34000          GO TO READECHO;
34100       END;
34200       % ADJUST FOR NEW PANDORA
34300       FOR J:=1 STEP 1 UNTIL 80 DO A[J+244]:=A[J*2+243];
34400       FOR J:=1 STEP 1 UNTIL 80 DO
34500       BEGIN
34600          IF A[J+244] GTR AMPLTHRESH THEN ELSE
34700          BEGIN
34800             IF A[J+1+244] GTR AMPLTHRESH THEN ELSE
34900             BEGIN
35000                IF A[J+2+244] GTR AMPLTHRESH THEN ELSE
35100                BEGIN
35200                   LONGDURATION:IF (A[405]+A[406]+A[419]+A[420]) NEQ 0 THEN
35300                   BEGIN
35400                      LOCAL:=TRUE;
35500                      NEWA[580]:=1;
35600                      NEWA[578]:=J-1;
35700                      IF J-1 EQL 0 THEN
35800                      BEGIN
35900                         WRITE (LP,<"NO AMPLITUDES",F5.0>,A[454]);
36000                         GO TO READECHO;
36100                      END;
36200                      GO TO SORTOUT;
36300                   END
36400                   ELSE BEGIN
36500                      LOCAL:=FALSE;
36600                      NEWA[580]:=0;
36700                      NEWA[579]:=J-1;
36800                      IF J-1 EQL 0 THEN
36900                      BEGIN
37000                         WRITE (LP,<"NO AMPLITUDES",F5.0>,A[454]);
37100                         GO TO READECHO;
37200                      END;
37300                      GO TO SORTOUT;
37400                   END;
37500                END;
37600             END;
37700          END;
37800       END;
37900       GO TO LONGDURATION;
38000       SORTOUT:IF LOCAL THEN
38100       BEGIN
38200          FOR I:=1 STEP 1 UNTIL NEWA[578] DO
38300          BEGIN
38400             IF I LEQ 30 THEN
38500             BEGIN
38600                NEWA[I]:=A[2*I+3];NEWA[I+60]:=A[2*I+123];
38700             END;
38800             NEWA[I+120]:=A[244+I];
38900          END;
39000       END
39100       ELSE BEGIN
39200          FOR I:=1 STEP 1 UNTIL NEWA[579] DO
39300          BEGIN
39400             IF I LEQ 30 THEN
39500             BEGIN
39600                NEWA[I+280]:=A[2*I+3];NEWA[I+340]:=A[2*I+123];
39700             END;
39800             % A SINGLE WEST COAST ECHO WILL GET LOCAL AMPLITUDES
39900             NEWA[I+400]:=A[I+244];
40000          END;
40100       END;
40200    END;
40300    RANGEARRANGE:DUDRANGE:=0;
40400    % REMOVE RANGES THAT ARE VERY SMALL OR ASSOCIATED
40500    %  WITH SMALL AMPLITUDES WHEN GLITCH COULD OPERATE.
```

```
40600       FOR I:=1 STEP 1 UNTIL 16 DO
40700       BEGIN
40800          IF LOCAL THEN IF A[I+244] LSS RANGETHRESH THEN
40900          A[I+404]:=0;
41000          IF A[404+I] LEQ RTHRESH THEN
41100          BEGIN
41200             A[I+404]:=0;
41300             DUDRANGE:=DUDRANGE+1;
41400          END;
41500       END;
41600       IF DUDRANGE GTR 14 THEN
41700       BEGIN
41800          WRITE(LP,<"NO SUITABLE RANGE VALUES",F5.0>,A[454]);
41900          GO TO READECHO;
42000       END;
42100       % # OF RANGE VALUES IS (16-DUDRANGE).
42200    END OF ARRANGE;
42300
42400

42500    PROCEDURE REGRESSION(N,POSN,AMPL,RESULT);
42600    INTEGER N;
42700    REAL ARRAY RESULT[1],AMPL[1];
42800    INTEGER ARRAY POSN[1];
42900    % THIS PROCEDURE FITS A STRAIGHT LINE TO A SET OF DATA.
43000    % RESULT[1] IS THE SLOPE,2 IS THE INTERCEPT ,3 IS THE
43100    % CORRELATION COEFFICIENT,4 IS THE MEAN AMPLITUDE.
43200    % REGRESSTDDEV IS THE STD. DEVIATION
43300    % INPUTS:=N,THE # OF POINTS,POSN THE # OF EACH
43400    % POINT,AMPL IS THE AMPLITUDE.
43500    BEGIN
43600       INTEGER I,SUMX,SUMXX;
43700       REAL SUMY,SUMYY,COEFF1,COEFF2,COEFF3,SUMXY;
43800       % FIND SUMS OF X,Y,XY,X*X,Y*Y.
43900       FOR I:=1 STEP 1 UNTIL N DO
44000       BEGIN
44100          SUMX:=SUMX+POSN[I];
44200          SUMY:=SUMY+AMPL[I];
44300          SUMXX:=SUMXX+POSN[I]**2;
44400          SUMXY:=SUMXY+POSN[I]*AMPL[I];
44500          SUMYY:=SUMYY+AMPL[I]**2;
44600       END;
44700       COEFF1:=SUMXY-SUMX*SUMY/N;
44800       COEFF2:=SUMXX-SUMX*SUMX/N;
44900       COEFF3:=SUMYY-SUMY*SUMY/N;
45000       RESULT[1]:=COEFF1/COEFF2;
45100       RESULT[2]:=SUMY/N-RESULT[1]*SUMX/N;
45200       IF COEFF2 GTR 0 THEN
45300       BEGIN
45400          IF COEFF3 GTR 0 THEN
45500          BEGIN
45600             REGRESSTDDEVN:=SQRT(COEFF3/(N-1));
45700             RESULT[3]:=SQRT(COEFF1*COEFF1/COEFF2/COEFF3);
45800          END ELSE RESULT[3]:=REGRESSTDDEVN:=0;
45900       END
46000       ELSE RESULT[3]:=REGRESSTDDEVN:=0;
46100       RESULT[4]:=SUMY/N;
46200    END OF REGRESSION;
46300
46400

46500    PROCEDURE AMPLITUDE(START,DURATION,C);
46600    VALUE DURATION;
46700    INTEGER START,DURATION;
46800    REAL ARRAY C[1];
46900    % AMPLITUDE FINDS MAX+POSN,AVERAGE SIZE AND FITS A
47000    % CURVE TO LOG OF NEWA AFTER MOVING 25% TO AVOID
47100    % PLASMA RESONANCE.
47200    BEGIN
47300       REAL SNRSUM;INTEGER START2;
47400       C[5]:=0;SNRSUM:=0;
47500       FOR I:=1 STEP 1 UNTIL DURATION DO
47600       BEGIN
47700          SNRSUM:=SNRSUM+NEWA[START+I];
47800          IF NEWA[START+I] GEQ C[5] THEN
47900          BEGIN
48000             C[5]:=NEWA[START+I];
48100             C[6]:=I;
48200          END;
48300       END;
48400       %NOW C[5] IS MAX,C[6] IS POSN OR RISETIME.
48500       %FIND AVERAGE AMPLITUDE.
48600       C[7]:=SNRSUM/DURATION;
```

```
48700       %ALLOW FOR PLASMA RESONANCE.
48800       START2:=(DURATION-C[6])*0.25+C[6];
48900       % LIMIT FITS TO 0.3S FOR FADING
49000       DURATION:=MIN(DURATION,45);
49100       %NEED 5 PULSES TO FIT LINE.
49200       IF (DURATION-START2) GEQ 5 THEN
49300       BEGIN
49400          INTEGER J,KOUNT;INTEGER ARRAY PLACE[1:160];
49500          REAL ARRAY LNEWA[1:160];
49600          KOUNT:=J:=0;
49700          FOR I:=START2 STEP 1 UNTIL DURATION DO
49800          BEGIN
49900             KOUNT:=KOUNT+1;
50000             IF NEWA[START+I] GTR AMPLTHRESH THEN
50100             BEGIN
50200                J:=J+1;
50300                LNEWA[J]:=LN(NEWA[START+I]);
50400                PLACE[J]:=KOUNT;
50500             END;
50600          END;
50700          C[8]:=J;
50800          IF J GEQ 5 THEN REGRESSION(J,PLACE,LNEWA,C)
50900          ELSE C[1]:=C[2]:=C[3]:=C[4]:=C[8]:=0;
51000       END
51100       ELSE BEGIN
51200          C[1]:=C[2]:=C[3]:=C[4]:=C[8]:=0;
51300       END;
51400    END OF AMPLITUDE;
51500
51600

51700    PROCEDURE RANGE;
51800    % RANGE  FINDS MEAN AND STD
51900    % DEVIATION TWICE IF NECESSARY.
52000    BEGIN
52100       REAL SUMR,SUMRR,MEAN,SIG;
52200       INTEGER J;
52300       J:=SUMR:=SUMRR:=0;
52400       IF DUDRANGE LSS 16 THEN
52500       BEGIN
52600          %FIND MEAN AND SIG
52700          FOR I:=405 STEP 1 UNTIL 420 DO
52800          BEGIN
52900             IF A[I] GTR 0 THEN
53000             BEGIN
53100                SUMR:=SUMR+A[I];
53200                SUMRR:=SUMRR+A[I]*A[I];
53300                J:=J+1;
53400             END;
53500          END;
53600          RANGENUM:=J;
53700          IF J EQL 0 THEN J:=1;
53800          MEAN:=SUMR/J;
53900          IF J EQL 1 THEN J:=2;
54000          SIG:=(SUMRR/(J-1)-SUMR*SUMR/J/(J-1));
54100          IF SIG LSS 0 THEN SIG:=1000000;
54200          SIG:=SQRT(SIG);
54300          % ELIMINATE VALUES > 1 SIG FROM MEAN IF SIG
54400          % GTR 10 BITS, UNLESS ALL VALUES ARE >1 SIG.
54500          IF SIG GTR 10 THEN
54600          BEGIN
54700             J:=SUMR:=SUMRR:=0;
54800             FOR I:=405 STEP 1 UNTIL 420 DO
54900             BEGIN
55000                IF ABS(A[I]-MEAN) LSS SIG THEN
55100                BEGIN
55200                   SUMR:=SUMR+A[I];
55300                   SUMRR:=SUMRR+A[I] *A[I];
55400                   J:=J+1;
55500                END;
55600             END;
55700             IF J GTR 1 THEN
55800             BEGIN
55900                MEAN:=SUMR/J;
56000                SIG:=(SUMRR/(J-1)-SUMR*SUMR/J/(J-1));
56100                IF SIG LSS 0 THEN SIG:=1000000;
56200                SIG:=SQRT(SIG);
56300                RANGENUM:=J;
56400             END;
56500          END;
56600          % CONVERT TO KILOMETRES,SUBTRACTING RX DELAY
56700          % AND HALF PULSE WIDTH.
56800          MEANRANGE:=MEAN*3@5/1.2@6/2-RXDELAY-4.95;
```

```
56900          RANGESIG:=SIG*3@5/1.2@6/2;
57000       END
57100       ELSE BEGIN
57200          MEANRANGE:=0;
57300          RANGESIG:=0;
57400       END;
57500    END OF RANGE;
57600
57700

57800    PROCEDURE DOPPLER;
57900    % DOPPLER FINDS THE POSITIVE AND NEGATIVE VELOCITY
58000    % VALUES. THE CLOCK RATE IS 5000 HZ,OFFSET IS
58100    % 30HZ,VELOCITY TOWARDS RX IS POSITIVE.
58200    BEGIN
58300       REAL DECHOTIME,DOPP1SUM,DOPP2SUM,DOPP1TIME,DOPP2TIME,
58400       TA,DOPP1SUM2,DOPP2SUM2,DOPP1MEAN,DOPP2MEAN;
58500       INTEGER J,PRF,DOPP1NUM,DOPP2NUM,DOPP1END,DOPP2END;
58600       LABEL REDO1,REDO2;
58700       BOOLEAN ONCETHRO;ONCETHRO:=FALSE;
58800       % USE ECHO DURATION - NEWA[578]
58900       PRF:=150;
59000       % ECHOTIME IS ECHO LENGTH IN SECS,DOPPTIME IS
59100       % SUM OF DOPPLER CLOCK CONVERTED TO SECS.
59200       % FIND RELIABLE DURATION
59300       DECHOTIME:=NEWA[578]/PRF;
59400       DOPP1SUM:=DOPP1TIME:=I:=0;
59500       WHILE DOPP1TIME LEQ DECHOTIME AND I LSS 16 DO
59600       BEGIN
59700          I:=I+1;
59800          DOPP1SUM:=DOPP1SUM+A[420+I];
59900          DOPP1TIME:=DOPP1SUM/5000;
60000       END;
60100       J:=I-1;
60200       % DONT INCLUDE LAST ZERO CROSS
60300       % SET ALL PAST THE END TO ZERO.
60400       FOR I:=J+1 STEP 1 UNTIL 16 DO A[420+I]:=0;
60500       % IGNORE FIRST COUNT
60600       A[421]:=0;
60700       DOPP1END:=J;
60800       % REPEAT FOR OTHER OFFSET.
60900       DOPP2SUM:=DOPP2TIME:=I:=0;
61000       WHILE DOPP2TIME LEQ DECHOTIME AND I LSS 16 DO
61100       BEGIN
61200          I:=I+1;
61300          DOPP2SUM:=DOPP2SUM+A[436+I];
61400          DOPP2TIME:=DOPP2SUM/5000;
61500       END;
61600       J:=I-1;
61700       FOR I:=J+1 STEP 1 UNTIL 16 DO A[436+I]:=0;
61800       A[437]:=0;
61900       DOPP2END:=J;
62000       % REJECT SPURIOUS SHORT AND LONG COUNTS -
62100       % FILTER ASYMMETRY.
62200       FOR I:=2 STEP 1 UNTIL DOPP1END DO
62300       BEGIN
62400          TA:=A[420+I];
62500          IF TA GTR 25 AND TA LSS 240 THEN ELSE A[420+I]:=0;
62600       END;
62700       FOR I:=2 STEP 1 UNTIL DOPP2END DO
62800       BEGIN
62900          TA:=A[436+I];
63000          IF TA GTR 25 AND TA LSS 240 THEN ELSE A[436+I]:=0;
63100       END;
63200       REDO1:DOPP1SUM:=DOPP1SUM2:=DOPP1NUM:=0;
63300       FOR I:=2 STEP 1 UNTIL 16 DO
63400       BEGIN
63500          TA:=A[420+I];
63600          IF TA NEQ 0 THEN
63700          BEGIN
63800             DOPP1SUM:=DOPP1SUM+TA;
63900             DOPP1SUM2:=DOPP1SUM2+TA*TA;
64000             DOPP1NUM:=DOPP1NUM+1;
64100          END;
64200       END;
64300       %  IF MORE THAN 8 HALF CYCLES DROP 1ST FOUR
64400       IF DOPP1NUM GEQ 8 AND NOT ONCETHRO THEN
64500       BEGIN
64600          A[422]:=A[423]:=A[424]:=0;
64700          ONCETHRO:=TRUE;
64800          GO TO REDO1;
64900       END;
```

```
65000          NEED THREE HALF CYCLES
65100          DOPP1NUM LSS 3 THEN
65200          BEGIN
65300          VELOCITY1:=1000;DOPP1SIG:=0;
65400          END ELSE
65500       BEGIN
65600          DOPP1MEAN:=DOPP1SUM/DOPP1NUM;
65700          DOPP1SIG:=((DOPP1SUM2-DOPP1SUM*DOPP1SUM/DOPP1NUM
65800          )/(DOPP1NUM-1));
65900          IF DOPP1SIG LSS 0 THEN DOPP1SIG:=10000;
66000          DOPP1SIG:=SQRT(DOPP1SIG);
66100          VELOCITY1:=5.69*(5000/2/DOPP1MEAN-30);
66200          DOPP1SIG:=5.69*(5000/2/DOPP1MEAN/DOPP1MEAN)*DOPP1SIG;
66300       END;
66400       % REPEAT FOR OTHER OFFSET.
66500       ONCETHRO:=FALSE;
66600       REDO2:DOPP2SUM:=DOPP2SUM2:=DOPP2NUM:=0;
66700       FOR I:=2 STEP 1 UNTIL 16 DO
66800       BEGIN
66900          TA:=A[436+I];
67000          IF TA NEQ 0 THEN
67100          BEGIN
67200             DOPP2SUM:=DOPP2SUM+TA;
67300             DOPP2SUM2:=DOPP2SUM2+TA*TA;
67400             DOPP2NUM:=DOPP2NUM+1;
67500          END;
67600       END;
67700       IF DOPP2NUM GEQ 8 AND NOT ONCETHRO THEN
67800       BEGIN
67900          A[438]:=A[439]:=A[440]:=0;
68000          ONCETHRO:=TRUE;
68100          GO TO REDO2;
68200       END;
68300       IF DOPP2NUM LSS 3 THEN
68400       BEGIN
68500          VELOCITY2:=1000;DOPP2SIG:=0;
68600       END ELSE
68700       BEGIN
68800          DOPP2MEAN:=DOPP2SUM/DOPP2NUM;
68900          DOPP2SIG:=((DOPP2SUM2-DOPP2SUM*DOPP2SUM/DOPP2NUM)
69000          /(DOPP2NUM-1));
69100          IF DOPP2SIG LSS 0 THEN DOPP2SIG:=10000;
69200          DOPP2SIG:=SQRT(DOPP2SIG);
69300          VELOCITY2:=5.69*(30-5000/2/DOPP2MEAN);
69400          DOPP2SIG:=5.69*(5000/2/DOPP2MEAN/DOPP2MEAN)*DOPP2SIG;
69500       END;
69600    END OF DOPPLER;
69700
69800

69900    PROCEDURE PHASEHEIGHT(D,START,DURATION,EMAX);
70000    REAL ARRAY D[0];
70100    INTEGER START,DURATION,EMAX;
70200    % PHASEHEIGHT FINDS ANGLES OF ELEVATION USING
70300    % CALIBRATION DATA. IT THEN FINDS "UNAMBIGUOUS"
70400    % HEIGHT USING RANGE VALUE.
70500    BEGIN
70600       REAL PHASESUM1,PHASESUM2,PHASESUM12,PHASESUM22,
70700       PDATA1,PDATA2,PHASEMEAN1,PHASEMEAN2,MINDIFF,DIFFH,GGAMMA,
70800       RTHETA,RALFA;
70900       INTEGER KOUNT,N,ENDD,START2;
71000       REAL ARRAY BETA[1:5],HEIGHT[0:5],ALFA[1:5],
71100       THETA[1:5];
71200       % FIND START FOR HEIGHT,REJECTING PHASES WHOSE AMPLITUDE
71300       % IS LESS THAN 0.7 OF MAX.
71400       ENDD:=MIN(DURATION,30);
71500       ENDD:=MIN(EMAX+3,ENDD);
71600       IF EMAX GTR 3 THEN START2:=EMAX-3 ELSE START2:=1;
71700       FOR I:=START2 STEP 1 UNTIL ENDD DO
71800       IF NEWA[START+I] LSS 0.7*NEWA[START+EMAX] THEN
71900       NEWA[START-120+I]:=NEWA[START-60+I]:=0;
72000       % FIND MEAN,STD DEVIATION OF PHASES
72100       PHASESUM1:=PHASESUM2:=PHASESUM12:=PHASESUM22:=
72200       KOUNT:=0;
72300       IF COS12POS THEN
72400       BEGIN
72500          FOR I:=START2 STEP 1 UNTIL ENDD DO
72600          BEGIN
72700             PDATA1:=NEWA[START-120+I];
72800             IF PDATA1 NEQ 0 THEN
72900             BEGIN
73000                PHASESUM1:=PHASESUM1+PDATA1;
73100                PHASESUM12:=PHASESUM12+PDATA1*PDATA1;
73200                KOUNT:=KOUNT+1;
```

```
73300            END;
73400         END;
73500         IF KOUNT EQL 0 THEN KOUNT:=1;
73600         PHASEMEAN1:=PHASESUM1/KOUNT;
73700         IF KOUNT EQL 1 THEN KOUNT:=2;
73800         D[4]:=PHASEMEAN1;
73900         D[5]:=(PHASESUM12/(KOUNT-1)-PHASESUM1*PHASESUM1
74000         /KOUNT/(KOUNT-1));
74100         % WATCH FOR ROUNDOFF ERRORS WHEN SIG=0
74200         IF D[5] LSS 0 THEN D[5]:=ABS(D[5]);
74300         D[5]:=SQRT(D[5]);
74400         IF PHASEMEAN1 LSS 0 THEN PHASEMEAN1:=PHASEMEAN1+2*PIE;
74500      END ELSE
74600      BEGIN
74700         FOR I:=START2 STEP 1 UNTIL ENDD DO
74800         BEGIN
74900            PDATA1:=NEWA[START-120+I];
75000            IF PDATA1 LSS 0 THEN PDATA1:=PDATA1+2*PIE;
75100            IF PDATA1 NEQ 0 THEN
75200            BEGIN
75300               PHASESUM1:=PHASESUM1+PDATA1;
75400               PHASESUM12:=PHASESUM12+PDATA1*PDATA1;
75500               KOUNT:=KOUNT+1;
75600            END;
75700         END;
75800         IF KOUNT EQL 0 THEN KOUNT:=1;
75900         PHASEMEAN1:=PHASESUM1/KOUNT;
76000         IF KOUNT EQL 1 THEN KOUNT:=2;
76100         D[4]:=PHASEMEAN1;
76200         D[5]:=(PHASESUM12/(KOUNT-1)-PHASESUM1*PHASESUM1
76300         /KOUNT/(KOUNT-1));
76400         IF D[5] LSS 0 THEN D[5]:=ABS(D[5]);
76500         D[5]:=SQRT(D[5]);
76600         IF PHASEMEAN1 LSS 0 THEN PHASEMEAN1:=PHASEMEAN1+2*PIE;
76700      END;
76800      KOUNT:=0;
76900      IF COS13POS THEN
77000      BEGIN
77100         FOR I:=START2 STEP 1 UNTIL ENDD DO
77200         BEGIN
77300            PDATA2:=NEWA[START-60+I];
77400            IF PDATA2 NEQ 0 THEN
77500            BEGIN
77600               PHASESUM2:=PHASESUM2+PDATA2;
77700               PHASESUM22:=PHASESUM22+PDATA2*PDATA2;
77800               KOUNT:=KOUNT+1;
77900            END;
78000         END;
78100         D[6]:=KOUNT;
78200         IF KOUNT EQL 0 THEN KOUNT:=1;
78300         PHASEMEAN2:=PHASESUM2/KOUNT;
78400         IF KOUNT EQL 1 THEN KOUNT:=2;
78500         D[7]:=PHASEMEAN2;
78600         D[8]:=(PHASESUM22/(KOUNT-1)-PHASESUM2*PHASESUM2
78700         /KOUNT/(KOUNT-1));
78800         IF D[8] LSS 0 THEN D[8]:=ABS(D[8]);
78900         D[8]:=SQRT(D[8]);
79000         IF PHASEMEAN2 LSS 0 THEN PHASEMEAN2:=PHASEMEAN2+2*PIE;
79100      END ELSE
79200      BEGIN
79300         FOR I:=START2 STEP 1 UNTIL ENDD DO
79400         BEGIN
79500            PDATA2:=NEWA[START-60+I];
79600            IF PDATA2 LSS 0 THEN PDATA2:=PDATA2+2*PIE;
79700            IF PDATA2 NEQ 0 THEN
79800            BEGIN
79900               PHASESUM2:=PHASESUM2+PDATA2;
80000               PHASESUM22:=PHASESUM22+PDATA2*PDATA2;
80100               KOUNT:=KOUNT+1;
80200            END;
80300         END;
80400         D[6]:=KOUNT;
80500         IF KOUNT EQL 0 THEN KOUNT:=1;
80600         PHASEMEAN2:=PHASESUM2/KOUNT;
80700         IF KOUNT EQL 1 THEN KOUNT:=2;
80800         D[7]:=PHASEMEAN2;
80900         D[8]:=(PHASESUM22/(KOUNT-1)-PHASESUM2*PHASESUM2
81000         /KOUNT/(KOUNT-1));
81100         IF PHASEMEAN2 LSS 0 THEN PHASEMEAN2:=PHASEMEAN2+2*PIE;
81200         IF D[8] LSS 0 THEN D[8]:=ABS(D[8]);
81300         D[8]:=SQRT(D[8]);
81400      END;
```

```
81500       % ACCOUNT FOR DIFFERENTIAL PHASES.
81600       PHASEMEAN1:=PHASEMEAN1-DIFF12;
81700       PHASEMEAN2:=PHASEMEAN2-DIFF13;
81800       % PUT IN USEFUL RANGES
81900       IF PHASEMEAN1 GEQ 2*PIE THEN PHASEMEAN1:=PHASEMEAN1-2*PIE;
82000       IF PHASEMEAN1 GEQ 2*PIE THEN PHASEMEAN1:=PHASEMEAN1-2*PIE;
82100       IF PHASEMEAN1 LSS 0 THEN PHASEMEAN1:=PHASEMEAN1+2*PIE;
82200       IF PHASEMEAN1 LSS 0 THEN PHASEMEAN1:=PHASEMEAN1+2*PIE;
82300       IF PHASEMEAN2 LSS -PIE THEN PHASEMEAN2:=PHASEMEAN2+2*PIE;
82400       IF PHASEMEAN2 LSS -PIE THEN PHASEMEAN2:=PHASEMEAN2+2*PIE;
82500       IF PHASEMEAN2 GEQ PIE THEN PHASEMEAN2:=PHASEMEAN2-2*PIE;
82600       IF PHASEMEAN2 GEQ PIE THEN PHASEMEAN2:=PHASEMEAN2-2*PIE;
82700       %FIND POSSIBLE VALUES OF BETA REMEMBERING ONLY
82800       %300<R<400 KM ARE VALID.
82900       FOR I:=1 STEP 1 UNTIL 4 DO
83000       BEGIN
83100          N:=I+16;
83200          BETA[I]:=(PHASEMEAN1+2*N*PIE)/20/2/PIE;
83300          IF BETA[I] GTR 1 THEN BETA[I]:=1;
83400          BETA[I]:=ARCCOS(BETA[I]);
83500       END;
83600       %FIND GGAMMA-NO AMBIGUITY
83700       GGAMMA:=(PHASEMEAN2/1.6/2/PIE);
83800       IF GGAMMA GTR 1 THEN GGAMMA:=1;
83900       GGAMMA:=ARCSIN(GGAMMA);
84000       %NOW FIND THE FOUR HEIGHTS
84100       HEIGHT[I]:=I:=0;
84200       WHILE (HEIGHT[I] LSS 70 OR HEIGHT[I] GTR 120)
84300       AND I LSS 5 DO
84400       BEGIN
84500          I:=I+1;
84600          ALFA[I]:=ARCTAN(SIN(GGAMMA)/COS(BETA[I]));
84700          THETA[I]:=COS(BETA[I])/COS(ALFA[I]);
84800          IF THETA[I] GTR 1 THEN THETA[I]:=1;
84900          THETA[I]:=ARCCOS(THETA[I]);
85000          HEIGHT[I]:=SQRT(RE*RE+MEANRANGE*MEANRANGE+
85100          2*RE*MEANRANGE*SIN(THETA[I]))-RE;
85200       END;
85300       IF I LEQ 4 THEN
85400       BEGIN
85500          D[0]:=HEIGHT[I];
85600          D[2]:=THETA[I]*57.296;
85700          D[3]:=ALFA[I]*57.296;
85800       END ELSE
85900       %IF NO VALUES 70<H<120,TAKE NEAREST TO 95 KM
86000       BEGIN
86100          MINDIFF:=35;KOUNT:=1;
86200          FOR I:= 1 STEP 1 UNTIL 4 DO
86300          BEGIN
86400             DIFFH:=ABS(HEIGHT[I]-95);
86500             IF DIFFH LSS MINDIFF THEN
86600             BEGIN
86700                MINDIFF:=DIFFH;
86800                KOUNT:=I;
86900             END;
87000          END;
87100          D[0]:=HEIGHT[KOUNT];
87200          D[2]:=THETA[KOUNT]*57.296;
87300          D[3]:=ALFA[KOUNT]*57.296;
87400       END;
87500       % FIND HEIGHT UNCERTAINTY
87600       RTHETA:=D[2]/57.296;
87700       RALFA:=D[3]/57.296;
87800       D[1]:=SIN(RTHETA)*RANGESIG+D[0]*COS(RTHETA)/(2*PIE*SIN(
87900       RTHETA)**2)*(ABS(SIN(RALFA)/1.6*(D[8]+CALSIG13))+
88000       ABS(COS(RALFA)/20*(D[5]+CALSIG12)));
88100    END OF PHASEHEIGHT;
88200
88300

88400    PROCEDURE LINEDENSITY;
88500    % LINE DENSITY IS CALCULATED FOR SUITABLE LOCAL ECHOES FROM
88600    % ELEVATION,AZIMUTH,RANGE,HEIGHT AND AMPLITUDE INFORMATION.
88700    BEGIN
88800       REAL VTR,R0;
88900       % IS THE ECHO SUITABLE.
89000       IF OPUT[17] LSS 7 OR OPUT[17] GTR 20 THEN
89100       OPUT[52]:=0 ELSE
89200       BEGIN
89300          IF ABS(OPUT[18]) GTR 8  OR OPUT[4] GTR 245 THEN
89400          OPUT[52]:=0 ELSE
```

```
89500           BEGIN
89600              % FIND INITIAL RADIUS
89700              R0:=(EXP((OPUT[15]-100)/5))**0.4;
89800              % FIND POWER GAIN
89900              VTR:=200*(COS(9.4*OPUT[18]/57.296))**1.5*
90000              (EXP(-(ABS(OPUT[17]-22)**3/1800)))**2;
90100              OPUT[52]:=2.22@4*OPUT[4]*(OPUT[8]*1.0@3)**1.5*
90200              EXP(0.305*R0*R0)/VTR;
90300           END;
90400        END;
90500     END OF LINEDENSITY;
90600
90700
90800     PTRA:=POINTER(A);PTROUT:=POINTER(OPUT);
90900     FILEND:=FALSE;
91000     READ (CARD,/,CALTHRESH,GOODCALTHRESH,RANGETHRESH,AMPLTHRESH,
91100     PHASETHRESH,RTHRESH,STARTDAYS,STARTHRS,STARTMINS
91200     ,DIFF12,CALSIG12,DIFF13,CALSIG13);
91300     WRITE(LP,*/,CALTHRESH,GOODCALTHRESH,RANGETHRESH,AMPLTHRESH,
91400     PHASETHRESH,RTHRESH,STARTDAYS,STARTHRS,STARTMINS
91500     ,DIFF12,CALSIG12,DIFF13,CALSIG13);
91600     %CARDECHOES[0] IS THE TOTAL NUMBER OF THESE ECHOES
91700     READ (CARD,/,FOR I:=0 STEP 1 UNTIL 600 DO CARDECHOES[I]);
91800     RE:=6367.65;PIE:=4*ARCTAN(1);RXDELAY:=3.10;
91900     READECHO:IF NOT FILEND THEN
92000     READ (MAGTAPE,2730,PTRA)[EOF] ELSE
92100     BEGIN
92200        WRITE (LP,<"END OF TAPE">);
92300        GO TO FINISH;
92400     END;
92500     GO TO SKIP;
92600     EOF:FILEND:=TRUE;
92700     SKIP:PHASESORT;
92800     IF A[455] EQL 0 THEN IF NOT3PHASES THEN
92900     BEGIN
93000        WRITE(LP,<"NOT THREE PHASES ON CALIBRATION",F5.0>,
93100        A[454]);
93200        GO TO READECHO;
93300     END ELSE CALIBRATE;
93400     IF A[455] EQL 1 THEN DDOUBLE:=FALSE ELSE
93500     DDOUBLE:=TRUE;
93600     ARRANGE;
93700     % NOW CALL UP AMPLITUDE AS NECESSARY,CHECKING
93800     % FOR ANY WEST COAST ONLYS
93900     IF NOT DDOUBLE AND NOT LOCAL THEN
94000     BEGIN
94100        WRITE (LP,<"WEST COAST ONLY",F5.0>,A[454]);
94200        GO TO READECHO;
94300     END;
94400     AMPLITUDE(120,NEWA[578],CL);
94500     FOR I:=0 STEP 1 UNTIL 7 DO OPUT[I]:=CL[I+1];
94600     OPUT[0]:=-OPUT[0]*123.01;
94700     RANGE;
94800     OPUT[8]:=MEANRANGE;OPUT[9]:=RANGESIG;OPUT[10]:=RANGENUM;
94900     IF NEWA[578] GTR 0 THEN
95000     BEGIN
95100        DOPPLER;
95200        OPUT[11]:=VELOCITY1;OPUT[12]:=DOPP1SIG;
95300        OPUT[13]:=VELOCITY2;OPUT[14]:=DOPP2SIG;
95400     END ELSE OPUT[11]:=OPUT[12]:=OPUT[13]:=OPUT[14]:=0;
95500     IF MIN(NEWA[578],30)-OPUT[5] LSS 2 THEN
95600     BEGIN
95700        WRITE(LP,<"NOT TWO PHASES FROM LOCAL MAX",F5.0>,A[454]);
95800        GO TO READECHO;
95900     END;
96000     PHASEHEIGHT(DL,120,NEWA[578],OPUT[5]);
96100     FOR I:=0 STEP 1 UNTIL 8 DO OPUT[15+I]:=DL[I];
96200     IF DDOUBLE THEN
96300     BEGIN
96400        AMPLITUDE(400,NEWA[579],CR);
96500        FOR I:=1 STEP 1 UNTIL 8 DO OPUT[23+I]:=CR[I];
96600        OPUT[24]:=-OPUT[24]*123.01;
96700        IF MIN(NEWA[579],30)-OPUT[29] LSS 2 THEN
96800        BEGIN
96900           WRITE(LP,<"NOT TWO PHASES FROM WC MAX",F5.0>,A[454]);
97000           GO TO READECHO;
97100        END;
97200        PHASEHEIGHT(DR,400,NEWA[579],OPUT[29]);
97300        FOR I:=0 STEP 1 UNTIL 8 DO OPUT[32+I]:=DR[I];
97400        OPUT[41]:=57.296*ARCCOS(COS(OPUT[17]/57.296)*COS(
97500        OPUT[34]/57.296)*COS((OPUT[18]-OPUT[35])/57.296)
97600        + SIN(OPUT[17]/57.296)*SIN(OPUT[34]/57.296));
97700     END ELSE FOR I:=24 STEP 1 UNTIL 41 DO
```

```
 97800     OPUT[I]:=0;
 97900     ECHOTIME:=A[1]+60*A[2]+3600*A[3]+24*3600*A[4];
 98000     OPUT[42]:=NEWA[580];OPUT[43]:=(ECHOTIME-CALTIME)/60;
 98100     % TIME OF DAY-UNCHANGED
 98200     OPUT[44]:=A[1];OPUT[45]:=A[2];OPUT[46]:=A[3];
 98300     OPUT[47]:=A[4];OPUT[48]:=A[454];
 98400     % CHECK FOR PERSISTENTS
 98500     IF OPUT[48] GTR 5 THEN
 98600     BEGIN
 98700        IF ABS(OPUT[8]-RANGECHECK) LSS 5 AND
 98800        ABS(ECHOTIME-TIMECHECK) LSS 60 THEN
 98900        OPUT[49]:=1 ELSE OPUT[49]:=0;
 99000     END ELSE OPUT[49]:=0;
 99100     OPUT[50]:=NEWA[578];OPUT[51]:=NEWA[579];
 99200     LINEDENSITY;
 99300     TIMECHECK:=ECHOTIME;RANGECHECK:=OPUT[8];
 99400     WRITE(LP,<13F10.4>,FOR I:=0 STEP 1 UNTIL
 99500     51 DO OPUT[I]);
 99600     WRITE(LP,<E8.2>,OPUT[52]);
 99700     WRITE(OUTPUT,318,PTROUT);
 99800     GO TO READECHO;
 99900     FINISH:LOCK(OUTPUT,CRUNCH);
100000 END OF MAIN PROGRAM.
```

```
 SSS  EEEE  L     EEEE   CCC  TTTTT  OOO  RRRR
S   S E     L     E     C   C   T   O   O R   R
S     E     L     E     C       T   O   O R   R
 SSS  EEE   L     EEE   C       T   O   O RRRR
    S E     L     E     C       T   O   O R R
S   S E     L     E     C   C   T   O   O R  R
 SSS  EEEEE LLLLL EEEEE  CCC    T    OOO  R   R
```

278 RECORDS, CREATED 30/01/80

```
 100 BEGIN
 200    % SELECTOR READS PROCESSED METEOR RECORDS PRODUCED
 300    % BY ANALYSE ,SELECTS   THEM IF THEY MEET CERTAIN
 400    % SELECTION REQUIREMENTS,SOME OF WHICH ARE READ
 500    % FROM CARDS AND FINDS VARIOUS FREQUENCY DISTRIBUTIONS.
 600    FILE LP(KIND=PRINTER,MAXRECSIZE=22);
 700    FILE CARD(KIND=READER);
 800    FILE MAGTAPE(FILETYPE=7);
 900    LABEL READECHO,EOF,FINISH,SKIP,NEXTAPE;
1000    INTEGER ARRAY NUM[1:100];
1100    REAL ARRAY A[0:52],POSN[1:10000],VARBLE[1:10000],ADELTA,EDELTA,
1200    HDELTA[1:20];
1300    REAL MINRANGE,MAXRANGE,CORRELN,MAXAZMTH,HEIGHTSIG,
1400    RANGESIG,DB,DA,DE,DGAMMA,DBETA,MINSPEC,MEAN,
1500    EBETA,MAXTIME,MINTIME,EGAMMA,D12,D13,
1600    MAXSPEC,HMIN,HMAX,MAXALPHA,MINALPHA,BP;
1700    INTEGER RISETIME,MAXAMPLITUDE,PHASENUM,CALIBRNTIME,
1800    RANGENUM,I,J,N,TMODE,L,K,KOUNT;
1900    BOOLEAN FILEND;
2000    POINTER PTRA;
2100    REAL AZMTH,ELEVN,HEIGHT,REPLUSH,RE,REPLUSH2,RADAZMTH,
2200    DEGTORAD,RADELEVN,RANGE,CS,CORADRLAT,TLAT,TLONG,
2300    RADTLAT,RADTLONG,PIE,RADRLAT,B,GGAMMA,RADRLONG,
2400    RLAT,RLONG,DECLINATION,RADDECLINATION,INCLINATION,RADINCLINATION,
2500    E,RADANGLE,RADSPECANGLE,OFFSPECULARANGLE;

2600    PROCEDURE OFFSPECANGLE;
2700    %THIS PROCEDURE CALCULATES THE OFF SPECULAR ANGLE FOR
2800    %EACH SELECTED ECHO.
2900    BEGIN
3000       AZMTH:=22.75+A[18];ELEVN:=A[17];HEIGHT:=A[15]*1000;
3100       REPLUSH:=RE+HEIGHT;REPLUSH2:=REPLUSH*REPLUSH;
3200       RADAZMTH:=DEGTORAD*AZMTH;RADELEVN:=DEGTORAD*ELEVN;
3300       RANGE:=SQRT(REPLUSH2-(RE*COS(RADELEVN))**2)-RE*SIN(RADELEVN);
3400       CS:=ARCCOS((RE*RE+REPLUSH2-RANGE*RANGE)/2.0/RE/REPLUSH);
3500       CORADRLAT:=ARCCOS(COS(PIE/2.0-RADTLAT)*COS(CS)+
3600       SIN(PIE/2.0-RADTLAT)*SIN(CS)*COS(RADAZMTH));
3700       RADRLAT:=PIE/2.0-CORADRLAT;
3800       B:=ARCSIN(SIN(PIE/2.0-RADTLAT)*SIN(RADAZMTH)/SIN(CORADRLAT));
3900       IF RADAZMTH GEQ PIE/2.0 AND RADAZMTH LSS 3*PIE/2.0 THEN
4000       GGAMMA:=B ELSE GGAMMA:=PIE-B;
4100       RADRLONG:=RADTLONG-ARCSIN(SIN(CS)*SIN(RADAZMTH)/SIN(CORADRLAT));
4200       RLAT:=RADRLAT/DEGTORAD;RLONG:=RADRLONG/DEGTORAD;
4300       DECLINATION:=0.8*((-0.206*(170.0-RLONG)+RLAT)-46.0)+23.33;
4400       INCLINATION:=0.71*((0.261*(170.0-RLONG)+RLAT)-46.0)+71.1;
4500       E:=ARCSIN(RE*COS(RADELEVN)/REPLUSH);
4600       RADDECLINATION:=DEGTORAD*DECLINATION;
4700       RADINCLINATION:=DEGTORAD*INCLINATION;
4800       RADANGLE:=ARCCOS(-COS(E)*SIN(RADINCLINATION)-
4900       SIN(E)*COS(RADINCLINATION)*COS(GGAMMA+RADDECLINATION));
5000       RADSPECANGLE:=PIE/2.0-RADANGLE;
5100       OFFSPECULARANGLE:=RADSPECANGLE/DEGTORAD;
5200    END OF OFFSPECANGLE;
5300    TLAT:=43.625;TLONG:=172.4;PIE:=4.0*ARCTAN(1.0);
5400    DEGTORAD:=PIE/180;N:=0;RE:=6367650;
5500    RADTLAT:=DEGTORAD*TLAT;RADTLONG:=DEGTORAD*TLONG;
5600    PTRA:=POINTER(A);
5700    READ(CARD,/,CORRELN,MAXAMPLITUDE,RISETIME,MINRANGE,
5800    MAXRANGE,RANGESIG,HEIGHTSIG,MAXAZMTH,PHASENUM,CALIBRNTIME,
5900    MINSPEC,MAXSPEC,TMODE,
6000    HMIN,HMAX,MAXALPHA,MINALPHA,MAXTIME,MINTIME);
6100    WRITE(LP,*/,CORRELN,MAXAMPLITUDE,RISETIME,MINRANGE,
6200    MAXRANGE,RANGESIG,HEIGHTSIG,MAXAZMTH,PHASENUM,CALIBRNTIME,
6300    MINSPEC,MAXSPEC,TMODE,
6400    HMIN,HMAX,MAXALPHA,MINALPHA,MAXTIME,MINTIME);
6500    FILEND:=FALSE;
6600    READECHO:IF NOT FILEND THEN
6700    READ(MAGTAPE,318,PTRA)[EOF] ELSE
6800    BEGIN
6900       WRITE(LP,<"END OF TAPE",/>);
7000       GO TO NEXTAPE;
7100    END;
```

```
 7200    GO TO SKIP;
 7300    EOF:FILEND:=TRUE;
 7400    % NOW SELECT DESIRED ECHOES.
 7500    SKIP:IF A[0] LEQ 0 THEN GO READECHO;
 7600    IF A[2] LSS CORRELN THEN GO READECHO;
 7700    IF A[4] GTR MAXAMPLITUDE THEN GO READECHO;
 7800    IF A[5] GTR RISETIME THEN GO READECHO;
 7900    IF A[8] LSS MINRANGE THEN GO READECHO;
 8000    IF A[8] GTR MAXRANGE THEN GO READECHO;
 8100    IF A[9] GTR RANGESIG THEN GO READECHO;
 8200    IF A[10] LSS 5 THEN GO READECHO;
 8300    IF A[16] GTR HEIGHTSIG THEN GO READECHO;
 8400    %CORRECT FOR UNEVEN GROUND AND TROPOSPHERIC REFRACTION
 8500    A[17]:=*-0.15;
 8600    A[17]:=ARCCOS(1.00023*COS(A[17]*DEGTORAD))/DEGTORAD;
 8700    A[15]:=SQRT(RE*RE/1@6+A[8]*A[8]+2*RE/1@3*A[8]*SIN(DEGTORAD
 8800    *A[17]))-RE/1@3;
 8900    IF A[15] LSS HMIN OR A[15] GTR HMAX THEN GO READECHO;
 9000    IF ABS(A[18]) GTR MAXAZMTH THEN GO READECHO;
 9100    IF A[21] LSS PHASENUM THEN GO READECHO;
 9200    IF A[42] EQL 0 THEN GO READECHO;
 9300    IF A[43] GTR CALIBRNTIME THEN GO READECHO;
 9400    IF A[49] EQL 1 THEN GO READECHO;
 9500    IF A[52] LSS MINALPHA OR A[52] GTR MAXALPHA THEN GO TO READECHO;
 9600    IF A[46]+A[45]/60 LSS MINTIME OR A[46]+A[45]/60 GTR MAXTIME
 9700    THEN GO READECHO;
 9800    CASE TMODE OF
 9900    BEGIN
10000       %TMODE 0 - HEIGHT DISTRIBUTION
10100       BEGIN
10200          FOR K:=1 STEP 1 UNTIL 50 DO
10300          BEGIN
10400             IF A[15] GTR 69+K AND A[15] LEQ 70+K THEN
10500             BEGIN
10600                NUM[K]:=*+1;
10700                MEAN:=*+A[15];KOUNT:=*+1;
10800                GO TO READECHO;
10900             END;
11000          END;
11100          GO TO READECHO;
11200       END;
11300       %TMODE 1 - RANGE DISTRIBUTION
11400       BEGIN
11500          FOR K:=1 STEP 1 UNTIL 30 DO
11600          BEGIN
11700             IF A[8] GTR 295+K*5 AND A[8] LEQ 300+K*5 THEN
11800             BEGIN
11900                NUM[K]:=*+1;
12000                MEAN:=*+A[8];KOUNT:=*+1;
12100                GO TO READECHO;
12200             END;
12300          END;
12400          GO TO READECHO;
12500       END;
12600       %TMODE 2 - AZIMUTH DISTRIBUTION
12700       BEGIN
12800          FOR K:=1 STEP 1 UNTIL 60 DO
12900          BEGIN
13000             IF A[18] GTR -31+K AND A[18] LEQ -30+K THEN
13100             BEGIN
13200                NUM[K]:=*+1;
13300                MEAN:=*+A[18];KOUNT:=*+1;
13400                GO TO READECHO;
13500             END;
13600          END;
13700          GO TO READECHO;
13800       END;
13900       %TMODE 3 - ELEVATION DISTRIBUTION
14000       BEGIN
14100          FOR K:=1 STEP 1 UNTIL 70 DO
14200          BEGIN
14300             IF A[17] GTR 4.5+K/2 AND A[17] LEQ 5+K/2 THEN
14400             BEGIN
14500                NUM[K]:=*+1;
14600                MEAN:=*+A[17];KOUNT:=*+1;
14700                GO TO READECHO;
14800             END;
14900          END;
15000          GO TO READECHO;
15100       END;
15200       %TMODE 4 - LOG(Q) DISTRIBUTION
15300       BEGIN
15400          FOR K:=1 STEP 1 UNTIL 45 DO
15500          BEGIN
```

```
15600            IF LOG(A[52]) GTR 11.4+K/10 AND LOG(A[52]) LEQ 11.5+K/10 THEN
15700            BEGIN
15800               NUM[K]:=*+1;
15900               MEAN:=*+LOG(A[52]);KOUNT:=*+1;
16000               GO TO READECHO;
16100            END;
16200         END;
16300         GO TO READECHO;
16400      END;
16500      %TMODE 5 - POSITIVE AZIMUTH HEIGHT DISTRIBUTION
16600      BEGIN
16700         IF A[8] LSS 0 THEN GO READECHO;
16800         FOR K:=1 STEP 1 UNTIL 50 DO
16900         BEGIN
17000            IF A[15] GTR 69+K AND A[15] LEQ 70+K THEN
17100            BEGIN
17200               NUM[K]:=*+1;
17300               MEAN:=*+A[15];KOUNT:=*+1;
17400               GO TO READECHO;
17500            END;
17600         END;
17700         GO TO READECHO;
17800      END;
17900      %TMODE 6 - NEGATIVE AZIMUTH HEIGHT DISTRIBUTION
18000      BEGIN
18100         IF A[18] GTR 0 THEN GO READECHO;
18200         FOR K:=1 STEP 1 UNTIL 50 DO
18300         BEGIN
18400            IF A[15] GTR 69+K AND A[15] LEQ 70+K THEN
18500            BEGIN
18600               NUM[K]:=*+1;
18700               MEAN:=*+A[15];KOUNT:=*+1;
18800               GO TO READECHO;
18900            END;
19000         END;
19100         GO TO READECHO;
19200      END;
19300      %TMODE 7 - UNCERTAINTIES
19400      BEGIN
19500         DB:=20*LOG(A[4]/4);
19600         FOR K:=1 STEP 1 UNTIL 16 DO
19700         BEGIN
19800            IF DB GTR 19+K AND DB LEQ 20+K THEN
19900            BEGIN
20000               DA:=DEGTORAD*A[18];BP:=SQRT(A[21]);DE:=DEGTORAD*A[17];
20100               DGAMMA:=ARCSIN(COS(DE)*SIN(DA));
20200               DBETA:=ARCCOS(COS(DE)*COS(DA));
20300               D12:=20;D13:=1.6;
20400               EBETA:=(A[20]+0.04)/(2*PIE*D12*SIN(DBETA))/BP;
20500               EGAMMA:=(A[23]+0.04)/(2*PIE*D13*COS(DGAMMA))/BP;
20600               ADELTA[K]:=*+1/(1+TAN(DA)**2)*(COS(DGAMMA)/COS(DBETA)*
20700               EGAMMA+SIN(DGAMMA)*SIN(DBETA)/COS(DBETA)**2*EBETA)/
20800               DEGTORAD;
20900               EDELTA[K]:=*+(SIN(DA)*COS(DGAMMA)*EGAMMA+COS(DA)*
21000               SIN(DBETA)*EBETA)/SIN(DE)/DEGTORAD;
21100               HDELTA[K]:=*+A[16]/BP;
21200               NUM[K]:=*+1;
21300               GO TO READECHO;
21400            END;
21500         END;
21600         GO TO READECHO;
21700      END;
21800   END OF FIRST CASE;
21900   NEXTAPE:CASE TMODE OF
22000   BEGIN
22100      BEGIN
22200         WRITE(LP,<"MID HEIGHT = ",F5.1,X4,I4>,FOR I:=1
22300         STEP 1 UNTIL 50 DO [69.5+I,NUM[I]]);
22400         IF KOUNT EQL 0 THEN KOUNT:=1;
22500         WRITE(LP,*/,MEAN,KOUNT,MEAN/KOUNT);
22600      END;
22700      BEGIN
22800         WRITE(LP,<"MID RANGE = ",F8.1,X4,I4>,FOR I:=1
22900         STEP 1 UNTIL 30 DO [297.5+5*I,NUM[I]]);
23000         IF KOUNT EQL 0 THEN KOUNT:=1;
23100         WRITE(LP,*/,KOUNT,MEAN,MEAN/KOUNT);
23200      END;
23300      BEGIN
23400         WRITE(LP,<"MID AZIMUTH = ",F5.1,X4,I4>,FOR I:=1
23500         STEP 1 UNTIL 60 DO [-30.5+I,NUM[I]]);
23600         IF KOUNT EQL 0 THEN KOUNT:=1;
23700         WRITE(LP,*/,MEAN,KOUNT,MEAN/KOUNT);
23800      END;
```

```
23900       BEGIN
24000          WRITE(LP,<"MID ELEVATION = ",F5.1,X4,I4,X4,
24100          "NORMALISED VALUE = ",I4>,FOR I:=1 STEP 1 UNTIL 70
24200          DO [4.75+I/2,NUM[I],SQRT(NUM[I]/COS(DEGTORAD*(4.75+I/2))**2
24300          *SQRT(SIN(DEGTORAD*(4.75+I/2))))]);
24400          IF KOUNT EQL 0 THEN KOUNT:=1;
24500          WRITE(LP,*/,MEAN,KOUNT,MEAN/KOUNT);
24600       END;
24700       BEGIN
24800          WRITE(LP,<"MID LOG(ALPHA) = ",F5.1,X4,I4>,FOR I:=1
24900          STEP 1 UNTIL 45 DO [11.45+I/10,NUM[I]]);
25000          IF KOUNT EQL 0 THEN KOUNT:=1;
25100          WRITE(LP,*/,MEAN,KOUNT,MEAN/KOUNT);
25200       END;
25300       BEGIN
25400          WRITE(LP,<"POSITIVE AZIMUTH MID HEIGHT = ",F5.1,X4,I4>,FOR I:=1
25500          STEP 1 UNTIL 50 DO [69.5+I,NUM[I]]);
25600          IF KOUNT EQL 0 THEN KOUNT:=1;
25700          WRITE(LP,*/,KOUNT,MEAN,MEAN/KOUNT);
25800       END;
25900       BEGIN
26000          WRITE(LP,<"NEGATIVE AZIMUTH MID HEIGHT = ",F5.1,X4,I4>,FOR I:=1
26100          STEP 1 UNTIL 50 DO [69.5+I,NUM[I]]);
26200          IF KOUNT EQL 0 THEN KOUNT:=1;
26300          WRITE(LP,*/,MEAN,KOUNT,MEAN/KOUNT);
26400       END;
26500       BEGIN
26600          FOR I:=1 STEP 1 UNTIL 16 DO
26700          BEGIN
26800             IF NUM[I]  EQL 0 THEN NUM[I]:=1;
26900             ADELTA[I]:=*/NUM[I];EDELTA[I]:=*/NUM[I];HDELTA[I]:=*/NUM[I];
27000          END;
27100          WRITE(LP,<"AZIMUTH UNCERTAINTY = ",F5.2,X2,
27200          "ELEVATION UNCERTAINTY = ",F6.3,X2,"HEIGHT UNCERTAINTY = ",
27300          F5.2,X2,"NUMBER OF ECHOES = ",I4,X4,"S/N = ",F5.1>,
27400          FOR I:=1 STEP 1 UNTIL 16 DO [ADELTA[I],EDELTA[I],
27500          HDELTA[I],NUM[I],19.5+I]);
27600       END;
27700    END OF SECOND CASE;
27800    FINISH:END.
```